TRANSITION METAL NITRIDE SURFACES AND ELECTRONS: AN AES/LEED STUDY OF THE FORMATION OF TRANSITION METAL NITRIDE SURFACES AND THE EFFECT OF ELECTRON STIMULATION

By

YAN CHEN

A thesis

submitted to the School of Graduate Studies

in partial fulfilment of the requirements

for the degree

Doctor of Philosophy

McMaster University

February 1995

TRANSITION METAL NITRIDE SURFACES AND ELECTRONS

DOCTOR OF PHILOSOPHY (1995)
(Chemistry)

McMASTER UNIVERSITY
Hamilton, Ontario

TITLE: Transition Metal Nitride Surfaces and Electrons: An AES/LEED Study of the Formation of Transition Metal Nitride Surfaces and the Effect of Electron Stimulation

AUTHOR: Yan Chen (McMaster University)

SUPERVISOR: Professor P. T. Dawson

NUMBER of PAGES: xxviii, 228

ABSTRACT

This thesis reports a comprehensive study of transition metal nitride surfaces and the effects of electron beam stimulation on the adsorption processes. Since the nitrides of transition metals in the fourth to sixth group of the periodic table have important industrial applications as coating materials and heterogeneous catalysts, the understanding of the surface nitriding processes has tremendous technological importance.

AES studies have been carried out on the N-Zr system over a wide energy range which has led to the identification of new Auger cross transition features induced by nitriding and to an understanding of the intensity variation and energy shift of Auger features during nitriding. Consequently, a quantitative surface analysis method has been established for this system.

The effect of electron beam stimulation on the processes of ammonia adsorption and nitride film growth has been investigated on polycrystalline Ti, Cr, Zr, W and three single crystal tungsten surfaces. This study demonstrates methods for performing experiments properly when surface science tools utilising electron probes are used, and provides a potential application for the development of new techniques for preparing transition metal nitride films.

Titanium and tungsten represent extremes in the stability of their nitrides. Extensive studies of the interaction of ammonia with these metals are reported in this thesis.

The adsorption of N_2 and NH_3 gases with and without electron beam stimulation has been studied on titanium surfaces. This has led to an understanding of many surface processes including the adsorption of gas molecules, the diffusion of nitrogen atoms into the bulk and the initial stage of nitride film growth. It has been found that only with electron stimulation does the adsorption and diffusion behaviour of N_2 gas mimic that of ground state NH_3 gas.

AES and LEED studies on the interaction of NH_3 with tungsten single crystal surfaces have been performed including the stimulation effect of electrons in ammonia adsorption. Nitrogen desorption and diffusion have been observed during annealing and surface structural changes have been monitored. A remarkable surface reconstruction involving nitrogen atom transfer from the outermost layer to the underlayer has been revealed on the W(100) surface. These results lead to new insights into the complex surface chemistry of the NH_3-W(100) system.

ACKNOWLEDGEMENT

My special thanks and gratitude to my supervisor, Dr. P. T. Dawson for his great patience, consistent interest and encouragement over the course of this study. He has introduced me to the most challenging research field, surface science, and guided me throughout the duration of my graduate work. I deeply appreciate his keen criticism, invaluable advice and suggestions in the preparation of the thesis.

My sincere thanks to Dr. A. J. Yarwood and Dr. R. S. Dumont, who served as members of my Ph. D. Supervisory Committee. Their interest, advice and encouragement are gratefully appreciated.

I would like to thank Dr. K. K. Tzatzov for many discussions, valuable advice and suggestions in the preparation of this thesis.

I would like to thank C. Butcher, W. H. Gong in the Institute for Materials Research, and G. Innocenti, V. Perno in the Science Instrument and Student Machine Shop for their technical assistance.

I thank the following for providing financial assistance: McMaster University, in the form of a graduate assistantship; National Science and Engineering Research Council in the form of a graduate scholarship and a research grant to Dr. Dawson. I would also like to express my gratitude for the award of the James A. Morrison Memorial Scholarship.

Finally, my thanks to my parents, husband and son for their love, understanding and support throughout the duration of my graduate work.

TABLE OF CONTENTS

LIST OF FIGURES

at room temperature using the multi orifices gas doser. The background ammonia pressure was pumped down to $1x10^{-9}$ torr before AES analysis.

Figure 5-6. The Auger spectra of (a) pure chromium and (b) after 5 minutes ammonia adsorption at room temperature using the multi orifices gas doser.

Figure 5-7. The N(KLL) peak-to-peak height data are plotted versus ammonia adsorption time. The adsorption was carried out at room temperature using two methods: (a) the data are taken from separate adsorption experiments, which all started from a clean Cr surface; ammonia was pumped away before taking each Auger spectrum; (b) the sample surface was exposed to ammonia gas at a constant pressure of $2x10^{-6}$ torr and monitored by Auger continuously. In method (a), the electron beam bombardment effect is eliminated, while in method (b), the surface is exposed to ammonia gas and the electron beam simultaneously.

Figure 5-8. The Auger spectra taken from (a) pure titanium and (b) an ammonia saturated titanium surface which was prepared by method (a) described in figure 5-9.

Figure 5-9. The escape-depth-averaged nitrogen to titanium ratio, <x>, is plotted versus total ammonia dosing time. The data were obtained in three different ways: in (a) the Auger spectrum was taken after each minute ammonia dosing; in (b) the first Auger spectrum was taken after the first minute ammonia dosing, the next Auger spectrum was taken after continuous 10 minutes ammonia dosing with no electron bombardment of the surface, thereafter, Auger spectra were taken after each minute ammonia dosing ; (c) data were obtained from two separate ammonia adsorption experiments, both starting from a clean titanium surface and with no

and ammonia gas at 300 K. In (a) the increase of nitrogen concentration, <x>, with time is shown for the collision of nitrogen molecules from background gas at a pressure of $2x10^{-6}$ torr with simultaneous continuous electron bombardment for Auger analysis. For comparison the data for the adsorption of ammonia gas from figure 5-8 (a) are re-plotted against electron beam exposure time in curve (b). Electron stimulated adsorption of nitrogen gas to full coverage does not occur at 300 K unlike the behaviour observed for ammonia gas.

Figure 6-6. The escape-depth-averaged nitrogen to titanium ratio, <x>, after reaction with nitrogen gas as a function of sample temperature at five different gas fluxes: (a) $5.9x10^{13}$; (b) $2.4x10^{14}$; (c) $1.9x10^{15}$; (d) $3.0x10^{15}$ and (e) $7.0x10^{15}$ molecules cm^{-2} s^{-1}. There was no electron bombardment during gas dosing.

Figure 6-7. Low-energy MVV Auger spectra after the interaction of nitrogen gas with titanium at 760 K, using gas fluxes of (a) $5.9x10^{13}$ (b) $2.4x10^{14}$ (c) $1.9x10^{15}$ and (d) $7.0x10^{15}$ molecules cm^{-2} s^{-1}. The corresponding <x> values from the high-energy LMM spectra can be seen in figure 6-6.

Figure 6-8. The MVV low-energy Auger electron spectra of titanium after reaction with N_2 gas with a flux of $5.9x10^{13}$ molecules cm^{-2} s^{-1} at different surface temperatures: (a) 300 K (b) 640 K (c) 700 K (d) 760 K and (e) 810 K.

Figure 6-9. The MVV low-energy Auger electron spectra of titanium after reaction with N_2 gas with a flux of $7.0x10^{15}$ molecules cm^{-2} s^{-1} at different surface temperatures: (a) 300 K (b) 640 K (c) 760 K and (d) 960 K.

Figure 6-10. Scale model showing plan views of the basal plane of titanium on which (a) nitrogen atoms have been chemisorbed to one-half monolayer

Figure 7-6. Beam incidence geometry.

Figure 7-7. The W(NNN) Auger peak intensity ratios, I(G)/I(N), where I(G) was determined with a glancing and I(N) with a normal incidence primary beam for (a) a clean metal surfaces; (b) an 800 K ammonia reacted surfaces; and (c) a highly covered surface prepared by electron beam stimulated ammonia adsorption at 300 K.

Figure 7-8. The absence of ammonia adsorption at 300 K on the sample produced by ammonia interaction with a W(100) sample at 800 K. The Auger spectrum shown in (a) was taken after 30 minutes ammonia surface reaction at 800 K; after (a), ammonia gas with a flux of 5.7×10^{15} molecules cm^{-2} s^{-1} was dosed on the surface for 10 minutes at 300 K and the Auger spectrum obtained after the adsorption is shown in (b); the difference spectrum (b)-(a) is shown in (c).

Figure 7-9. The effect of electron beam stimulation on adsorption at 300 K was examined for the W(100) surface after 800 K ammonia reaction. The N(KLL) peak-to-peak height is plotted against beam time. In this experiment ammonia gas was introduced into the chamber and kept at constant pressure dynamically, and the surface was monitored by AES continuously.

Figure 7-10. Annealing profiles of W(100) for two nitrogen coverages. The high coverage sample was prepared by electron beam stimulated ammonia adsorption at 300 K and its annealing profiles are shown with solid lines. The low coverage sample was prepared by ammonia adsorption at 300 K without electron beam stimulation and its annealing profiles are shown with dashed lines. At each annealing temperature, the sample was held at constant temperature for 10 minutes in vacuum and an Auger spectrum was taken after the sample was cooled to room temperature.

Figure 7-11. The fractional advancement of the transition, x, is plotted against annealing time at constant temperature, where x is defined by equation 7-1.

Figure 7-12. A plot of lnt against 1/T, where t is the time required to achieve 90% completion at temperature T. The activation energy for the transition process was calculated from the slope as 256 kJ mol^{-1}.

Figure 7-13. LEED patterns observed with an electron beam energy of 200 eV from a low nitrogen coverage W(100) sample, prepared by ammonia adsorption at 300 K. (a) the clean W(100) surface; (b) after ammonia adsorption with a gas flux $5.7x10^{15}$ molecules cm^{-2} s^{-1} for 10 minutes; (c) after 600 K annealing; (d) after 700 K annealing; (e) after 750 K annealing; (f) after 800 K annealing; (g) after 850 K annealing; and (h) after 900 K annealing. At each temperature the sample was annealed in vacuum for 10 minutes.

Figure 7-14. LEED beam indexing: (a) for pattern a, (b) for pattern c, (c) for pattern e, and (d) for pattern h shown in figure 7-13.

Figure 7-15. LEED results with a beam energy of 200 eV from a fully-covered nitrogen on W(100) surface prepared by electron beam stimulated ammonia adsorption at 300 K. (a) after 700 K annealing; (b) after 750 K annealing.

Figure 7-16. A scale drawing of the W(100), W(110) and W(111) planes; the planar atomic density, ρ, and the distance between the nearest planes, d, for these three orientations are given.

Figure 7-17. Calculated sputter depth profiles for (a) a nitrogen underlayer distribution model, and (b) a nitrogen overlayer model are shown with solid lines. The initial nitrogen distribution models are shown with dashed lines.

LIST OF TABLES

GLOSSARY

$\gamma_{i,XYZ}$	Auger transition probability
$D(E_A)$	Electron detector efficiency
E_a	Activation energy
E_A	Auger electron energy
E_P	Primary electron beam
I_A	Auger current
$I_{i,XYZ}$	Auger current of the XYZ transition from atom i
$j(E)$	Secondary-emission current
λ_p	Inelastic electron mean free path of the primary beam
λ_m	Inelastic mean free path of Auger electrons in monolayer
$\sigma_0(E)$	Inelastic electron-electron scattering cross section
S_A	Sensitivity factor for element A
$T(E_A)$	Transmission efficiency of the analyzer
U_{eff}	Hole-hole interaction energy
Φ	Work function
ν	Pre-exponential factor
$\langle x \rangle$	Escape-depth-averaged nitrogen to metal atomic ratio
AES	Auger electron spectroscopy
EELS	Electron energy loss spectroscopy
FEM	Field emission microscope
IMFP	Inelastic mean-free path
LEED	Low energy electron diffraction
PPHt	Peak-to-peak height
RFA	Retarding field analyzer
STM	Scanning tunnelling microscope

TDS	Thermal desorption spectroscopy
UHV	Ultra-high vacuum
UPS	Ultraviolet photoemission spectroscopy
XPS	X-ray photoelectron spectroscopy

CHAPTER ONE

INTRODUCTION

1.1. TRANSITION METAL NITRIDE SURFACES

The nitrides of transition metals in the fourth to sixth group of the periodic table have both theoretical and technological interest. Table 1-1 compares the melting points of nitrides with those of the parent transition metals [Toth, 1971]. Most of the transition metals in this group form refractory nitrides with extremely high melting points. The transition metals in the lower right corner of the table, Mo and W, are exceptions in that they form unstable nitrides which decompose at relatively low temperature. In fact, tungsten is a catalyst for the ammonia synthesis/decomposition reaction, and its nitrides are interesting reaction intermediates. The physical and chemical properties of these nitrides have been reviewed by Toth [1971], Schwarzkopf et al. [1953] and Benesovksy et al. [1981]. This group of nitrides is characterized by high melting points (except molybdenum nitride and tungsten nitride), ultrahardness (comparable to diamond), good electrical and thermal conductivity, and slow resistance to corrosion. Because of their unique properties, these nitrides are widely used as refractory, wear and corrosion resistant surface coatings [Buhl et al., 1981; Komiya et al., 1979], and thin-film

Table 1-1. Comparison of the melting points of transition metals and their nitrides

Ti	1677°C	V	1917°C	Cr	1900°C
Zr	1852°C	Nb	2487°C	Mo	2610°C
Hf	2222°C	Ta	2997°C	W	3380°C

TiN	2949°C	VN	2177°C	CrN	1500°C
ZrN	2982°C	NbN	2204°C	MoN	D
HfN	3387°C	TaN	3093°C	WN	D

* D means that the material decomposes at a relatively low temperature, less than 800°C.

interconnections in integrated circuits [Pokela et al., 1991; Nakasaki et al., 1988].

Owing to the loss of neighbouring atoms and changes in the effective force constants for the surface atoms, the atoms at the surface of an alloy experience an environment quite different from that in the bulk. The surface composition may differ from that of the bulk because of adsorption and segregation, and the surface structure may differ from that of the bulk because the surface atoms seek new equilibrium positions. Sometimes, surface reconstruction can be induced by the change of surface composition. Since the performance of a catalyst or a thin film depends largely on its surface properties, the investigations of physical-chemical processes that influence the surface composition and surface structure are of great importance. An understanding of the interaction between nitrogen containing gas molecules and transition metal surfaces, including adsorption, diffusion, and the initial stages of nitride film growth, are critical to the formation of nitrides and important in their applications.

1.2. THE EFFECTS OF ELECTRON STIMULATION ON SURFACES

When surface science probes which use an electron beam for surface analysis are applied to study surface science processes, electrons can actively participate in these processes. There have been several reports on the perturbing effects of electron beam irradiation during Auger electron spectroscopy (AES) and low energy electron diffraction (LEED) analysis, and the effects of electronic excitation, charging and beam heating

during AES were reviewed by Pantano and Madey [1981]. It has been found that an electron beam impinging on a gas covered surface may cause the desorption of ions and neutrals, the dissociation of the molecules on the surface, and conversion of the adlayer into a new binding state. In many cases, the original objective of these studies was not to study beam damage, but rather adsorption behaviour. However, the perturbing effects of the electron beam upon either the adsorbate or the substrate often necessitated a characterization of the electron beam effect. These investigations turn out to develop new techniques based on these effects. For example, electron stimulated desorption has become an established analysis technique and has been reviewed by Menzel [1975].

1.3. SCOPE OF THE THESIS

The purpose of this research is to study the interaction of nitrogen containing gas molecules with transition metal surfaces including the adsorption of gas molecules, the initial stage of nitride film growth, and nitrogen atom bulk diffusion, and to investigate the electron stimulation effect on these surface processes.

To achieve this objective, quantitative surface analysis methods needed to be developed to determine the chemical composition of the surface layer. AES is one of the most widely used methods for chemical analysis of surfaces. Recent developments have improved our ability to convert Auger spectra into surface concentrations. The composition in the outermost layer, the most interesting layer for surface science processes, can be determined by low energy AES experiments. Extensive Auger studies on the N-Ti and N-V systems have been carried out in our laboratory, and quantitative

analysis methods have been developed for these two systems [Dawson, and Tzatzov, 1985; 1986; 1987; 1990; 1991_1]. In this research, these quantitative Auger studies have been extended to the N-Zr system. Consequently, a technique for the quantification of Auger spectra of zirconium nitrides in a wide energy region, including zirconium NVV and MNN Auger transitions has been developed.

Ammonia adsorption and the effect of electron beam stimulation have been studied on Ti, Cr, Zr and W surfaces. In this group of transition metals, Ti, Cr and W are situated in the upper left, upper and lower right corners of table 1-1. They have quite different physical and chemical properties. Especially Ti and W have very different affinities toward nitrogen. Titanium forms a typical refractory nitride while tungsten is a catalyst for ammonia synthesis/decomposition reaction and only forms unstable nitrides. However, the experimental results show similarities for Ti, Cr and W in the behaviour towards ammonia adsorption at 300 K and electron beam stimulation effects on ammonia adsorption. On the other hand, Zr is the next element following Ti in the same group of the periodic table, and the chemistry of Zr is similar to that of Ti. However, the experimental results show quite different behaviour towards ammonia adsorption by Zr and Ti. A possible explanation lies in the geometric factor, since in these four transition metals, zirconium has the biggest lattice parameter. If the geometric factor is the key effect here, then it is important to carry out studies on well characterized single crystal surfaces.

The contrast between titanium and tungsten nitrides makes the investigation of the

surface processes and comparison of the surface properties particularly interesting for these two systems. Detailed studies have been focused on N-Ti and N-W, including the adsorption of nitrogen containing gas molecules, the initial stage of nitride film growth, and the bulk diffusion of nitrogen atoms.

To study the structural effect, this investigation has been extended to tungsten single crystal surfaces. LEED was used to monitor the change of surface structure, and AES was used to monitor the composition change in surface layers. This study has demonstrated that the interaction between adsorbed species and surface metal atoms induces surface reconstruction, and that this causes dramatic change in surface properties. The understanding of these surface processes is very important to the development of transition metal nitride thin film technology.

CHAPTER TWO

EXPERIMENTAL METHODS

2.1. SAMPLE PREPARATION

The samples used for this work were disks sliced from high purity rods which were mechanically polished, finally with 1 μm diamond paste, solvent degreased and transferred to the ultra high vacuum (UHV) system.

After each sample had been introduced into the UHV chamber, a series of tests was carried out to optimize the cleaning procedure for the sample. For example, when the polycrystalline tungsten sample was introduced into the chamber, C, O, and S impurities were detected by AES on its surface. The segregation and bulk diffusion temperature ranges of these impurities were determined by a series of annealing tests. Based on the information obtained from these tests, an optimized cleaning procedure was developed. The first step was to anneal the sample at 1100K to drive S and P to the surface, followed by Ar^+ ion sputtering to remove the outermost layers. The cycle of annealing-sputtering was repeated till no S and P could be detected by AES even after 1100 K annealing. The second step was to remove C as CO and CO_2 by dosing O_2 gas to the sample surface at ~1000 K. The final step of the procedure was to decompose the surface

oxide by flashing to ~2000 K. All samples were cleaned in an UHV chamber using an optimized cleaning procedure. In this way a clean surface zone was produced in the sample with a depth deep enough for the planned surface studies.

Transition nitride films were obtained in situ either by ion implantation of nitrogen ions with energies in the range of 3-5 kV, as in the preparation of zirconium nitride films or by NH_3 surface reaction, as in the preparation of tungsten nitrides.

2.2. THE DESIGN OF A SIMPLE GAS DOSER FOR SURFACE STUDIES

The introduction of gas molecules for interaction with the transition metal surfaces studied in this work was accomplished using a simple multi-orifice doser.

The main considerations in the design of a gas doser for surface science application were to get an enhanced gas flux at the surface of a sample with homogeneous distribution across the sample and to keep the background gas pressure in the UHV chamber at a low level. The gas dosers used for surface science can be divided into 2 groups: single-orifice and multi-orifice gas dosers. The single-orifice doser is simple in construction but usually produces large gas flux gradients across the sample. Madey [1972] showed that for a single-orifice gas doser with a ratio of thickness to radius, L/r, equal to one, the computed flux at the centre of the sample (10.8 mm away from the orifice) is 15% higher than the average flux, and the flux at the sample edge is 15% lower than the average flux. It has been demonstrated by Campbell and Valone

[1985] that a multichannel capillary array doser slightly larger than the sample can provide good constant flux across the sample if it can be placed a very short distance, ~0.1D from the sample, where D is the diameter of the sample. In our work, the average diameter of the samples is ~1cm. To bring a large doser within ~ 1 mm of the face of the sample is not possible. Besides, the construction and calibration of such a doser is difficult as discussed by Charles et al. [1984]. In the present work, the objective for the doser design is to overcome the large flux gradient problem of a single orifice doser with a design which is simple to construct. Finally a design with six orifices was chosen. The geometrical arrangement of the orifices in the gas doser has been optimized by theoretical calculation, and the doser examined by experimental tests.

The theoretical calculation of the gas flux distribution out of the nozzle of the doser [Campbell and Valone, 1985; Nanbu, 1985; Adamson et al., 1988] assumed a molecular flow regime where the mean free path is much greater than the thickness of the orifice and that intermolecular collisions within the orifice can be neglected. The form of the flux distribution from the orifice is usually assumed to follow a "cosine law", but in fact, the distribution strongly depends on thickness-diameter ratio of the orifice. Nanbu [1985] calculated the angular distribution of the flux, $P(\theta)$, by Monte-Carlo methods, and showed that even for a small thickness-diameter ratio, L/d, such as 0.3, the distribution of $p(\theta)$ showed a marked deviation from the "cosine law", figure 2-1.

In our design, the thickness-diameter ratio, $L/d = 2$ was chosen for each orifice to produce a sharper beam shape. The empirical equations deduced by Nanbu were used

to calculate the angular distribution, $p(\theta)$, for each orifice,

$$p(\theta) = 0.771 \cos\theta - 1.124 \cos^2\theta + 1.819 \cos^3\theta \qquad (\theta \geq \theta^*), \qquad (2\text{-}1)$$

$$P(\theta) = 0.3 \left[(\cos\theta / \cos\theta^*)^{15.86} - 1 \right] + 1.092 \qquad (\theta < \theta^*), \qquad (2\text{-}2)$$

with the definitions of the polar angles θ and θ^* as shown in figure 2-2.

In considering the design of a doser which is simple to construct and can satisfy the scientific requirements, we selected a design with six orifices hexagonally distributed on the doser. The total distribution of the flux out of these six orifices was computed for different geometrical arrangements of the orifices, and the geometrical arrangement which produced the most homogeneous flux distribution across the sample and contributed the smallest fraction of the flux to the background pressure was chosen. The calculated flux distribution is shown in figure 2-3.

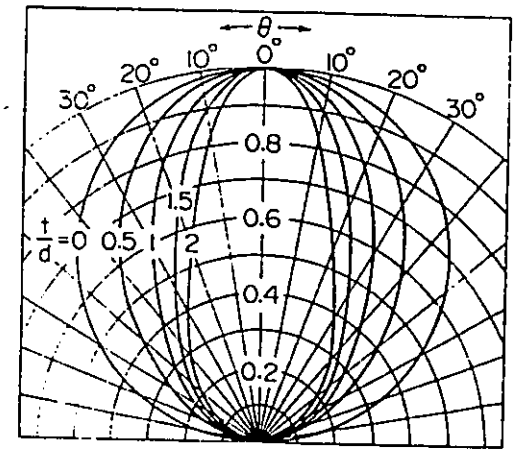

Figure 2-1. The angular distribution of the flux, $P(\theta)$, calculated by Monto-Carlo methods; after Nanbu (1985)

After the doser had been built, a hot oxygen dosing test was carried out on a stainless steel sample. A homogeneous blue colour was expected, but the results showed six intense spots, the image of the six orifices, on the sample. The only explanation for

the failure is that the gas fluxes before the orifices were not random. Since the calculation of the flux distribution is based on the molecular flow model, it is not valid when the gas flow before the orifices is directed. To avoid direct beams, a hemispherical copper sheet with a central hole was used to create a random molecular distribution before the orifices. Three stainless steel samples about 1.2 cm^2 in size were used to examine the performance of the modified doser with oxygen hot dosing. Different distances between the sample and the doser, 3 mm, 5 mm, 7mm, were used for these three tests. The sample 3 mm away from the doser showed six spots, the image of the six orifices; the sample 5 mm away from the doser still showed these spots but diffuse, the sample 7 mm away from the doser showed a nice homogeneous blue colour all over the sample except the edges. In the edges of the sample, one can find the boundary of the oxide, which means the flux is quite concentrated on the sample. As shown by the experimental results this design was successful and can meet all the requirements for surface science applications. The final design of the doser is schematically shown in figure 2-4.

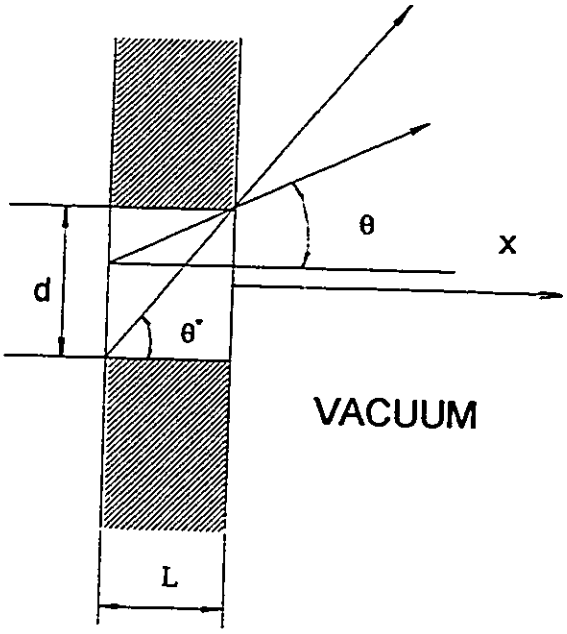

Figure 2-2. The definition of polar angles θ and θ'

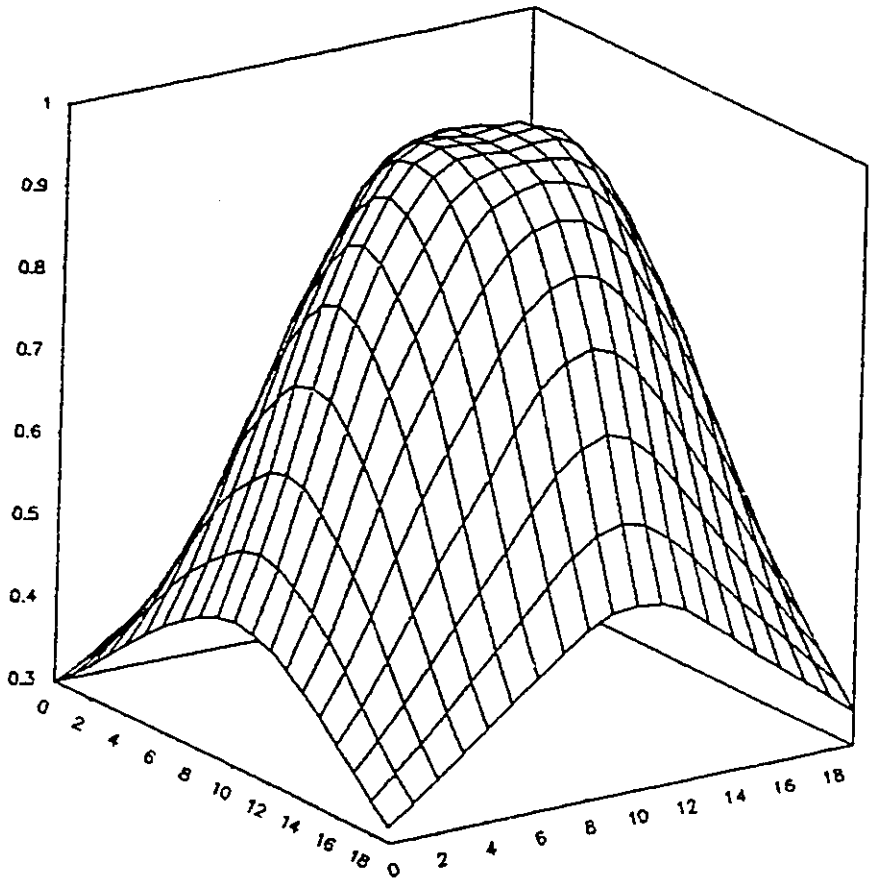

Figure 2-3. The calculated total flux distribution from six orifices in a hexagonal arrangement (the geometry of the orifices is shown in figure 2-4).

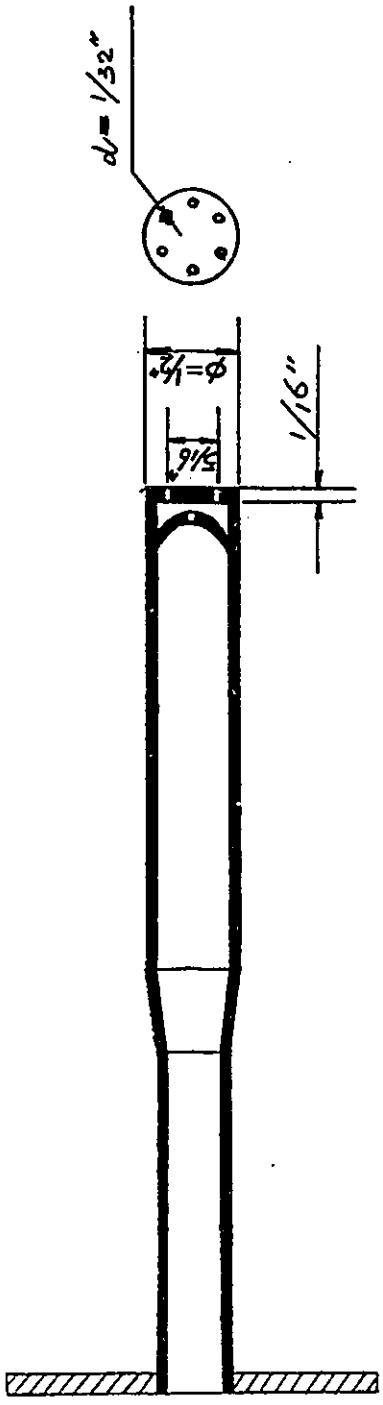

Figure 2-4. Schematic drawing of the gas doser.

2.3. SURFACE ANALYSIS BY AUGER ELECTRON SPECTROSCOPY

Surface analysis was performed by Auger Electron Spectroscopy (AES). In AES, the high energy incident electron beam strikes the target, penetrates with both elastic and inelastic scattering and eventually comes to rest at a depth of 1-2 μm, as shown in figure 2-5. The measurement of the energy spectrum of the emitted electrons is the whole basis of this technique. A typical overall energy spectrum of back-scattered electrons, shown in figure 2-6, has several distinct regions. At the primary beam energy, E_p, there is a sharp peak due to electrons that have been elastically scattered back out of the specimen. If the specimen is crystalline, these electrons will carry the diffraction information, which is exploited in techniques such as low energy electron diffraction. At the other end, is the large, broad peak of low energy secondary electrons. Superimposed on this secondary distribution are the peaks due to Auger electrons. The Auger effect is the de-excitation of an ionised atom by a non-radiative process. When an electron is ejected from the inner shell, X, of an atom, the atom can be subsequently de-excited by an electron falling from a higher level Y, the energy balance being removed by ejection of an electron from level Z. The last electron is called an Auger electron, and the process is called an XYZ Auger transition, schematically shown in figure 2-7. The kinetic energy of the Auger electron for the XYZ transition is approximately given by the expression:

$$E_{XYZ} = E_X - E_Y - E_Z - \Phi, \qquad (2\text{-}3)$$

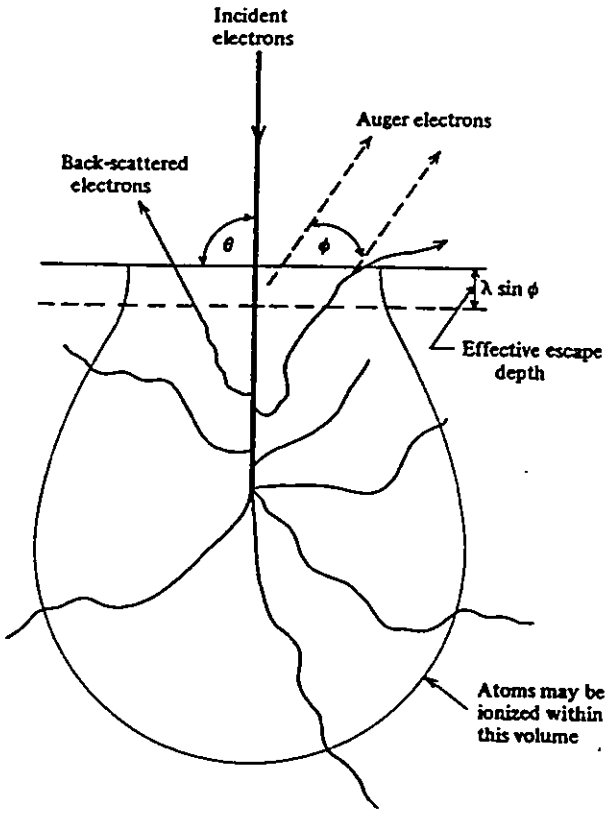

Figure 2-5. The spatial distribution of Auger production. After Bishop, H. E. (1989).

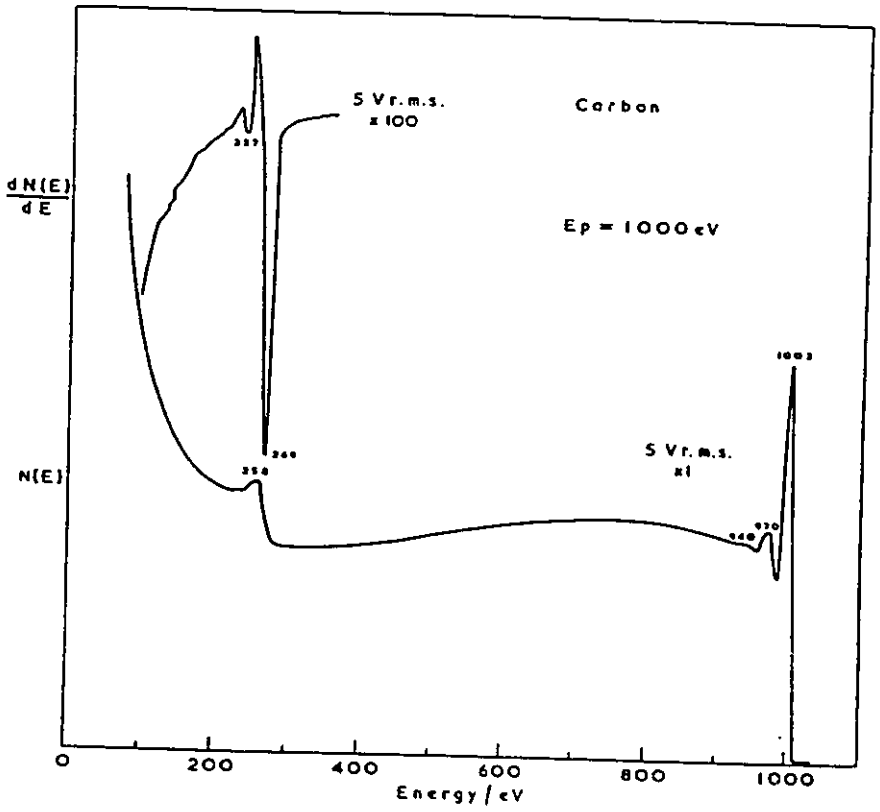

Figure 2-6. Lower curve: distribution of energies of secondary electrons ejected from a graphite surface by incident electrons of energy 1000 eV. Upper curve: differential distribution over the energy range containing the carbon KLL Auger peaks. After Briggs and Seah (1983).

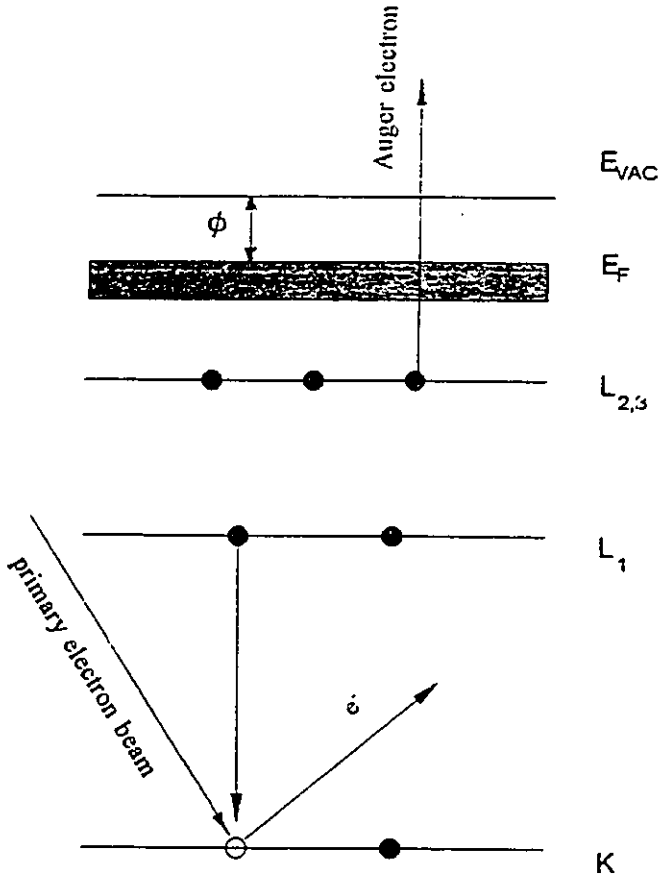

$$E_{KLL} = E(K) - E(L_1) - E(L_{2,3}) - \phi$$

Figure 2-7. The $KL_1L_{2,3}$ Auger process. The atom is ionized from the K energy level, and decays by filling this hole with an electron falling from the L_1 energy level. The excess energy available is taken up by the emission of an Auger electron from the $L_{2,3}$ energy level.

where Φ is the work function of the analyzer material.

The reason that AES is a surface-sensitive technique lies in the intense inelastic scattering that occurs for electrons in the low energy range so that Auger electrons from only the outermost layers of a solid survive to be ejected with characteristic energy and measured in the spectrum. The inelastic mean free path (IMFP) is defined as the characteristic distance travelled in a solid before a flux of Auger electrons with a given kinetic energy is reduced to 1/e of the original value through inelastic scattering events. The value of IMFP depends both on the matrix and the Auger electron energy. A compilation of existing experimental literature data due to Brundle [1974] is shown in figure 2-8. The data reveal that the analyzed energy windows used in this work, 15-520 eV, are in the most surface-sensitive region of the energy spectrum.

In this work, a four-grid retarding field analyzer (RFA) was used to perform Auger electron energy analysis [Briggs and Seah, 1983; Ertl and Kuppers 1974; Chang 1974; Thompson et al. 1984]. The inner and outer grids are grounded in order to provide a uniform field in the sample region and to shield the collector from capacitive coupling with the modulation on the other grids. The middle two grids are connected together and have the retarding potential applied to them. Superimposed on the retarding potential is a small modulation voltage from a signal source. The modulated collector current is then compared in the lock-in amplifier with the reference signal from the signal source. The collected current I is a function of the retarding potential V and the modulation signal, $k\sin\omega t$, and can be written as $I(V+k\sin\omega t)$. The Taylor expansion is then

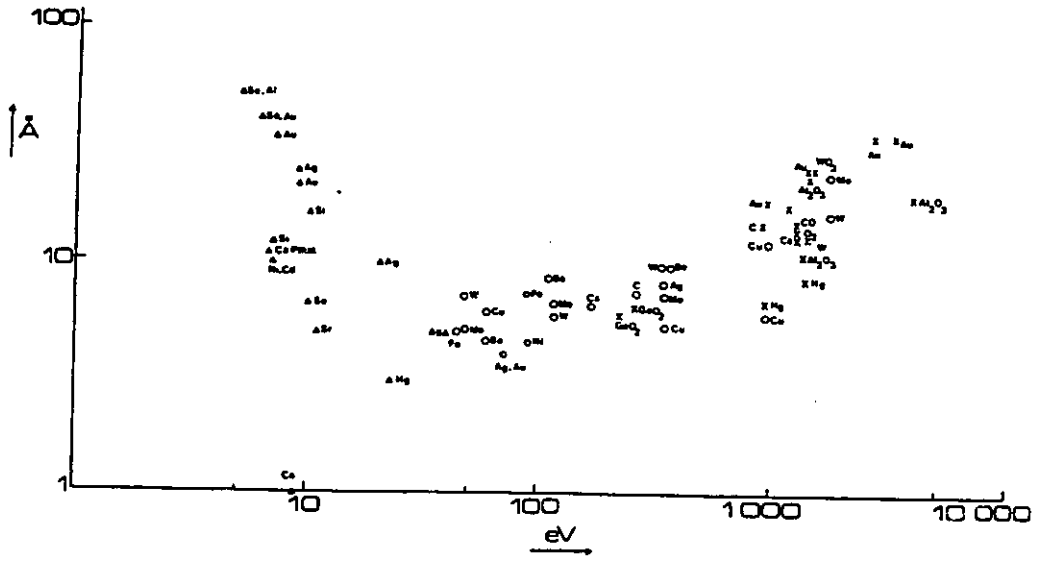

Figure 2-8. Experimental values for the electron mean free path in several materials, compiled by Brundle (1974).

$$I(V+k\sin\omega t)= I + k\sin\omega t(dI/dV) + k^2\sin^2\omega t(d^2I/dV^2)/\ 2! + \ldots . \qquad (2\text{-}4)$$

When this is rearranged algebraically, the coefficient of sinωt is found to be

$$k(dI/dV) + k^3(d^3I/dV^3)/\ 8 + \ldots, \qquad (2\text{-}5)$$

and the coefficient of cos2ωt to be

$$(k^2/4)(d^2I/dV^2) + (k^4/48)(d^4I/dV^4) + \ldots .$$

Since (dI/dV) is the energy distribution N(E) and (d^2I/dV^2) the differential distribution N'(E), the amplitude of the first harmonic is proportional to the former and of the second harmonic to the latter, provided the higher order derivatives can be neglected. In practice this will be obeyed if the modulation amplitude is less than half the width of an Auger peak. Differential analysis mode, N'(E) , was used in this work. The apparatus used for this work is shown schematically in figure 2-9.

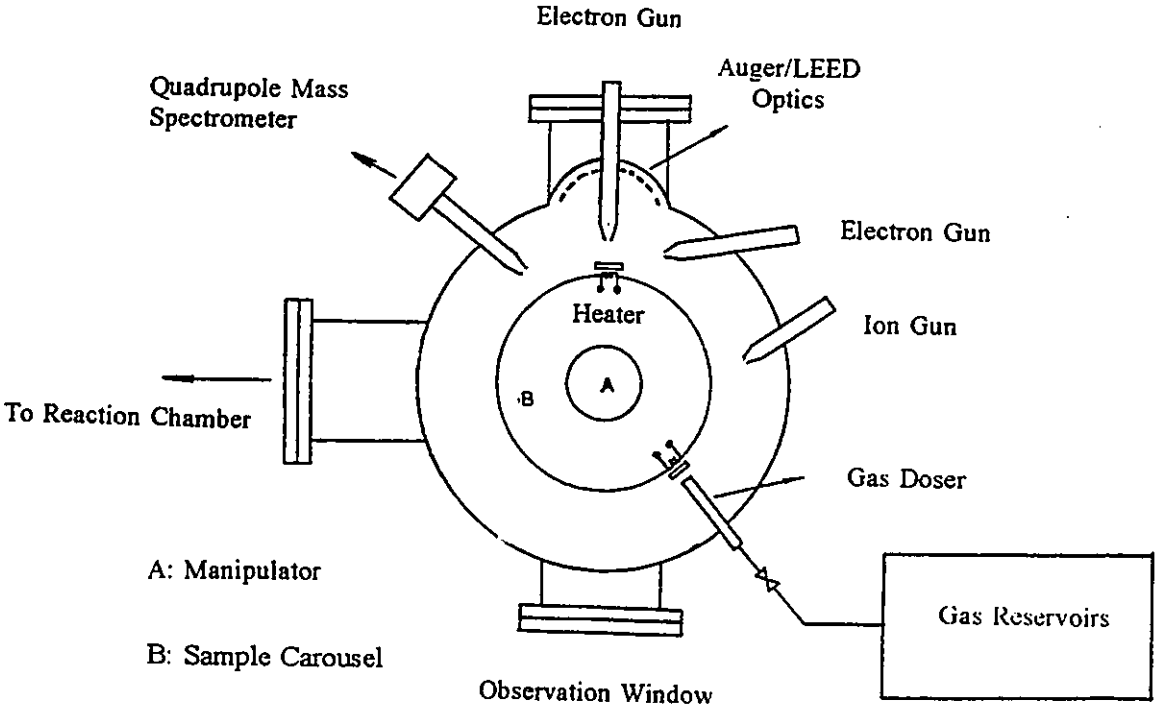

Figure 2-9. Schematic drawing of the ultra-high vacuum system.

2.4. SURFACE STRUCTURE STUDIED BY LEED

The microscopic surface structures of single crystal surfaces were studied by Low Energy Electron Diffraction (LEED). In the energy spectrum shown in figure 2-10, at E_p, the upper energy limit, an "elastic" peak is observed which actually is comprised of the elastically scattered electrons plus the "quasi-elastic" electrons that have lost a small amount of energy (~0.01 eV) by phonon scattering. It is the properties of the electrons in this peak which are measured in diffraction studies. The penetration of the primary electrons into the solid is limited primarily by inelastic events and it is estimated that at LEED energies the penetration depth is 3-10 Å [Bauer, 1970]. It follows that the elastic component of the emitted electrons can originate from only a few atomic layers parallel to the surface. The wavelength, λ, of the electrons is given by the de Broglie relation

$$\lambda=h/p\approx(150/E)^{1/2}\ , \qquad (2\text{-}6)$$

where h is Planck constant, p is the momentum of the electrons, and E is the kinetic energy in electron volts. In diffraction experiments if the surface atoms are arranged in a periodic lattice, the surface will act as a two dimensional (2D) grating and the interaction will produce a set of discrete diffracted beams. A plane wave incident on an atom or atoms within a unit cell will be scattered in all directions, but interference between waves scattered from neighbouring unit cells will restrict the net flux to those directions in which the scattered waves from all unit cells are in phase. This requires that the scattered waves from neighbouring cells differ only by an integral number of the wavelength λ, which is commonly called the Laue condition. Figure 2-10 shows a

diffraction from a one-dimensional array of scatterers which satisfy the Laue condition,

$$a(\sin \Theta_n - \sin \Theta_0) = n\lambda, \qquad (2\text{-}7)$$

or,

$$a(S_n' - S_0) = n\lambda, \qquad (2\text{-}8)$$

where a is the separation distance between scatterers; λ is the wavelength of the incident electrons; Θ_0 and Θ_n are the incident and diffraction angles respectively; S_0 and S_n' are the unit vectors of the incident and emergent beams respectively.

Several types of information can be obtained directly from observation and measurement of the geometrical features of the LEED pattern of diffracted beam terminations on a fluorescent screen or by means of a movable electron collector. For an ideally flat uniform surface the spot pattern presents the two-dimensional reciprocal net. In many instances one can reconstruct from the experimental LEED pattern the direct net using the following equations:

$$a_1 \cdot a_1^* = a_2 \cdot a_2^* = 1, \qquad (2\text{-}9)$$

and

$$a_1 \cdot a_2^* = a_2 \cdot a_1^* = 0, \qquad (2\text{-}10)$$

where a_1 and a_2 are the unit vectors of the real-space lattice, a_1^* and a_2^* are the unit vectors of the corresponding reciprocal lattice respectively. An example is shown in figure 2-11 to describe the relationship between the real lattice and its reciprocal lattice. Based

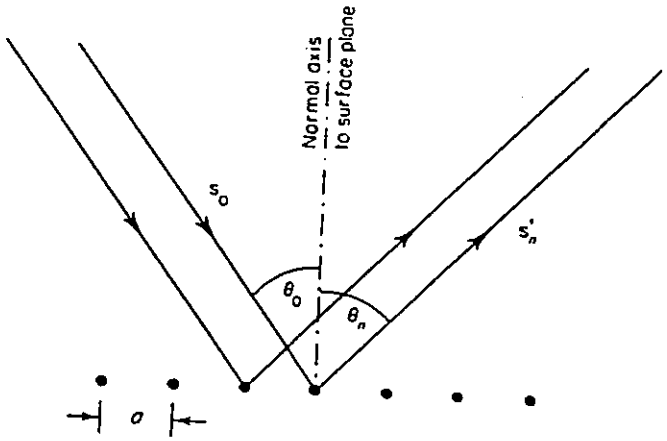

Figure 2-10. Laue diffraction from an one-dimensional array of scatterers.

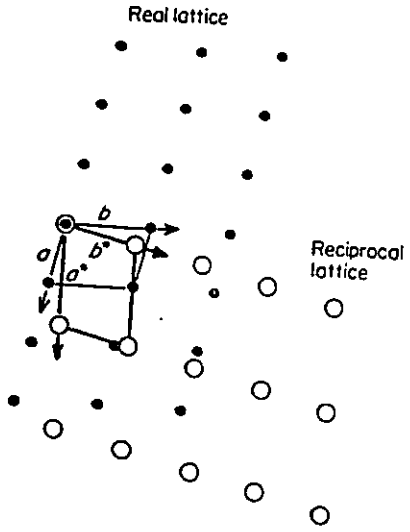

Figure 2-11. The relationship between an oblique direct lattice and its reciprocal lattice.

on this relationship, one can find the size and orientation of the real-space lattice, reveal the superlattices induced by reconstruction or by adsorbed monolayers and the possible presence of symmetrical domains.

The second use of LEED data, called LEED crystallography, constitutes the attempt to determine specific atomic positions within the surface unit mesh or in a three-dimensional unit cell including more than one layer at the surface. This is done by comparing the predictions of large-scale computer calculations applied to specific structural models with experimental intensity-voltage (I-V) curves for several diffraction beams. Structural and nonstructural parameters of the model are varied to produce the best comparisons. No effort has been made to determine specific atomic position in this work.

LEED/AUGER optics were used for this work. The electron optics assembly consisted of four concentric grids and a fluorescent screen, each containing a central hole through which the LEED gun is inserted. In a LEED experiment, the sample crystal is positioned at the focal point of the hemispherical screen. With this arrangement, diffraction beams emerging from the surface of the crystal travel radially toward the screen.

The screen is metallic and coated in a phosphorescent material. It is biased to 4-6 kV, so that approaching electrons are accelerated sharply on to the surface coating. Electrons which impinge on the screen create a glow proportional to the beam intensity. Just before the screen is a series of four hemispherical grids. The grid nearest the sample

is grounded so that the diffracted beams follow linear trajectories in field-free space. The second and third grids away from the sample are linked together and maintained at a potential a few volts below the incident electron beam. This pair of grids thus acts as an energy-selection grid: electrons which have lost more than a few volts have insufficient energy to pass this grid and do not reach the screen. The fourth grid is grounded, acting as a shield between the double grid and the screen to isolate the screen potential from the energy-selection potential.

2.5. SPUTTER DEPTH PROFILING

The understanding and modification of surface properties of materials often requires a detailed knowledge of the spatial distribution of specific elements in both the surface plane and as a function of depth normal to the surface.

Sputter profiling uses the combination of a surface sensitive analytical technique together with the continuous exposure of a new surface by ion beam sputtering. Ar^+ is the most commonly used sputtering ion beam since it does not form compounds with target constituents and so does not significantly alter bulk atomic concentrations.

The elemental concentrations are usually presented as a function of the sputtering time. The depth scale for the profile can be obtained by either measuring the depth of the eroded crater using a surface profilometer or interferometer or by calculating the eroded depth z, from the sputter time [King, 1992]. In the second method, the depth sputtered during a depth profile is related to the product of the ion beam current density, J (Am^{-2}),

the sputter time, t (s), and the sputter yield Y (atoms/ion) of the sample by

$$z = YJMt/1000e\rho Nn, \qquad (2\text{-}11)$$

where e is the electron charge, M is the target molar mass, ρ is the target atomic density (kg/cm^3), N is the Avogadra's number and n is the number of atoms in the target molecule.

In sputter depth profiling, quantification is often difficult because the sputter yield may alter during sputter profiling and the concentration in the target may change due to ion beam induced loss or gain of elements at the surface or in the bulk of the target.

In this study a 2 keV Ar^+ ion beam was used to sputter the samples, and the composition change was monitored by AES. In sputter depth profiling, Auger peak-to-peak heights of the atoms under study are plotted against sputter time. No effort has been made to convert the sputtering time to absolute sample depth.

2.6. EXPERIMENTAL PROCEDURE

Auger electron spectra were obtained in the derivative mode using a four grid retarding potential electron energy analyzer. In most Auger experiments, the electron gun in the centre of the LEED/AUGER optics was used, which produced a primary 2 kV, 25 μA electron beam of 0.1 mm diameter directed normal to the sample surface. When the effect of the incidence angle of the primary beam was studied, a glancing incidence electron beam of 2 kV, 25 μA was used which is directed at an angle of 80° from the

sample surface normal. The spectra were acquired digitally and the spectrometer was controlled by a microcomputer. Appropriate energy windows were swept consecutively taking 8 samples at each energy with the data averaged over multiple sweeps. The more surface sensitive low energy region was monitored with a sweep resolution of 0.2 eV and a modulation voltage of 1 V peak to peak. The transitions above 100 eV were monitored with a sweep resolution of 0.5 eV and a modulation voltage of 10 V peak to peak. For high resolution spectra a modulation voltage of 2 V peak to peak and a sweep resolution of 0.25 eV were used. The most common impurities, C, O, S, P, and Cl were continually monitored. The gas purity was monitored with a 1-200 amu quadrupole mass spectrometer.

Sputtering was performed using a rastered 2 KeV argon ion beam directed at 80 degree to the surface normal, and using a standard argon pressure of $5x10^{-5}$ torr, the ion beam current density, measured with a Faraday cup, was approximately 11 $\mu A\ cm^{-2}$.

Annealed surfaces were produced by electron bombardment heating of the back side of the sample which was mounted by 0.005 inch diameter tungsten wires on a sample holder made of tantalum. The sample temperature was monitored with a W/Re thermocouple spot-welded to the back side of the sample.

CHAPTER THREE

QUANTITATIVE AES

3.1. INTRODUCTION

AES is a widely used technique for the determination of surface composition. Although qualitative and semi-quantitative AES analysis can be routinely performed, quantitative analysis is still difficult for the following reasons:

(1) The observed intensities of Auger features depend on the atomic properties and the matrix properties of the sample and also on the detection condition of the instrument.

(2) As Auger electron signals are small features sitting on a large background of the secondary electron distribution, the determination of Auger intensities is difficult.

(3) The observed Auger signal from an element is strongly dependent on how it is distributed within the first few atomic layers of the surface.

To approach a quantitative application of AES, an understanding of the factors relevant to the specimen under study is important. Based on such an understanding, one could design proper analytical procedures and perform the calibration necessary to attain the desired accuracy.

In this chapter, the basic principles and practical approaches to quantitative Auger analysis will be introduced in section 3.2., and the theoretical and practical methods for background construction will be presented in section 3.3.

3.2. THE FIRST-PRINCIPLES APPROACH AND PRACTICAL METHODS

3.2.1. The first-principle approach

The fundamental formalism [Briggs and Seah, 1983] used for quantification is

$$I_{i,XYZ} = I_0\,\sigma_i(E_p)\,[\,1 + r_m(E_A,\alpha)\,]\,\gamma_{i,XYZ}\,R\,T(E_A)\,D(E_A)$$
$$\int_0^\infty N_i(z)\,\exp[-z/\lambda_m(E_A)\cos\theta\,]\,dz, \qquad (3\text{-}1)$$

where $I_{i,XYZ}$ is the Auger current of the XYZ transition from atom i; I_0 is the primary electron beam current incident on the sample at energy E_p; the term $\sigma_i(E_p)[1+r_m(E_A,\alpha)]$ represents the ionization cross-section of the core level X including the contribution of the primary electron beam induced ionization and the additional ionization, r_m, of the X level due to the back-scattered energetic electrons which will be a function of the Auger electron energy, E_A, and the angle of incidence of the electron beam, α; $\gamma_{i,XYZ}$ is the probability that an atom ionized in the X level will decay through an XYZ Auger transition; R is a surface roughness factor; $T(E_A)$ and $D(E_A)$ represent the transmission efficiency of the analyzer and the electron detector efficiency respectively; $N_i(z)$ is the i atom distribution with depth z into the sample surface; and $\lambda_m(E_A)$ is the inelastic mean

free path (IMFP) of Auger electrons in the matrix m. The characteristic depth from which Auger electrons can be emitted is $\lambda_m(E_A) \cos \theta$, where θ is the angle of emission to the surface normal.

In the above formalism there are several assumptions involved [Shimizu, R. 1983]. The sample is assumed homogenous in the plane parallel to the surface (xy) but the concentration varies with depth z. The Auger electron emission is considered isotropic with the Auger electron undergoing random inelastic scattering; the absorption effect along its path z represented using the IMFP λ_m by $\exp(-z/\lambda_m \cos \theta)$. Any crystallographic effects and contributions from other processes such as Coster-Kronig transitions are not considered to play a role.

The first-principles approach to quantitative AES requires the accurate measurement of the Auger current I_A and the direct calculation or measurement of all the factors on the right-hand side of equation 3-1. These factors depend on the excitation conditions, atomic properties of element i, properties of the matrix m and the instrument. Although some of these factors can be determined experimentally, some can be calculated theoretically or measured empirically such as the ionization cross-section, inelastic mean free path, and Auger transition probability, $\gamma_{i,XYZ}$. However the surface roughness factor, R, depends on matrix properties which are difficult to determine. Large errors can result due to uncertainties in many of the tems in the equation 3.1 and it is obvious that the first-principles approach to quantitative AES is very difficult. In favourable cases, the accuracy obtained is about a factor of 2 [Werner and Garten, 1984].

3.2.2. Practical methods

In practice, relative elemental sensitivity factors are extensively used for semi-quantitative analysis. In this method, the relative sensitivity factors of all detected elements are obtained by comparing the Auger signal intensity of the detected element with that of a reference element, usually the 351eV Ag (MNN) Auger signal. The relative sensitivity factors can be obtained from a published data base [Davis et al., 1976] or determined experimentally.

By assuming sample homogeneity with depth z, and with a spectrometer which primarily detects electrons along the direction θ to the surface normal, equation 3-1 can be simplified to:

$$I_{i,XYZ} = I_0 \, \sigma_i(E_p)[1+r_m(E_A,\alpha)] \, \gamma_{i,XYZ} \, R \, T(E_A) \, D(E_A) \, N_i \, \lambda_m(E_A) \cos \theta. \qquad (3\text{-}2)$$

If one measures the Auger signal from a test sample, A, and takes a spectrum of a reference standard, R, under the assumption of equal surface roughness and instrumental response, the relative intensity becomes:

$$I_A / I_R = [\sigma_A(1+r_A) \, \gamma_A \, N_A \, \lambda_A] / [\sigma_R(1+r_R) \, \gamma_R \, N_R \, \lambda_R], \qquad (3\text{-}3)$$

where the functional form and the XYZ notation have been dropped for clarity. It can be further simplified to:

$$N_A / N_R = I_A / I_R S_A \, , \qquad (3\text{-}4)$$

where S_A is the sensitivity factor of A:

$$S_A = [\sigma_A(1+r_A)\,\gamma_A\,\lambda_A] / [\sigma_R(1+r_R)\,\gamma_R\,\lambda_R]. \qquad (3\text{-}5)$$

When elemental or silver standards are not used, it is possible to express the atomic concentration as

$$C_x = (I_x / S_x) / (\Sigma (I_i / S_i), \qquad (3\text{-}6)$$

where the sum is over all detected elements with one appropriate transition per element.

There are several errors in this simple quantitative technique:

(1) matrix effects on escape depths and backscattering factors;

(2) chemical effects on peak shapes;

(3) surface topography.

For example, the dependence of Auger electron escape depth on the electronic structure of the host material may alter the depth of measurement in the specimen relative to that in a standard. Since the magnitude of the Auger signal is proportional to the number of atoms in the analyzed volume, a large escape depth will cause a corresponding increase in Auger signal of the element distributed throughout the escape depth layer. Chemical effects can change the peak-to-peak heights in the differentiate spectrum used as a measure of the Auger signal. Generally, a highly polished surface produces a larger Auger signal than a rough surface. This effect is minimized by determining concentration by equation (3-6) since surface roughness is expected to decrease all Auger peaks by nearly

the same percentage.

When a highly accurate quantitative analysis is desired, standards of known concentrations which are close to that of the actual specimens should be used. The most accurate method of quantitative AES is the method using external reference standards, that is to measure of Auger signal intensity from an element in a test sample and the intensity from the same element in a standard sample of known composition, sequentially under the same instrument settings. In this way, instrumental factors need not be known, furthermore when a reference standard has a composition close to the test sample, the matrix factors are also removed because the electron escape depth, back-scattering factors, and chemical effects are similar in both samples.

In this work, the external standard method was used in the study of zirconium nitride films, and the Auger spectrum of a bulk $ZrN_{0.88}$ alloy served as the external standard. The variation of peak intensities of Auger spectra of zirconium metal and its nitride films were quantitatively investigated, and the results will be given in chapter 4. Because of the instability of tungsten nitrides, no external standard sample is available for the quantification. Although a silver foil was used as a relative standard, the AES studies of tungsten nitrides in this work can only be considered to be semi-quantitative, as discussed above.

3.3 SPECTRAL DECONVOLUTION

As discussed in section 3.1, the measurement of AES peak intensity is difficult

because AES signals are small features sitting on the large background of the secondary electron distribution. It has been customary to measure the peak-to-peak height of the signal in the derivative energy spectrum. This method is only valid with three restrictions:

(1) the peak shapes are the same in the analysis and reference spectra;
(2) the analyzers used for the analysis and reference spectra have the same resolution;
(3) the same modulation is used for both analysis and reference spectra.

When the AES line shape changes due to the changes in the chemical environment, the areas under the Auger peaks from an integrated spectrum should be used to determine the Auger signal intensities instead of the peak-to-peak height of signals in the derivative spectrum. Furthermore, as the line shape of an Auger feature contains rich information about the chemical environment of the element of interest, line shapes are very important in the interpretation of an Auger spectrum. To extract information from line shapes and to obtain accurate signal intensities, Auger features should be separated from the superimposed background of secondary electron distribution, and the Auger spectrum should be deconvoluted. In this section, the nature of the secondary electron distribution will be discussed, and the method used for background construction in this work will be presented.

3.3.1. Secondary electron cascade in metals

For an electron to escape from a metal and be observed as a secondary electron it must have an energy of about ten volts or more relative to the bottom of the conduction

band. In this energy range, the main way it loses energy is by collision with conduction electrons in the metal. The phenomenon of secondary electron emission [Wolff, 1954; Sickafus, 1977] can be thought of as occurring in two distinct steps. The first step is the production of internal secondaries by collisions between fast primaries and electrons bound in the metal. The second is the subsequent cascade process in which these secondaries diffuse through the solid, multiplying and losing energy en route, until they either sink back into the sea of conduction electrons or reach the surface with sufficient energy to emerge as true secondary electrons. The significant inelastic events are two-electron processes in which the primary electron loses a discrete amount of energy to an electron of the solid giving rise to two electrons in excited states. Both these electrons are then subject to similar scattering events.

Several theoretical calculations have been made to predict the energy distribution of true secondaries, N(E) [Wolff, 1954; Hachenberg and Brauer, 1959; Seah, 1969]. Wolff applied the Boltzmann diffusion equation to describe the secondary-electron cascade. He assumed that the potential which causes electron-electron scattering was the Coulomb field, screened by the plasma of conduction electrons; electron-electron scattering is spherically symmetric (in the centre of mass system) up to ~100 eV; the motion of the conduction electrons, compared with those in the cascade, could be ignored. With these assumptions, the secondary-emission current is given by the following expression:

$$j(E) = \{ P(E) / [\eta_c \sigma_0(E) (1-7E_F/5E)] \} (E_p/E)^x. \qquad (3\text{-}7)$$

In this equation, $\sigma_0(E)$ is the inelastic electron-electron scattering cross section, E_F is the

Fermi energy, η_e is the number density of conduction band electrons, and P(E) is a geometrical factor which gives the probability that an electron with energy E striking the surface will have a large enough normal velocity to overcome the work function and escape. For a spherically symmetric distribution, P(E) is given by

$$P(E) = 1- [(\phi + E_F)/ E]^{1/2} , \qquad (3\text{-}8)$$

where ϕ is the work function. Equation 3-7 is only valid when the primary electron energy is less than 100 eV. According to Wolff, electrons with energy greater than 100 eV must be followed individually. These fast electrons produce secondaries by small-angle Coulomb scattering, which are distributed in energy according to a $1/E^2$ law.

Other theories have also been set forth in the literature, e.g. Seah [1969] predicted that the form of emission normal to the surface is given by

$$N(E) \propto [\mu^2 (E+E_i)^m]^{-1}, \qquad (3\text{-}9)$$

with

$$\mu^2 = (E+E_i)/E , \qquad (3\text{-}10)$$

and Sickafus' form [1977],

$$j(E)=AE^{-m}E_p^{-n}, \qquad (3\text{-}11)$$

is based on the linearized cascade observed in a log j(E) vs log(E) plot.

3.3.2. Background step under the Auger peak

An analysis of the source of the background signal made by Sickafus [1977]

shows that the background on the low-energy side of the peak is comprised of a step, figure 3-3 (c), due to the inelastic scattering of Auger electrons emitted from surface atoms and backscattered from the bulk, plus an increasing contribution due to inelastic scattering of Auger electrons from bulk atoms, i.e. below the escape depth, emitted towards the surface. This problem is the same as that in XPS and it can be solved by use of the background devised by Shirley [1972], in which the background intensity at a point is determined, by an iterative analysis, to be proportional to the intensity of the total peak area above the background at higher energies.

3.3.3. Spectral deconvolution procedure used in this work

In practice, almost all spectral deconvolution routines try to fit the background with certain functions which generate a smooth and featureless curve under the Auger peaks, but the result depends strongly on the boundary conditions.

It can be seen from the typical AES spectrum shown in figure 3-1 that, in the derivative mode, Auger peaks in the higher energy region are sitting on a flat background, therefore one could simply subtract a straight line from the spectrum. However, the AES peaks in the low-energy region are sitting on a steep background, and this makes the construction of a smooth, monotonically varying background very difficult. An alternative method has been successfully used in our laboratory in analyzing low-energy AES spectra of vanadium and its nitride films [Dawson and Tzatzov, 1990], in which, the low-energy AES spectrum of the stoichiometric nitride was used as the background for all other spectra. In this way, whatever the merits of this approximation, the results certainly

represent the spectral changes which accompany the decrease in nitrogen concentration.

The spectral deconvolution method used in this work involves six sequential steps. The first step is the construction of a smooth background through the Auger features in the derivative spectrum. For AES spectra of zirconium and its nitride films in the MNN transition energy region, the background was fitted by a Gaussian derivative function:

$$dN(E)/dE = -A(E - E_0) \exp[-B(E - E_0)^2], \qquad (3\text{-}12)$$

A Zr MNN AES spectrum and the background fitted by this function are shown in figure 3-3 (a). However, in the low energy region, the integrated Auger spectrum of the stoichiometric zirconium nitride was used as background, figure 3-2 (b). After background subtraction, it can be seen that the integrated spectrum is comprised of steps under Auger peaks, i.e. the "Shirley steps", figure 3-2 (c) and 3-3 (c). The "Shirley steps" were computed iteratively using the Sickafus [1977] method and subtracted from the spectrum. As mentioned in the previous section , the intensity of the step at a point is proportional to the intensity of the total peak area above the background at higher energies. It is notable that the "Shirley step", shown in figure 3-2 (c), for the low energy spectrum is very small in comparison with the Auger peak area above it. This is caused by the background fitting method used in the low energy region. The Auger spectrum of the stoichiometric zirconium nitride has "Shirley steps". When it was used as background in low energy region, and subtracted from all the other spectra, the "Shirley steps" involved in the background was also subtracted. The computed step shown in figure 3-2 (c) is the difference of the "Shirley steps" from the measured sample and that of

the stoichiometric zirconium nitride. Therefore, it is a relative "Shirley step" and is small. After the subtraction of the "Shirley steps" the final step of the procedure is the deconvolution of the AES peaks, which is shown in Figure 3-2 (d) for low energy Zr(NVV) Auger spectrum.

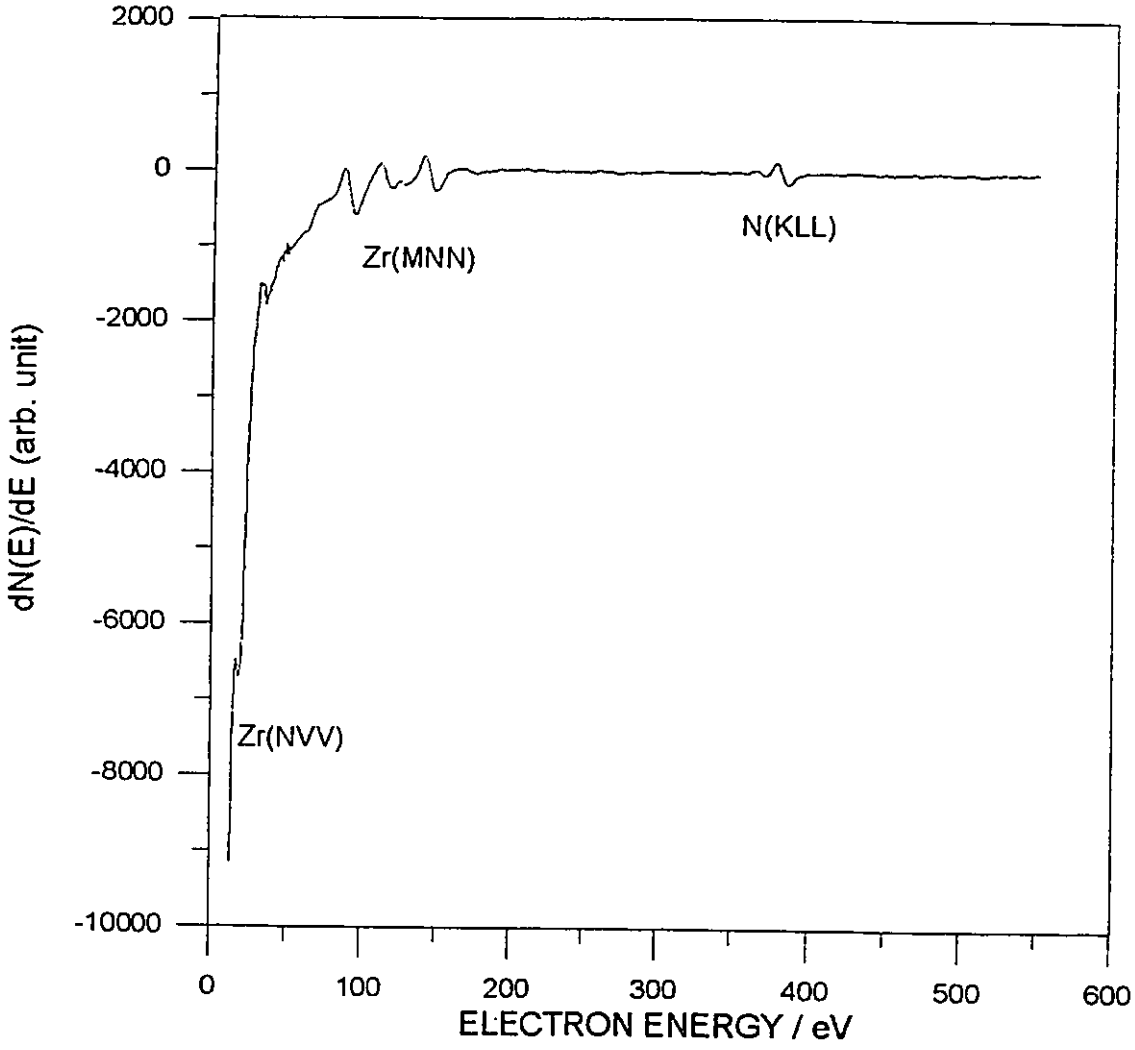

Figure 3-1. Derivative Auger spectrum of a zirconium nitride film.

Figure 3-2. Deconvolution of the low energy Auger spectrum of a $ZrN_{0.72}$ film. (a) the experimental derivative spectrum; (b) the integrated spectrum and the integrated stoichiometric nitride spectrum used as background; (c) the spectrum obtained by subtracting the background and the computer simulated "Shirley" step; and (d) the final spectrum after subtracting the step, star symbols, and the simulated spectrum, which uses a Gaussian peak shape for fitting both "metal" and "nitride" peaks, square symbols. Also shown in (d) are the component "metal" and "nitride" peaks for the simulated spectrum.

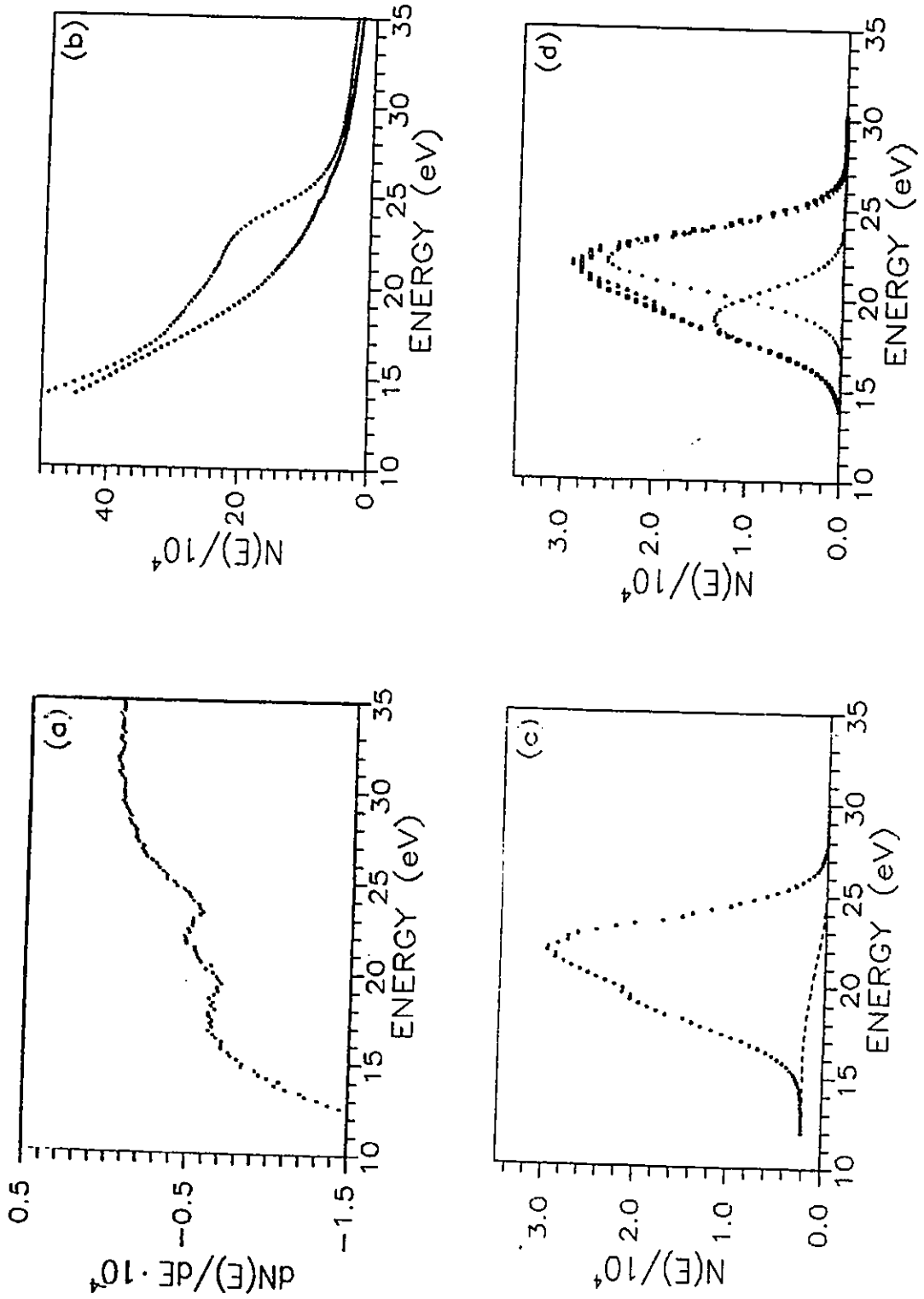
(a)
(b)
(c)
(d)
ENERGY (eV)
dN(E)/dE · 10⁴
N(E)/10⁴

Figure 3-3. Deconvolution of the Zr(MNN) Auger spectrum of a $ZrN_{0.33}$ film. (a) the experimental derivative spectrum and the computed background; (b) the spectrum after subtracting background ; (c) the integrated spectrum and the simulated "Shirley" steps; and (d) the final spectrum after subtracting the steps.

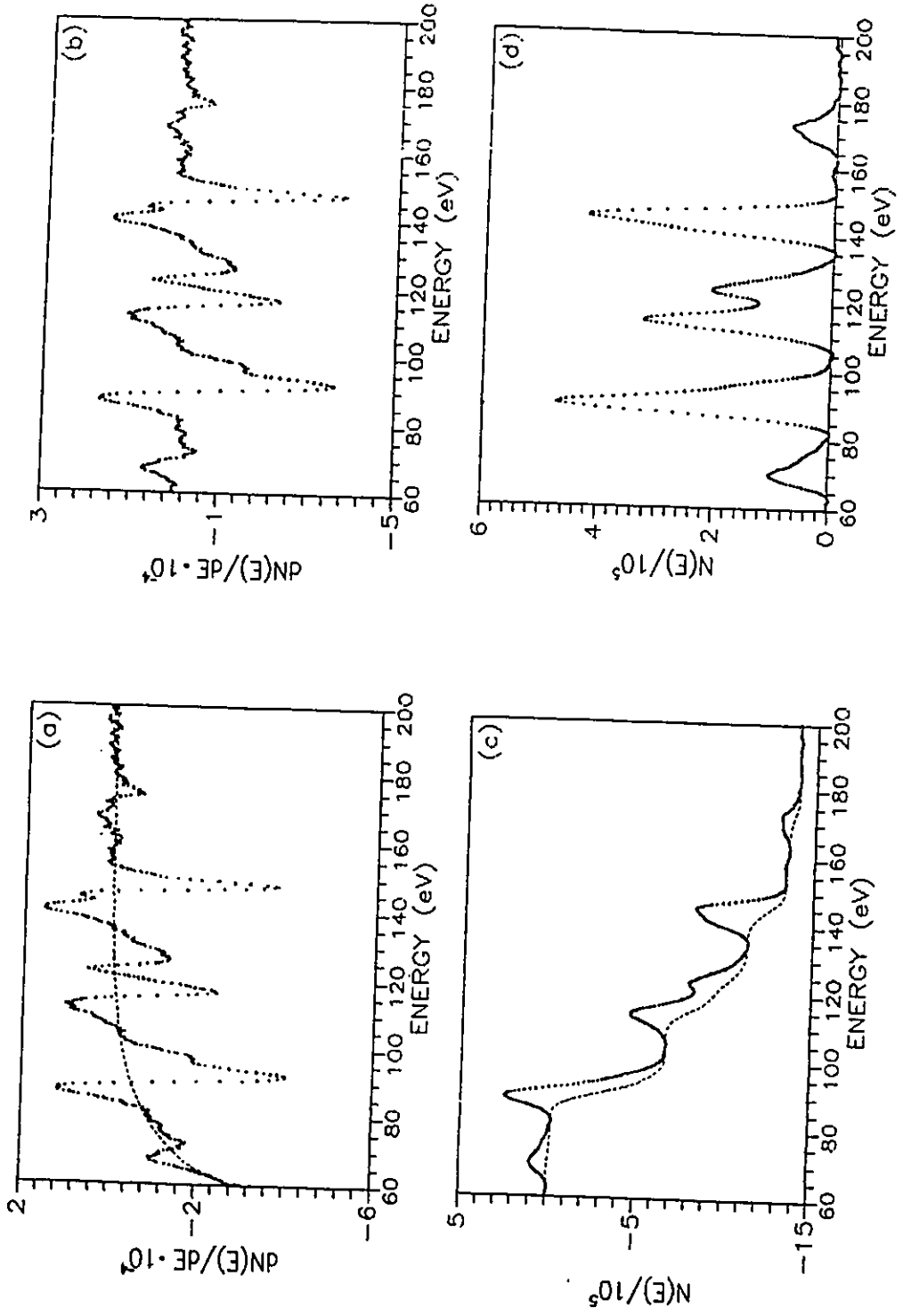
(a)
(b)
(c)
(d)
ENERGY (eV)
ENERGY (eV)
ENERGY (eV)
ENERGY (eV)
dN(E)/dE · 10⁴
dN(E)/dE · 10⁴
N(E)/10⁵
N(E)/10⁵

CHAPTER FOUR

QUANTITATIVE AES STUDIES

OF N/Zr THIN FILMS

4.1. INTRODUCTION

Zirconium is a second row transition metal just below titanium in the period table. Zirconium nitrides are hard, refractory, interstitial compounds with important technical applications as surface coatings. The nitride phase has an extremely wide stoichiometric range, and since the physical properties will depend greatly on the composition of the nitride it is important to have methods for accurate surface analysis available.

Zirconium has a strong low-energy AES feature at 23 eV identified as an Zr(NVV) transition, and exhibits a rich Auger electron emission structure between 90 to 180 eV, which arises predominantly from the decay of Zr(3d), i.e. $M_{4,5}$ core holes. In the first report [Dawson et al., 1991_2] of the low energy electron spectra of the zirconium nitride system, we identified an very strong feature at about 3 eV in energy as an adsorbate-induced surface resonance feature. The aim of the present work is to develop a technique for quantification of Auger spectra of zirconium nitrides in a wide energy

region, including both the zirconium NVV and MNN Auger transitions.

In the low-energy region, 10-100 eV, the inelastic mean free paths of Auger electrons have the smallest values. figure 2-8, and so the low-energy AES spectrum is extremely sensitive to the outmost layer, and is therefore a good surface probe. In the table of nine transition metals, table 1-1, zirconium, titanium and vanadium form the upper left corner. It is interesting to compare the low-energy AES spectrum of zirconium nitride to that of titanium nitride and vanadium nitride which have been reported by our laboratory [Dawson and Tzatzov, 1986; 1990; 1991_1]. In this study, a new Auger feature induced by nitriding has been identified in the low-energy region. The intensity change and energy shift of low energy Auger features have been followed during sputter profiling of implanted zirconium nitride films.

In a study of the adsorption properties of zirconium with different adsorbates, O_2, N_2, CO, NO, and D_2, Foord et. al. [1980] found that the intensities of Zr MNN Auger peaks vary in an unusual way. The degree of adsorption-induced attenuation of the Zr Auger signals increases considerably as the kinetic energy of the Zr Auger electron increases. This very remarkable effect cannot be accounted for in terms of electron escape depth arguments because its energy dependence is in the opposite direction. They suggested that the relative attenuation effects must be related to the changes in the zirconium valence band induced by adsorbates which change the probability of Auger electron emission. Following them, several investigators [Tanabe et al., 1987; Jungblut et al., 1988; Sanz et al., 1987; Betteridge et al., 1991; Zhou et al., 1984; Axelsson et al.,

1985] studied the oxidation of zirconium using Auger electron spectroscopy. High resolution spectra revealed that oxidation of zirconium causes peaks that involve emission of valence band electrons to be strongly attenuated and new features that are due to Auger cross-transitions to be formed [Tanabe et al., 1987; Jungblut et al., 1988; Sanz et al., 1987].

In this study, high resolution AES and spectrum deconvolution techniques were used in the energy region 60-180 eV to study the influence of nitriding on the Zr MNN AES transitions. Four new Auger features induced by nitriding have been separated and identified. The intensity variations and energy shifts of Auger features in the energy region have been followed during the profiling of ion implanted zirconium nitride films.

In this chapter, the quantitative AES analysis of zirconium nitride films in a wide energy region and the interaction of nitrogen with zirconium surfaces will be presented and discussed.

4.2. EXPERIMENTAL PROCEDURE

In this work, the zirconium nitride film was prepared in situ by implanting nitrogen ions into the zirconium disk which was sliced from a zone-refined rod and cleaned before use. We have observed that even using a 2 keV nitrogen ion flux for implantation, traces of oxygen can seriously reduce nitrogen uptake. Hence the key step for making zirconium nitride film with high nitrogen concentration is to start with a clean and oxygen-free zirconium surface. The zirconium nitride film prepared in this way has a composition close to stoichiometric, deduced by a comparison of the AES spectra of the implanted film and the $ZrN_{0.88}$ standard sample. The implanted ZrN sample was sputtered with 2 kV argon ions. At various sputtering stages, Auger electron spectra were collected to represent ZrN_x films of differing nitrogen concentration.

4.3. NVV SPECTRA OF Zr AND ZrN_x

4.3.1. Auger spectra of Zr and a standard nitride sample

In figure 4-1, the Auger spectrum of a $ZrN_{0.88}$ bulk standard sample is shown together with the Auger spectrum of a pure zirconium metal sample. A well-shaped strong feature near 23 eV can be seen in AES spectrum of pure zirconium sample. In the spectrum of $ZrN_{0.88}$ the feature at 23 eV is much reduced in intensity, and an additional small feature can be seen about 4 eV lower in energy. To simplify discussion, the feature at 23 eV will be referred to as a "metal" feature and the new feature will be referred to as a "nitride" feature.

4.3.2. The AES spectra of zirconium nitride films

The AES spectrum of a zirconium nitride surface prepared by ion implantation is shown together with the spectra collected at various sputtering stages of the sample in figure 4-2. It can be seen that both the "metal" feature and the "nitride" features change in amplitude with the nitrogen concentration. The amplitude of the "metal" feature increases as the nitrogen concentration is reduced by ion sputtering whereas the amplitude of the "nitride" feature is small for a high nitride surface and zero for the pure metal surface but has a maximum between these two states. Also, it can be noticed that both "metal" and "nitride" features slightly shift towards lower energy when nitrogen atoms are removed by sputtering.

After data processing, the deconvoluted Auger peaks for the pure metal and

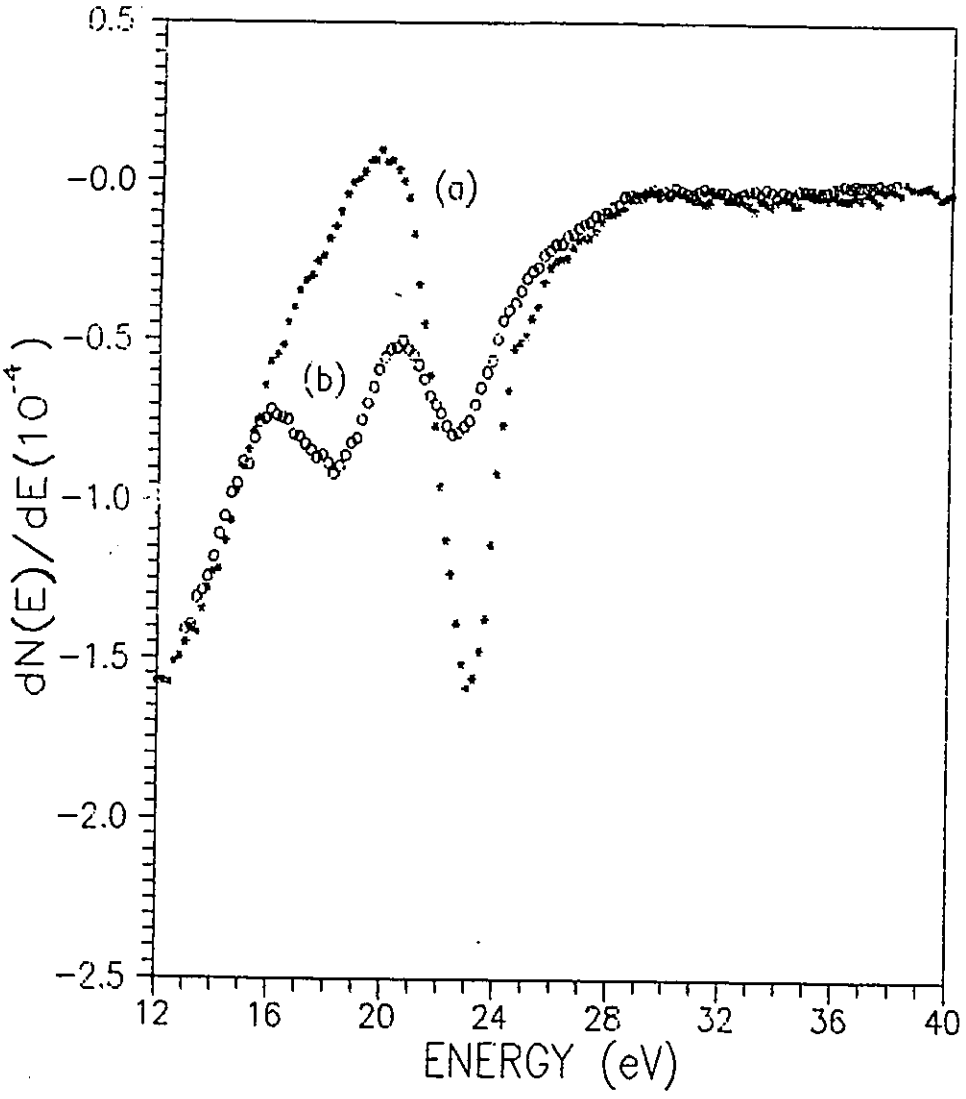

Figure 4-1. Derivative Auger spectra in the energy range 12-40 eV, for (a) Zr; and (b) a standard bulk zirconium nitride sample, $ZrN_{0.88}$.

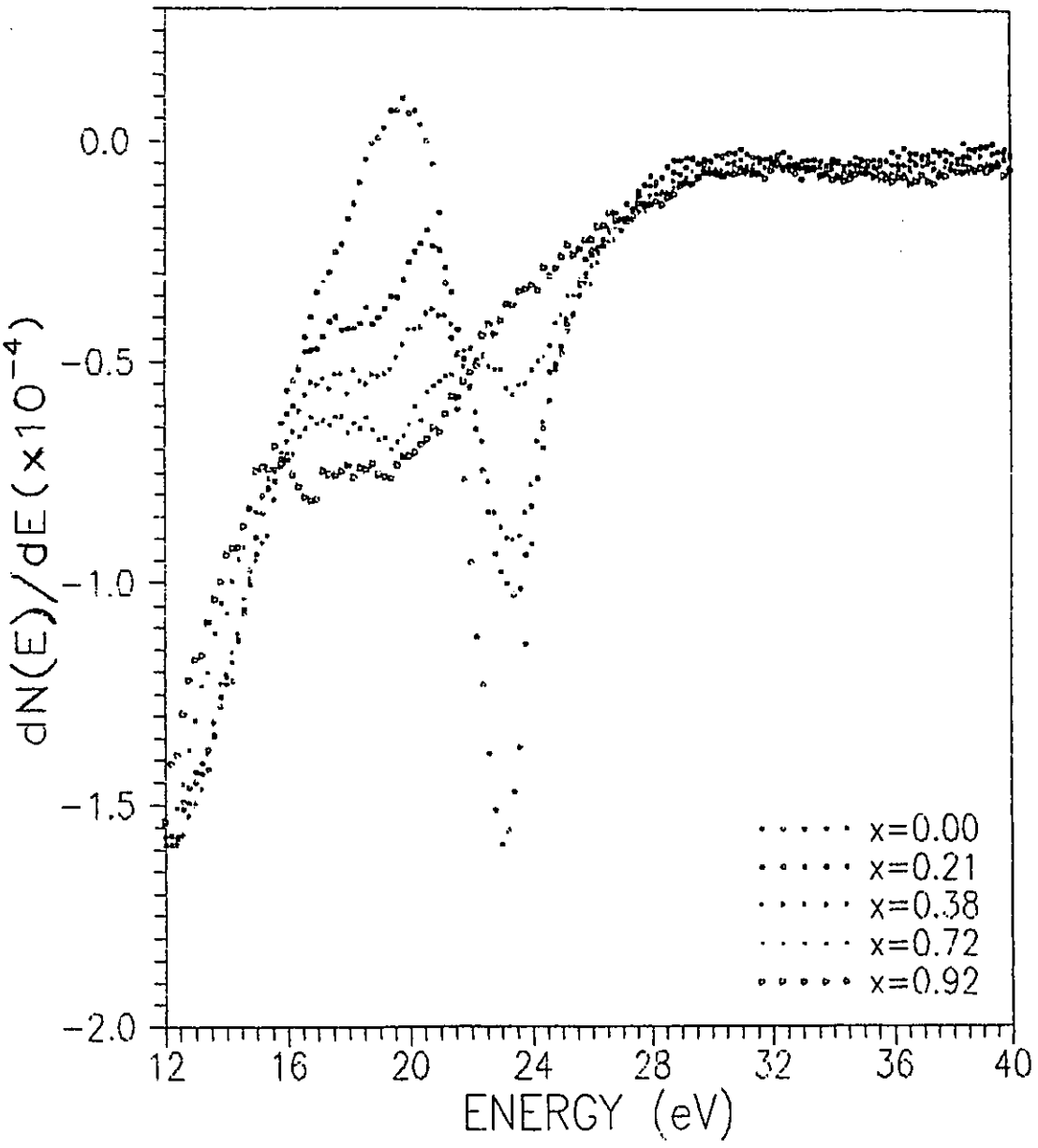

Figure 4-2. Auger spectrum of pure Zr and selected spectra obtained at various stages in the sputter profiling of a ZrN film prepared by nitrogen ion implantation. Composition of these films are: $ZrN_{0.21}$ $ZrN_{0.38}$ $ZrN_{0.72}$ and $ZrN_{0.92}$, as simulated by method described in section 3.3.3.

zirconium nitride films with different nitrogen concentration are compared in figure 4-3. The existence of two features can be seen clearly in these spectra. The area of the "metal" and "nitride" component peaks are plotted in figure 4-4 as a function of the relative nitrogen to zirconium atomic ratio, x, which is determined by the peak ratio of the nitrogen KLL peak to zirconium $M_{4,5}N_1N_{2,3}$ peak, calibrated using standard zirconium nitride bulk samples. The "metal" peak area decreases linearly with x, whereas the "nitride" peak area reaches a maximum value around x=0.5~0.6, thereafter slowly decreases in intensity. The energy shift of the two peaks, relative to the pure metal's peak position, are shown in figure 4-5. It can be seen that, almost in parallel, both peaks shift to higher energies with the increasing nitrogen concentration.

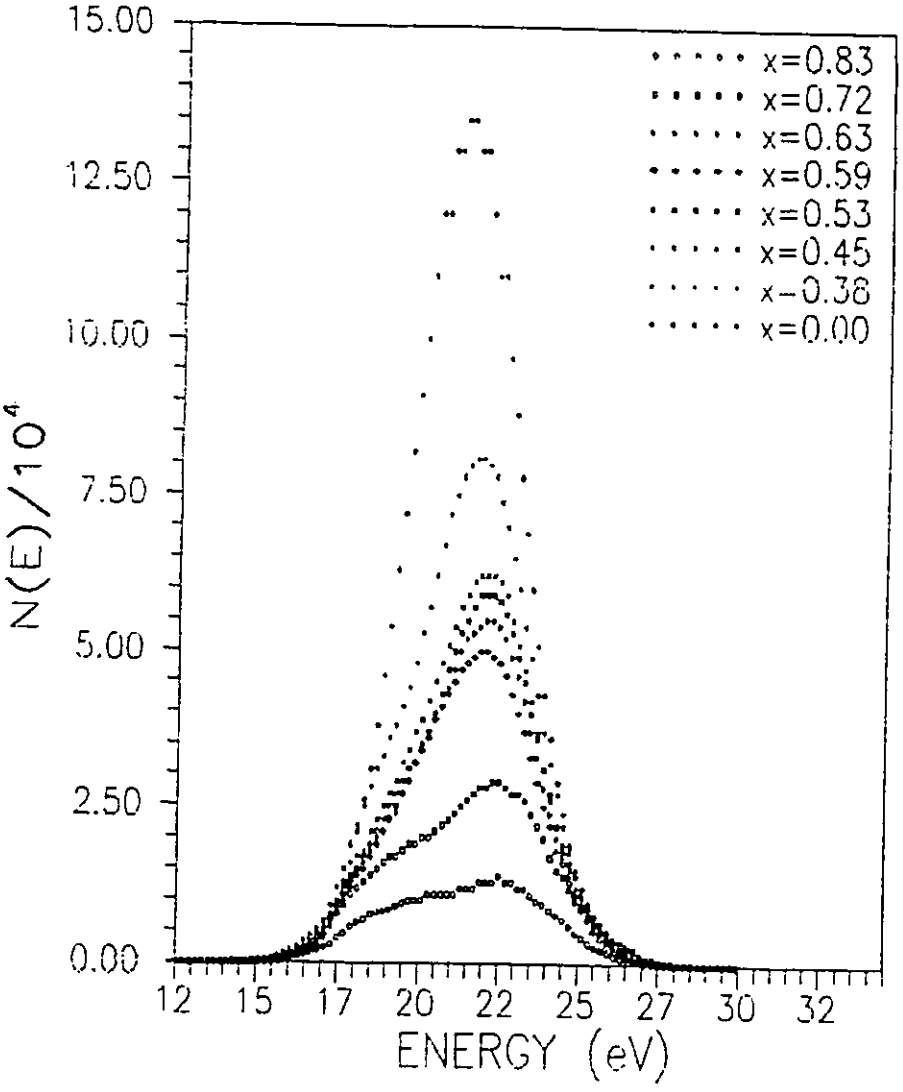

Figure 4-3. The integrated spectra of pure Zr and seven sputtered ZrN_x films with x=0.38, 0.45, 0.53, 0.59, 0.63, 0.72, 0.83, obtained by subtracting background and step.

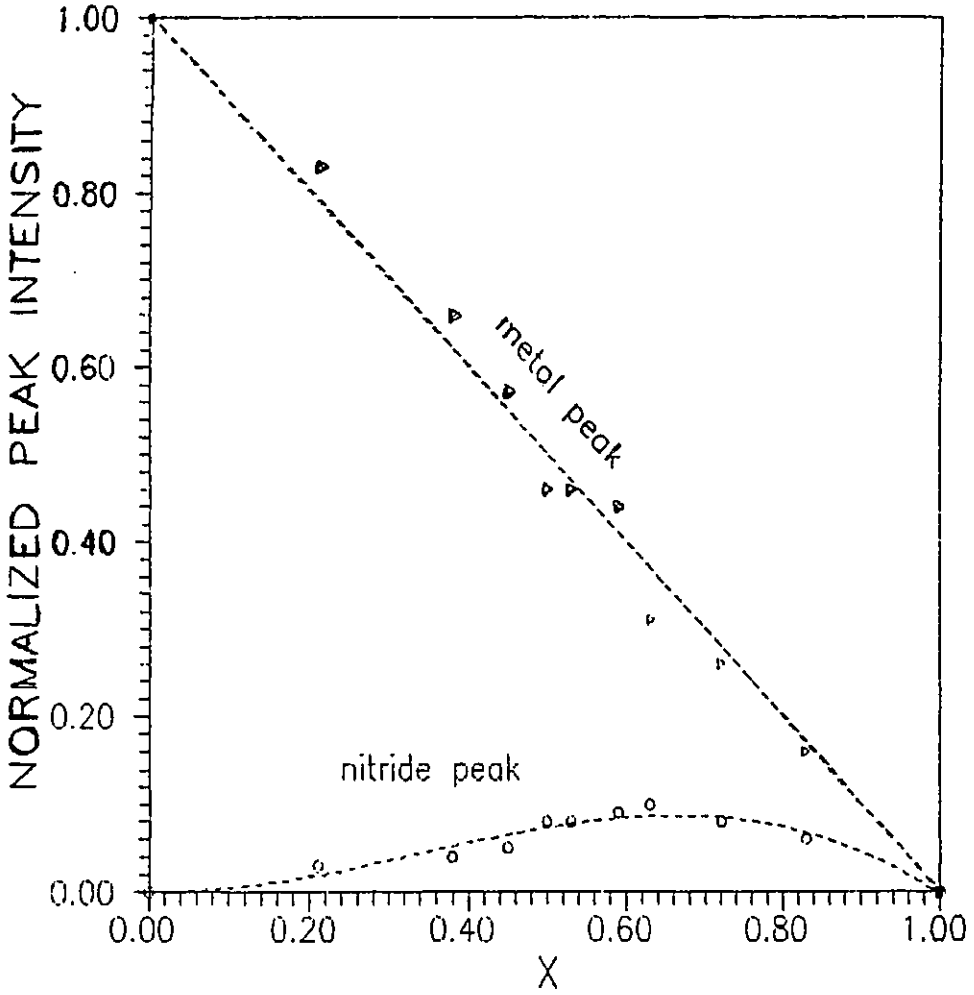

Figure 4-4. The fractional contributions of the "metal" and "nitride" peaks to the deconvoluted integral spectra of the sputtered ZrN_x films are shown as a function of x.

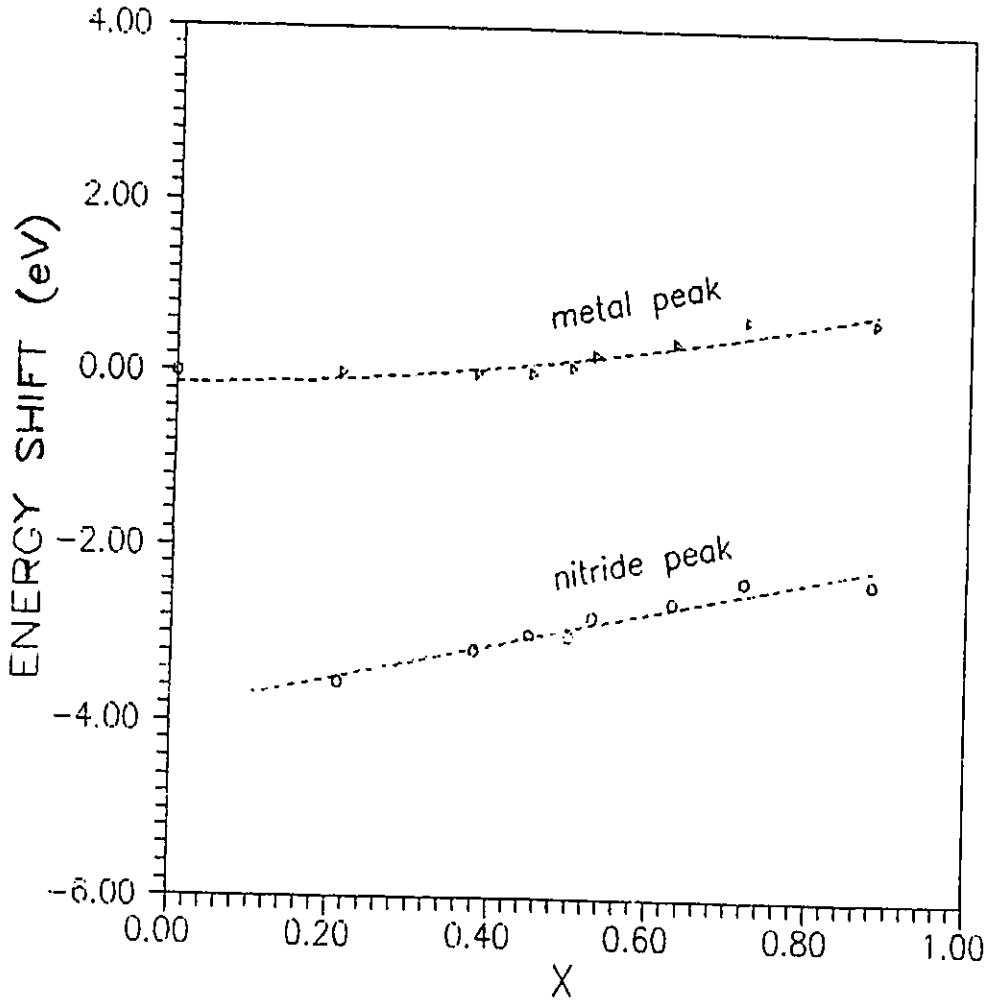

Figure 4-5. The peak shifts of the "metal" and "nitride" features relative to the pure metal position.

4.4 DISCUSSION OF THE NVV AES SPECTRA OF Zr AND ZrN_x

4.4.1. The origin of features in the NVV AES spectra

The "metal" feature at about 23 eV in the low energy Auger spectra of pure zirconium can be assigned as the super Coster-Kronig transition, Zr(NVV) or in the equivalent notation Zr(4p)Zr(4d)Zr(4d). The energy position of this feature can be checked by the following equation,

$$E_{NVV} = E[Zr(4p)] - E[Zr(4d)] - E[Zr(4d)] - U_{eff} - \phi, \qquad (4\text{-}1)$$

where U_{eff} is the final state hole-hole interaction energy and ϕ is the work function of the collector of the analyzer. Using E[Zr(4p)] = 29.7 eV and E[Zr(4d)] = 0.5 eV [Hochst et al., 1981; 1982] and putting the observed Auger electron energy, 23 eV, on the left side of the equation, gives reasonable value for the sum of the analyzer work function, ϕ, and hole-hole interaction energy, U_{eff}.

As revealed by a UPS and ELS study [Hochst et al., 1982], the valence band of zirconium nitride, the 4d state, is hybridized with the nitrogen 2p state in zirconium nitride. The energy difference between the Zr(4d) state and the hybridized N(2p) state is about 4 eV, which is the energy difference being observed between the "metal" feature and the "nitride" feature. Therefore the "nitride" feature can be assigned as the Auger cross-transition, Zr(4p)Zr(4d)N(2p), where N(2p) is refers to the hybridized nitrogen 2p state, and the transition is shown in figure 4-6. Corresponding cross transitions were

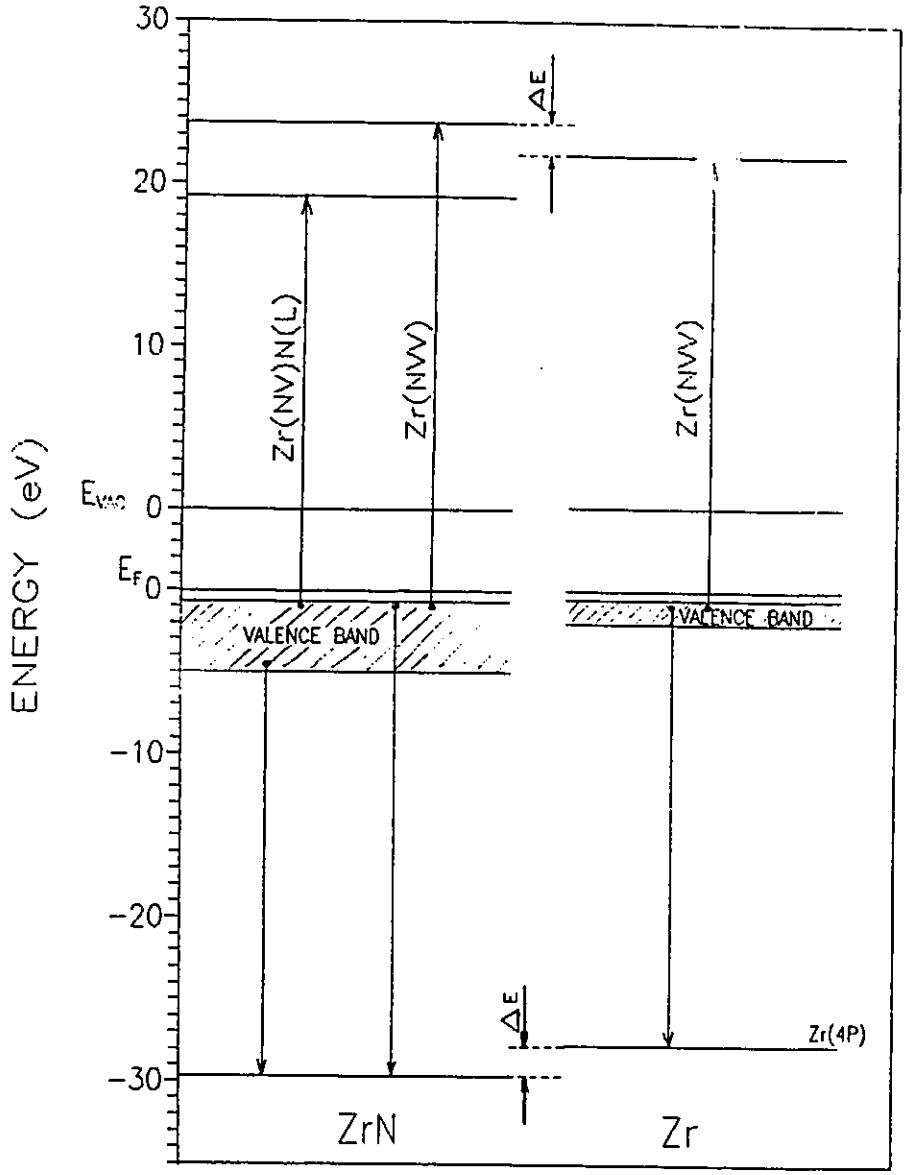

Figure 4-6. The low energy Auger transition for Zr and ZrN. The origin of the "nitride" feature for ZrN and the energy shift of the "metal" feature from pure Zr metal to ZrN caused by the change of Zr(4p) binding energy are shown.

found in low energy Auger spectra of titanium nitride [Dawson and Tzatzov, 1986] and vanadium nitride [Dawson and Tzatzov, 1990].

4.4.2. The variation of peak intensity with composition

As shown in Figure 4-4, the intensity of the "metal" feature decreases linearly with the increase of the nitrogen to zirconium atomic ratio, x. The linear variation in the intensity of the "metal" peak with x in MN_x is not equivalent to a linear variation in peak intensity with the metal concentration, or mole fraction x_M, since this is not a linear function of x, i.e. $x_M=(1+x)^{-1}$. This surprising result can be understood by a consideration of the crystal chemistry of these transition metal nitrides. The nitride phases of zirconium are interstitial phases [Toth, 1971] in which the nitrogen atoms occupy octahedral holes in the metal atom layers, figure 4-7, which are hexagonal close packed for the α-phase and face centred cubic for the B1 structure ZrN. For both structures there are an equal number of octahedral holes and metal atoms, n, and the hole-metal and metal-hole coordination numbers are both equal to six. In both structures the number of occupied holes will be equal to the number of nitrogen atoms, n. Therefore,

$$\text{Number of unoccupied holes} = n_{Zr}-n_N = n_{Zr}(1-x) \qquad (4\text{-}2)$$

and the number of unoccupied holes will decrease linearly with the increase of the atomic ratio x. The intensity of the "metal" peak decreases linearly with x, which suggests a linear dependence of the intensity of the "metal" peak on the number of the unoccupied holes. Thus the electrons contributing to the "metal" peak are those Zr(4d) electrons associated with the unoccupied octahedral holes in the nitride structure since these will

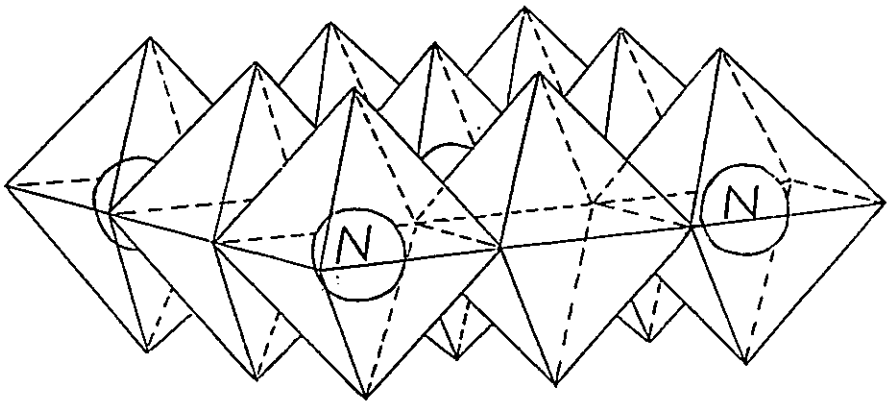

Figure 4-7. In the B1 ZrN structure, nitrogen atoms occupy octahedral holes in the metal atom layers.

be relatively unperturbed in energy, in contrast to the Zr 4d electrons associated with occupied holes which will be bonded to nitrogen.

The variation of the intensity of the "nitride" peak is quite different from the "metal" peak. It increases with the mole ratio,x, passes through a maximum at x=0.5~0.6 and then slowly decreases, figure 4-4. This peak has been assigned to a cross transition, Zr(4p)Zr(4d)N(2p), and clearly requires the existence of Zr(4d) and N(2p) states, with significant overlap. As discussed above the Zr(4d) state is associated with an unoccupied octahedral hole, and clearly the N(2p) state is associated with an occupied octahedral hole, in such a model the cross transition requires the existence of adjacent occupied and unoccupied octahedral holes The intensity of the Auger feature will be proportional to the total number of adjacent occupied and unoccupied octahedral holes, which can be expressed as following:

$$n_{Zr}(1-x)6(n_N/n_{Zr})=6n_{Zr}x(1-x), \qquad (4-3)$$

where $n_{Zr}(1-x)$ is the number of unoccupied octahedral holes, 6 is the coordination number, and n_N/n_{Zr} is the probability that an adjacent hole is occupied. This function will have a maximum value at x=0.5, in agreement with the observed variation of the "nitride" peak intensity. But the low energy Auger spectrum of the stoichiometric nitride does not give a zero amplitude for the "nitride" peak, as would be implied by this model, although the amplitude is very small. The zero amplitude for stoichiometric nitride shown in figure 4-4 is simply a result of using the spectrum of the stoichiometric nitride as background. There are two possible explanations, either the existence of vacancies in both the metal

and the nitrogen sub-lattices for the stoichiometric nitride, or the possible contribution from intra-hole cross transitions in addition to the inter-hole transitions. Intra-hole cross transitions could involve Zr(4d) orbitals in occupied holes which are directed so as not to overlap with the N(2p) orbital.

4.4.3. Auger electron energy shift with composition

Figure 4-5 shows the energy shift of the "metal" peak and the "nitride" peak. The "metal" peak shifts very little until x equal to 0.5 and thereafter moves faster to higher energies, which again suggests that the composition where the octahedral holes are statistically half occupied is significant. The behaviour of the "nitride" peak is different, it shifts almost linearly with the increase of the x to higher energy. Since the "metal" and "nitride" Auger transitions both involve the same initial Zr(4p) hole, the energy shift of the Zr(4p) state from pure zirconium to zirconium nitride could cause the "metal" and "nitride" peaks shift in the same direction. The XPS data [Hochst et al., 1982] showed that from pure zirconium to stoichiometric nitride the energy of Zr(4p) state shifts from -27.8 to -29.7 eV, which is in the right direction to interpret the observed shifts of the "metal" and "nitride" peaks in the low energy Auger spectra. If this is the reason for energy shift of these low energy peaks, then the Zr MNN Auger transitions involving Zr(4p) state in the energy region from 70-200 eV should also show an energy shift on nitriding. The expected energy shift has been observed in the study of ZrN MNN Auger transitions, which agree very well with the explanation of ZrN NVV peak shift on nitriding, and the detailed results will be presented in the following sections of this chapter.

4.5. MNN SPECTRA OF Zr AND ZrN_x

4.5.1. The MNN AES spectra of Zr and ZrN_x

In figure 4-8, the Auger spectrum of zirconium metal is compared with the Auger spectrum of a zirconium nitride film prepared by nitrogen ion implantation. The Auger spectra show six features in the energy range from 60-200 eV, which all originate in the Zr(3d), i.e. $M_{4,5}$, core energy level. In table 4-1. the energy positions and origins of theses Auger transitions are listed, together with the alternative X-ray notations.

Table 4-1. Zr(MNN) Auger transitions

E/eV	Origin	X-ray notation
72	Zr(3d)(4s)(4s)	$M_{4,5}N_1N_1$
93	Zr(3d)(4s)(4p)	$M_{4,5}N_1N_{2,3}$
116	Zr(3d)(4p)(4p)	$M_{4,5}N_{2,3}N_{2,3}$
125	Zr(3d)(4s)(4d)	$M_{4,5}N_1V^*$
146	Zr(3d)(4p)(4d)	$M_{4,5}N_{2,3}V^*$
174	Zr(3d)(4d)(4d)	$M_{4,5}VV^*$

* *Where V is the valence state.*

Comparing the spectrum of Zr and that of ZrN, it can be seen that the attenuations of

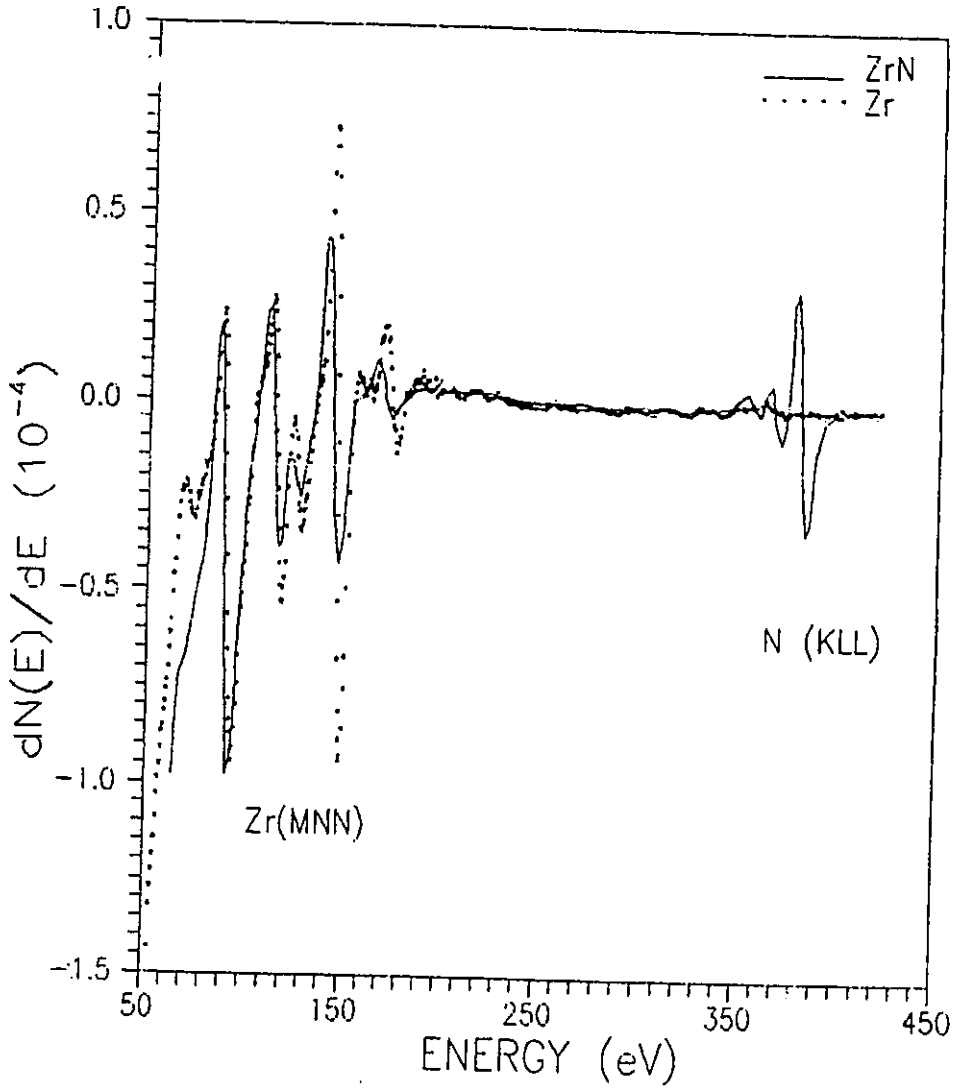

Figure 4-8. Derivative Auger spectra of Zr (points), and ZrN (solid line) in the energy range of 50-450 eV.

$M_{4,5}N_1V$, $M_{4,5}N_{2,3}V$, and $M_{4,5}VV$ features are quite remarkable whereas the amplitude of $M_{4,5}N_1N_{2,3}$ feature at ~93 eV is the same for the metal and the nitride. The $M_{4,5}N_1N_1$ feature at ~72 eV for pure metal seems almost disappear for the nitride, but since this feature is situated on the steep background, the attenuation might be confused by the change of background. Figure 4-8 also shows that all peaks in this energy region shift to lower energy position from pure metal to nitride. The peak ratio of the MNN feature at 93 eV to the MNV feature at 146 eV changes linearly with the escape-depth-averaged nitrogen to zirconium atomic ratio, <x>, shown in figure 4-9. This observation could allow us to explain anomalies in the literature [Dawson, 1991] for N-Ti surface analysis as will be discussed in the next chapter (5.4.3).

4.5.2. The high resolution AES spectra of ZrN_x films

To examine the changes of the zirconium MNN Auger peaks caused by nitriding, high resolution Auger spectra were recorded during sputter profiling of a zirconium nitride film prepared by nitrogen ion implantation, figure 4-10. The composition of each film was determined by the peak ratio of the nitrogen KLL peak to the zirconium $M_{4,5}N_1N_{2,3}$ peak, calibrated with the standard bulk zirconium nitride sample. From the high resolution spectra, it can be seen that the intensities of $M_{4,5}N_{2,3}V$ and $M_{4,5}VV$ features decrease with increase of nitrogen concentration. However, in these high resolution spectra, new features appear on nitriding. The intensity of these "nitride" features increase with nitrogen concentration. Similar changes near the $M_{4,5}N_1V$ peak at ~125 eV are not so clear owing to peak overlap in this energy region, but the change of peak shape is

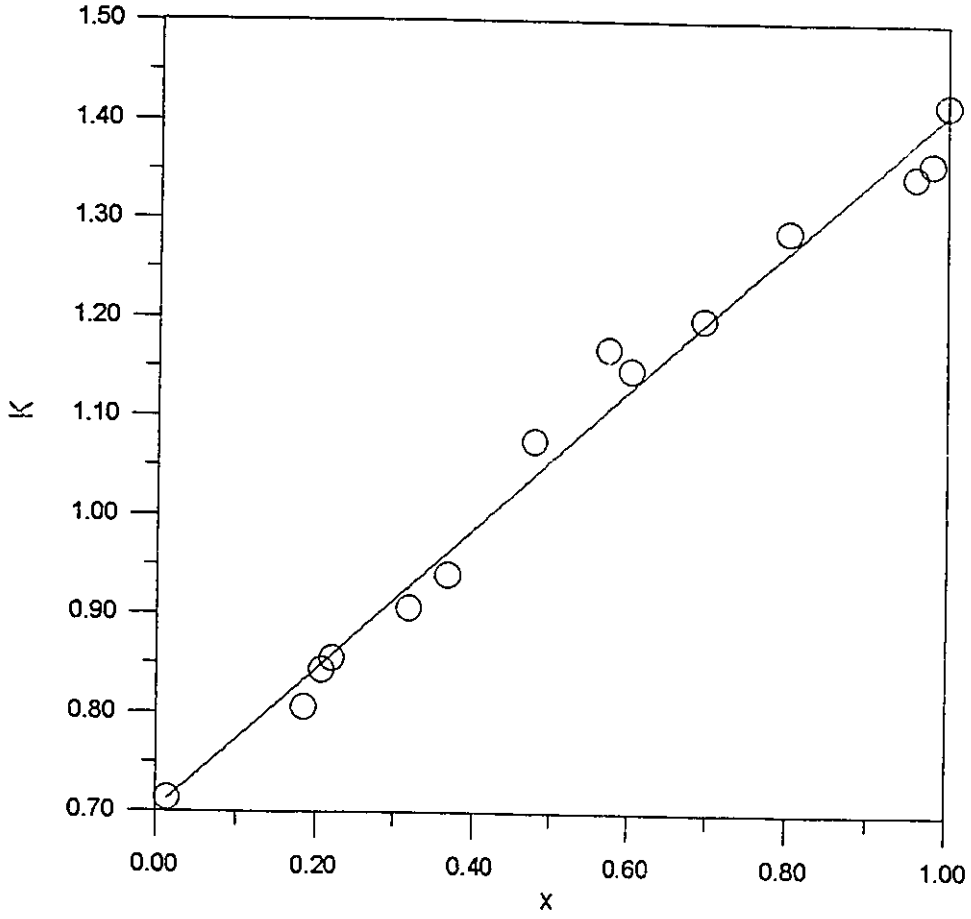

Figure 4-9. The peak ratio of the MNN feature at 93 eV to the MNV feature at 146 eV, K, changes linearly with x, the nitrogen to zirconium atomic ratio.

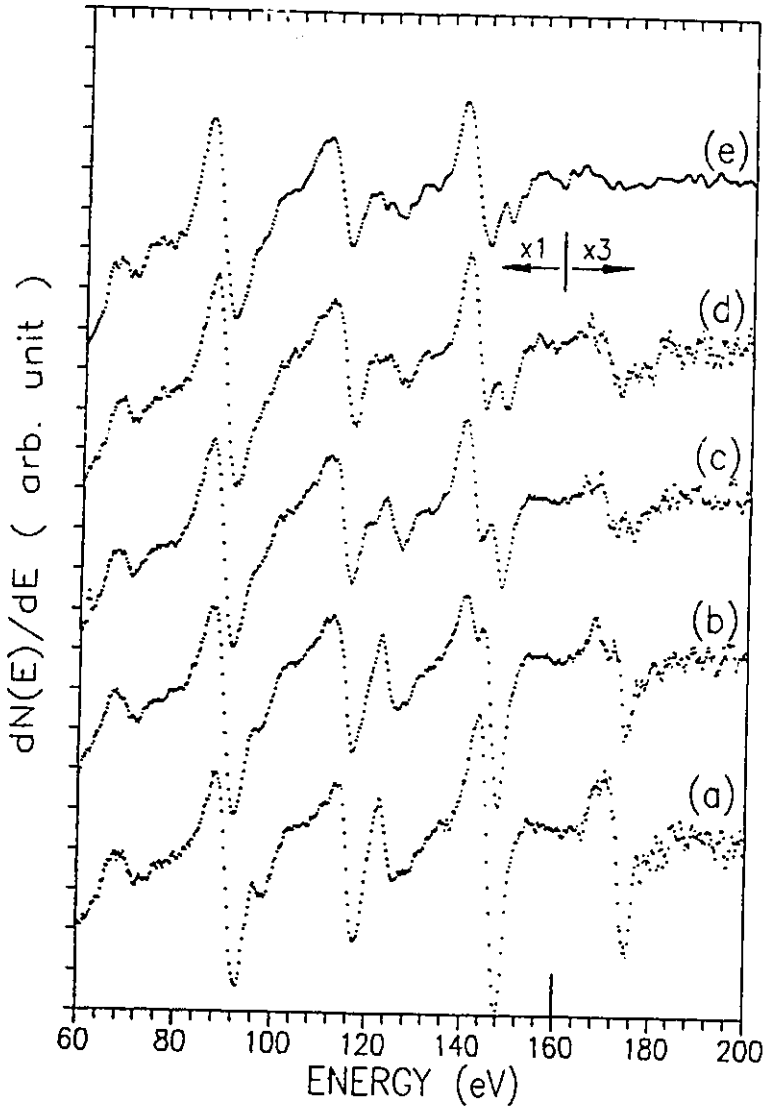

Figure 4-10. Derivative high resolution Auger spectra of (a)Zr; and ZrN_x films prepared by sputtering a nitrogen ion implanted nitride film: (b) $ZrN_{0.33}$ (c) $ZrN_{0.68}$ (d) $ZrN_{0.88}$; and (e) a $ZrN_{0.92}$ film made by NH_3 surface reaction. The composition of the zirconium nitride films was determined from the N(KLL) to $Zr(M_{4,5}N_1N_{2,3})$ peak ratio , calibrated by standards.

obvious.

In figure 4-11 the computed component spectra and their sum has been plotted to compare with the deconvoluted experimental spectra. A Gaussian peak shape has been used for fitting all the peaks. The spectra of zirconium nitride films show four new features at ~120 eV, ~130 eV, ~141 eV and ~170 eV near those "metal" features involving the emission of valence electrons. The spectra also show that the magnitude of the zirconium MNN features which do not involve the valence band essentially do not change on nitriding. We will focus on the changes in the MNV and MVV features and "metal" features will be used to represent the unperturbed MNV and MVV features in the following discussion.

4.5.3. Intensity variations and energy shifts of peaks on nitriding

The change in peak areas of the four new features and Zr metal features is plotted against x, the nitrogen to zirconium atomic ratio, in figure 4-12 (a), which is normalized with $A_{0,T}$, the total area of metal features of the pure zirconium Auger spectrum. The areas of the three metal features decrease while the areas of the four new features increase with x. When the sum of the areas of all new features and metal features for each ZrN_x film is plotted against x, figure 4-12 (b), it is remarkable to find that the total area is essentially constant from x=0 to 0.9.

In figure 4-13, the energy shift of the six zirconium MNN Auger peaks is plotted against x. The peaks can be divided into two groups according to their energy shift

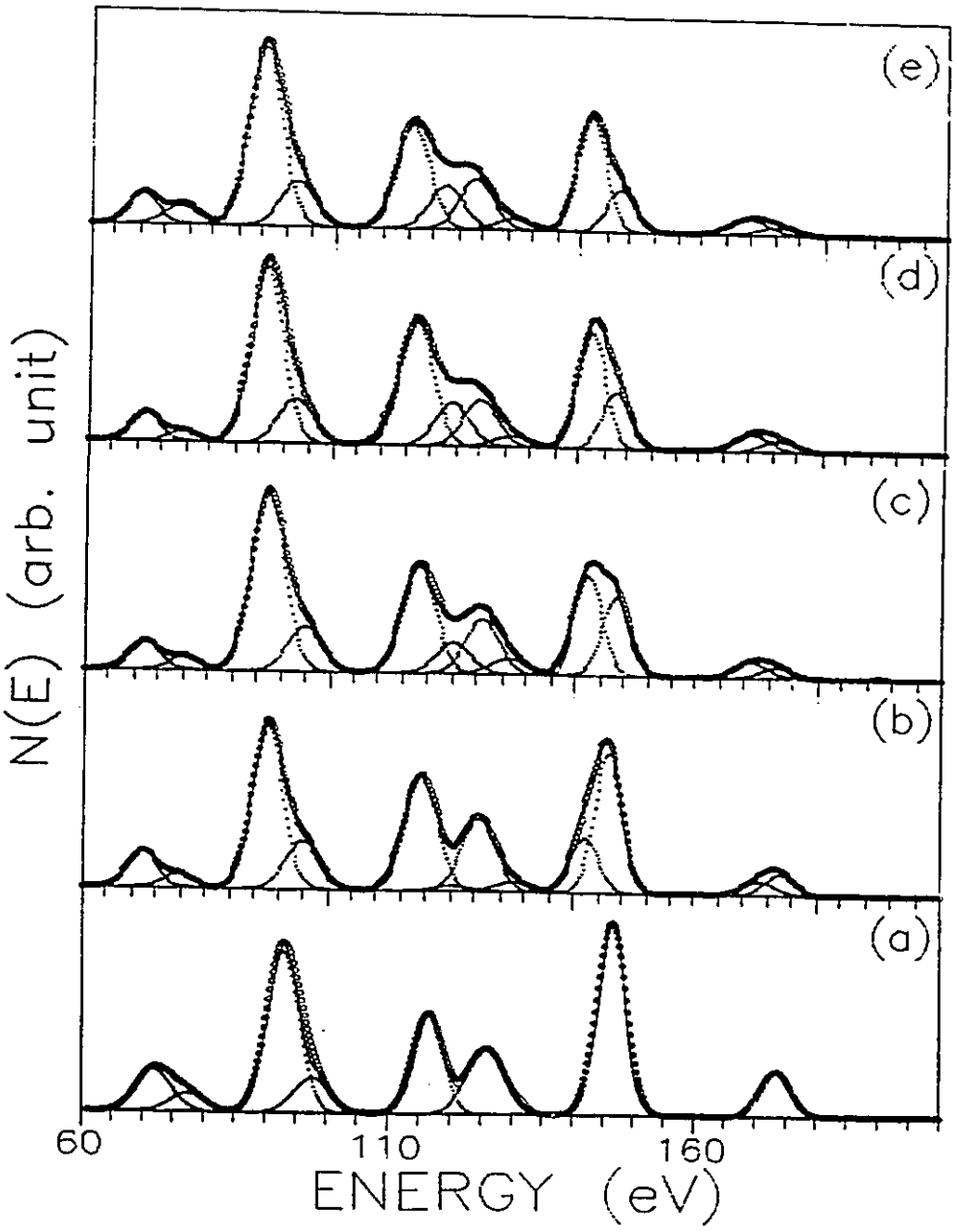

Figure 4-11. Deconvoluted experimental Auger spectra (solid line) and simulated spectra (circles) for: (a) Zr; (b) $ZrN_{0.33}$; (c) $ZrN_{0.68}$; (d) $ZrN_{0.88}$; and (e) $ZrN_{0.92}$. The calculated component peaks are also shown for the spectra.

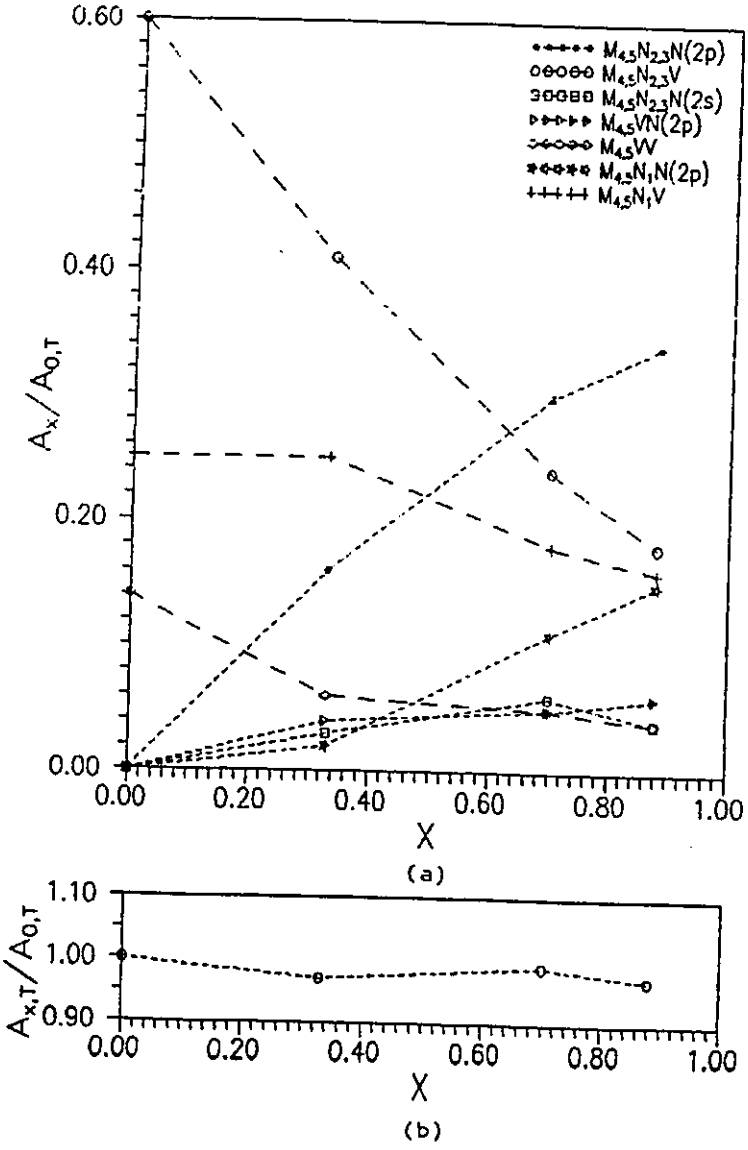

Figure 4-12. (a) The Auger peak areas of the "metal" and "nitride" features change with x. A_x is the peak area for ZrN_x and $A_{0,T}$ is the total peak area of the "metal" features for pure Zr metal. (b) The total peak area of the "metal" and "nitride" features for ZrN_x films remains constant with x.

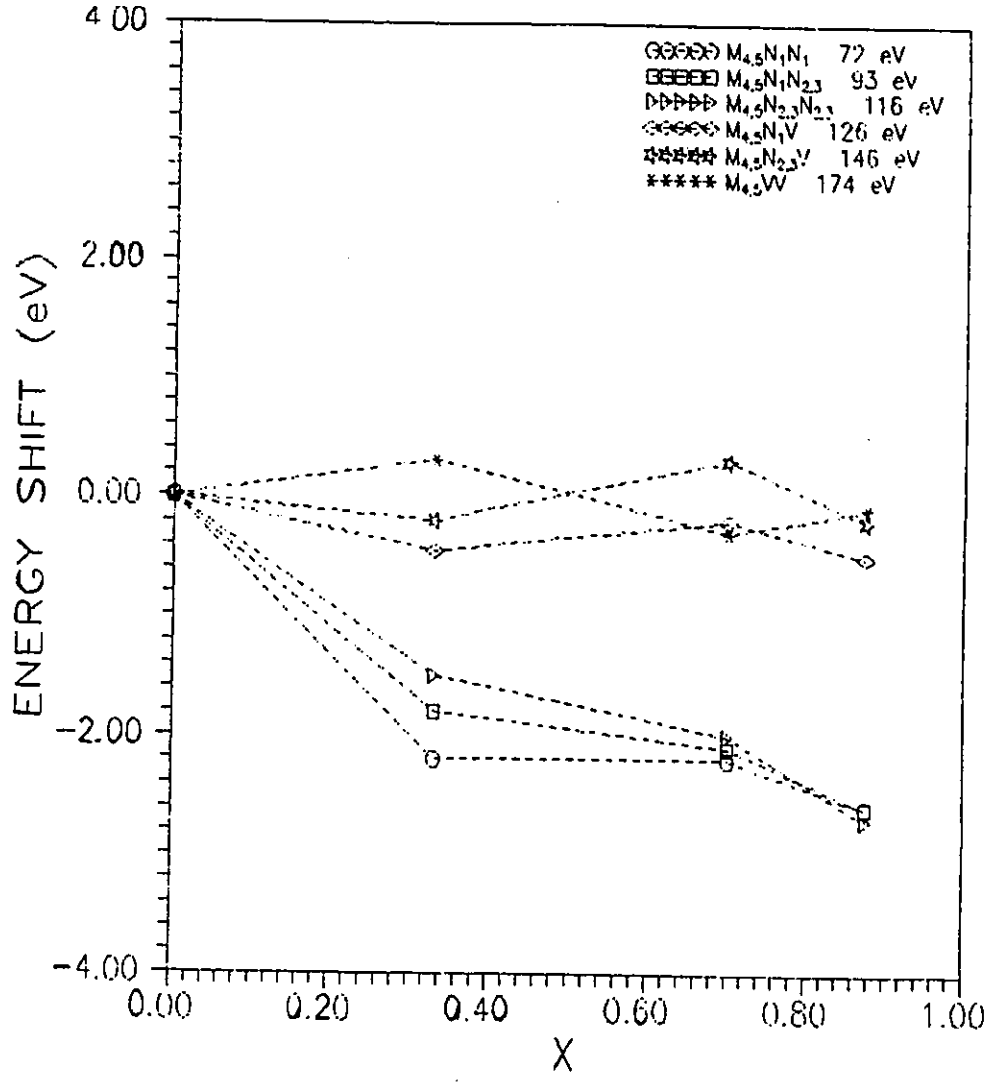

Figure 4-13. Energy shifts of the zirconium MNN peaks relative to the peak positions for pure metal.

behaviour. In the first group of peaks, $M_{4,5}N_1V$, $M_{4,5}N_{2,3}V$ and $M_{4,5}VV$ Auger features, all of which involve valence electron do not shift with x, whereas the other group of peaks, $M_{4,5}N_1N_1$, $M_{4,5}N_1N_{2,3}$, and $M_{4,5}N_{2,3}N_{2,3}$ features, which do not involve valence electrons, shift to lower energy with x.

4.6. DISCUSSION OF THE MNN AES SPECTRA OF Zr AND ZrN

4.6.1. The origin of "nitride" features in MNN AES spectra

It can be seen that the "nitride" peaks at 120 eV, 141 eV and 170 eV have one feature in common, that is, they are all situated 4~5 eV lower in energy than a "metal" feature which involves the emission of a valence electron. In the study of the low energy Auger spectra of zirconium nitrides (section 4.3-4.4), a "nitride" feature about ~4 eV lower in energy than the metal NVV feature was resolved. It was identified as a Zr(4p)Zr(4d)N(2p) Auger cross transition because the energy difference between the zirconium 4d state and the hybridized nitrogen 2p state is about 4 eV [Hochst et al., 1982]. Now in the medium energy region, 60-200 eV, the observed 120 eV "nitride" feature is ~5 eV lower in energy than the $M_{4,5}N_1V$ "metal" feature; the 141 eV "nitride" feature is ~5 eV lower in energy than the $M_{4,5}N_{2,3}V$ "metal" feature; and the 170 eV "nitride" feature is about ~4 eV lower in energy than the $M_{4,5}VV$ "metal" feature. Comparing the MNN and NVV spectra, it is reasonable to concluded that the hybrid N(2p) state in the zirconium valence band can also induce Auger cross transitions in MNN energy region. So the new features at 120 eV, 141 eV and 170 eV can be assigned to Zr(3d)Zr(4s)N(2p), Zr(3d)Zr(4p)N(2p) and Zr(3d)Zr(4d)N(2p) transitions respectively. The energy position of these features was checked by the following equation,

$$E_{xyz}=E_x-E_y-E_z-U_{eff}-\phi. \qquad (4\text{-}4)$$

For example, putting the peak position for Zr(3d)Zr(4p)N(2p), 141 eV, into the left side

of this equation, and using E[Zr(3d)]=181 eV, E[Zr(4p)]=29.7 eV, and E[N(2p)]=4.5 eV, the calculation gives reasonable values, 5.8 eV, for the sum of the analyzer work function, ϕ, and the hole-hole interaction energy, U_{eff}.

The small "nitride" feature at 130 eV, figure 4-11, cannot be interpreted as an Auger cross transition induced by the hybriding of the N(2p) state into zirconium valence band. This feature is situated 11 eV lower in energy than the Zr(3d)Zr(4p)N(2p) feature. This is the energy difference between the binding energy of the N(2p) and N(2s) states and so a possible interpretation for this feature could be the Auger cross transition, Zr(3d)Zr(4p)N(2s). The weak amplitude of this feature suggests a small transition probability for this cross transition.

In a study of the adsorption properties of zirconium by Auger electron spectroscopy, Foord et. al. [1980] mentioned the possibility of zirconium core holes relaxing via cross transitions involving the adsorbate valence level, and pointed out that the expected energy range for cross transitions is 110-170 eV. Since they recorded low resolution Auger spectra without background substraction and peak deconvolution, no such expected cross transitions were resolved. Several investigators reported Auger cross transitions in this energy region for Zr-O system [Tanabe et al., 1987; Jungblut et al., 1988; Sanz et al., 1987; Betteridge et al., 1991], which are the Zr(3d)Zr(4p)O(2p) cross transition at about 7 eV lower in energy than the metal Zr(3d)Zr(4p)Zr(4d) feature and Zr(3d)O(2p)Zr(4d) cross transitions at about 6 eV lower in energy than the metal Zr(3d)Zr(4d)Zr(4d) feature, where O(2p) represents the hybridized valence state.

Considering the energy difference of O(2p) in zirconium oxide [Tanabe et al., 1987] and N(2p) in zirconium nitride [Hochst et al., 1982], it can be easily recognised that the ~141 eV and ~170 eV features are Auger cross transitions for zirconium nitride corresponding to those cross transitions reported for zirconium oxide.

4.6.2. Peak intensity variation with composition

The variations of peak intensity are plotted in figure 4-12. It can be seen that all three "metal" features attenuate with x, and all four "nitride" features grow with x.

The attenuation of the "metal" features and the growth of the "nitride" features suggests that a part of $M_{4,5}$ core holes decay passes through Auger cross transitions on nitriding, and so the intensity of individual feature changes with nitrogen concentration. In figure 4-12, the ratio of $A_{x,T}/A_{0,T}$ is plotted against x, where $A_{x,T}$ is the total peak area of the four "nitride" features and three "metal" features for ZrN_x and $A_{0,T}$ is the total area of the three "metal" features for pure zirconium metal. A constant total intensity against x is shown in the figure 4-12. It suggests that the total number of Auger transitions arising from the decay of $M_{4,5}$ core holes is roughly the same for pure zirconium metal and for ZrN_x films. This behaviour is different from that of the NVV transitions. In a previous study, an interesting phenomenon was observed in the low energy Auger spectra of titanium [Dawson and Tzatzov, 1986] vanadium [Dawson and Tzatzov, 1990] and zirconium [Dawson et al., 1991_2] nitrides, where for the stoichiometric nitride, MN, the total intensity of the metal and nitride features is very small. This means that the decay of the metal core holes, 3p for Ti and V, 4p for Zr, passes through other processes for

nitrides, and the processes were indeed found as Auger features in the very low energy region [Dawson and Tzatzov, 1991_1], M(3p)N(2s)M(3d) at ~15 eV, and N(2s)N(2p)M(3d) at ~5 eV.

4.6.3. Energy shift of the zirconium MNN peaks

The low resolution AES spectra, Figure 4-8, show that all the Zr MNN peaks shift to lower energy when going from pure Zr to its nitride. On nitriding, the N(2p) states hybridize with the Zr(4d) state to produce a new feature in the valence band density of states ~4 eV below the 4d level. This gives rise to new features shifted down in energy by ~4 eV in both the NVV and MNN spectra already discussed in section 4.4.1 and 4.6.1. In this section, different energy shifts caused by the energy changes of Zr core levels on nitriding will be discussed.

The energy shift behaviour of Zr (MNN), including MNV and MVV peaks, can be divided into two groups, figure 4-13. The valence features, i.e. MNV and MVV peaks, do not shift with x; while the non-valence features, i.e. MNN peaks, shift with x. During nitriding, the valence band of zirconium is influenced by nitrogen to the largest extent, and the effect on inner energy states decreases with the electron binding energy. Hochst et al. [1982] reported the binding energy data for zirconium core levels for both the pure metal and the nitride. The binding energy of the Zr(4p) level for ZrN is about 1.9 eV higher than that of the pure metal, and the difference for Zr(3d) is 1.2~1.3 eV. In considering this effect let us take the $M_{4,5}N_{2,3}N_{2,3}$ peak as an example. The peak position for the pure metal and nitride can be calculated by equation 4-4, and indicates an energy

shift of 2.5~2.6 eV to lower energy for zirconium nitride. This agrees very well with the experimentally determined energy shift. Therefore, the nitrogen-induced energy shift can be interpreted by the changes of the binding energy of core levels of zirconium. Figure 4-14 and 4-15 show energy maps for the Auger transitions, and the theoretically calculated energy shift for each peak. The experimentally determined energy shifts are very consistent with the calculations, except for the ~174 eV feature which becomes very small and noisy in the nitride spectrum, making it difficult to determine an accurate position.

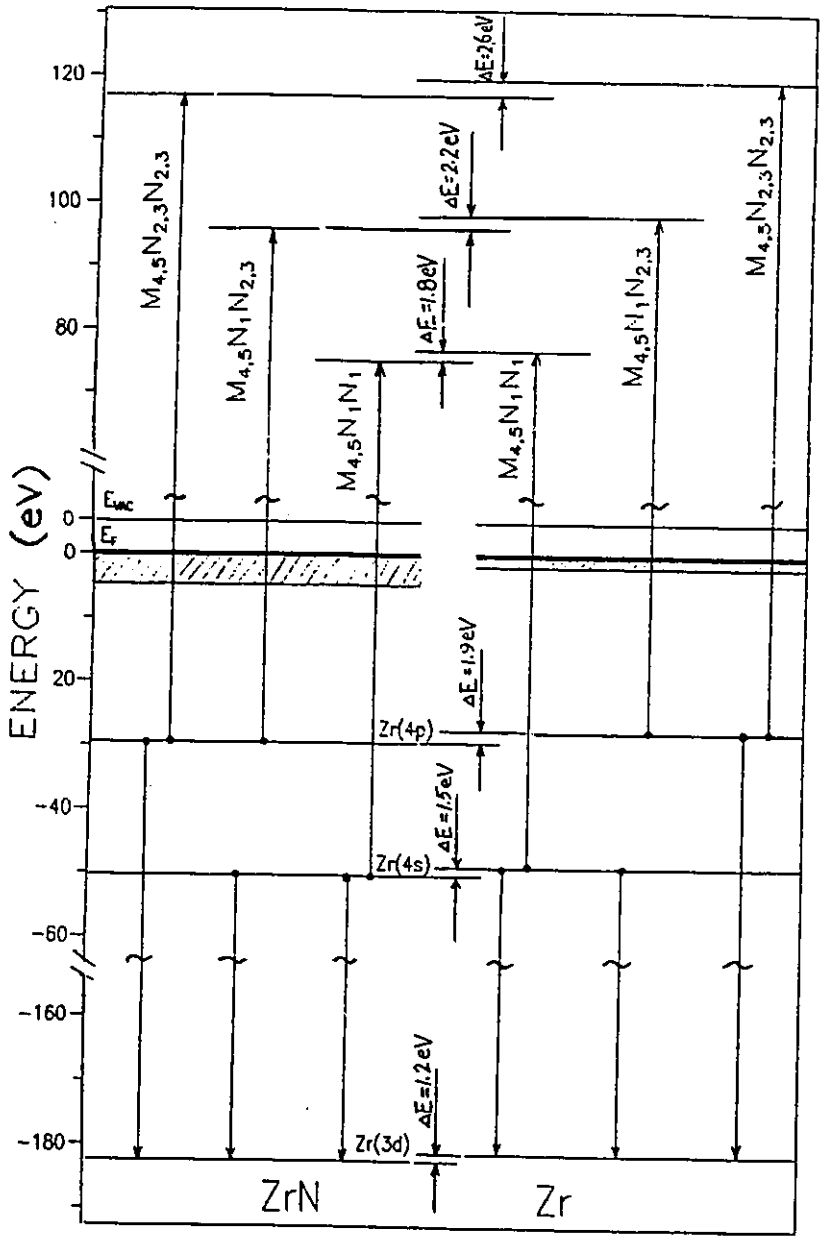

Figure 4-14. MNN Auger transitions for Zr and ZrN showing energy shift of each peak from pure metal to nitride caused by changes in the binding energy of the Zr core levels.

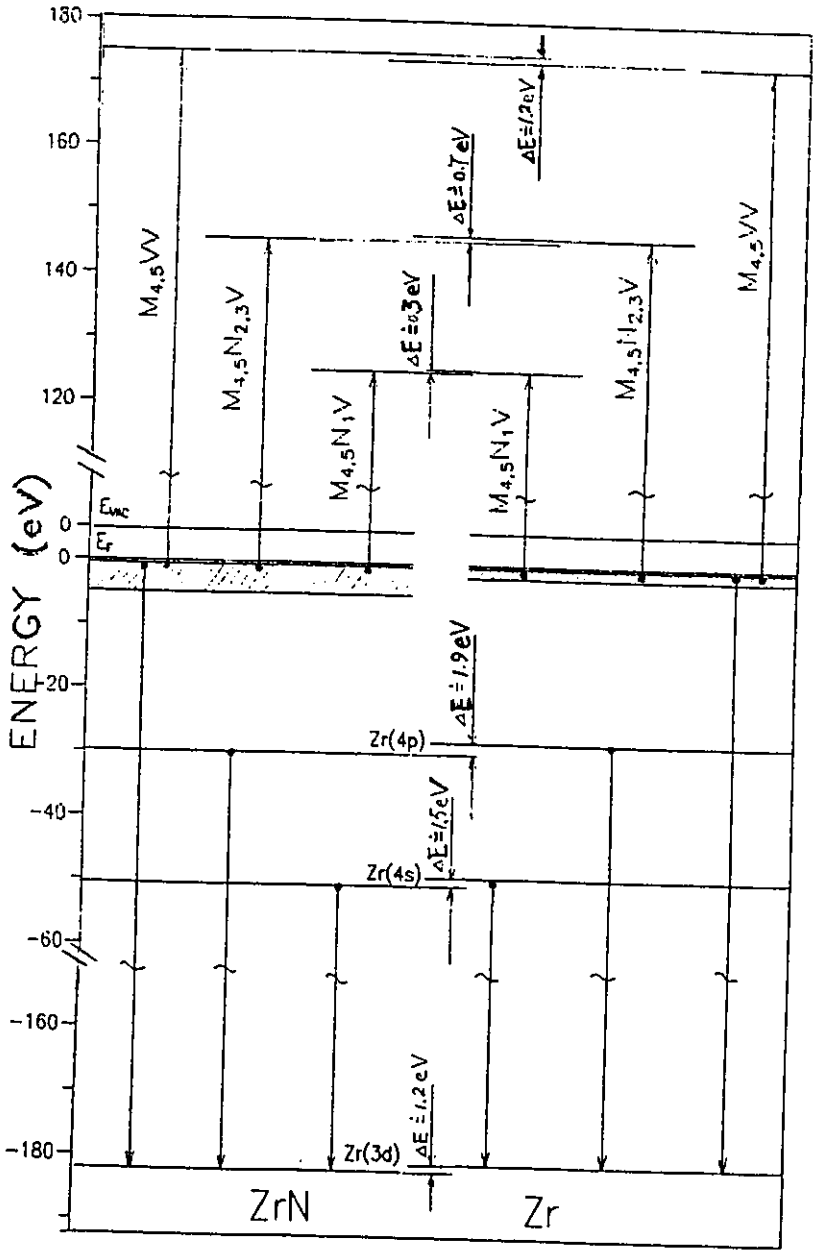

Figure 4-15. MNV and MVV Auger transitions for Zr and ZrN, showing the small energy shift of these peaks arising from changes in the binding energy of Zr core levels.

4.7. CONCLUSIONS

The nitriding of zirconium induces "nitride" Auger features in both the NVV and MNN Auger spectra. In NVV Auger spectra, a "nitride" feature was found about 4 eV lower in energy than the "metal" NVV feature, and identified as an Auger cross transition, Zr(4p)Zr(4d)N(2p). The intensities of the "metal" and "nitride" Auger features vary with the nitrogen concentration of the nitride film. The "nitride" feature has a maximum intensity around x=0.5. The intensity of the "metal" feature decreases linearly with the nitrogen to metal atomic ratio, x, which provides a good quantitative method for the analysis of zirconium nitride films. The linear relationship between the "metal" feature and the nitrogen to metal atomic ratio can be interpreted as the intensity of this feature varies with the number of unoccupied octahedral holes in the nitride structure. And the intensity variation of the "nitride" feature is consistent with the requirement for adjacent occupied and unoccupied holes for this transition to occur. The energy shift of these two features is consistent with the shift of Zr(4p) binding energy on nitriding reported in XPS studies [Hochst et al., 1982].

Using high resolution Auger spectra and data processing procedures, the so-called "abnormal" attenuation of the MNN Auger peaks of zirconium on nitriding can be well understood. In the MNN transition energy region, four "nitride" features have been detected in high resolution Auger spectra, and they have been assigned to Zr(3d)Zr(4s)N(2p), Zr(3d)Zr(4p)N(2s), Zr(3d)Zr(4p)N(2p) and Zr(3d)N(2p)Zr(4d) Auger cross transitions. The intensity of all MNN "nitride" features increase with the nitrogen to zirconium atomic ratio. The intensity of metal MNN features which involve only zirconium core energy levels change very little on nitriding, whereas the intensity of MNV and MVV features decrease with the nitrogen to zirconium atomic ratio. As the

total intensity of Auger transitions arising from the zirconium $M_{4,5}$ core level does not change with composition, it is suggested that the total number of Auger transitions arising from the decay of $M_{4,5}$ core holes remains constant. The energy shifts of the Auger peaks correlates very well with the changes of binding energy of zirconium core levels.

For zirconium nitride films, we have developed quantitative Auger analysis methods for both the NVV and MNN Auger spectra. They can be used for the purpose of practical quantitative analysis of zirconium nitride films. The difference in depth resolution of the low and higher energy Auger electrons can provide a method to probe the concentration depth profile for nitride films as previously reported for titanium nitride films [Dawson and Tzatzov, 1987].

CHAPTER FIVE

THE ADSORPTION OF AMMONIA ON TRANSITION METALS AND ELECTRON IRRADIATION EFFECTS

5.1 INTRODUCTION

Ammonia is used widely in preparing transition metal nitrides, especially for the sixth-group transition metals which cannot effectively be nitrided in a nitrogen atmosphere. Studying the interaction of ammonia gas molecules with transition metal surfaces is important to the understanding of the initial stages of nitride film growth.

Electron bombardment of surfaces during AES measurements may cause changes in the concentration or chemical state of surface species by a number of processes, including dissociation of surface molecules and desorption of ionic and neutral fragments. The earlier studies on electron beam effects have been reviewed by Pantano and Madey [1981]. In addition to the surface composition changes caused by electron stimulated desorption, in the presence of background gases, electron irradiation can lead to changes

in surface composition due to electron stimulated adsorption. Due to the strong adsorption of ammonia gas by the walls of the ultra-high vacuum system and the subsequent slow desorption, the residual pressure of ammonia in the system during analysis is usually high. Therefore, the primary concern in this work is the effect of electron stimulated adsorption. The electron stimulated adsorption of various species on clean metal surfaces has been discussed by a number of investigators. Coad et. al. [1970] showed the enhanced adsorption of oxygen on Si under the electron beam. They concluded that the enhanced oxidation under electron beam bombardment can be caused by CO in the residual gas. Joyce and Neave [1973] have reported similar electron stimulated adsorption of carbon on Si derived from CO, CO_2 and hydrocarbons.

A mechanism for electron stimulated adsorption was suggested by Kirby and Lichman [1974] based on their LEED-Auger studies of the adsorption of CO and O_2 on Si. They suggested that although an equilibrium between adsorbed and gaseous species exists for given conditions of pressure and temperature, adsorbed molecular species may be dissociated by an electron beam. One of the dissociated species desorbs while the other may diffuse or chemically react with the substrate. It has been suggested that the gas first adsorbs into a weakly bound state, is then dissociated by the electron beam, and finally is either chemisorbed on the surface or diffuses into the bulk. In the absence of the beam, the weakly bound molecules simply desorb from the surface. This interpretation is consistent with the electron stimulated adsorption of N (from NH_3) on Ru(001) [Danielson et al., 1978] and the beam induced oxidation of polycrystalline Ni [Verhoeven and Los, 1976]. An alternative model has been proposed by Neave and Joyce [1977].

They believe that ionization of oxygen molecules in gas phase by the electron beam is responsible for the enhanced adsorption on GaAs.

In this chapter, the NH_3 adsorption properties and the effect of electron stimulation on NH_3/Ti, NH_3/Cr, NH_3/Zr, and NH_3/W systems will be compared and discussed. Although the chemistry of Ti is similar to Zr and differs from that of W, it is surprising to see that the behaviour of NH_3 adsorption on Ti is remarkably similar to that on W while the behaviour of Zr is very different from all the other transition metals studied in this work.

5.2 EXPERIMENTAL PROCEDURE

The ammonia gas used in this work was supplied by Matheson Gas Products Inc. with a purity 99.998%, and it was introduced and stored in a glass gas reservoir. Then it was further purified by distillation using liquid nitrogen traps. In most ammonia adsorption experiments, the sample was turned to face the multi-orifice gas doser during adsorption. The gas flux was determined by measuring pressure decay in the gas reservoir and controlled at 5.7×10^{15} molecules $cm^{-2} s^{-1}$ by a leak valve. During ammonia dosing, the background gas pressure in the chamber was about 10^{-7} torr. The sample was turned away from the dosing position at the end of adsorption, and the leak valve was turned off immediately. At first, the background pressure quickly dropped to 5×10^{-8} torr. The pressure drop became very slow thereafter because of the slow pumping speed of ammonia gas.

In other experiments designed to investigate the effect of the electron beam on ammonia adsorption, the background ammonia gas pressure was kept constant dynamically. The sample was kept away from the dosing position to avoid enhanced gas dosing and limit exposure to the background ammonia gas.

5.3 EXPERIMENTAL RESULTS

5.3.1. The adsorption of ammonia on tungsten at 300 K

Figure 5-1 shows the Auger spectrum of a clean tungsten surface in the energy range of 110-240 eV. The Auger peaks at 150-200 eV arise from W(NNN) Auger transitions [Haas et al., 1970]. The Auger spectra taken after 3 and 5 minutes ammonia dosing using the multi-orifice gas doser at room temperature are shown in figure 5-2 (a) and (b) respectively. These two experiments both started from a clean tungsten surface. The difference spectrum of (b)-(a), shown in figure 5-2 (c), is featureless indicating that the ammonia adsorption has reached saturation on the tungsten surface after 3 minutes dosing with a gas flux of 5.7×10^{15} molecules cm^{-2} s^{-1} at room temperature.

In an attempt to increase the precision, Auger spectra were taken after 5 minutes ammonia adsorption under the same condition as before but taking three sweeps. It was observed that the nitrogen N(KLL) Auger peak was significantly larger than that of the previous single sweep experiment, figure 5-3. A longer electron beam exposure time producing an increased N uptake, provides evidence for electron stimulated NH_3 adsorption on tungsten surfaces with an ammonia background pressure of about 10^{-8} torr. No electron beam was present during the initial 5 minutes high flux dosing.

An experiment was designed to confirm the effect of electron beam stimulation of the adsorption of NH_3 on a W surface. First, ammonia gas was dosed on the clean tungsten sample for 5 minutes at room temperature with no electron beam. Following this,

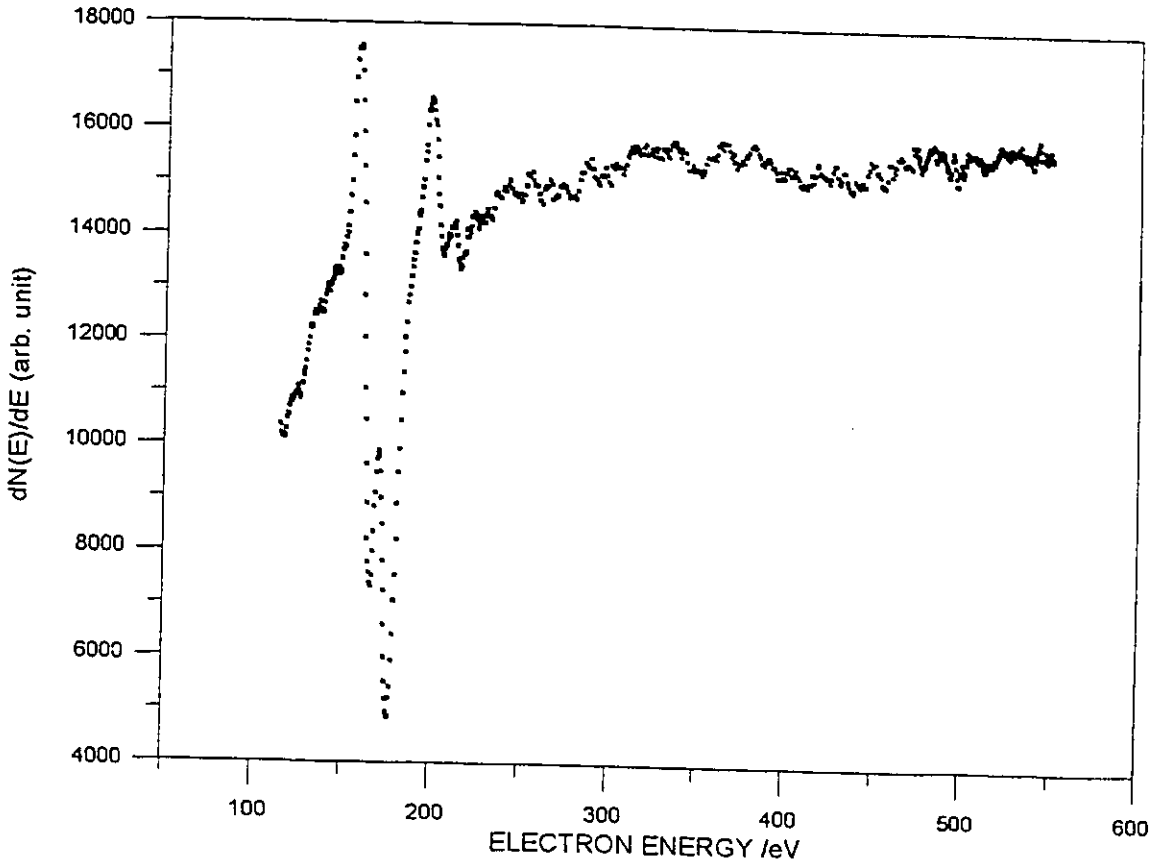

Figure 5-1. The NNN Auger spectrum of tungsten.

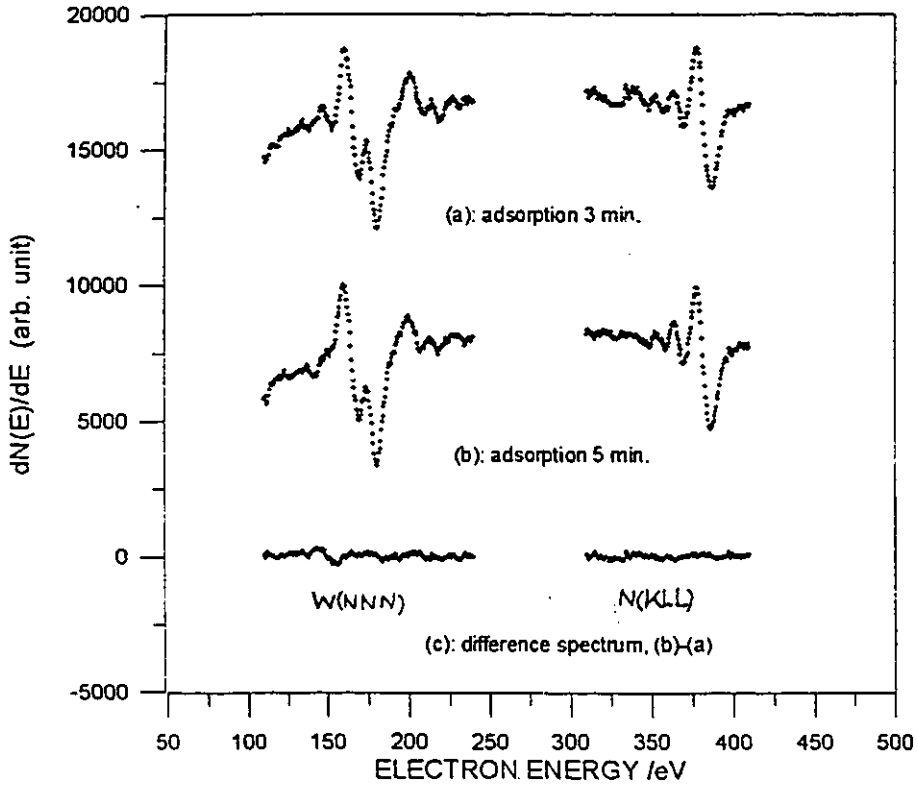

Figure 5-2. Auger spectra taken after (a) 3 minutes and (b) 5 minutes ammonia interaction with tungsten at room temperature with a gas flux 5.7×10^{15} molecules cm^{-2} s^{-1}. The difference spectrum is shown in (c).

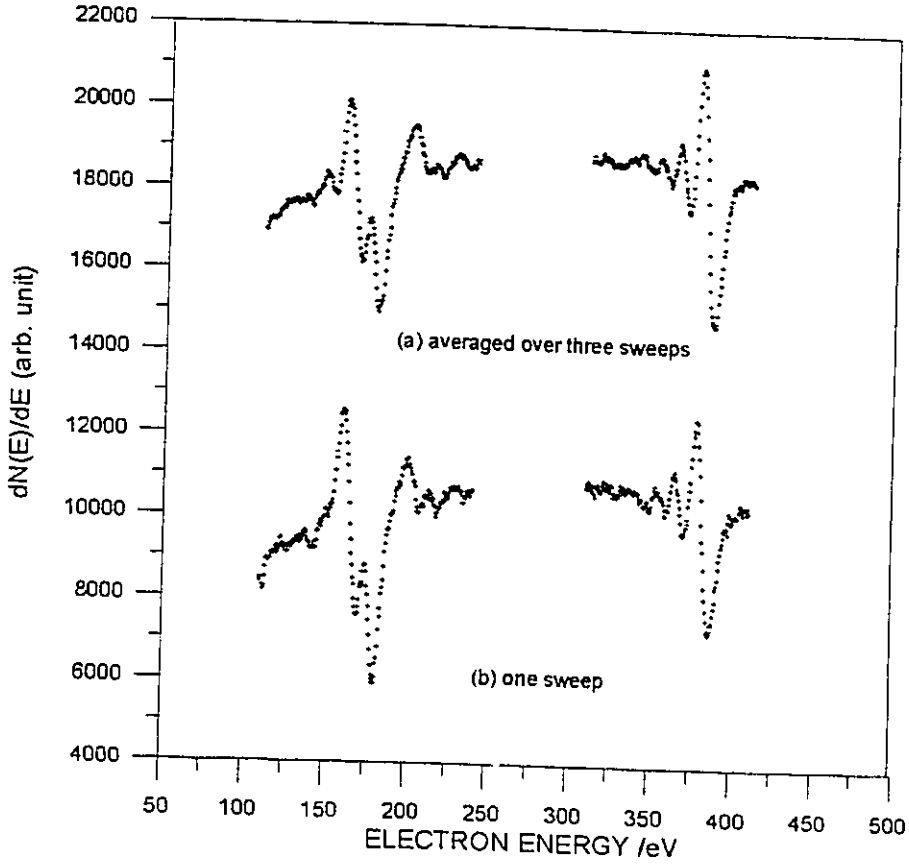

Figure 5-3. Auger spectra taken after room temperature ammonia adsorption, (a) averaged over three sweeps and (b) one sweep.

five Auger spectra were taken from five different sampling positions on the sample. During the analysis, the ammonia background pressure was about $5x10^{-8}$ torr. The peak-to-peak heights of N(KLL) peak obtained from different sampling positions are shown in figure 5-4 (a). After this analysis, an electron beam of 2 keV and 10 μA was aligned with the centre of the sample for a 15 minute exposure. The background ammonia pressure was slowly pumped down to ~$2x10^{-8}$ torr by the end of this beam exposure. On the same sampling positions, another five Auger spectra were taken after the electron beam exposure. The peak-to-peak heights of N(KLL) peak from theses spectra are shown in figure 5-4 (b). It is obvious that the nitrogen uptake from ammonia adsorption is enhanced in the sample centre which received a ~4 times longer electron beam exposure than the other sampling positions. The nitrogen peak-to-peak height value at the centre of the sample reached 6130 (arbitrary) units, figure 5-4 (b), with electron beam stimulated adsorption. Figure 5-5 shows another AES spectrum which was also taken after 5 minutes ammonia dosing at room temperature, but in this experiment, the sample was not exposed to electron beam until the background pressure had been pumped down to 10^{-9} torr. It can be seen that when the electron beam effect was carefully avoided, the N(KLL) peak-to-peak height value at saturation was only 2500.

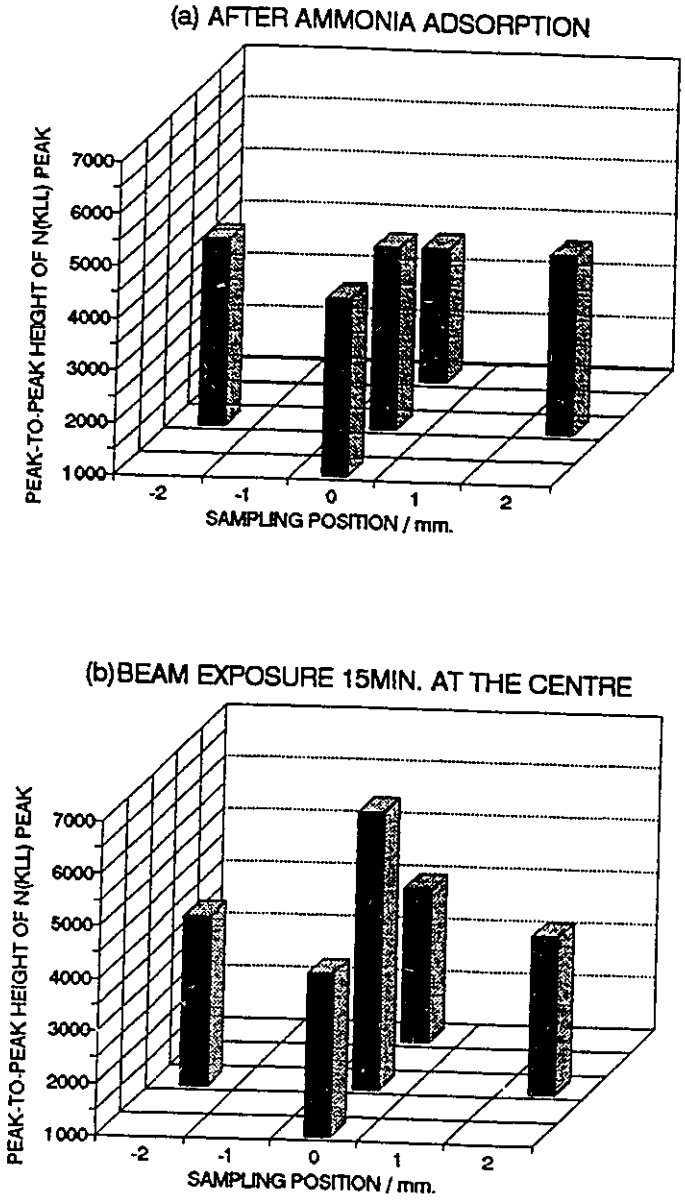

Figure 5-4. The nitrogen KLL peak-to-peak heights at different sampling positions are plotted (a) after 5 minutes ammonia adsorption using the multi orifices gas doser at room temperature and (b) after a further 15 minutes electron beam bombardment at the centre of the surface, the background ammonia pressure decreased from ~$5x10^{-8}$ to $2x10^{-8}$ torr during electron beam exposure.

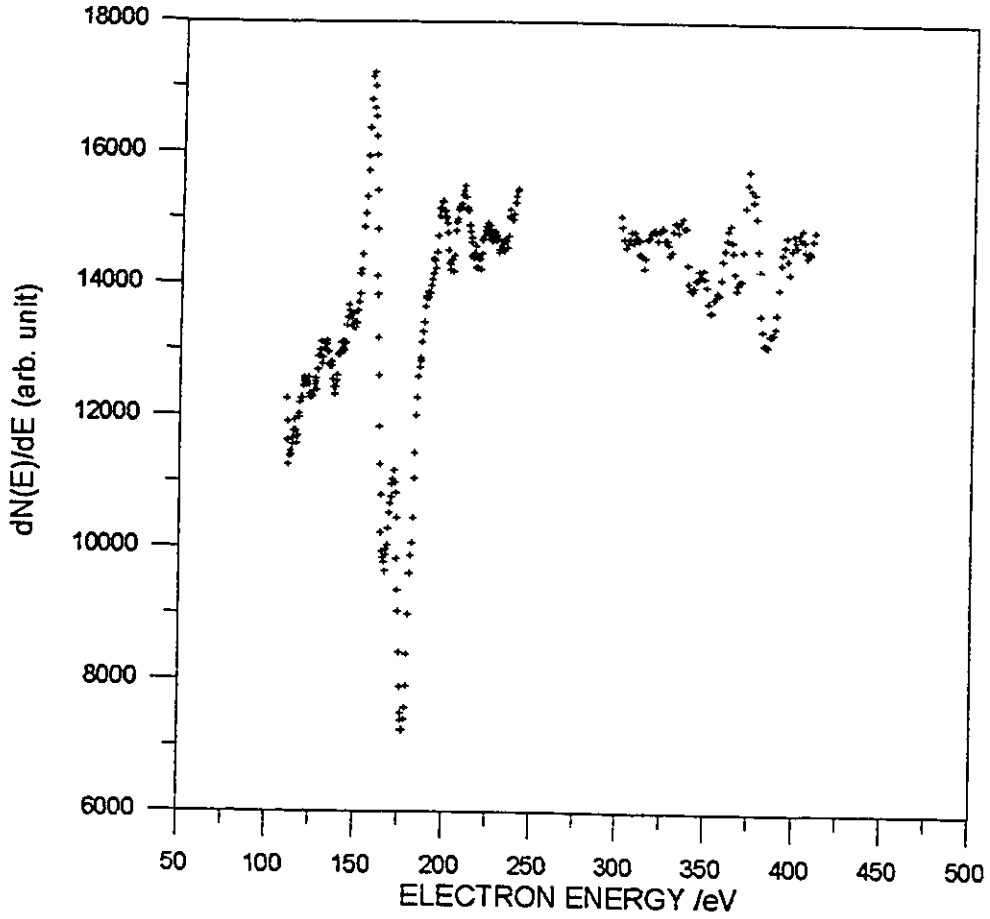

Figure 5-5 The AES spectrum of tungsten taken after 5 minutes ammonia adsorption at room temperature using the multi orifices gas doser and the background ammonia pressure was pumped down to $1x10^{-9}$ torr before AES analysis .

5.3.2. The adsorption of ammonia on chromium at 300 K

The Auger spectra taken from a clean chromium surface and after 5 minutes ammonia adsorption using the multi-orifice gas doser at room temperature are shown in figure 5-6 (a) and (b) respectively. The three Cr(LMM) Auger peaks at ~490 eV, ~531eV and ~573 eV originate in the Cr(2p)(3s)(3d), Cr(2p)(3p)(3d) and Cr(2p)(3d)(3d) Auger transitions. The peak-to-peak height value for nitrogen KLL Auger peak after ammonia adsorption, figure 5-6 (b), is 2300 (arbitrary) units, and the peak-to-peak height ratio of N(KLL) to Cr(2p)(3p)(3d) peak, is ~0.35.

An experiment was designed to examine whether there is also an electron beam enhanced ammonia adsorption on chromium surface as tungsten. The adsorption was performed in two different ways, marked method (a) and method (b) in figure 5-7. In method (a), there are three adsorption experiments. The multi-orifice gas doser with a gas flux 5.7×10^{15} molecules cm^{-2} s^{-1} was used for the first two adsorption experiments. The data of the third adsorption experiment came after the chromium surface had been treated with ammonia for 30 minutes by being exposed to background ammonia gas at 2×10^{-6} torr. This represents a flux of 9.8×10^{14} molecules cm^{-2} s^{-1}. In method (a), the electron stimulation effect was minimized since each ammonia adsorption experiment started with a clean Cr surface and the ammonia background pressure was pumped down before taking an Auger spectrum. It can be seen that the room temperature ammonia adsorption is saturated with a nitrogen peak-to-peak height value at about 2300.

In method (b), the adsorption experiment started with an ammonia saturated

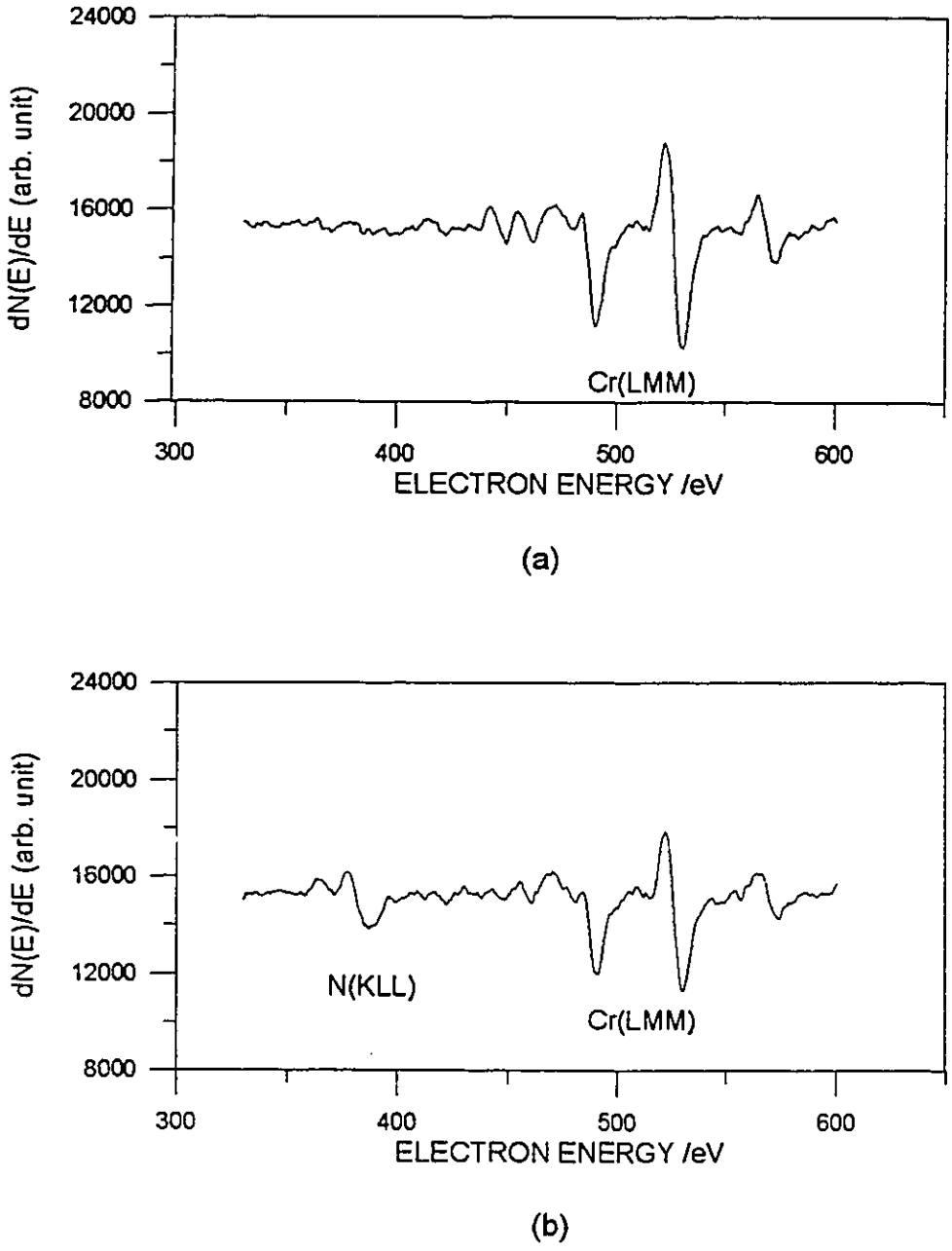

Figure 5-6. The Auger spectra of (a) pure chromium and (b) after 5 minutes ammonia adsorption at room temperature using the multi orifices gas doser.

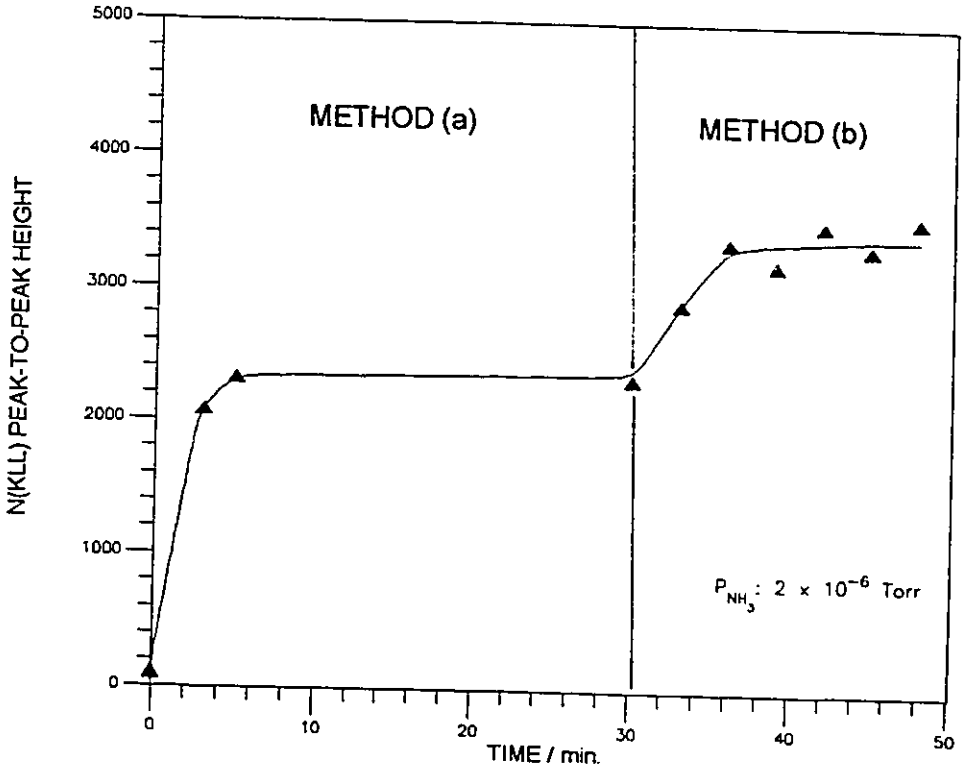

Figure 5-7. The N(KLL) peak-to-peak height data are plotted versus ammonia adsorption time. The adsorption was carried out at room temperature using two methods: (a) the data are taken from separate adsorption experiments, which all started from a clean Cr surface; ammonia was pumped away before taking each Auger spectrum; (b) the sample surface was exposed to ammonia gas at a constant pressure of $2x10^{-6}$ torr and monitored by Auger continuously. In method (a), the electron beam bombardment effect is eliminated, while in method (b), the surface is exposed to ammonia gas and the electron beam simultaneously.

surface, which was prepared with method (a). Ammonia gas was introduced into the chamber and kept at $2x10^{-6}$ torr dynamically by controlling the gas inlet and outlet valves. The sample was facing the analyzer and its surface composition was continuously monitored by AES. In this way, the sample was continuously exposed to the gas flux and the electron beam used for AES analysis. The enhanced ammonia adsorption on chromium by electron beam stimulation is revealed by the step shown in the curve of figure 5-7. The peak-to-peak height of N(KLL) peak increased to ~3500, and the peak ratio of N(KLL) to Cr($LM_{2,3}M_{4,5}$) increased to ~0.66 by electron beam stimulation.

5.3.3. The adsorption of ammonia on titanium at 300 K

Figure 5-8 (a) shows the Auger spectra taken from a clean Ti surface and (b) an ammonia saturated Ti surface, which was prepared by method (a) described in this section. This energy region, contains the Ti(LMM) Auger peaks, and the two main peaks are from the Ti(LMM) transition at 384 eV and the Ti(LMV) transition at 420 eV. The peak-to-peak height ratio of these two peaks, P(385)/P(420), is about 0.73 for pure titanium, which agrees well with the value previously reported by this laboratory [Dawson and Tzatzov, 1985]. The spectrum shown in figure 5-8 (b) shows a much higher value of this ratio, P(385)/P(420), because of the overlap of the N(KLL) transition with the Ti(LMM) transition. The composition of N/Ti system can be determined by using the following equation, which is a widely accepted procedure, previously developed in this group [Dawson and Tzatzov, 1985],

$$P_{N(KLL)} = P_{385eV} - K_{Ti}\, P_{420eV} \qquad (5\text{-}1)$$

where P_{385eV} is the combined Ti + N peak height at 385 eV for a sample N/Ti, $P_{N(KLL)}$ is the contribution of nitrogen to the height of 385 eV peak, P_{420eV} is the 420 eV peak height for N/Ti, K_{Ti} is the peak height ratio of Ti 384 eV peak to Ti 420 eV peak for pure Ti. The average atomic ratio of N/Ti over the analysis depth can be calculated as

$$\langle x \rangle = (P_{N(KLL)} / P_{420eV}) / P_{rel}, \qquad (5\text{-}2)$$

where P_{rel} equals to 1.90, which is the ratio of the spectrometer sensitivity factors, s_N / s_{Ti}. The combined peak height at 385 eV for the spectrum shown in figure 5-8 (b) is 17800,

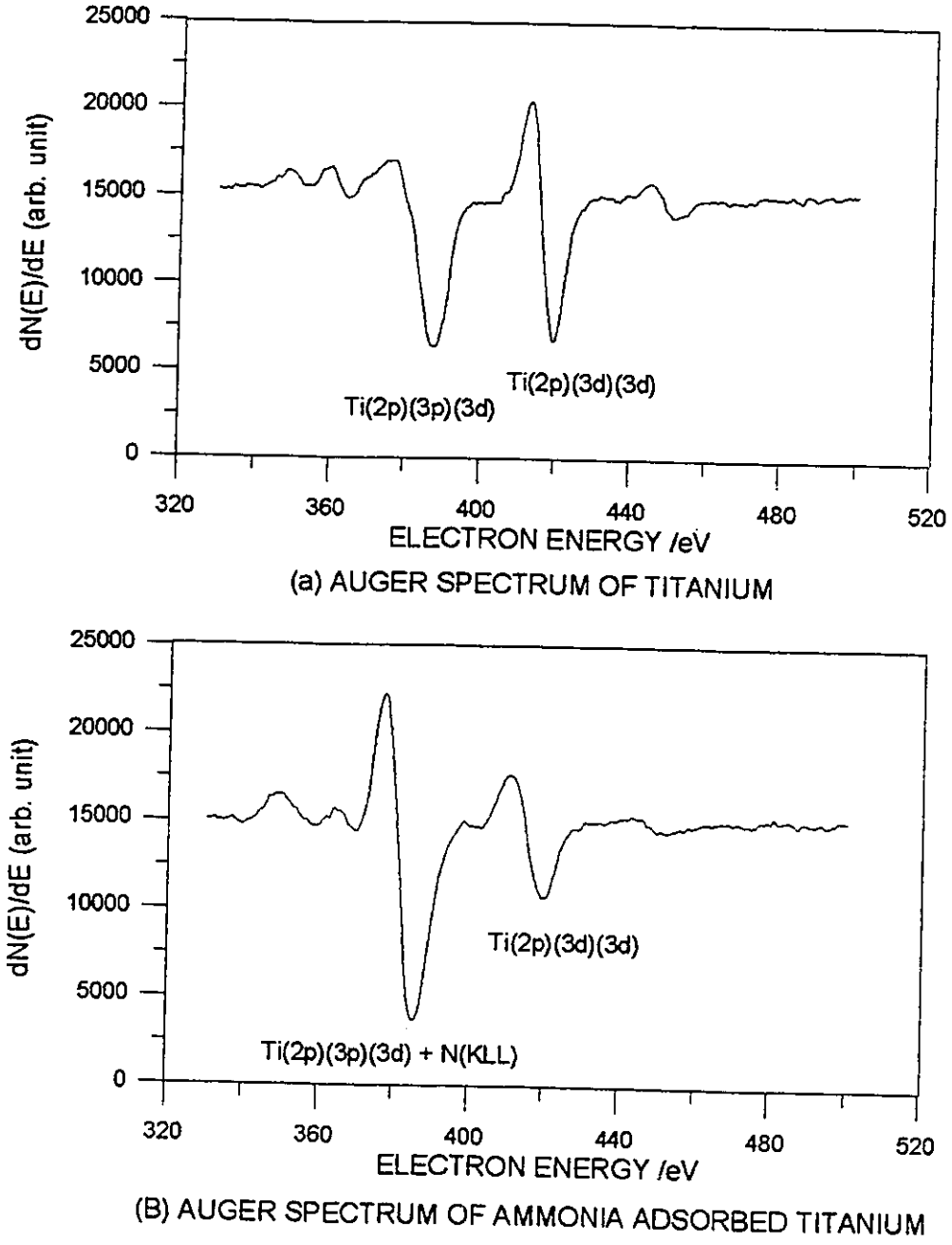

Figure 5-8. The Auger spectra taken from (a) pure titanium and (b) an ammonia saturated titanium surface which was prepared by method (a) described in figure 5-9.

and the peak height at 420 eV is 7500. The calculated nitrogen peak height for spectrum (b) is 12325 and <x> is 0.86.

Figure 5-9 shows a plot of the escape depth averaged N/Ti atomic ratio, <x>, calculated from room temperature experimental Auger spectra with equation 5-2, against the ammonia dosing time. The data shown in figure 5-9 were obtained from three experiments carried out by different methods. In experiment (a), the Ti sample was turned to face doser, and dosed with an ammonia flux $5.7x10^{15}$ molecules cm^{-2} s^{-1} for one minute. After the dosing, the ammonia flux was turned off, and the Ti sample was analyzed by AES. In this way, the Auger spectrum was taken after each minute NH_3 dosing. It is shown by curve (a) that the average atomic ratio <x> increases with ammonia dosing time until t=10 minutes, where it reaches a high saturation value at an <x> value around 0.86. The Auger spectrum at saturation is shown in figure 5-8 (b). In data set (c), two ammonia adsorption data are given, which were obtained from separate adsorption experiments, both starting with a clean Ti surface. Auger spectra were taken after continuous ammonia dosing for 7 minutes in the first experiment, and 10 minutes for the second experiment. The <x> values obtained from these two experiments are ~0.4. This is only about half the saturation <x> value in curve(a). Once again, the difference in saturation value of x shown in experiments (a) and (c) suggests the possible stimulation effect of the electron beam irradiation used for AES analysis. The experiment (b), shown in Figure 5-9 curve (b), was designed to confirm the electron irradiation effect on the uptake of NH_3 by Ti at room temperature. At the beginning, the experiment was carried out under the same condition as curve(a), the first Auger spectrum following the clean Ti surface spectrum

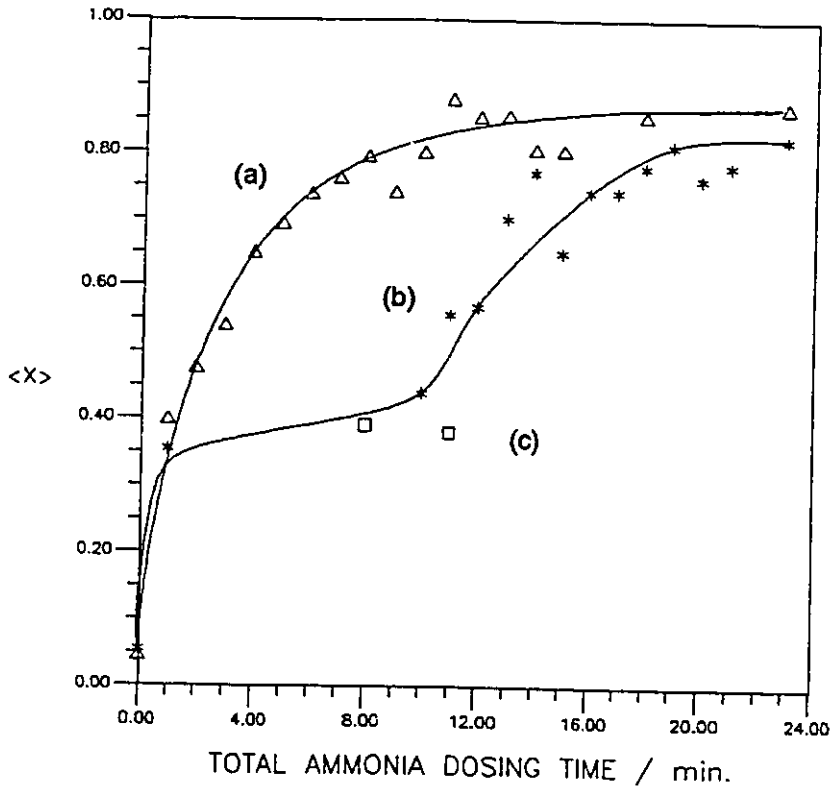

Figure 5-9. The escape-depth-averaged nitrogen to titanium ratio, <x>, is plotted versus total ammonia dosing time. The data were obtained in three different ways: in (a) the Auger spectrum was taken after each minute ammonia dosing; in (b) the first Auger spectrum was taken after the first minute ammonia dosing, the next Auger spectrum was taken after continuous 10 minutes ammonia dosing with no electron bombardment of the surface, thereafter, Auger spectra were taken after each minute ammonia dosing ; (c) data were obtained from two separate ammonia adsorption experiments, both starting from a clean titanium surface and with no electron beam bombardment during gas exposure.

was taken after the first minute NH_3 exposure. The next Auger spectrum was taken after 10 minutes continuous ammonia dosing without electron bombardment. Thereafter, Auger spectra were taken after each 1 min. exposure again until the total exposure time reaches 23 min. It is worth noting that the increase of <x> in curve (b) with 10 minutes ammonia dosing is little more than caused by 1 minute dosing in experiment (a). If we ignore the 10 minutes continuous dosing, shift all the experimental points after the 10 minutes dosing in curve(b) left by 10 minutes, they will all fit very well with curve(a). It is obvious that the electron stimulation effect for NH_3/Ti is quite similar to that observed for the NH_3/W and NH_3/Cr systems.

5.3.4. The adsorption of ammonia on zirconium at 300 K

The Auger spectra taken from a clean zirconium surface and following ammonia adsorption at room temperature are shown in figure 5-10 (a) and (b) respectively. The spectrum shown in figure 5-10 (b) was taken after three minutes ammonia dosing with an ammonia gas flux of 5.7×10^{15} molecules cm^{-2} s^{-1}. In this experiment, the electron probe of the Auger analysis was not used until the ammonia pressure in the chamber had been pumped down to 10^{-9} torr, so that any electron beam effects on ammonia adsorption were carefully avoided. The absolute peak-to-peak height value for N(KLL) peak, figure 5-10 (b), is 7365 (arbitrary) units and the peak-to-peak height ratio of N(KLL) peak at 386 eV to $Zr(M_{4,5}N_1N_{23})$ at 95 eV has reached 0.55, which is close to the value, 0.53, obtained from a standard bulk nitride sample, $ZrN_{0.74}$, in this laboratory.

Figure 5-11 shows a plot of N(KLL) peak-to-peak height values against ammonia gas exposure time for an ammonia adsorption experiment. In this experiment, ammonia gas was introduced into the chamber and kept at a constant pressure of 1×10^{-7} torr. The AES analysis was arranged to sweep the N(KLL) peak energy region four times in one analysis. During the analysis, the beam current was 25 μA. The time interval between two analyses was 1.3 minutes, and the beam current was ~1 μA between analyses. In the beginning, the sample was facing the analyzer, and continuously analyzed by AES for 13 minutes. Following that, the sample was turned away from the analyzer position to avoid any electron beam exposure for 12 minutes. Then it was turned back to the analyzer position and analyzed by AES. Two AES analyses were performed on the

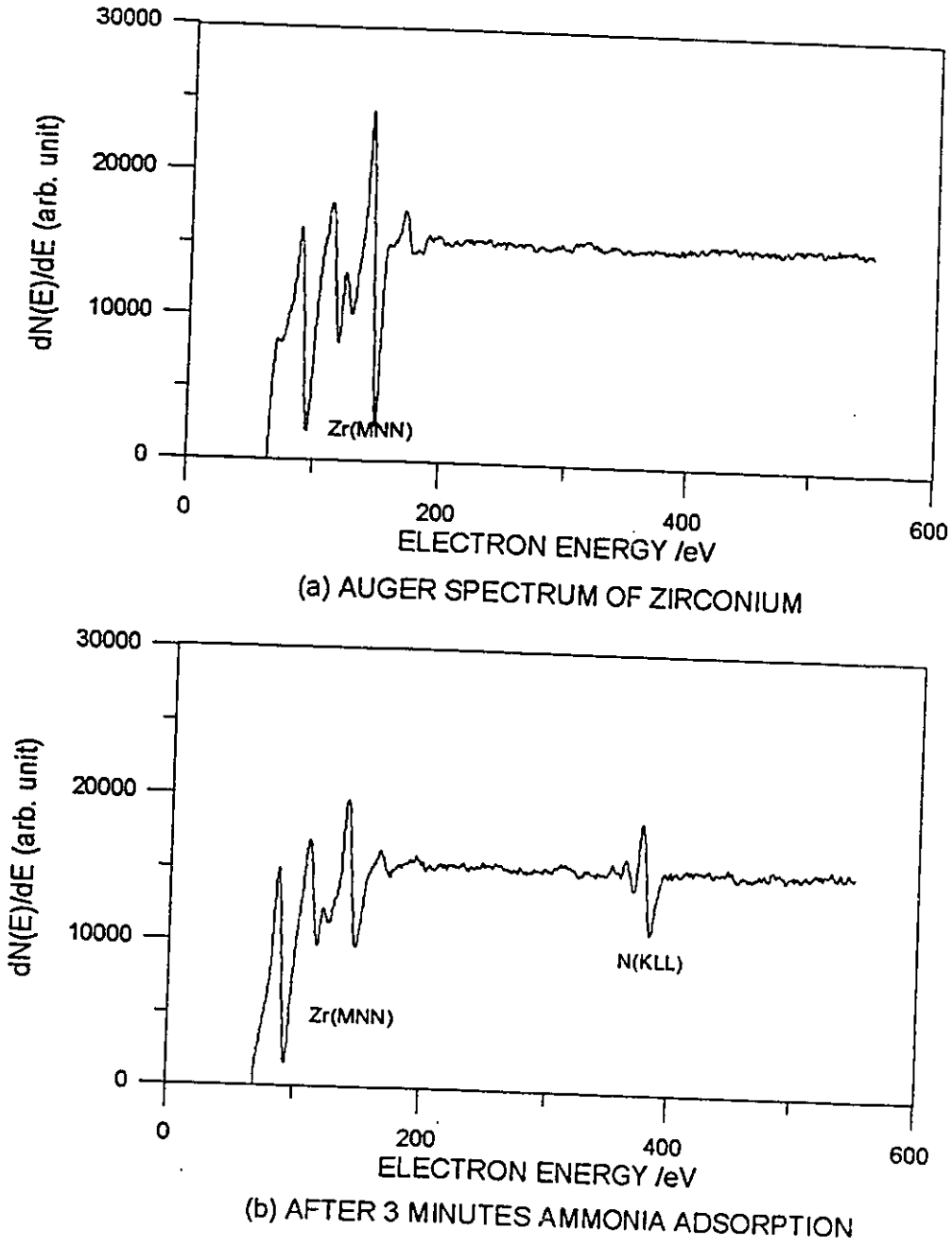

Figure 5-10. The Auger spectra of (a) pure zirconium and (b) zirconium after three minute ammonium adsorption at room temperature.

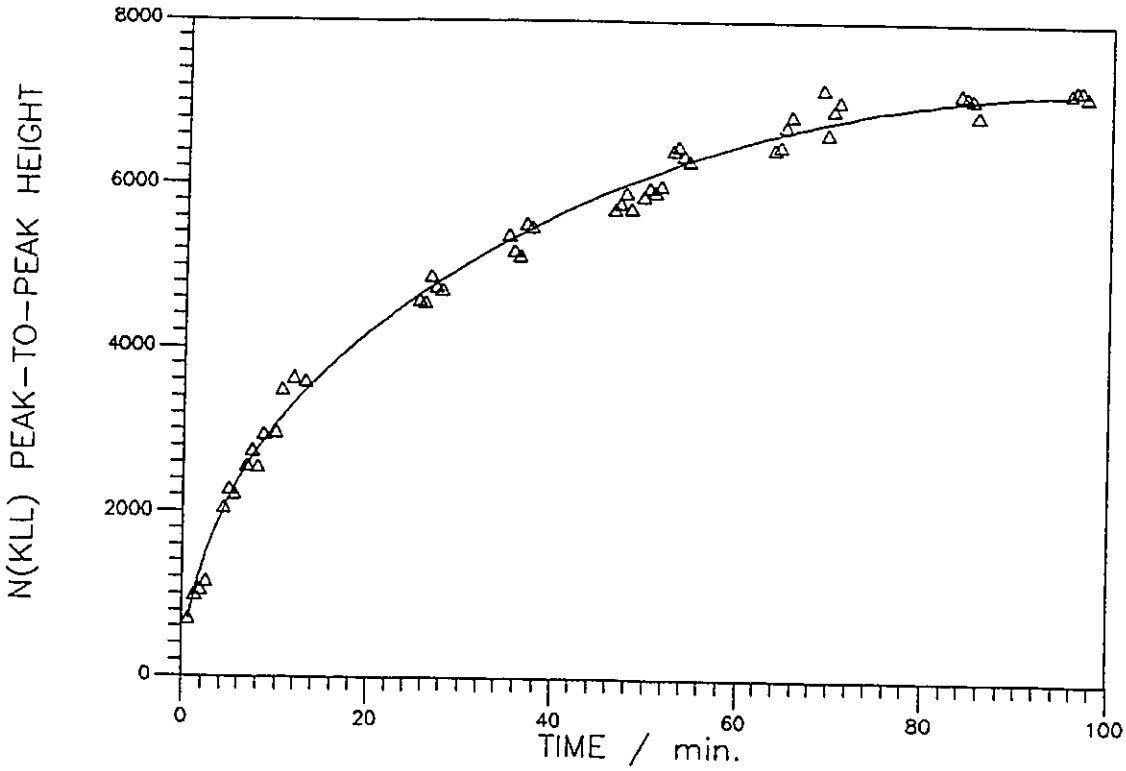

Figure 5-11. The nitrogen KLL peak-to-peak height data are plotted versus ammonia gas exposure time. The ammonia pressure was kept at $1x10^{-7}$ torr during the adsorption and the electron beam was turned off between groups of Auger spectra. The detailed experimental procedure is described in the text.

surface, one provided the four N(KLL) spectra and the other analyzed a wider energy region to check wether there are impurities accumulated on the surface. After the analysis, the sample was turned away again for 8 minutes, and so the procedure was repeated with alternative beam on and beam off on the sample for a total of 96 minutes. It can be seen that the curve in figure 5-11 is formed by several groups of data. Within each group, the sample was exposed to the electron beam of AES, and between each group, the sample was not exposed to any electron beam. If the electron stimulation effect is the same as that of observed from tungsten, chromium and titanium, one would not expect to see a smooth nitrogen uptake curve, but rather steps in the nitrogen coverage since adsorption would occur only when the electron beam was present. The nitrogen uptake curve in figure 5-11 reaches an absolute peak-to-peak height value for N(KLL) peak of 7123 ± 106 at saturation.

5.4 DISCUSSION

5.4.1. Electron stimulated ammonia adsorption

The experimental results for ammonia adsorption on W, Cr, and Ti showed strong evidence for electron beam enhanced adsorption. For tungsten, an extra 15 minutes electron beam exposure at the centre of the sample produced a significantly higher nitrogen concentration in the centre than rest of the surface, figure 5-4. It was known that at room temperature, the adsorption of ammonia on tungsten surface leads to a saturation nitrogen coverage of a half monolayer [Peng and Dawson, 1971; Anderson and Estrup, 1968]. Estrup and Anderson [1968] showed a C(2x2) LEED pattern for a W(100) surface after room temperature ammonia adsorption, and it suggests that the adsorption sites for nitrogen atoms are the next-near-neighbour sites on the W(100) lattice. They [Anderson and Estrup, 1968] also demonstrated that by electron bombardment of the surface, ammonia adsorption on the C(2x2) surface leads to a (1x1) pattern, which suggested that the nitrogen atoms occupy the nearest neighbour sites and the surface reached a full monolayer coverage. For chromium, it was shown that without electron beam stimulation, adsorption stopped at a peak-to-peak height ratio of N(KLL) to Cr($LM_{2,3}M_{4,5}$) about 0.35, and this peak ratio can be increased to 0.66 by continuous electron beam irradiation. For titanium, experimental results, figure 5-8, showed that the value of the escape-depth-averaged nitrogen to titanium mole ratio can be doubled, from x~0.4 to x~0.86, by electron bombardment.

There are two possible ways to enhance ammonia adsorption by electron beam

irradiation, either by ammonia molecule excitation in the gas phase or after adsorption on the transition metal surface. The probability that dissociation or activation of the ammonia molecules occurs in the gas phase, can be estimated from the fraction of electrons in the beam which collide with gas molecules as

$$F = N_C / N_T = 1\text{-}e^{-d/L}, \qquad (5\text{-}3)$$

where N_C is the number of collisions between electrons and gas molecules; N_T is the total number of electrons in the beam; d is the distance between the electron gun to the sample surface, which is about 7.5 cm in our system; and L is the mean free path of the electrons, which is about 9 km in $2x10^{-8}$ torr NH_3 gas, and therefore

$$F = 1\text{-}e^{-0.075m/9000m} \sim 8x10^{-6}.$$

For electron stimulation, in these experiments, the electron beam used for AES analysis was used exclusively, with a beam current of 25 μA, and a beam diameter of 0.1 mm. Since 1A = 6.23 x 10^{18} electron s^{-1}, in every second the electron beam provides ~$1.56x10^{14}$ electron bombardments on $3x10^{-4}$ cm^2 of surface, and ~$1.2x10^9$ electrons will hit a gas molecule in their path. Based on the atomic density data [Feldman and Mayer, 1986], $5.65x10^{22}$ atoms cm^{-3} for Ti, $8.33x10^{22}$ atoms cm^{-3} for Cr, and $6.30x10^{22}$ atoms cm^{-3} for W, we can assume a monolayer coverage of ~$1x10^{15}$ nitrogen atom cm^{-2}. The size of these samples is about 1 cm^2, and so to increase a half-monolayer nitrogen coverage to a full-monolayer coverage requires $5x10^{14}$ activated ammonia molecules. Even if we assume that every ammonia molecule is activated by a single electron collision, none is

deactivated, all strike the sample surface, and are chemisorbed, it would take more than 100 hours to reach a full monolayer coverage. This means that gas phase activation is negligible. However, the electron collision frequency with the sample surface is $5x10^{17}$ cm^{-2} s^{-1} and thus weakly adsorbed NH_3 molecules will suffer 500 electron collisions per second. Thus we can conclude that the activation or dissociation of the ammonia molecule occurs on the transition metal surfaces, and not via gas phase activation. This conclusion is supported by the experimental results shown in figure 5-4. Enhanced ammonia adsorption was not observed on the whole sample surface, but only where the electron beam strikes the surface.

5.4.2. Ammonia adsorption on zirconium

Zirconium was unique among the four metals studied in that the electron beam seemed to have no effect on ammonia adsorption. The important question which arises is whether this is because the electron beam is ineffective or unnecessary, i. e. does saturation correspond to a half or fully covered surface? This question will be addressed in the following discussion.

The peak-to-peak height ratio of N(KLL) to $Zr(M_{4,5}N_1N_{2,3})$ after 3 minutes ammonia adsorption reached 0.55, which is close to the value obtained from a standard bulk nitride sample, $ZrN_{0.74}$. Since nitrogen bulk diffusion can be neglected at 300 K, nitrogen from ammonia adsorption is expected to remain in the outermost layer. The high peak-to-peak height ratios of N(KLL) to $Zr(M_{4,5}N_1N_{2,3})$ suggests that ammonia adsorption at 300 K produces a higher nitrogen concentration on the outermost surface than that of

the bulk standard sample, $ZrN_{0.74}$. The intensity ratio of the nitrogen to zirconium Auger peaks can be estimated as follows.

The intensity ratio of the Auger signals for a homogeneous sample can be expressed as

$$I_N/I_{Zr} = S_N N_N / S_{Zr} N_{Zr} \qquad (5\text{-}4)$$

where I_{Zr} and I_N are the intensities of the Auger signal for the zirconium and nitrogen peaks; S_N and S_{Zr} are the relative sensitivity factors for the nitrogen and zirconium peaks; N_N and N_{Zr} are the concentrations of nitrogen and zirconium atoms respectively. For the bulk standard sample, $ZrN_{0.74}$, the intensity ratio is 0. 53, so $S_N/S_{Zr} = 0.53/0.74 = 0.71$. For a primary beam at normal incidence, the contribution of the zth layer to the Auger signal intensity can be estimated by the simplified equation,

$$I_z = I_0 \exp(- z / \lambda_m), \qquad (5\text{-}5)$$

where I_z and I_0 are the intensities of Auger signal for the zth layer and top layer respectively; λ_m is the inelastic mean free path of the Auger electrons in layers.

For ammonia adsorption on zirconium, if it is assumed that the saturation is reached with one monolayer nitrogen,

then $$I_N = I_{0,N} = S_N N_{0,N}, \qquad (5\text{-}6)$$

and $$I_{Zr} = S_{Zr} N_{Zr} [\exp(- 1/\lambda_m) + \exp(-2/\lambda_m) + \exp(- 3/\lambda_m) + ...], \qquad (5\text{-}7)$$

where $N_{0,N}$ is the number of nitrogen atoms on the outermost layer, and N_{Zr} is the number of zirconium atoms in each layer of the zirconium sample. In the following calculation, we assume $\lambda_m \sim$ 2 monolayer for $Zr(M_{4,5}N_1N_{2,3})$ peak, which is consistent with the value 0.6 nm calculated from an equation deduced by Seah and Dench [1979]. The intensity ratio can be calculated as

$$I_N/I_{Zr} = S_N N_{0,N}/S_{Zr}N_{Zr} [\exp(-1/\lambda_m) + \exp(-2/\lambda_m) + \exp(-3/\lambda_m) + \ldots], \qquad (5\text{-}8)$$

with $\sum \exp(-z/\lambda_m) = 1.4$ for five layers, $S_N/S_{Zr} = 0.71$, and $N_{0,N}/N_{Zr} = 1$ for a monolayer of nitrogen, and the calculated intensity ratio is

$$I_N/I_{Zr} = 0.71/1.4 = 0.5,$$

which is close to the experimental observation, 0.55. According to this estimation, the zirconium sample after 3 minutes ammonia adsorption with an ammonia gas flux of 5.7×10^{15} molecules cm^{-2} s^{-1} forms a full-monolayer nitrogen on the surface.

The surface coverage of nitrogen can also be estimated by comparing the absolute nitrogen peak-to-peak height with those from other transition metals. In doing so, the matrix effects should be considered. Dawson [1991] has reported the study of the nitrogen KLL Auger intensities from the nine transition metal nitride films prepared by high temperature reaction with ammonia gas, and calculated the matrix contributions to N(KLL) peak from the density of nitrogen, the back-scattering factor and the attenuation length, figure 5-12. The total matrix effect can be expressed as the product of these matrix effects, and it is plotted in figure 5-13. It can be seen that the total matrix effects

Figure 5-12. Calculated values for the three matrix dependent properties affecting the measured Auger signal in nine transition metal nitrides from Group IV, V and VI and Periods 4,5, and 6. (a) The nitrogen atom density in the matrix is calculated from the X-ray structures of the stoichiometric nitride phase. (b) The back-scattering factor for the ionization of nitrogen K-shell electrons by 2 kV primary electrons is determined from the atomic number, Z, using an equation developed to represent the results of Monte Carlo calculations, [Ichimura et al., 1983]. (c) The attenuation length for 385 eV N(KLL) Auger electrons are calculated using the tabulated data for the metals of Ebel et al. [1988].

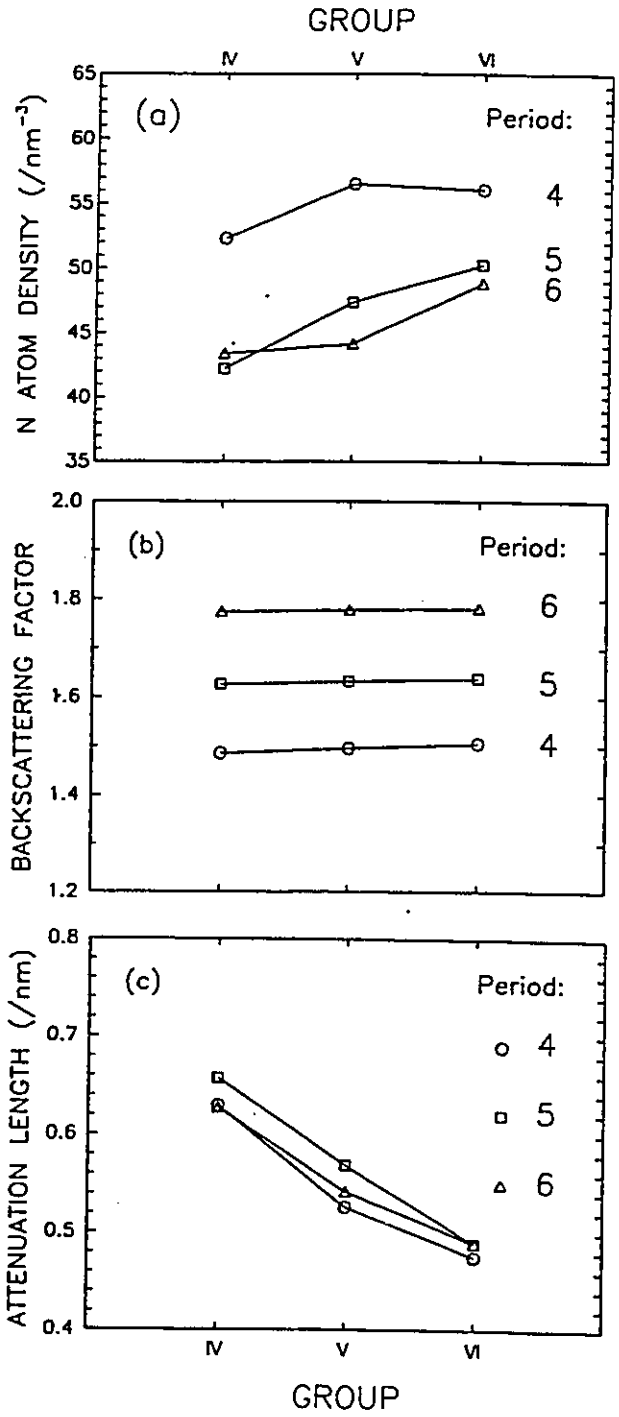
GROUP
IV
V
VI
(a)
Period:
4
5
6
N ATOM DENSITY (/nm^{-3})
65
60
55
50
45
40
35
(b)
Period:
6
5
4
BACKSCATTERING FACTOR
2.0
1.8
1.6
1.4
1.2
(c)
Period:
4
5
6
ATTENUATION LENGTH (/nm)
0.8
0.7
0.6
0.5
0.4
IV
V
VI
GROUP

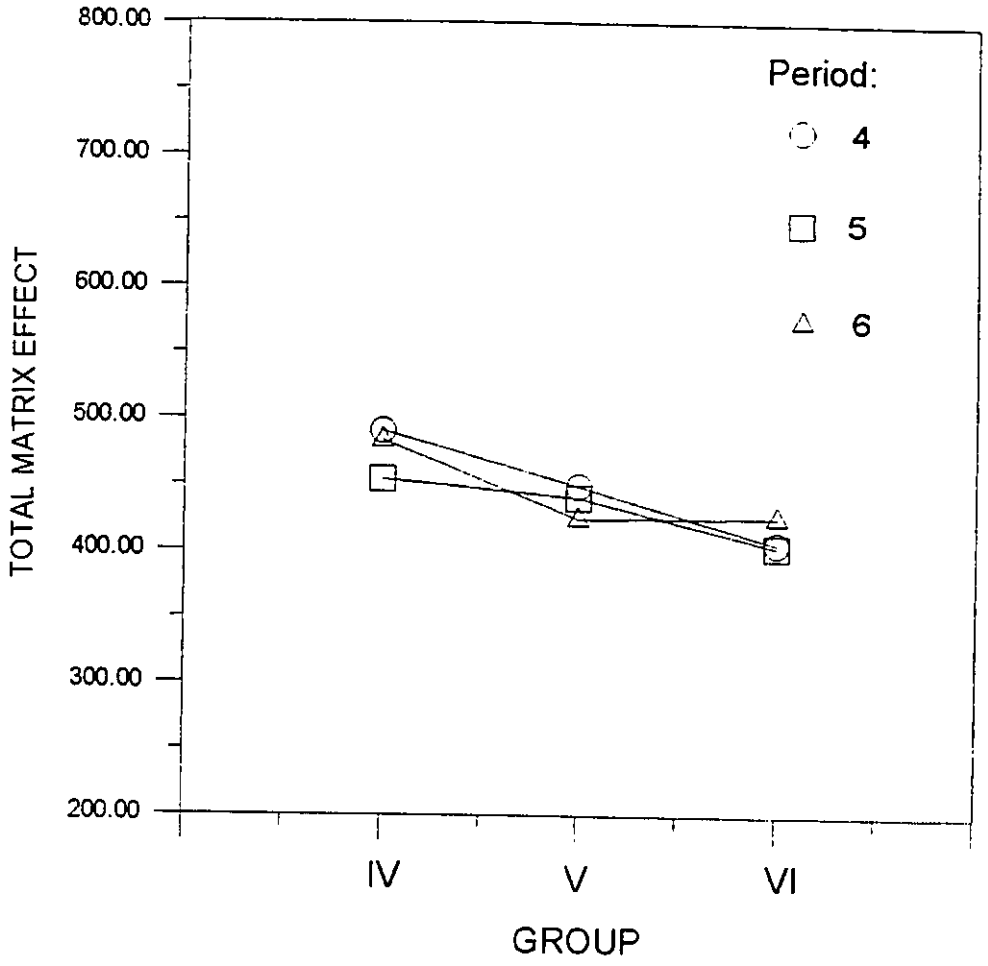

Figure 5-13. The total contribution of the matrix effects to nitrogen KLL Auger peak calculated as the product of atomic density, back-scattering factor, and the attenuation length.

for these nine transition metal nitrides are from 406 to 490, with the lowest value for Mo, and the highest value for Ti. Using equation 3-2, assuming the instrument conditions and the incidence of the primary beam are the same, and assume all the samples have equal surface roughness, the estimated N(KLL) peak intensity for these nine transition metal nitrides will be quite close. In this work, extensive ammonia adsorption experiments have been performed on titanium and tungsten surfaces, statistical Auger intensity data for a full-monolayer coverage and a half-monolayer coverage are available. Because the nitrogen peak overlaps with the titanium LMM peak at 385 eV, it makes the direct measurement of the nitrogen peak-to-peak height impossible in N-Ti system. Although the nitrogen peak-to-peak height can be calculated by equation 5-1, the calculated values are anomalously high [Dawson, 1991], which will be discussed in section 5.4.3. The nitrogen peak-to-peak height value obtained in the absence of electron beam irradiation after room temperature ammonia adsorption on tungsten surface, including polycrystalline sample and three single crystal samples, is 2500 ± 200, corresponding to a half-monolayer nitrogen coverage; and the value obtained with electron stimulation is 6000 ± 400, corresponding to a full-monolayer nitrogen coverage. The comparison of the absolute N(KLL) peak-to-peak heights from the NH_3-Zr, 7365, with that of the NH_3-W system suggests that after 3 minutes ammonia adsorption, the zirconium surface is fully covered with a monolayer of nitrogen.

The experimental results, figure 5-11, show that with electron beam bombardment, the saturation value for the nitrogen peak-to-peak height, 7123 ± 106 is about the same as that obtained from the adsorption without electron beam bombardment, figure 5-10 (b).

Electron beam bombardment during ammonia adsorption does not change the saturation nitrogen coverage on zirconium, and this corresponds to a fully covered surface. Electron stimulation is not ineffective, it is not required for zirconium surfaces.

5.4.3. The anomalous N(KLL) intensity calculated from Ti(LMM) spectrum

The calculated nitrogen peak-to-peak height for Ti after ammonia adsorption is anomalously high compared with that from other transition metal nitrides. The peak height calculation, equation 5-1, involves the assumption that the relative intensity of the 384 and 420 eV Ti peaks does not change on nitriding, and uses the observed intensity of the 420 eV peak in the nitride to subtract the Ti contribution from the combined peak at 384 eV. This might be a false assumption since we observed different attenuation behaviours for zirconium MNN peaks on nitriding, section 4.5. Since zirconium is situated adjacent to titanium in the periodic table, it has the same valence band structure and crystal structure as titanium, and they both form hard, refractory, interstitial nitrides. Remarkably, the MNN to MNV peak ratio for pure zirconium, 0.72, is the same as the LMM to LMV peak ratio for pure titanium, 0.73, within an experimental error. The change of the relative ratio of the equivalent peaks in zirconium can be applied to N-Ti system. The equivalent peaks in zirconium are the 93 eV peak, Zr(3d)Zr(4p)Zr(4p), and the 146 eV peak, Zr(3d)Zr(4p)V. In the low resolution spectra, figure 4-8, the 146 eV peak shows large attenuation, while the 93 eV peak does not attenuate on nitriding. The ratio of the 93 eV peak to the 146 eV peak is 0.72 for the metal, and 1.41 for the nitride. If we use 1.41 for k_{Ti} in equation 5-1 to calculate the nitrogen peak intensity for a

nitrogen fully covered titanium surface, the calculation produces a value comparable to that of tungsten and zirconium,

$$P_N = 17800 - 1.41x7500 = 7225,$$

and the anomaly is removed. The analysis procedure for titanium nitride [Dawson and Tzatzov, 1985] is still valid since the determination of the average nitrogen to titanium atomic ratio, <x>, does not require that the relative intensity of the Ti peaks is independent of nitrogen concentration, only that if it varies, it does so linearly. It has been found that the peak ratio, k, changes linearly with x for N-Zr system indeed, shown in figure 4-9.

5.4.4. Why ammonia adsorption is different on titanium and zirconium

In view of the similar physical and chemical properties of zirconium and titanium, one would expect to see similar behaviour on ammonia adsorption, but experimental results show that the behaviour of ammonia adsorption on zirconium is quite different from that on titanium surfaces. For titanium, the results of figure 5-9 show that the electron bombardment of the adlayer in the presence of about $2x10^{-8}$ torr ammonia gas leads to a saturated adlayer with an escape-depth-averaged nitrogen to titanium mole ratio of ~0.86. However in the absence of such electron stimulation the adlayer saturates at only half of this value, 0.4. At 300 K, diffusion of nitrogen into the bulk of the sample can be neglected and so we will assume that these values represent the saturated and half-saturated surfaces respectively. For zirconium, ammonia adsorption at 300 K produces a

fully saturated ammonia adlayer without electron beam stimulation.

The lattice parameter for Zr is ~9.5% larger than that for Ti and therefore the adsorption site spacing on the surface is correspondingly larger. This leads to a straightforward explanation for the differences in NH_3 adsorption behaviour. Figure 5-14 shows the proposed model for ammonia adsorption on titanium, which, although polycrystalline is represented by the hcp basal plane. At first, the nitrogen atoms are occupying next-near-neighbour sites which are assumed to represent a more stable adlayer than when nitrogen atoms occupy adjacent sites. At room temperature, in the absence of electron stimulation, chemisorption ceases at this point. In order to account for the electron stimulated adsorption we propose that ammonia can weakly adsorb on this half-covered surface, perhaps with hydrogen bonding to nitrogen adatoms. This ammonia is reversibly adsorbed at low coverage. With electron excitation it can lead to cleavage of the N-H bond, leading to a fully covered chemisorbed nitrogen adlayer at 300 K. Figure 5-15 shows the plan views of the basal plane of zirconium half-covered by chemisorbed nitrogen atoms from ammonia adsorption and half-covered by weakly adsorbed ammonia molecules. Since the chemisorption of ammonia does not cease at a half-covered surface, it is possible that a transition state involving adjacent zirconium atoms might be able to facilitate the dissociation of the N-H bonds in the weakly adsorbed ammonia, leading to a full coverage. As titanium has a smaller unit cell, a=2.95 Å and c=4.68 Å, than zirconium, a=3.23 Å and c=5.14 Å, this dissociation can not occur on titanium surface without electron beam bombardment because the surface is too crowded to allow the transition state to form, compare figure 5-14 (b) with figure 5-15.

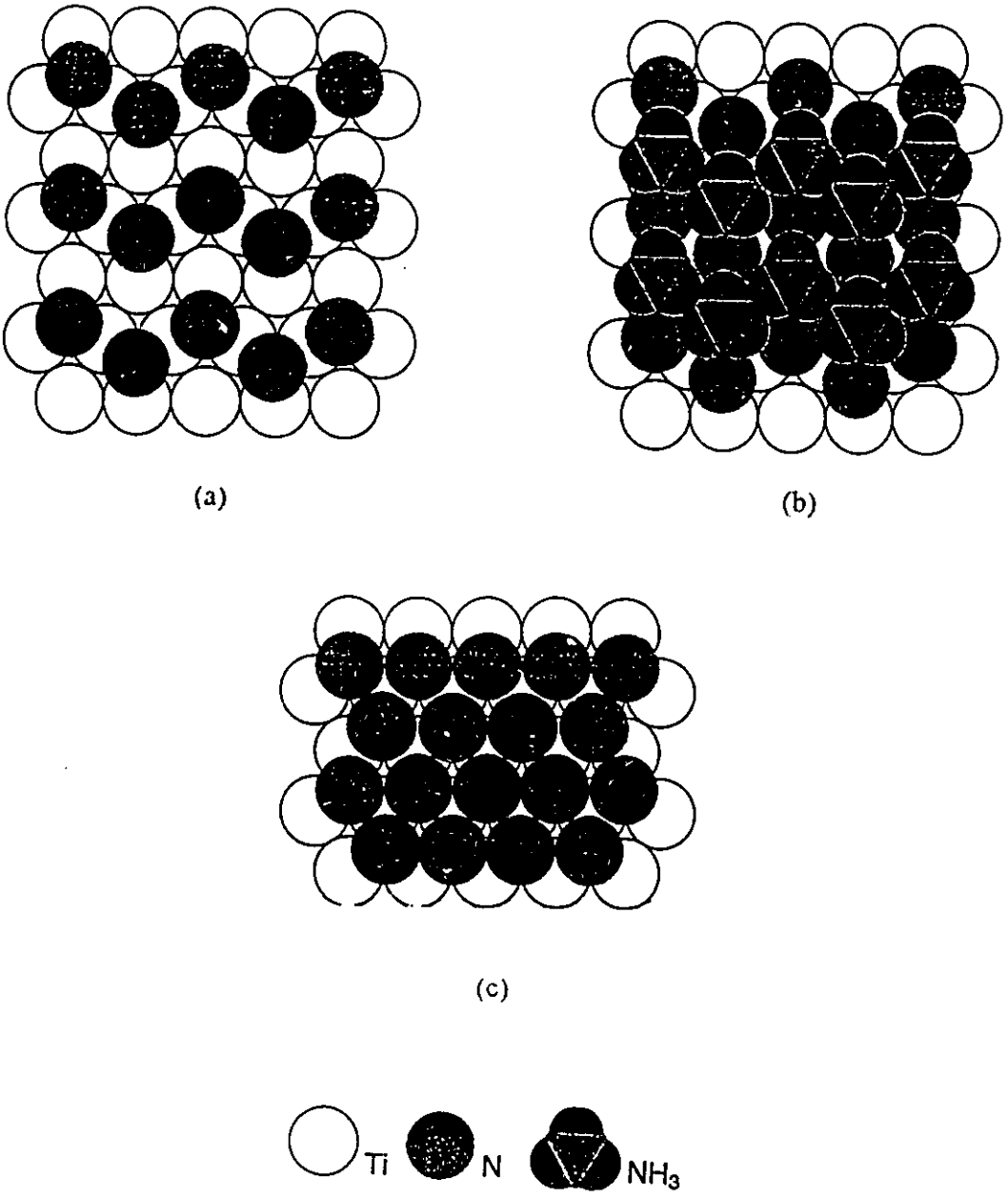

Figure 5-14. Scale model showing plan views of the basal plane of titanium on which (a) nitrogen atoms from ammonia have been chemisorbed to one-half monolayer coverage, the adatoms occupy rows of next-near-neighbour sites; in (b) ammonia molecules are weakly adsorbed on the nitrogen half-covered surface (the saturated surface shown would require high gas flux); with electron excitation this can lead to (c) a fully covered nitrogen chemisorbed layer.

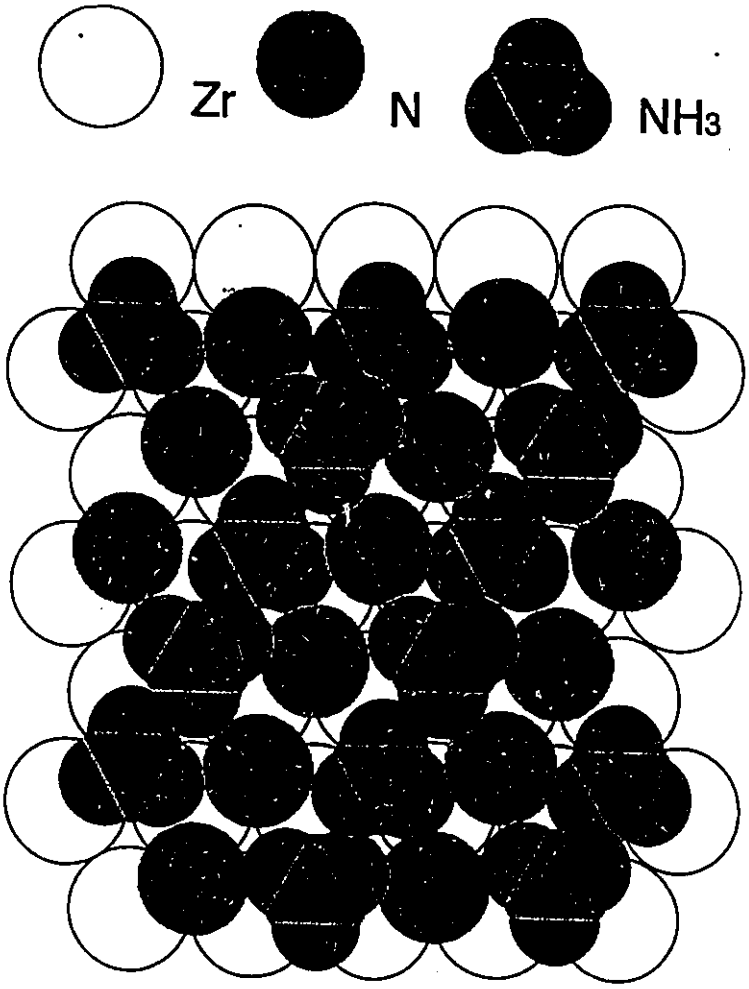

Figure 5-15. Scale model showing plan views of the basal plane of zirconium half-covered by chemisorbed nitrogen atoms and half-covered by weakly adsorbed ammonia molecules in the high flux limit. This will lead to a fully covered chemisorbed nitrogen adlayer with further N-H bond dissociation by a possible transition state involving adjacent zirconium atoms.

5.4.5. The similarity of NH_3/Ti and NH_3/W

As titanium is a first row fourth-group transition metal in the periodic table, and tungsten is situated in the third row and sixth-group, they have quite different physical and chemical properties. Titanium forms a very stable refractory nitride. Nitrogen sorption on titanium has been found to be irreversible even at high temperature [Nagasaka and Yamashina., 1972; Elsworth and Holland., 1963; Elsworth et al., 1965], while tungsten nitride is unstable and decomposes at temperature as low as 800°C. It is surprising that similar ammonia adsorption behaviour at room temperature was observed for these two transition metal surfaces. The results of ammonia adsorption on tungsten and titanium show that in both systems, the adsorption at room temperature ceases at low nitrogen coverage, but with electron bombardment, it can reach a fully covered nitrogen adlayer. The interaction of nitrogen containing gas molecules with titanium and tungsten surfaces were investigated further and these studies will be described in chapter 6 and chapter 7 respectively.

If the geometric factor is the key effect affecting the ammonia adsorption behaviour as discussed in section 5.4.4, it was concluded that further research work needed to include studies on well defined single crystal surfaces. This work will be described in chapter 7.

5.5. CONCLUSIONS

There are very strong electron beam effects in the chemisorption of ammonia on tungsten, chromium, and titanium surfaces. At room temperature, ammonia adsorption produces about half monolayer nitrogen coverage on these metal surfaces in the absence of electron beam irradiation. Electron beam irradiation can activate or dissociate weakly adsorbed ammonia molecules on these metal surfaces, thereby increasing the nitrogen coverage to a full monolayer.

The behaviour of ammonia adsorption on zirconium is different from the other transition metals. A full monolayer nitrogen coverage is formed on a zirconium surface after just 3 minutes ammonia adsorption with an ammonia gas flux of 5.7×10^{15}molecules $cm^{-2}s^{-1}$. Electron beam stimulation is not required for this process. This is a result of the larger interatomic spacing for zirconium when compared with the other metals.

By investigation of the change in relative peak height for the MNN and MNV transitions in Zr on nitriding it has been possible to explain a pronounced anomaly observed in calculated nitrogen intensities for nitrogen in Ti. This anomaly arises from the assumption that the relative metal peak heights are nitrogen concentration independent. Applying the Zr data to Ti removed the anomaly.

CHAPTER SIX

THE ADSORPTION OF NH_3 AND N_2 ON TITANIUM

6.1. INTRODUCTION

Titanium nitride is one of the most useful coating materials and also has important electronic applications. The fundamental information about the kinetics of nitrogen sorption and implantation, and the structure and stoichiometry of the nitride film are of great interest in many fields of science and technology, ranging from getter pumping to the production of thin films as wear and corrosion resistant coatings. The early work on the determination of the nitrogen sticking probability and the sorption capacity have been reviewed [Harra and Hayward, 1967; Harra, 1976; Grigorov and Tzatzov, 1983]. The observation that the sticking probability and the sorption capacity of titanium films for nitrogen sorption depend on the film thickness [Harra and Hayward, 1967; Harra, 1976] and also suggestions that superstoichiometric nitride films can be formed indicate the need for non-destructive methods for determining composition depth profiles. To fulfil this requirement, an experimental procedure using AES surface analysis method was reported by Dawson and Tzatzov [Dawson and Tzatzov, 1987]. In this procedure, both low-energy and high-energy Auger spectra were used to determine the depth distribution of nitrogen in the nitride film produced by nitrogen adsorption. Since the low-energy, ~25 eV, and

high energy, ~400 eV, Auger electrons have widely different inelastic mean free paths, they can be used to provide the compositions in different depth of the sample films. Based on this information and a straightforward adsorption-diffusion model, the depth distribution of nitrogen in inhomogeneous films and the diffusion coefficient can be determined. The quantitative AES analysis methods for N/Ti system have been reported by Dawson and Tzatzov [1985; 1986].

The early work [Dawson and Tzatzov, 1987] used diatomic gas, N_2, and since there is a big difference in bonding type between NH_3 and N_2, it might be anticipated that different N sorption behaviours would be observed. The aim of this part of work is to investigate and compare the adsorption properties of ammonia and nitrogen on titanium surface.

In this chapter, the results of ammonia and nitrogen adsorption on titanium are presented and mechanisms of adsorption, dissociation, surface diffusion and bulk N diffusion for NH_3-Ti and N_2-Ti systems are proposed and discussed, with special emphasis on the role played by electron bombardment.

6.2. EXPERIMENTAL RESULTS

6.2.1. Effect of NH_3 and N_2 adsorption on the Auger spectrum of titanium

In figure 6-1, the low-energy and high-energy Auger spectra of a pure titanium sample is shown together with those following nitrogen and ammonia adsorption. The multi-orifice gas doser was used for these gas adsorption experiments. The adsorption of N_2 gas was performed at 760 K with a N_2 gas flux of $3x10^{15}$ molecules cm^{-2} s^{-1}, and the adsorption of NH_3 was performed at 900 K with a gas flux of $5.7x10^{15}$ molecules cm^{-2} s^{-1}.

In the MVV Low-energy Auger spectrum, titanium has a "metal" Auger feature at 27 eV, which originates in Ti(3p)Ti(3d)Ti(3d) super Coster-Kronig transition. About 4 eV lower in energy, there appears a "nitride" feature on nitriding. These two features have been thoroughly studied by Dawson and Tzatzov [1985, 1986]. The intensity variations of these two features with nitrogen concentration are essentially the same as those of zirconium, which is described in chapter 4, section 4.3 and 4.4. The Auger features in the LMM energy region have been presented in chapter 5, section 5.3.3.

The quantitative method used in this work is that previously reported by Dawson and Tzatzov [1985, 1986]. The escape-depth-averaged nitrogen to titanium atomic mole ratio, <x>, was determined from the high-energy Auger spectrum using the method described in chapter 5, section 5.3.3.

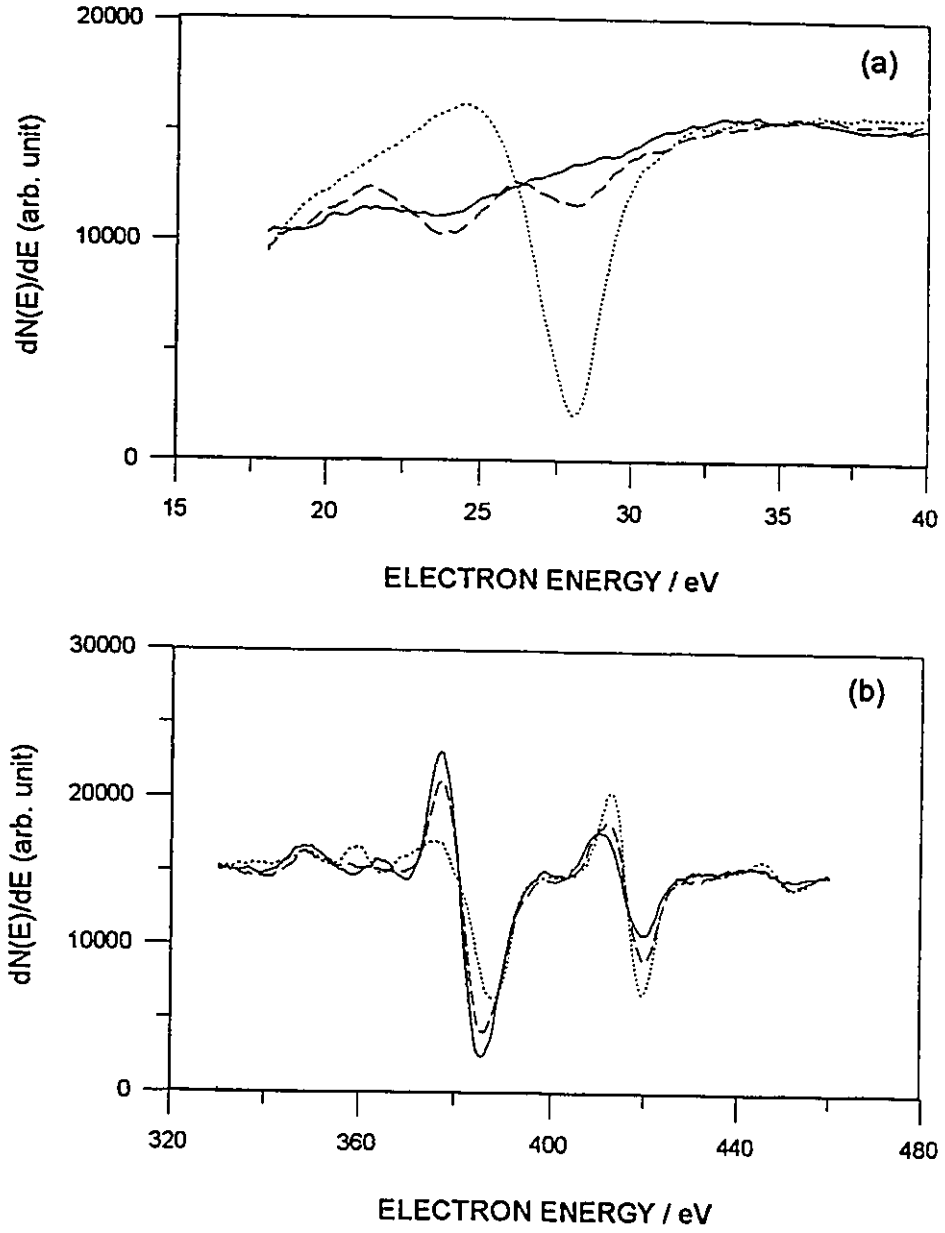

Figure 6-1. Auger electron spectra of titanium (dotted line) and titanium after reaction with nitrogen gas (dashed line) and after reaction with ammonia gas (full line). The MVV low-energy spectra and the LMM high-energy spectra are shown in (a) and (b) respectively. The nitrogen interaction was at 760K using a flux of $3x10^{15}$ molecules cm^{-2} s^{-1}, and the ammonia reaction was at 900K using a flux of $5.7x10^{15}$ molecules cm^{-2} s^{-1}.

6.2.2. Ammonia adsorption on titanium

Figure 6-2 shows the results of ammonia adsorption at sample temperatures of 615, 730, 895 and 990 K with an ammonia gas flux of 5.7×10^{15} molecules cm^{-2} s^{-1}. After the first one minute dose, the escape-depth-averaged nitrogen to titanium mole ratio approaches or exceeds 0.8, which is the value observed with electron stimulation at 300K.

The escape-depth-averaged nitrogen to titanium mole ratio at saturation is plotted versus the sample temperature in figure 6-3 for this flux and three lower gas fluxes. In this figure, the 300 K value for the nitrogen coverage is the value observed in the absence of electron stimulation. The nitrogen surface concentration increases with temperature at all gas fluxes passes through a maximum and then decreases for all but the highest ammonia gas flux. Furthermore, the temperature at which the nitrogen concentration reaches the maximum value increases with gas flux.

The low-energy Auger spectra collected after ammonia adsorption to saturation at 300, 615, 730, 830 and 890 K with the lowest ammonia gas flux, 1.5×10^{14} molecules cm^{-2} s^{-1}, corresponding to figure 6-3 curve a, are shown in figure 6-4. Figure 6-4, spectrum (a) shows that 300 K adsorption produces a nitrogen half covered surface in the absence of electron stimulation. The absence of a "metal" Auger feature at ~27 eV and the small "nitride" feature in ~23 eV observed in spectra (b) and (c) suggests that at elevated temperature, 615 and 730 K, even with the smallest gas flux, the surface is saturated with a fully covered nitrogen layer. However, even at further higher temperatures, 830 and 890K, where the curve (a) in figure 6-3 has passed its maximum <x> value, the nitrogen

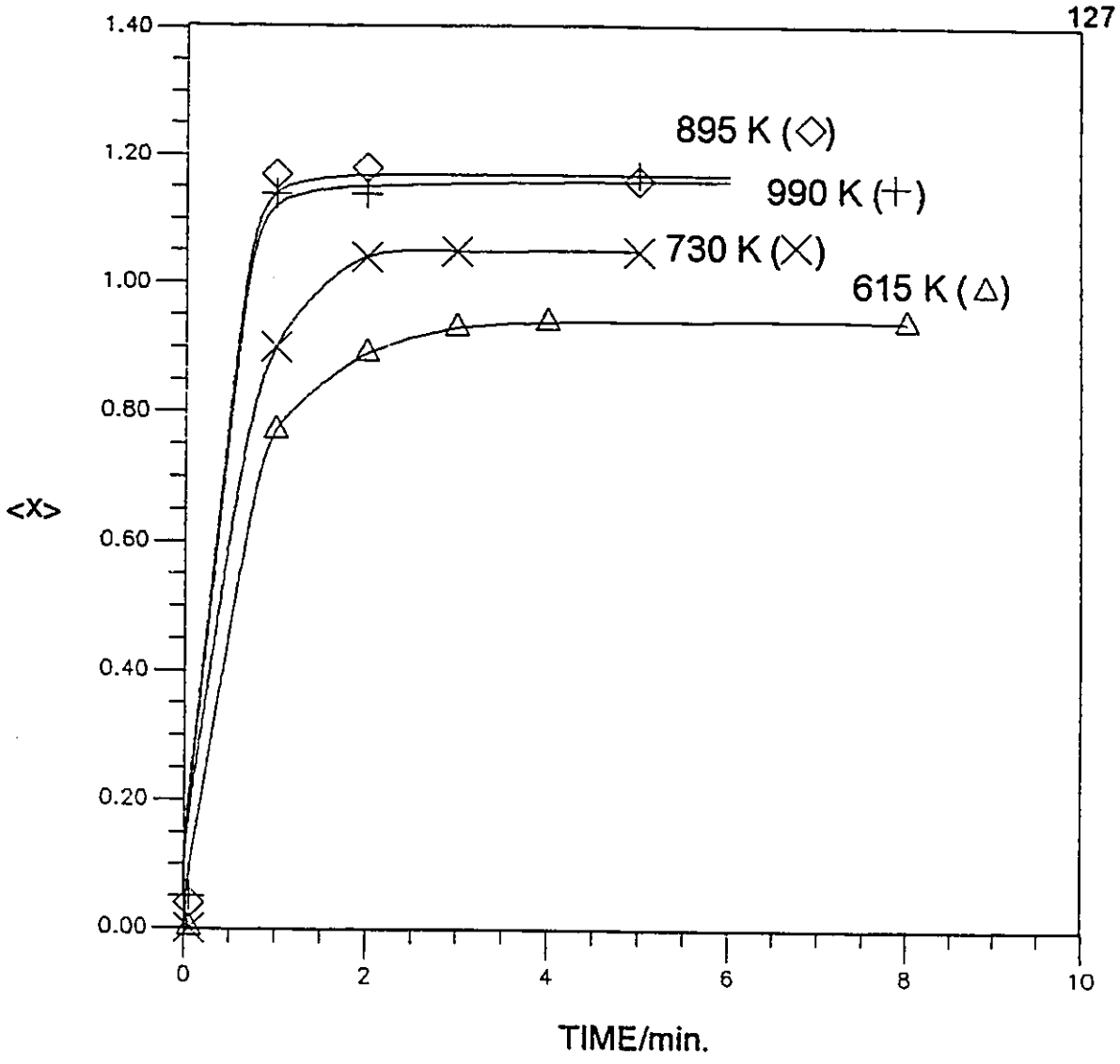

Figure 6-2. The escape-depth-averaged nitrogen to titanium mole fraction <x>, calculated from the LMM Auger spectra using equation (5-2), after reaction with NH_3 gas with a flux of 5.7×10^{15} molecules cm^{-2} s^{-1} at different sample temperatures.

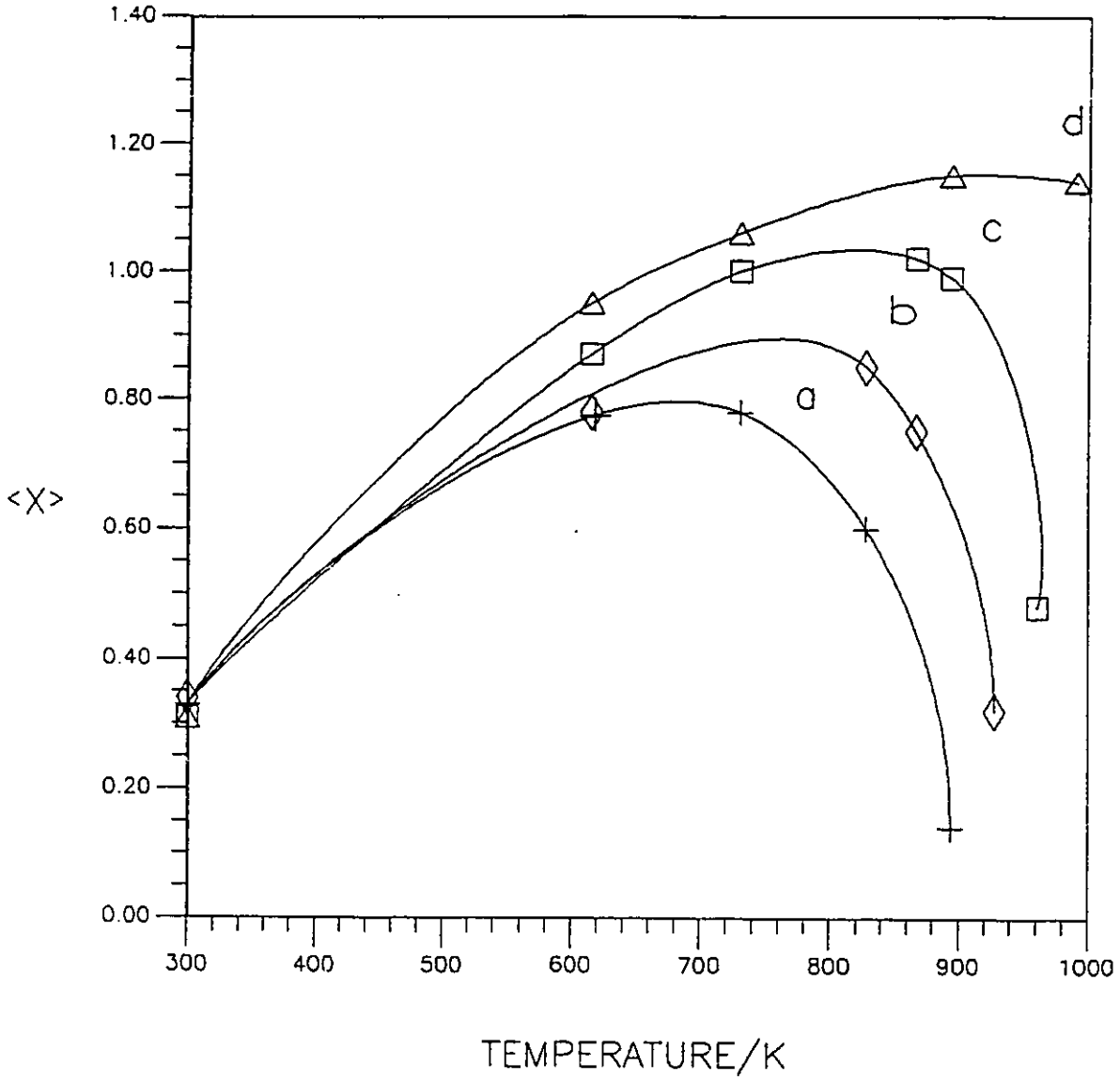

Figure 6-3. The escape-depth-averaged nitrogen to titanium mole fraction <x>, calculated using equation (5-2), after reaction with NH_3 gas versus sample temperature for four different gas fluxes: (a) 1.5×10^{14} (b) 3.6×10^{14} (c) 1.6×10^{15} and (d) 5.7×10^{15} molecules cm^{-2} s^{-1}.

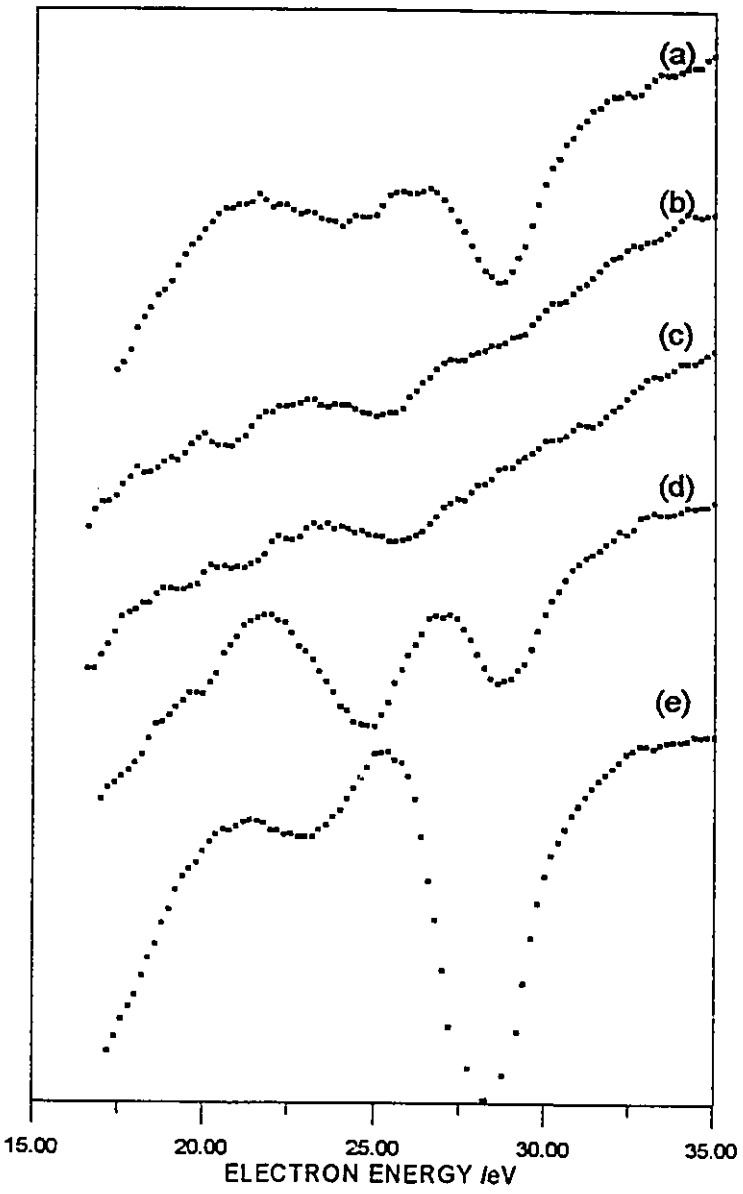

Figure 6-4. The MVV low-energy Auger electron spectra of titanium after reaction with NH_3 gas with a gas flux of $1.5x10^{14}$ molecules/sec.cm^2 at different surface temperatures: (a) 300 K (b) 615 K (c) 730 K (d) 820 K and (e) 890 K.

coverage on surface decreases dramatically as revealed by an increasing "metal" feature in figure 6-4 spectra (d), (e).

6.2.3. Nitrogen adsorption on titanium

In figure 6-5 the variation of the escape-depth-averaged nitrogen to titanium mole ratio for the adsorption of nitrogen gas using a constant background pressure of $2x10^{-6}$ torr is plotted against electron beam exposure time. In this experiment the sample was continuously exposed to the analysis electron beam. For comparison, the data for ammonia adsorption at room temperature, shown in figure 5-8 curve (a), is re-plotted in figure 6-5 as a function of electron beam exposure time. The results show that at 300 K, electron beam irradiation can not stimulate the adsorption of nitrogen gas to full coverage, in contrast with the behaviour of ammonia.

The results for N_2 adsorption at different temperatures and different gas fluxes are plotted in figure 6-6. The escape-depth-averaged nitrogen to titanium mole ratios are much lower than those for NH_3 adsorption, figure 6-3. At 300 K, the adsorption saturated at $\langle x \rangle \sim 0.3$. A maximum nitrogen to titanium ratio is observed at a sample temperature close to 760 K, but this temperature is insensitive to gas flux, unlike the data shown in figure 6-3.

Low-energy Auger spectra, corresponding to the steady states of figure 6-6, curve a, b, c, and d, are shown in figure 6-7, (a), (b), (c) and (d) respectively. The equivalent spectrum for figure 6-6, curve d is shown in figure 6-1 (a). All five spectra show two

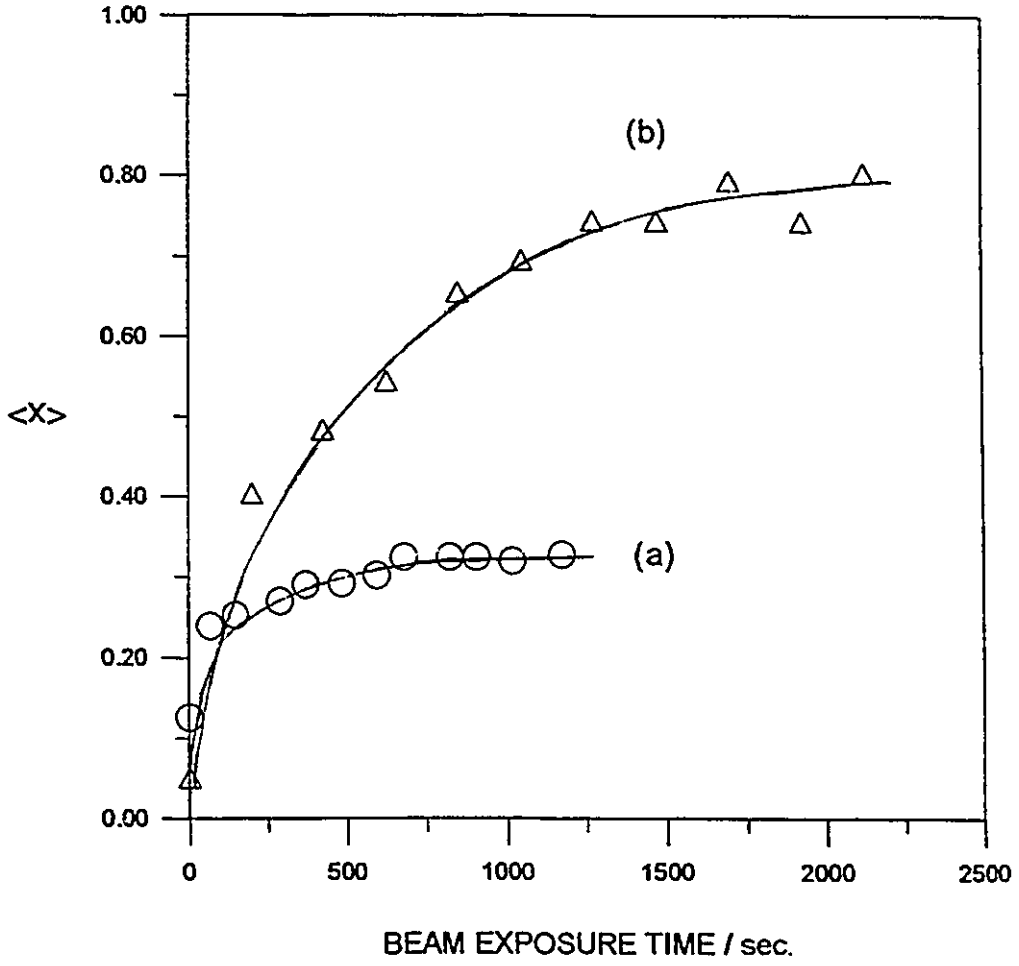

Figure 6-5 The effect of electron beam exposure on the chemisorption of nitrogen and ammonia gas at 300 K. In (a) the increase of nitrogen concentration, <x>, with time is shown for the collision of nitrogen molecules from background gas at a pressure of $2x10^{-6}$ torr with simultaneous continuous electron bombardment for Auger analysis. For comparison the data for the adsorption of ammonia gas from figure 5-8 (a) are re-plotted against electron beam exposure time in curve (b). Electron stimulated adsorption of nitrogen gas to full coverage does not occur at 300 K unlike the behaviour observed for ammonia gas.

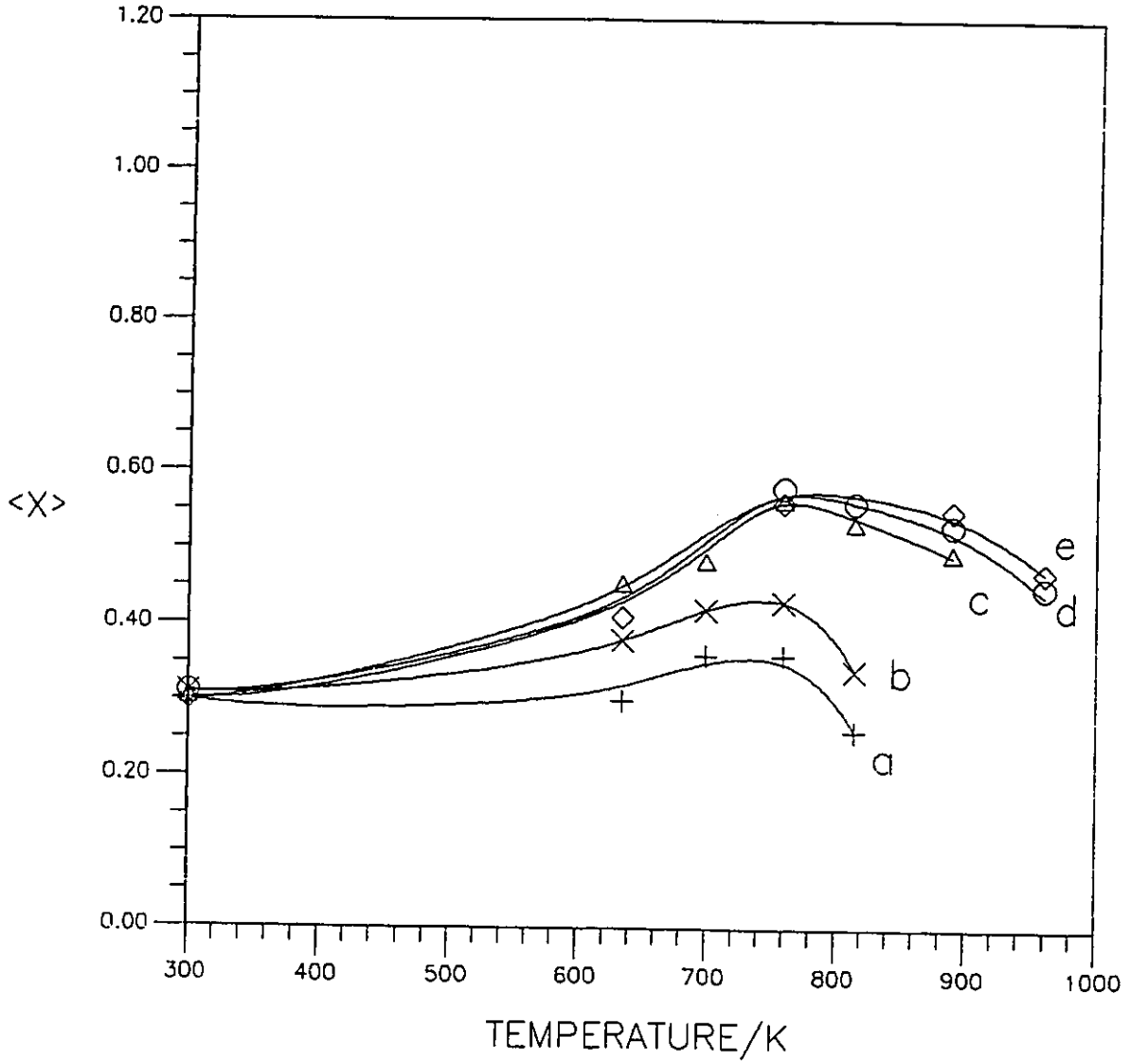

Figure 6-6. The escape-depth-averaged nitrogen to titanium ratio, <x>, after reaction with nitrogen gas as a function of sample temperature at five different gas fluxes: (a) 5.9×10^{13}; (b) 2.4×10^{14}; (c) 1.9×10^{15}; (d) 3.0×10^{15} and (e) 7.0×10^{15} molecules/s.cm^2. There was no electron bombardment during gas dosing.

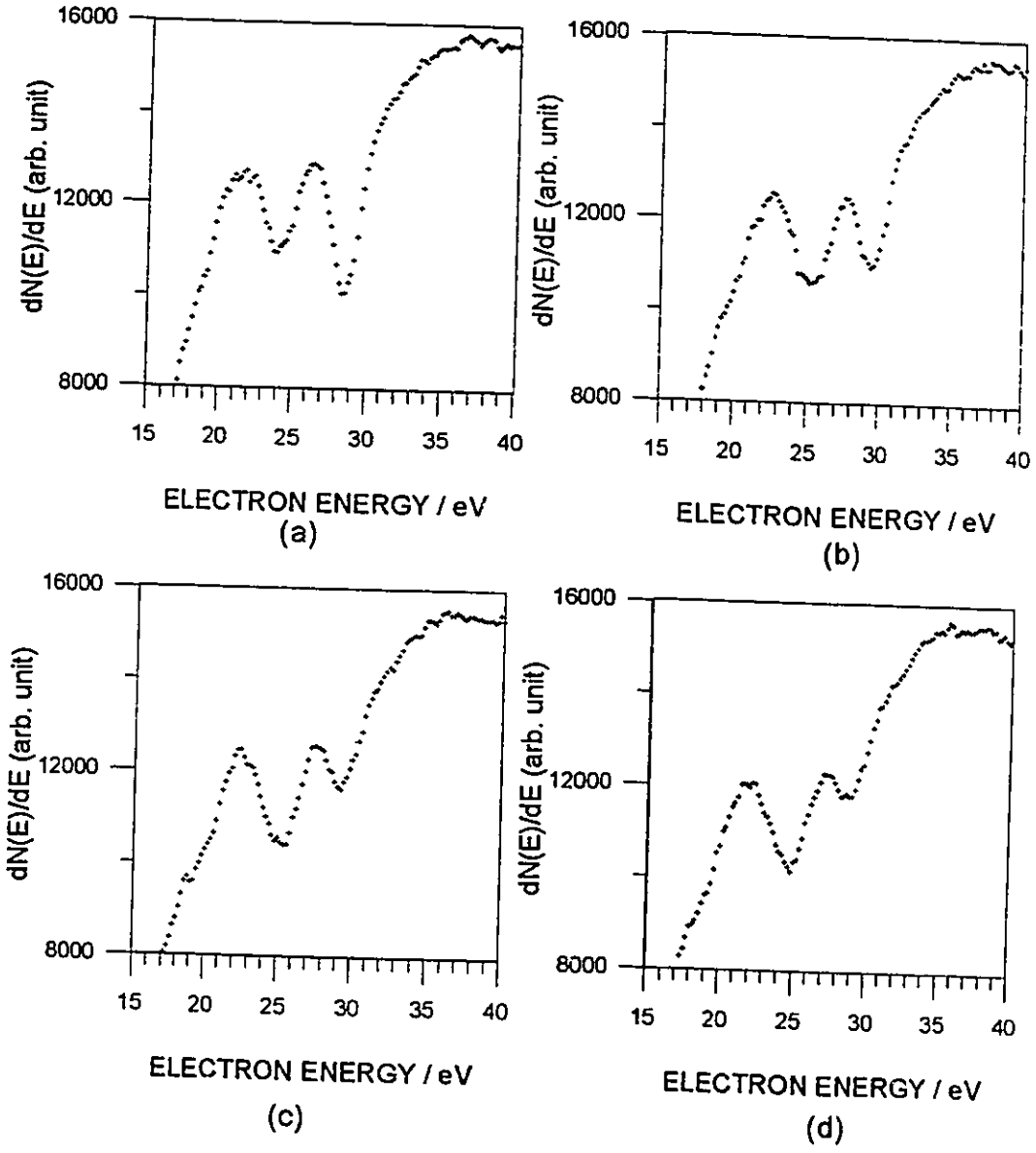

Figure 6-7. Low-energy MVV Auger spectra after the interaction of nitrogen gas with titanium at 760 K, using gas fluxes of (a) 5.9×10^{13} (b) 2.4×10^{14} (c) 1.9×10^{15} and (d) 7.0×10^{15} molecules cm^{-2} s^{-1}. The corresponding <x> values from the high-energy LMM spectra can be seen in figure 6-6.

Auger peaks, "nitride" and "metal" peak, which are the characteristic features for a surface partly covered with nitrogen. Two sets of low-energy spectra corresponding to figure 6-6 curve (a) and (e), i.e. the two experiments with the lowest and the highest N_2 gas fluxes, are shown in figure 6-8, 6-9. For the low gas flux experiment, figure 6-8, by increasing the temperature to 640 K the "nitride" peak increases and the "metal" peak decreases slightly. The spectra (c) and (d) collected after 700 and 760 K N_2 adsorption show the same magnitudes of both "nitride" and "metal" peak as that of spectrum (b). The calculated nitrogen surface coverage from these three low-energy spectra are the same, 0.45 monolayer. At even higher temperature, 810K, the spectrum, (e), shows a large "metal" peak and a small "nitride" peak, which corresponds to a nitrogen surface coverage 0.3 monolayer. For the high flux experiment, figure 6-9, the low-energy spectra show that the nitrogen surface coverage increases with temperature until 760K, then drops at even higher temperature. The saturated nitrogen surface coverage is ~0.7 monolayer, which is higher than that of the low gas flux experiment.

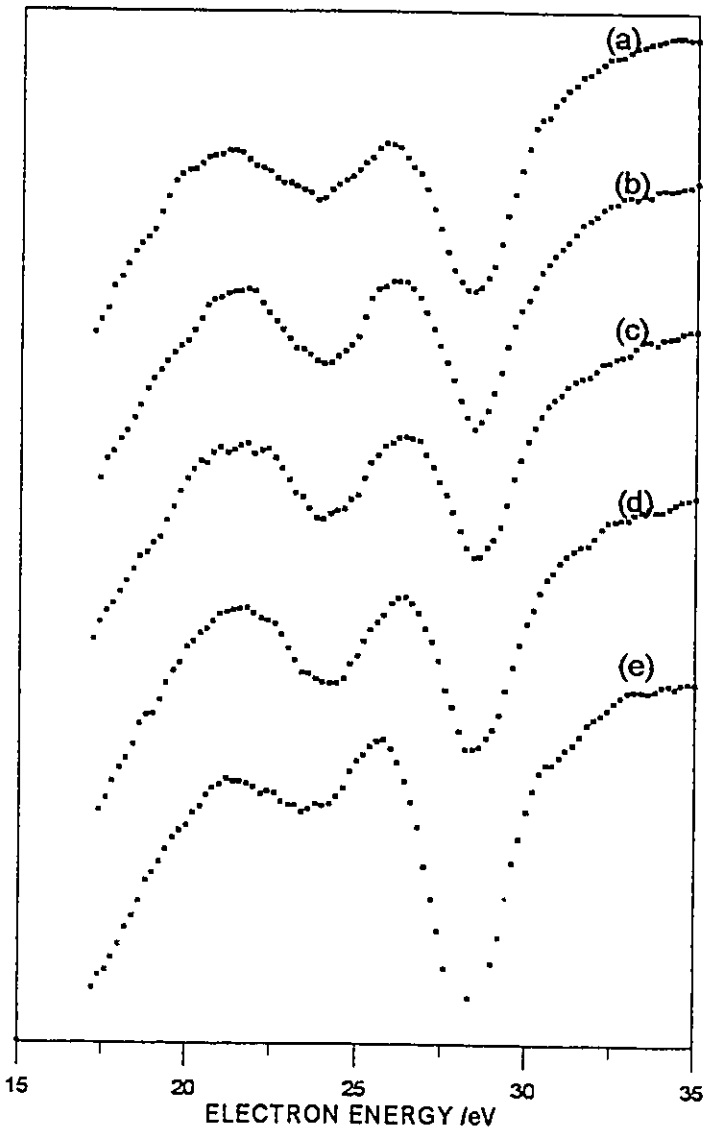

Figure 6-8. The MVV low-energy Auger electron spectra of titanium after reaction with N_2 gas with a flux of 5.9×10^{13} molecules/s.cm^2 at different surface temperatures: (a) 300 K (b) 640 K (c) 700 K (d) 760 K and (e) 810 K.

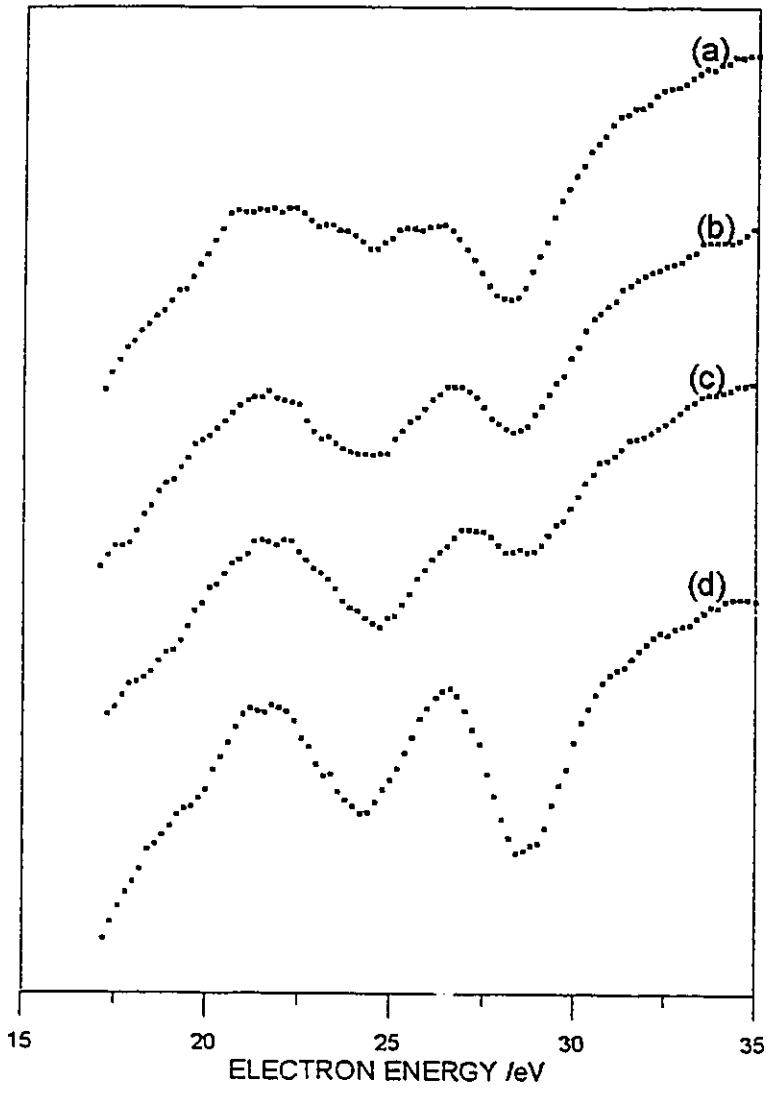

Figure 6-9. The MVV low-energy Auger electron spectra of titanium after reaction with N_2 gas with a flux of 7.0×10^{15} molecules/s.cm^2 at different surface temperatures: (a) 300 K (b) 640 K (c) 760 K and (d) 960 K.

6.3. DISCUSSION

6.3.1 NH_3 adsorption and diffusion

At elevated temperatures lateral displacement of the nitrogen adatoms in the half-covered state, figure 6-10 (a), could permit ammonia adsorption on sites where N-H bond breaking and N chemisorption can take place, figure 6-10 (b), and N atom migration into the titanium lattice also becomes possible . The results of figure 6-2 show that at elevated temperatures without electron beam stimulation, after a one minute ammonia dose the escape-depth-averaged nitrogen to titanium mole ratio, <x>, approaches or exceeds the saturated value for room temperature adsorption with electron stimulation.

At steady state, the composition in the surface region will be determined by the balance between the rate of adsorption into the surface layer and diffusion away from the surface into the bulk. As nitrogen sorption on titanium has been found to be irreversible even at high temperature [Nagasaka and Yamashina, 1972; Elsworth et al., 1963; 1965], the effect of nitrogen desorption will be ignored in the discussion. The results shown in figure 6-3 can be interpreted quite well with a simple model previously used to illustrate the results of nitrogen adsorption [Dawson and Tzatzov, 1987]. The rate of adsorption can be written as

$$R_a = S(x_0, T)(dN_g/dt) \qquad (6\text{-}1)$$

where,

Figure 6-10. Scale model showing plan views of the basal plane of titanium on which (a) nitrogen atoms have been chemisorbed to one-half monolayer coverage, the adatoms occupy rows of next-near-neighbour sites. In (b) migration of some nitrogen adatoms to near-neighbour sites permits the adsorption of more ammonia molecules which, after N-H bond breaking at high temperature will ultimately lead to a fully occupied surface.

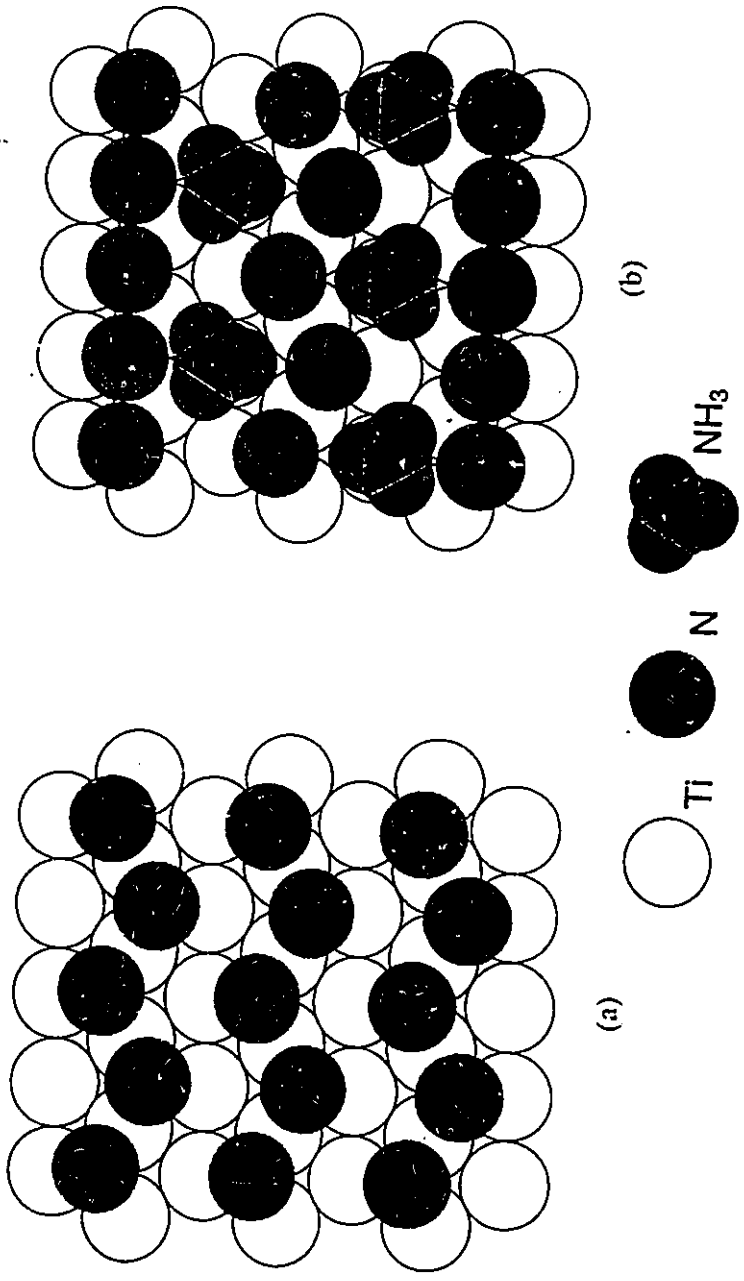
(b)
NH_3
N
Ti
(a)

$S(x_0, T)$ is the sticking probability, which is a function of surface coverage x_0 and temperature, if the adsorption is activated; (dN_g/dt) is the gas flux. The rate of surface atom diffusion into the bulk can be written as,

$$R_d = -D(T)(dx/dz)_0 \qquad (6\text{-}2)$$

where, D(T) is the diffusion coefficient and $(dx/dz)_0$ is the gradient of the nitrogen concentration at surface, $z = 0$.

Since the activation energy for diffusion will be larger than that for adsorption, the rate of adsorption is greater than the rate of diffusion at lower sample temperatures, and as shown by low-energy Auger spectra, figure 6-4 (c), the surface coverage is dynamically kept around unity. Therefore, the <x> value increases with sample temperature for a constant flux setting. At high temperature, the diffusion rate will exceed the maximum adsorption rate which is limited by the gas flux, and the concentration in the outer surface layer and the analyzed surface region will both decrease. At the maximum point of the curve the rate of adsorption is equal to the rate of diffusion,

$$S(x_0, T_{max})(dN_g/dt) = D(T_{max})(dx/dz)_0, \qquad (6\text{-}3)$$

where T_{max} is the temperature, at which the escape-depth-averaged nitrogen to titanium mole ratio will reach its maximum value, $\langle x \rangle_{max}$.

As the adsorption rate will increase with gas flux, (dN_g/dt), both T_{max} and $\langle x \rangle_{max}$ will increase with (dN_g/dt), as shown in figure 6-3. The activation energy for this process

can be determined from a plot of $\ln(dN_p/dt)$ versus T_{max}. This plot is shown in figure 6-11 for the three lower fluxes at which T_{max} can be best estimated. The slope indicates an apparent activation energy of 70 kJ/mol; identical with the value observed previously from electron stimulated N_2 adsorption [Dawson and Tzatzov, 1987] and that determined gravimetrically during the initial stages of nitrogen sorption in titanium at low pressure and temperature between 600 and 800°C [Nagasaka and Yamashina, 1972].

6.3.2. N_2 adsorption and diffusion

The room temperature N_2 adsorption results in figure 6-5 show that the adsorption saturation value of <x> is low, and cannot be increased to full coverage by electron beam stimulation. The binding energy of diatomic N_2 to the unoccupied sites on this surface must be so low that the coverage is negligible and electron stimulated adsorption is impossible, unlike the NH_3 case. At elevated temperatures, there is a slight increase in the <x> value, figure 6-6, but the maximum <x> value observed is only 0.57, much lower than 0.86, the <x> value for a full-monolayer nitrogen surface coverage. The increase in surface coverage observed between 300 and 760 K must be attributed to an increase in the sticking probability for activated adsorption, and the decrease of <x> value at temperatures higher than 760 K is caused by nitrogen bulk diffusion. The interaction time was 2 minutes for the experiments summarised in figure 6-6. This time was insufficient to produce a saturated surface for the two low fluxes of 5.9×10^{13} and 2.4×10^{14} molecules $cm^{-2}s^{-1}$, as shown by the low-energy spectra, figure 6-7 (a) and (b). For the three higher flux experiments, they all produce the same low and high energy Auger spectra,

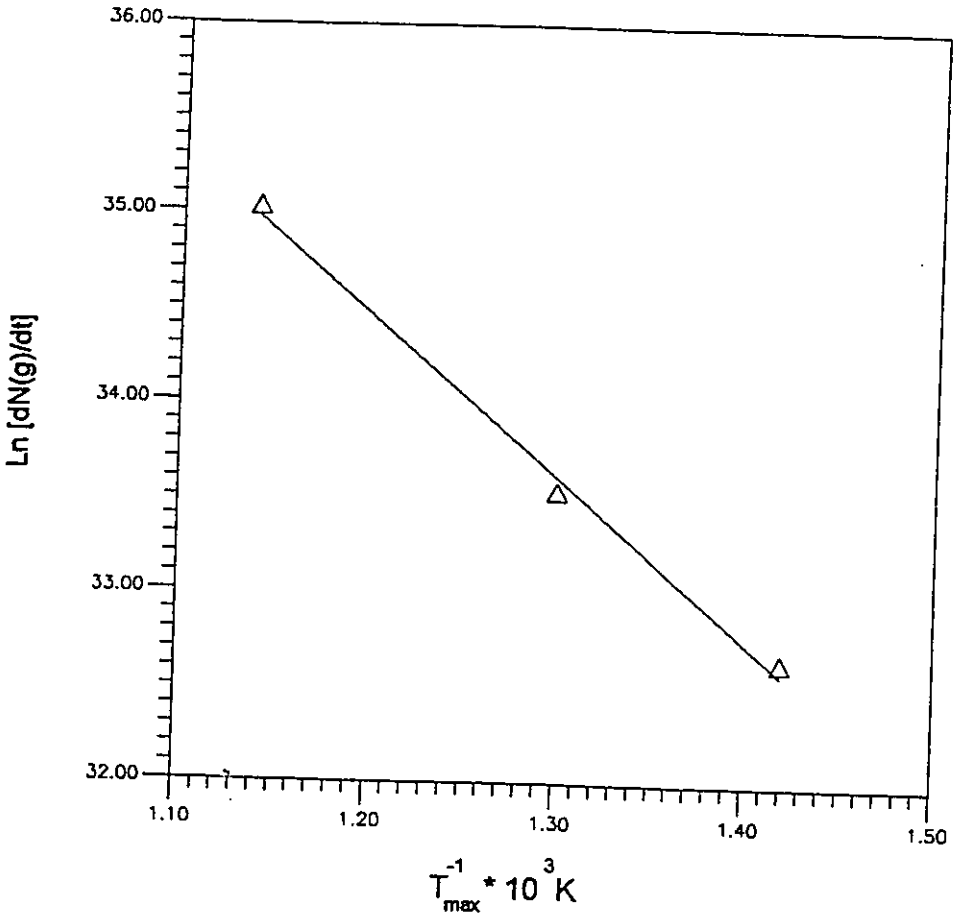

Figure 6-11 An Arrhenius plot of ln [dN(g)/dt] versus $1/T_{max}$ for the interaction of ammonia with titanium without electron stimulation. T_{max} is the sample temperature at which <x> attaines a maximum value for a given ammonia gas flux dN(g)/dt (see figure 6-3).

indicating a saturated but not fully covered nitrogen surface coverage. At this surface coverage the sticking probability for chemisorption of N drops orders of magnitude and the surface concentration becomes insensitive to increasing gas flux.

The N_2 adsorption results presented here are quite different from the data previously reported by Dawson and Tzatzov [1987], shown in figure 6-12. In the previous experiment on N_2 sorption, the experiment was performed in background N_2 gas with simultaneous electron bombardment, and surprisingly, this led to results identical with those observed in the present work for NH_3 in the absence of electron bombardment, compare figure 6-3 with 6-12. At elevated temperature, N-adatom migration permits N_2 to be weakly bound to the surface so that electron stimulated dissociation and chemisorption become possible. In this study the N_2 adsorption in the gas flux from the doser is separated in time from the electron beam interaction with the surface during Auger analysis. In the time interval between interrupting the gas flow and commencing the electron bombardment, the weakly adsorbed N_2 molecules will desorb and electron stimulated chemisorption is not possible.

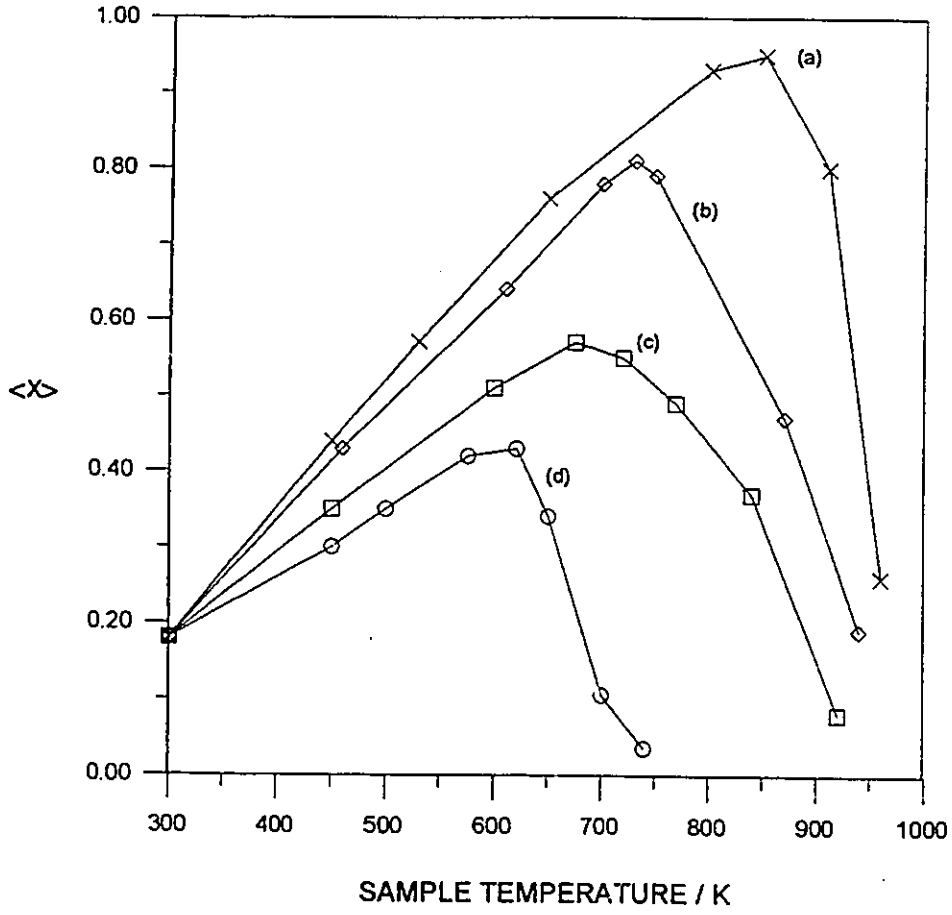

Figure 6-12 The escape-depth-averaged nitrogen to titanium ratio, <x>, after reaction with nitrogen gas as a function sample temperature at four different gas pressures; (a) $1x10^{-5}$ (b) $1x10^{-6}$ (c)$1x10^{-7}$ and (d) $1x10^{-8}$ torr. The gas doser was not used but the gas back-filled the chamber to the pressures indicated and the sample was simultaneously bombarded with electrons for Auger analysis. This data is taken from reference of Dawson and Tzatzov, 1987.

6.4. CONCLUSIONS

Ammonia adsorption at elevated temperatures in the range of 600 to 1000 K can produce a full monolayer nitrogen on titanium surface without electron stimulation. At even higher temperature the nitrogen surface coverage drops because of bulk diffusion. Without electron beam bombardment, the behaviour of ammonia adsorption is indistinguishable from those observed previously for the sorption of diatomic N_2 gas with electron stimulation.

Nitrogen adsorption at 300 K is saturated at low nitrogen surface concentration, and cannot be increased to full coverage by electron beam stimulation. At elevated temperatures, in the absence of electron bombardment, there is an increase in the surface nitrogen coverage, which can be attributed to an increase in the sticking probability for activated adsorption. At temperatures higher than 760 K, bulk diffusion causes the nitrogen surface coverage decrease. The activation energy for dissociative chemisorption beyond a half monolayer is so high that bulk diffusion of N atoms commences at temperatures lower than those required for population of the surface to full coverage.

CHAPTER SEVEN

INTERACTION OF AMMONIA WITH TUNGSTEN SINGLE CRYSTAL SURFACES

7.1. INTRODUCTION

Tungsten is situated diagonally opposite titanium in an important block of nine transition metals in groups 4, 5, and 6 of the periodic table. Unlike titanium, which forms a refractory nitride, tungsten forms unstable nitrides, which decompose at ~800°C. Since being tested as an ammonia catalyst in the early work of Mittasch and Haber [1950], tungsten has attracted a great deal of interest in its activity for ammonia adsorption and decomposition. The earlier work has been extensively reviewed by Grunze [1982], and Lambert and Bridge [1984].

Estrup and Anderson [1968] used LEED, TDS and $\Delta\phi$ measurements to investigate ammonia adsorption on the W(100) plane and reported that ammonia adsorption on W(100) at room temperature is non-dissociative. Hydrogen desorption occurs at ~800 K, leaving behind a C(2x2) structure, which was interpreted as one half-monolayer of NH_2. The C(2x2) NH_2 structure seemed to be capable of adsorbing NH_3 non-dissociatively to

yield an adlayer thought to contain bridge-bonded NH_2 species and terminally bonded NH_3 species. The NH_2 density could be increased to full monolayer coverage by exposure to NH_3 at ~800 K, and this surface displayed reversible adsorption-desorption properties towards NH_3. This NH_2 saturated surface seemed to decompose in two distinct stages (~1150 and ~1375 K), both of which involved the simultaneous loss of H_2 and N_2 from the surface. This interpretation has been strongly criticised [Dawson and Hansen, 1968; Dawson and Peng, 1970]. Estrup and Anderson deduced that the rate of hydrogen desorption is controlled by an N-H bond breaking process rather than H atom recombination. Results obtained by May et al. [1969] seem to agree somewhat with those of Estrup and Anderson. They studied NH_3 on W(211), and concluded that after saturation of the surface with ammonia at room temperature and heating to 500 K, one third of the surface hydrogen is evolved, leaving a residue with the stoichiometry NH_2. At 1200 K simultaneous desorption of H_2 and N_2 occurs.

Other studies [Dawson and Hansen, 1968; Wilf and Folman, 1976; Matsushita and Hansen, 1969] strongly conflict with the above results. In particular Dawson and Hansen performed a FEM study and found that NH_3 adsorption on W surfaces is non-dissociative at 200 K. On raising the temperature, ammonia dissociation to produce adsorbed hydrogen and nitrogen occurs between 200 to 400 K, and hydrogen desorption was complete by 600K leaving behind a β-N residue. They also proposed that the interaction of adsorbed N with gaseous NH_3 yields surface species such as NNH_3 and NNH_2. The decomposition of NNH_2 was suggested as the rate-limiting step for the overall decomposition reaction.

The reason for these conflicting experimental results and their interpretation originate in the complexities of the NH_3-W system:

(1) It has been demonstrated that the dissociation of ammonia on tungsten surface is a structure-sensitive process [Dawson and Hansen, 1968] and it commences earlier on the rougher planes [Dawson and Peng 1970]. McAllister and Hansen [1973] reported that the rate of decomposition depends on the crystallographic orientation of the specimen in the order W(111) > W(100) > W(110), indicating the highest activity for NH_3 dissociation on the W(111) surface.

(2) The nature of the surface intermediates is strongly dependent on the NH_3 partial pressure [Peng and Dawson 1974]. At high pressures, further reactions between NH_3(g) and the adsorbed layer can lead to the formation of H-containing complexes such as W_2N_3H. As in the investigation of Matsushita and Hansen [1969], these complexes are not formed at low pressure. Dawson [1974] reported the results of a total pressure variation determination of ammonia decomposition reaction rates on tungsten, which clearly showed that the reaction order for ammonia is zero at low pressure and 1/3 order above 10^{-1} torr. These results agree well with a mechanism proposed for ammonia decomposition in which the nitrogen desorption from the tungsten surface was suggested to be the rate-determining step for the reaction in the low pressure regime, and the decomposition of W_2N_3H, surface species formed in the high ammonia partial pressure, was suggested to be the rate-determining step in high pressure regime.

(3) Alnot et al. [1989] performed a thermal molecular beam study and showed that the

ammonia decomposition is strongly dependent on the surface temperature and nitrogen coverage. They showed that the surface nitrogen coverage decreases with increasing surface temperature. At high temperature, ~500 K, the saturation nitrogen coverage is not achieved even after 20 minutes interaction with a beam flux 2.4×10^{12} molecules cm^{-2} s^{-1}. It is claimed that the adsorption of NH_3 becomes the rate-determining step at high temperatures. These authors suggested that the critical factor in this system is the nitrogen surface coverage since N_{ads} poisons the ammonia chemisorption step.

In this chapter, an investigation on the interaction of ammonia with tungsten single crystal surfaces, including the stimulation effect of electrons on ammonia adsorption, nitrogen desorption and diffusion during annealing and the surface structure changes of W(100) induced by the chemisorbed nitrogen atoms, will be presented and discussed. The results lead to new insights into these complex processes.

7.2. EXPERIMENTAL RESULTS

7.2.1. The W(NNN) Auger spectra of W(100), W(110) and W(111)

Table 7-1 shows the peak-to-peak heights of the 160-180 eV W(NNN) peaks in the Auger spectra taken from three tungsten single crystal samples with (100), (110) and (111) orientations. As the W(NNN) peaks overlap each other, the intensity of the W(NNN) peaks is represented as the peak-to-peak height shown in figure 7-1..

Table 7-1. W(NNN) peak-to-peak heights (PPHt)* in W(100),W(110), and W(111) Auger spectra

Crystal Planes	PPHt (arb. unit)
W(100)	11713 ± 40
W(110)	13377 ± 140
W(111)	10515 ± 70

* *The definition of PPHt of W(NNN) peaks is shown in figure 7-1.*

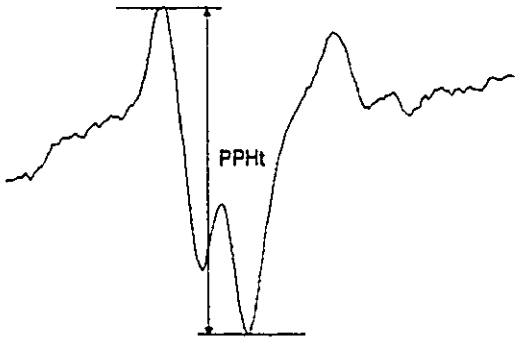

Figure 7-1. PPHt for the W(NNN) peaks.

7.2.2. Ammonia adsorption at 300 K

At room temperature, ammonia

adsorption experiments were performed on the three single crystal surfaces with a gas flux of $5.7x10^{15}$ molecules $cm^{-2}s^{-1}$ by using the gas doser. Electron irradiation during ammonia gas exposure was carefully avoided in these experiments. After each experiment, the gas flux was turned off and the Auger spectra were not taken until the background pressure was pumped down to 10^{-9} torr. Figure 7-2 shows the W(NNN) and N(KLL) Auger spectra of W(100) surface saturated with ammonia at 300 K. Similar spectra were obtained from NH_3/W(110) and NH_3/W(111) surfaces. The peak-to-peak heights of N(KLL) and W(NNN) peaks and their ratios for the three ammonia saturated surfaces are listed in table 7-2.

Table 7-2. PPHt of W(NNN) and N(KLL) peaks and PPHt ratios of N(KLL) to W(NNN) for the NH_3/W(100), NH_3/W(110) and NH_3/W(111) surfaces saturated at 300K

Crystal Planes	$PPHt_{W(NNN)}$	$PPHt_{N(KLL)}$	$PPHt_N/PPHt_W$
W(100)	9604 ± 78	2636 ± 56	0.274 ± 0.006
W(110)	10824 ± 87	2309 ± 72	0.212 ± 0.007
W(111)	9135 ± 184	2446 ± 57	0.268 ± 0.008

Sputter profiling experiments were performed on the NH_3/W(100), NH_3/W(110) and NH_3/W(111) samples saturated by ammonia adsorption at room temperature and the

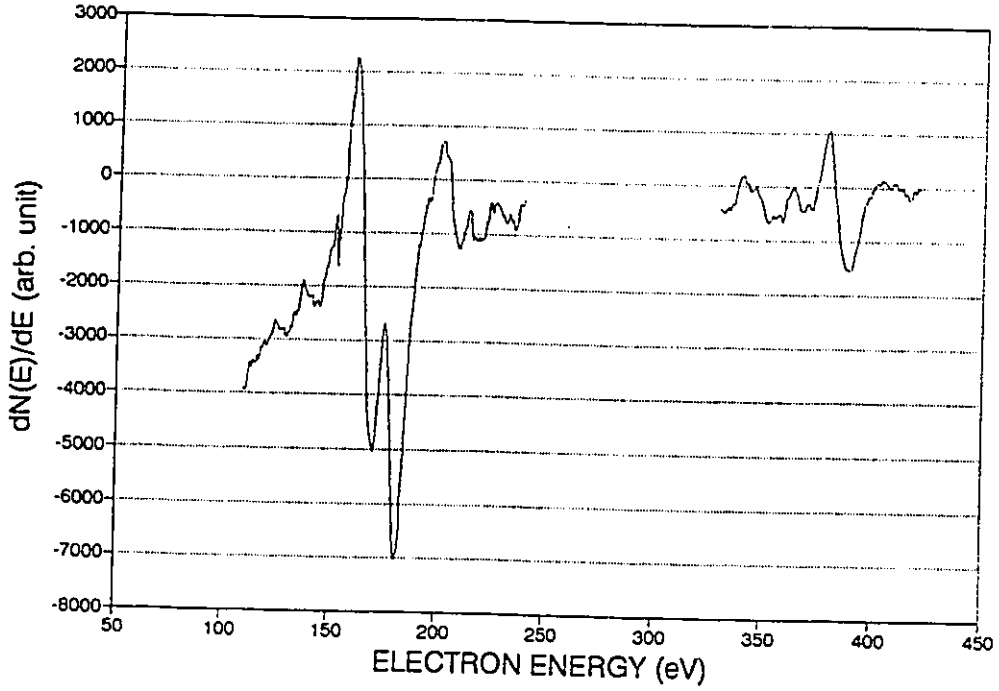

Figure 7-2. The Auger spectrum from a W(100) surface saturated by ammonia adsorption at 300 K.

results are shown in Figure 7-3. It can be seen that the peak-to-peak heights of the N(KLL) and W(NNN) peak decrease and increase, respectively, with sputter time, i. e. the depth into the sample.

7.2.3. Electron beam stimulated ammonia adsorption at 300 K

The influence of electron bombardment on ammonia adsorption has been examined on the three tungsten single crystal samples. All of them showed a strong electron beam effect. In these experiments, ammonia gas was introduced into the chamber and kept at a pressure of $8x10^{-7}$ torr dynamically, and the sample surface was monitored by AES continuously. Therefore, in these experiments, the sample surface was exposed to ammonia gas and bombarded by the electron beam simultaneously. It was observed that the N(KLL) Auger peak increases with time, surpasses the saturation values for non-activated 300 K ammonia adsorption, table 7-2, and saturates with the high peak-to-peak height values, shown in table 7-3. The W(NNN) Auger peak decreases with time as the surface nitrogen coverage increases for all three crystal planes. The N(KLL) to W(NNN) peak height ratios are identical within experimental error for activated adsorption, in contrast with the non-activated results.

The W(NNN) and N(KLL) Auger spectra taken for the nitrogen saturated W(100) surface after electron stimulated ammonia adsorption are shown in figure 7-4 (a). For comparison, the Auger spectra taken on a tungsten nitride thin film made by NH_3^+ ion implantation are shown in figure 7-4 (b). It is important to note that the nitrogen Auger peaks of (a) and (b) have the same magnitude while the magnitude of the tungsten Auger

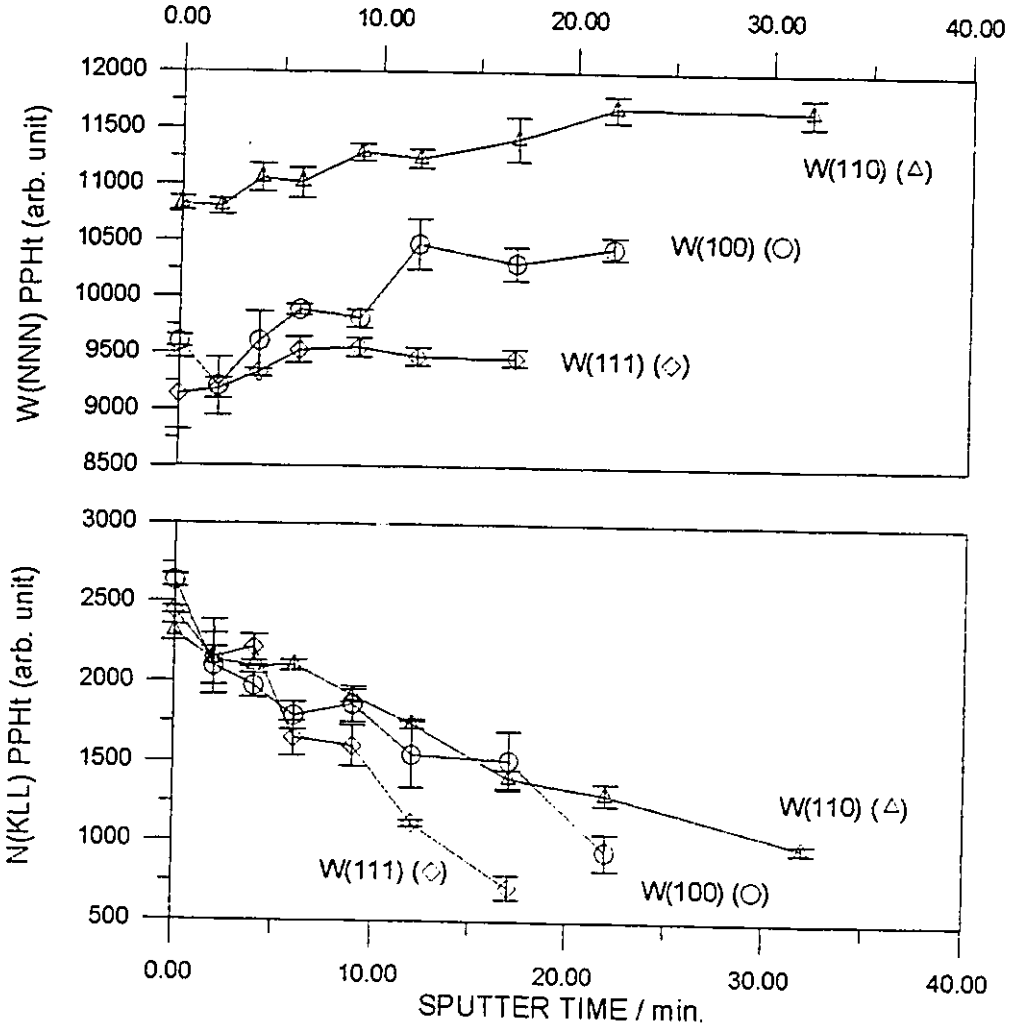

Figure 7-3. Sputter depth profiles for the W(100), W(110) and W(111) samples after ammonia adsorption at 300 K.

Table 7-3. Saturation peak-to-peak height values of W(NNN) and N(KLL) Auger peaks and their ratios for W(100), W(110) and W(111) surfaces after electron beam stimulated ammonia adsorption

Crystal Planes	$PPHt_{W(NNN)}$	$PPHt_{N(KLL)}$	$PPHt_N$ / $PPHt_W$
W(100)	5893 ± 283	5757 ± 322	0.98 ± 0.07
10)	6038 ± 441	5883 ± 467	0.97 ± 0.1
W(111)	6432 ± 328	6373 ± 278	0.99 ± 0.07

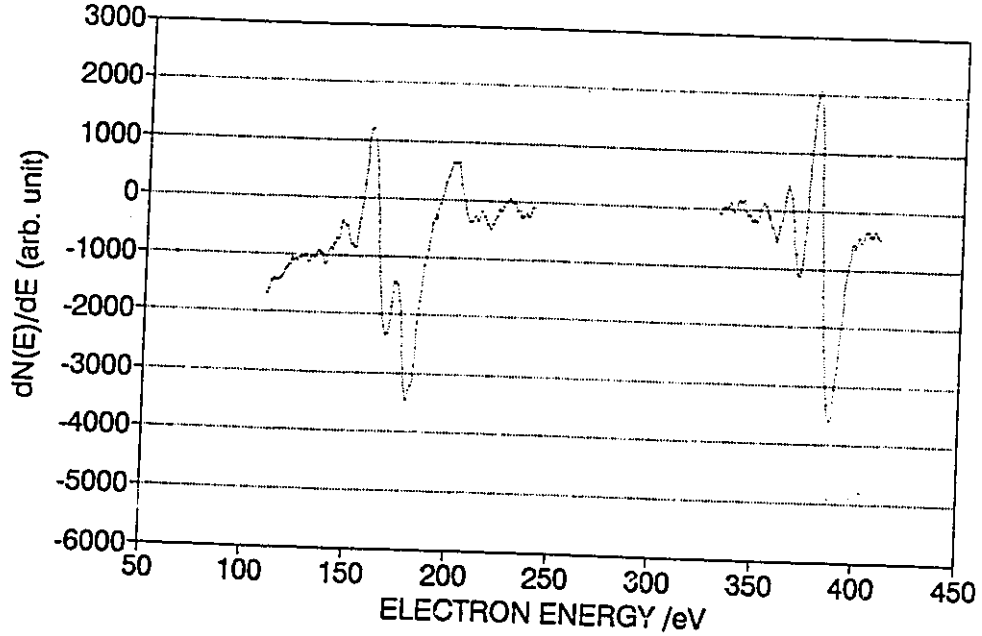

(a)

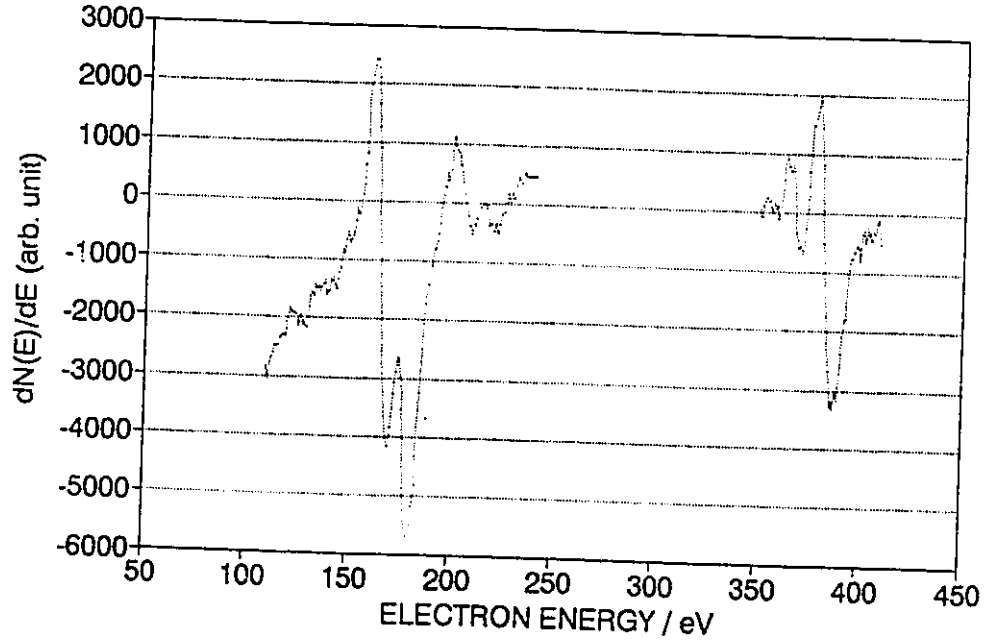

(b)

Figure 7-4. The Auger spectra of W(100): (a) after electron stimulated ammonia adsorption at 300 K; (b) after 2 keV NH_3^+ ion implantation.

peak in (a) is only about half that in (b).

7.2.4. Ammonia surface reaction at 800 K on W(100), W(110) and W(111)

Ammonia surface reactions were carried out with a substrate temperature of 800 K on the W(100), W(110) and W(111) surfaces. First, the sample was heated and kept at 800 K, then an ammonia gas flux of 5.7×10^{15} molecules $cm^{-2} s^{-1}$. was introduced with the sample surface facing the gas doser. After one hour ammonia reaction with constant substrate temperature and constant ammonia gas flux, the sample was turned away from the gas doser and heater position, and the gas flux and heater were turned off immediately. After the background pressure of the chamber was pumped down to 10^{-9} torr to minimize electron beam effects, Auger spectra were taken from these sample surfaces. The results are given in table 7-4.

Table 7-4. PPHt of W(NNN) and N(KLL) peaks and PPHt ratios of N(KLL) to W(NNN) for the W(100), W(110) and W(111) surfaces after one hour ammonia surface reaction at 800 K

Crystal Planes	$PPHt_{W(NNN)}$	$PPHt_{N(KLL)}$	$PPHt_N/PPHt_W$
W(100)	9887 ± 75	2105 ± 93	0.23 ± 0.01
W(110)	11868 ± 154	2353 ± 95	0.20 ± 0.008
W(111)	8950 ± 345	2202 ± 370	0.25 ± 0.04

Sputter depth profiling experiments were performed on these single crystal surfaces after ammonia surface reaction at 800 K, and the results are plotted in figure 7-5. The depth distributions of nitrogen shown in figure 7-5 are quite different from those for adsorption at 300 K, shown in figure 7-3. The most interesting result is the sputter profile for the W(100) sample. When the surface atoms were removed layer after layer by argon ion sputtering the profile shows that the nitrogen peak-to-peak height increases with sputter time to a value about 1.7 times higher than the value obtained from the outer surface and, correspondingly, the tungsten peak-to-peak height decreases with sputter time to a value about 0.8 of the value obtained from the outermost surface. Following this, the peak-to-peak heights of both nitrogen and tungsten peaks keep constant for about 10 minutes sputtering, and thereafter the nitrogen peak-to-peak height decreases and tungsten peak-to-peak height increases with sputter time. The nitrogen peak-to-peak height obtained from the outermost layer is small, ~2100, and so one can conclude that the nitrogen coverage on outermost layer of W(100) after 800 K ammonia reaction is low.

The depth profile for the W(111) surface shows a steady decrease of nitrogen peak-to-peak height and consequent increase of tungsten peak-to-peak height with sputter time, not like that for W(100). The sputter profile is not unlike that for 300 K adsorption, figure 7-3. On W(110), the variation of peak-to-peak height of the *tungsten* peak is more similar to that for W(100), showing a high value for the outermost layer, a decrease to a constant lower value for about 10 minutes sputtering and finally an increase again toward the high value for pure tungsten. However the variation of peak-to-peak height for *nitrogen* on W(110) is different from that of W(100). It shows a plateau for the first

Figure 7-5. Sputter depth profiles after one hour ammonia surface reaction at 800 K, on: (a) W(100); (b) W(110) and W(111) samples.

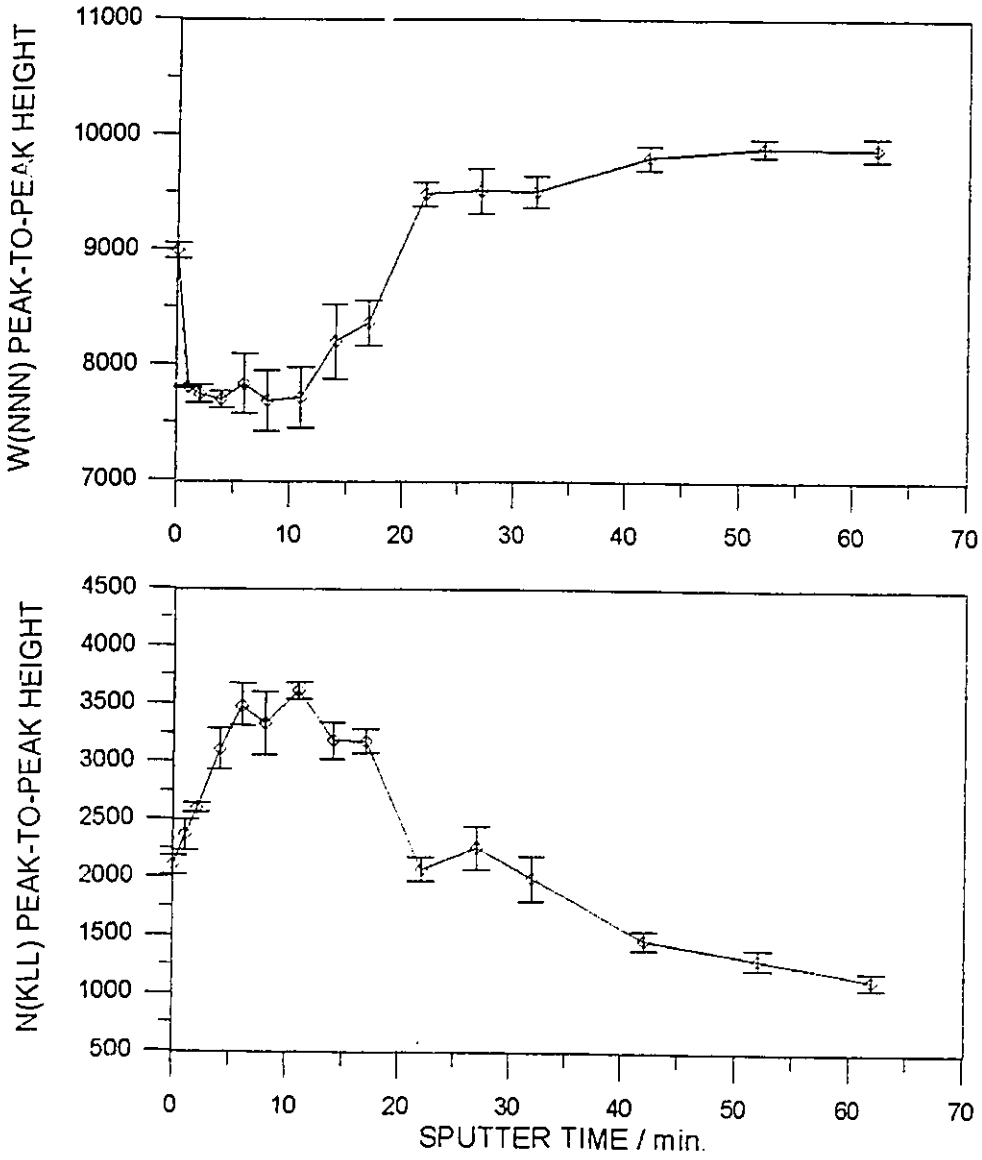

(a) Sputter depth profilng on W(100) sample.

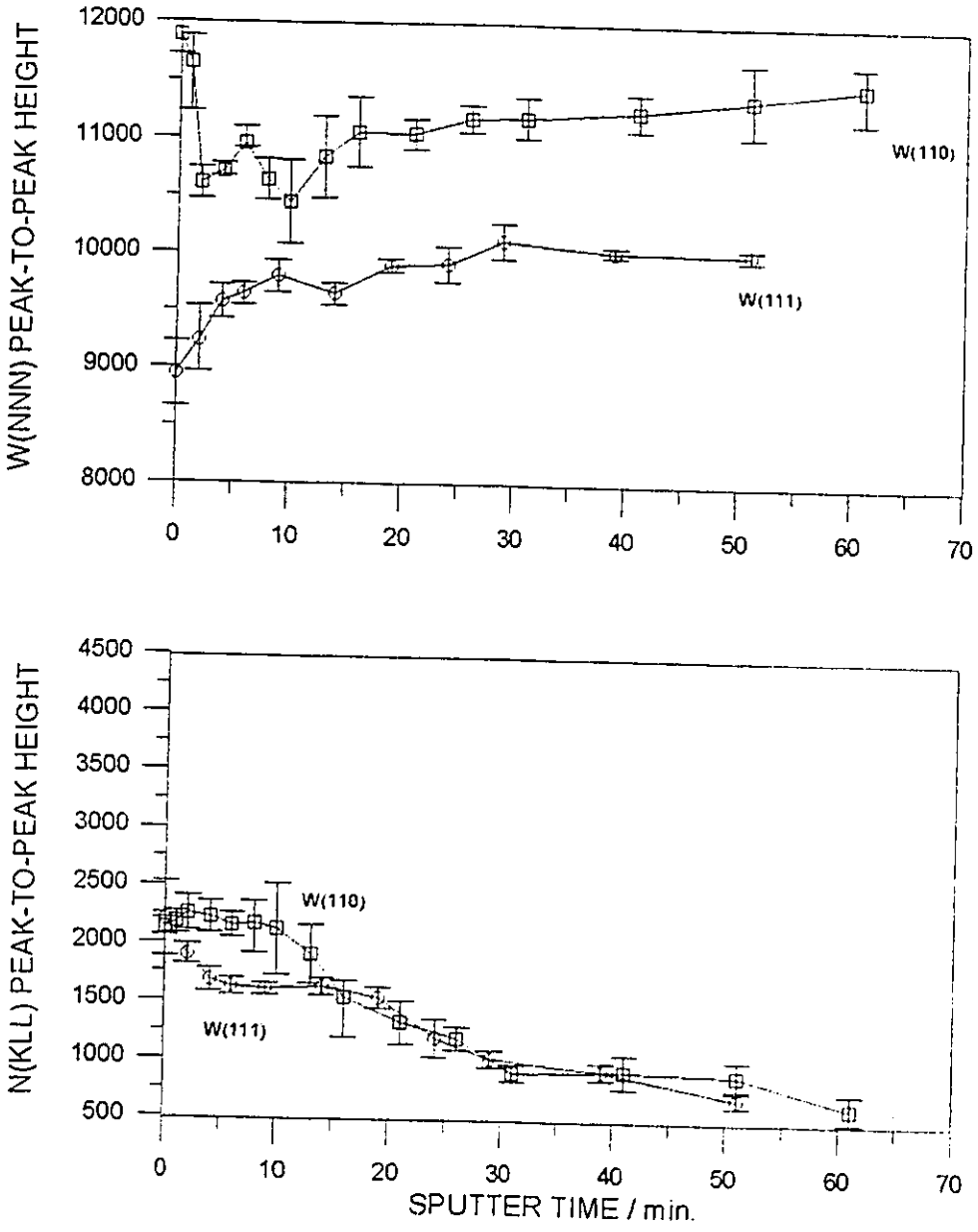

(b) Sputter depth profilings on W(110) and W(111) samples.

10 minutes sputtering, then decreases with sputter time.

The different nitrogen and tungsten Auger peak heights observed after reaction and before sputtering and also the differences in sputter profiles suggest that the distribution of nitrogen in the outer surface differs for different surface orientations. A comparison of the relative sensitivities with changing angle of incidence can be used to determine the spatial distribution of a sorbed layer.

7.2.5. Auger analysis with normal and glancing incidence primary beams

The three tungsten single crystal surfaces after ammonia surface reaction at 800K were analyzed by AES with both normal and glancing incidence beams. To avoid electron beam stimulated ammonia adsorption, Auger analysis was only performed after the total pressure in the chamber was pumped down to 10^{-9} torr. The geometry of the beam incidence is shown in figure 7-6.

The tungsten Auger peak intensity ratios, R= I(G)/I(N), obtained from clean tungsten single crystal surfaces are compared with those obtained from the same surfaces after ammonia surface reaction at 800K in figure 7-7 (a) and (b). The difference between the results for W(100) and

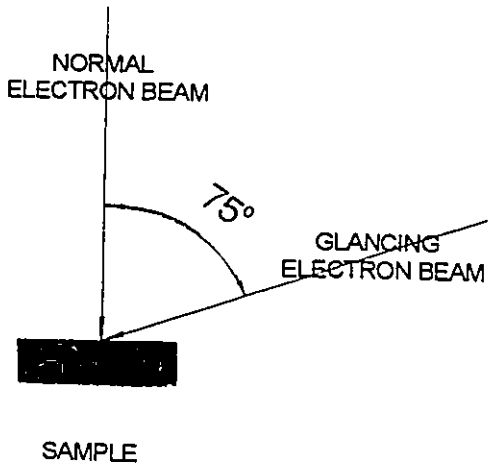

Figure 7-6. Beam incidence geometry.

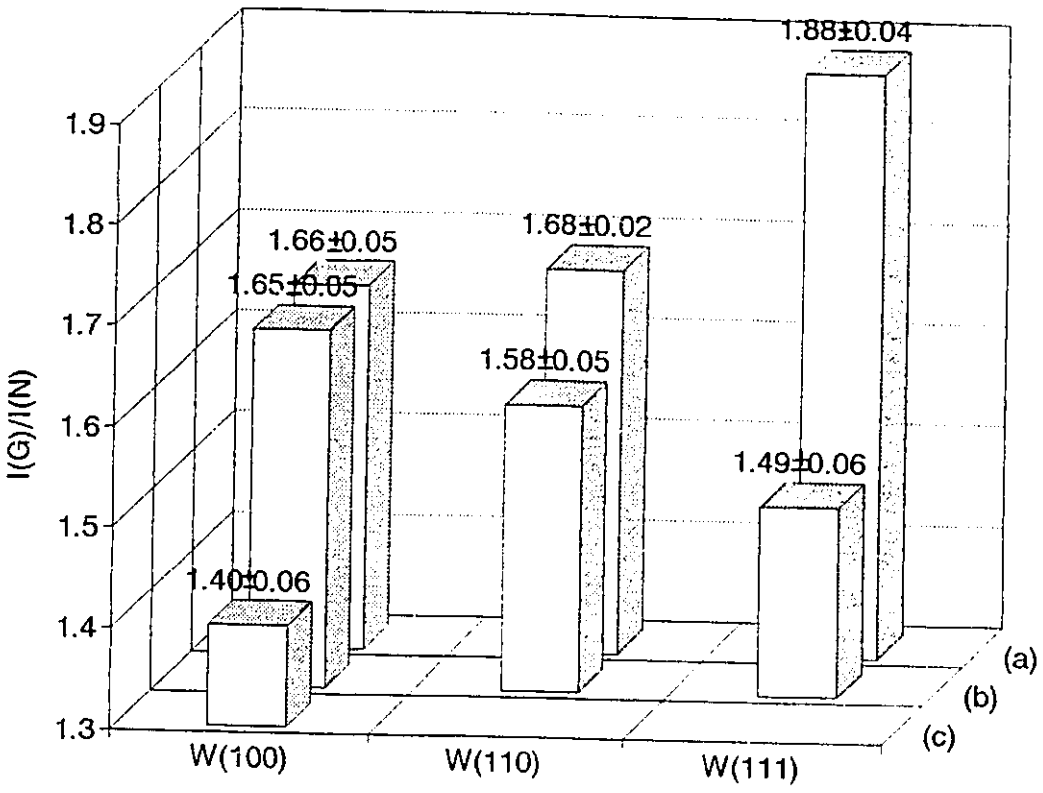

Figure 7-7. The W(NNN) Auger peak intensity ratios, I(G)/I(N), where I(G) was determined with a glancing and I(N) with a normal incidence primary beam for (a) a clean metal surfaces; (b) an 800 K ammonia reacted surfaces; and (c) a highly covered surface prepared by electron beam stimulated ammonia adsorption at 300 K.

W(111) is dramatic. The results on W(100) show $R_{WN} \approx R_W$, while on W(111), R_{WN} is much smaller than R_W.

This experiment has also been performed on a nitrogen fully covered W(100) surface, which was prepared by electron beam stimulated ammonia adsorption. The value obtained for R_{WN} is 1.40, figure 7-7 (c), which is significantly smaller than the R_W for W(100).

These results will be discussed in detail in section 7.4.2., where it will be shown that the N atoms are in sub-surface sites for W(100) but not for W(111). This is consistent with the picture suggested by the sputter depth profiles of figure 7-5.

7.2.6. Adsorption properties of the W(100) surface after ammonia reaction at 800 K

In order to sustain nitride film growth, the surface produced by high temperature reaction must be able to adsorb further NH_3. The adsorption properties of the W(100) surface after high temperature ammonia surface reaction were investigated at 300 K, and the results are shown in figure 7-8. Spectrum (a) was taken from W(100) after ammonia reaction at 800K and (b) is the spectrum taken after 10 minutes ammonia dosing with a gas flux of 5.7×10^{15} molecules $cm^{-2} s^{-1}$ at 300K. Both spectra were taken under ultra-high vacuum conditions. Also shown in figure 7-8 (c) is the (b)-(a) difference spectrum. Since the difference spectrum (c) is featureless we conclude that the 10 minute ammonia adsorption has made no contribution to the nitrogen coverage. The surface with sub-surface nitrogen, but no adsorbed nitrogen, produced by reaction at 800 K does not

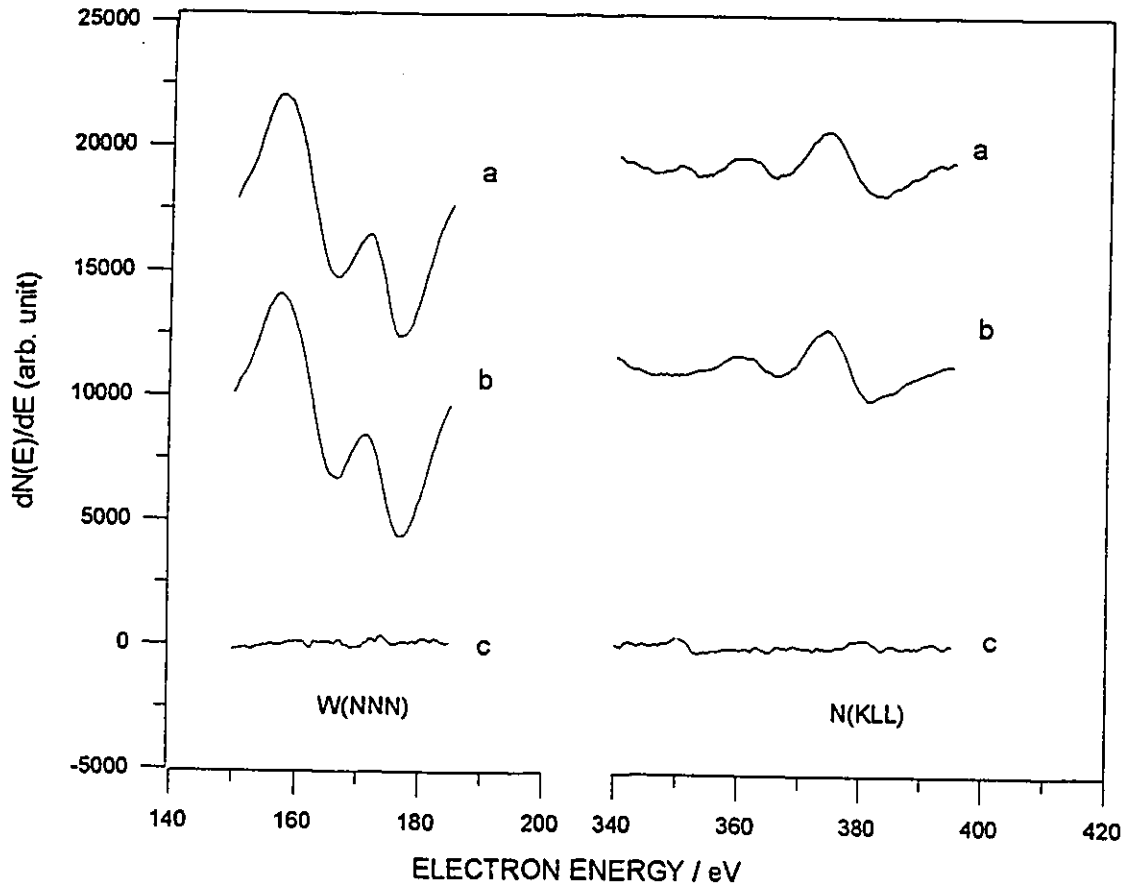

a. before adsorption; b. after adsorption; c. difference spectrum

Figure 7-8. The absence of ammonia adsorption at 300 K on the sample produced by ammonia interaction with a W(100) sample at 800 K. The Auger spectrum shown in (a) was taken after 30 minutes ammonia surface reaction at 800 K; after (a), ammonia gas with a flux of 5.7×10^{15} molecules cm^{-2} s^{-1} was dosed on the surface for 10 minutes at 300 K and the Auger spectrum obtained after the adsorption is shown in (b); the difference spectrum (b)-(a) is shown in (c).

adsorb ammonia at room temperature.

7.2.7. Electron stimulated adsorption of ammonia

The effect of electron beam stimulation on ammonia adsorption was studied on the inert surface produced by ammonia reaction at 800 K. The results are plotted in figure 7-9 and show that, under constant ammonia gas pressure and continuous electron beam bombardment, the nitrogen Auger peak-to-peak height increases with time, and saturates at a level ~3 times higher than the initial value. The rate of adsorption depends on ammonia partial pressure, the higher the ammonia partial pressure, the shorter the beam time required to reach saturation.

7.2.8. Annealing of the NH_3/W(100) surface

Annealing profiles have been measured for both the fully- and half-covered nitrogen on W(100) surfaces produced at 300 K. The nitrogen fully-covered surface was generated by electron stimulated ammonia adsorption at 300K, and the half-covered surface was generated by ammonia adsorption at 300K without electron beam stimulation. The W(NNN) and N(KLL) Auger spectra were recorded after the background pressure in the chamber was reduced to 10^{-9} torr. At each temperature, the sample was annealed at constant temperature for 10 minutes in vacuum, and the W(NNN) and N(KLL) Auger spectra were taken at room temperature. The anneal profiles are shown in figure 7-10. After low temperature annealing, below 600 K, both the tungsten and nitrogen Auger peaks show slight increases with annealing temperature for both the fully- and half-

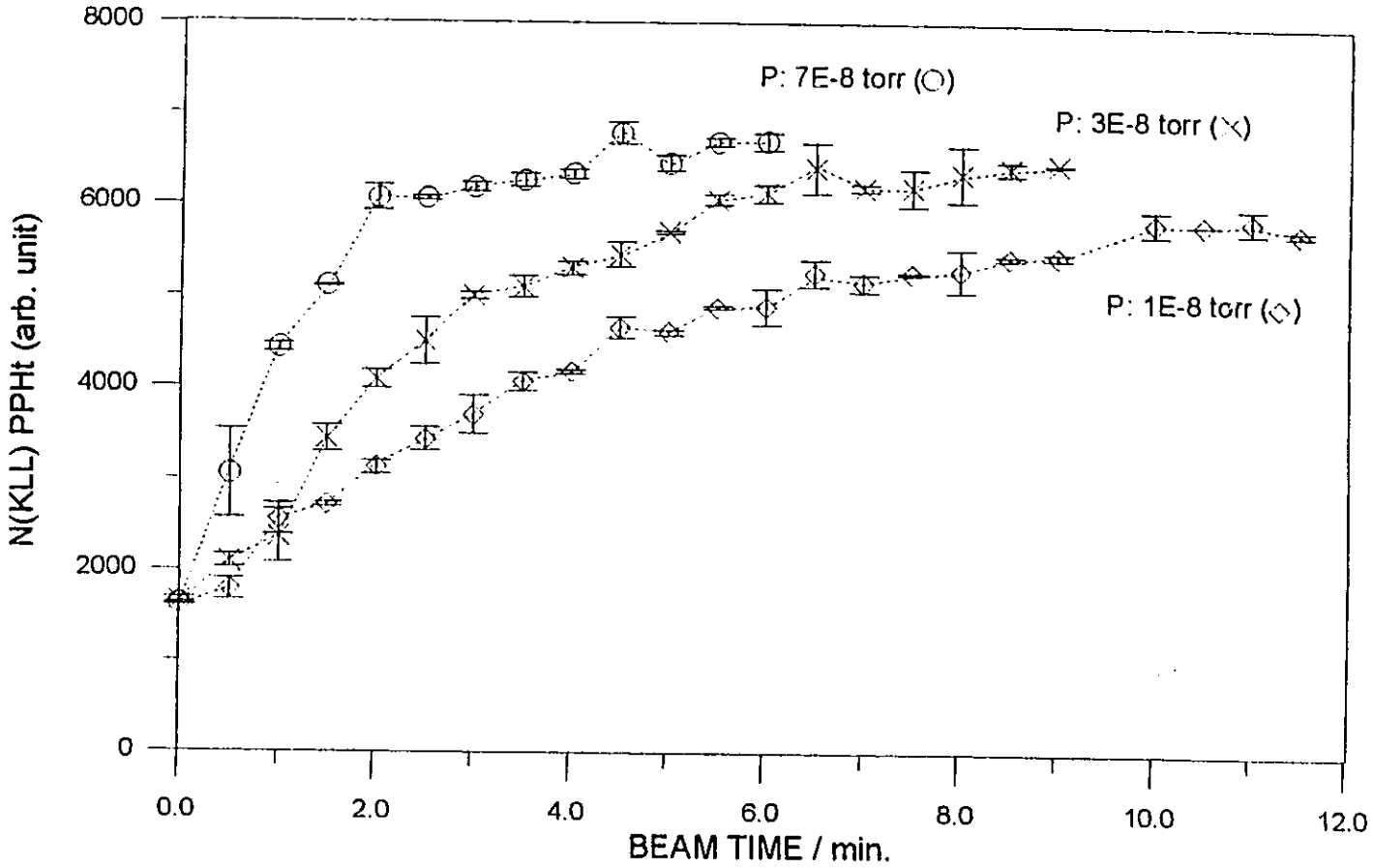

Figure 7-9. The effect of electron beam stimulation on adsorption at 300 K was examined for the W(100) surface after 800 K ammonia reaction. The N(KLL) peak-to-peak height is plotted against beam time. In this experiment ammonia gas was introduced into the chamber and kept at constant pressure dynamically, and the surface was monitored by AES continuously.

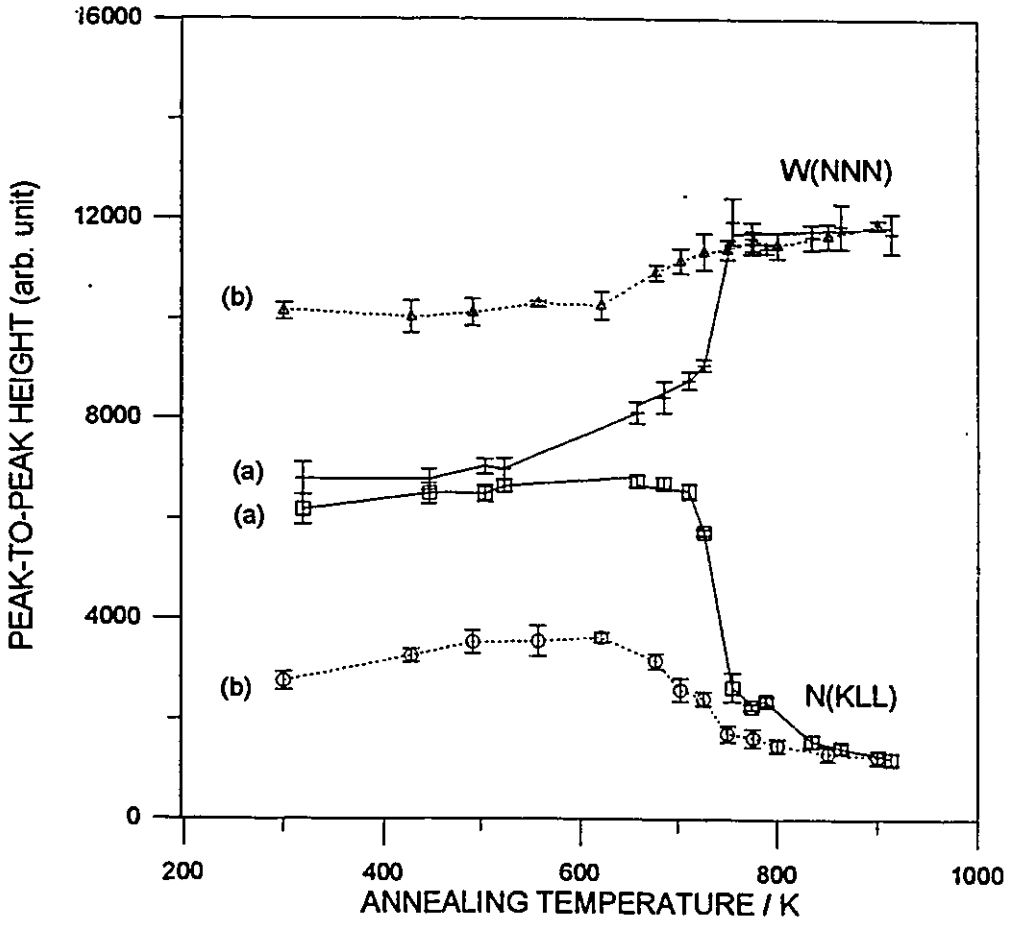

Figure 7-10. Annealing profiles of W(100) for two nitrogen coverages. The high coverage sample (a) was prepared by electron beam stimulated ammonia adsorption at 300 K and its annealing profiles are shown with solid lines. The low coverage sample (b) was prepared by ammonia adsorption at 300K without electron beam stimulation and its annealing profiles are shown with dashed lines. At each annealing temperature, the sample was held at constant temperature for 10 minutes in vacuum and an Auger spectrum was taken after the sample was cooled to room temperature.

covered surfaces. For the high-coverage surface, (a), at ~700 K, the nitrogen peak-to-peak height decreases and that of tungsten increases with annealing temperature. The transition happens over a narrow temperature range, such that the nitrogen peak-to-peak height at 750 K decreases three fold from that at 700 K. Following an inflection in the nitrogen curve, the curves reach another stable state with low nitrogen peak-to-peak height and high tungsten peak-to-peak height. A similar transition is also shown for the low-coverage surface, (b), but this occurs over a wider temperature interval, starting at ~ 620 K and ending at ~750 K.

To investigate the transition process, kinetic studies were performed on the fully-covered nitrogen on W(100) surface, and the data are shown in figure 7-11. In this figure, the fractional extent of the transition, x, is plotted versus time for different substrate temperatures, where,

$$x = \{[PPHt]_{HS} - [PPHt]_t\}/\{[PPHt]_{HS}-[PPHt]_{LS}\}. \qquad (7\text{-}1)$$

In this equation, [PPHt] is the nitrogen peak-to-peak height. The subscript HS identifies the state before the transition with a high nitrogen peak-to-peak height value, LS identifies the state after the transition with a low nitrogen peak-to-peak height value, and t identifies the measured value at time t. The fractional advancement of the transition, x is plotted against annealing time in figure 7-11 for five sample temperatures, 687, 707, 716, 736 and 755 K. The time required for the transition to reach 90% completion at these temperatures has been plotted versus 1/T in figure 7-12 and indicates an activation energy for the process of 256 kJ mol^{-1} K^{-1}.

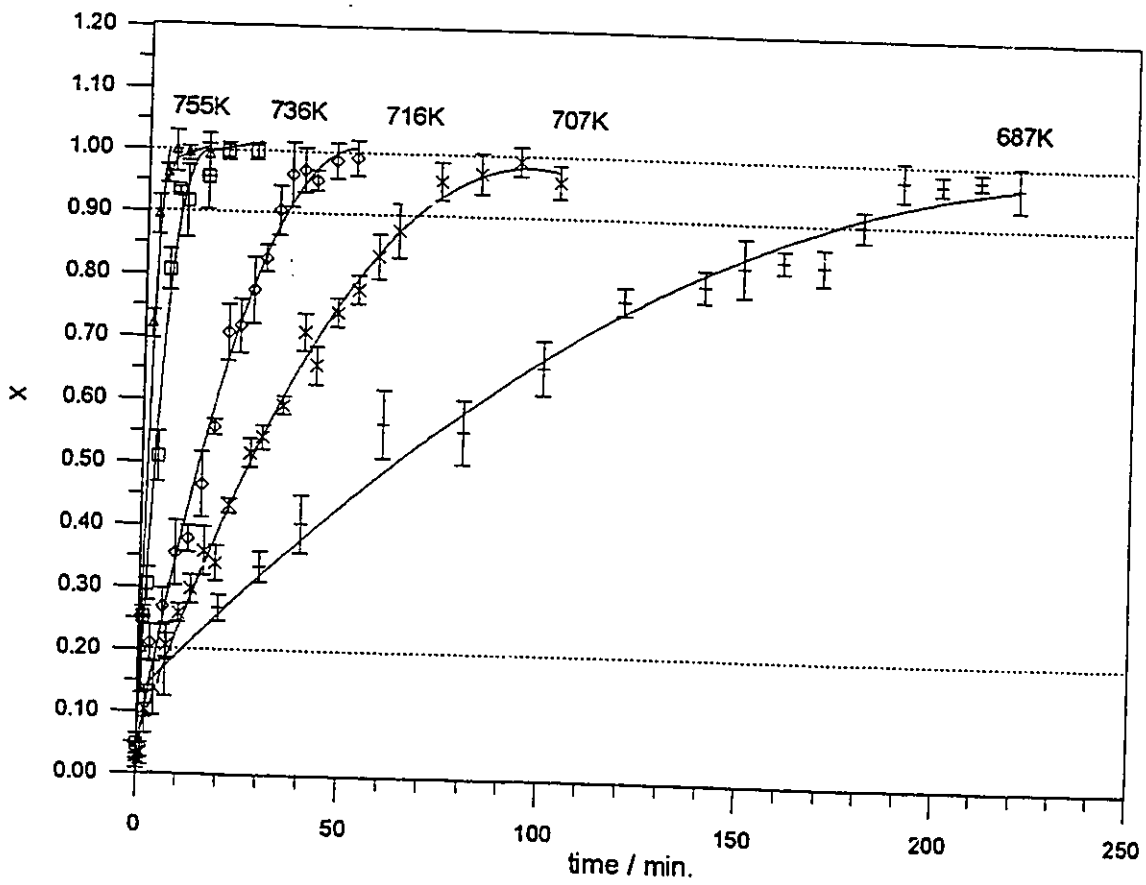

Figure 7-11. The fractional advancement of the transition, x, is plotted against annealing time at constant temperature, where x is defined by equation 7-1.

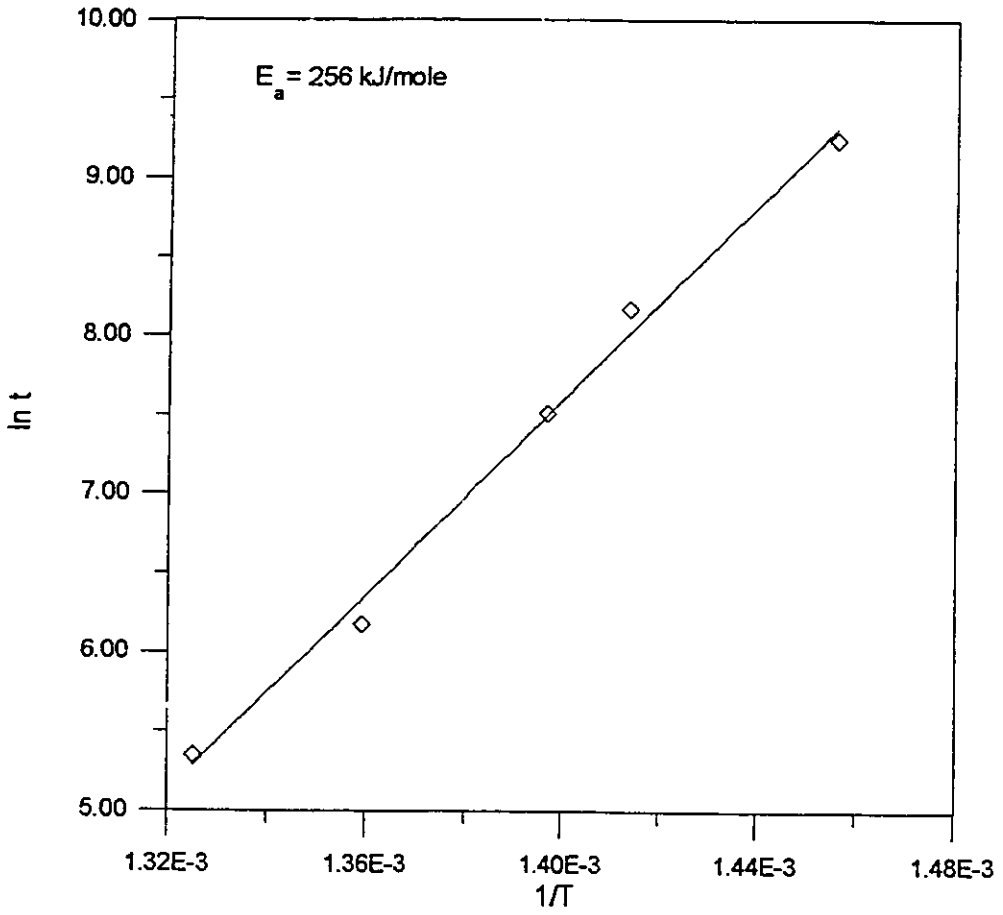

Figure 7-12. A plot of lnt against 1/T, where t is the time required to achieve 90% completion at temperature T. The activation energy for the transition process was calculated from the slope as 256 kJ mol^{-1}.

7.2.9. LEED patterns resulting from the interaction of NH_3 with the W(100) surface

Low energy electron diffraction (LEED) experiments were performed on nitrogen covered W(100) surfaces under the exact same conditions as for the annealing profiles, figure 7-10. The LEED patterns observed on annealing the nitrogen half-covered surface at a primary beam energy of 200 eV are shown in figure 7-13 (b)-(h). The beams observed in the LEED patterns, shown in figure 7-13, are indexed in figure 7-14 (a)-(d). Figure 7-13 (a) shows the (1x1) LEED pattern from the clean W(100) surface. The view of the centre and the lower right part of the screen is blocked by the sample holder and heaters. Thus the 00, 01, $0\bar{1}$ and $\bar{1}\bar{1}$ beams are obscured. Ammonia was dosed on the sample surface at 300 K with a gas flux 5.7×10^{15} molecules $cm^{-2} s^{-1}$. for 10 minutes. Since no electron beam exposure occurred during the adsorption, a half-covered surface was produced. After pumping down to a background gas pressure of 1×10^{-9} torr, the sample was turned from the dosing position to analysis position and examined by LEED. The pattern, figure 7-13 (b), shows an unchanged (1x1) pattern after ammonia adsorption but with a diffuse background. Annealing the surface in vacuum at 600 K for 10 minutes produces a P(4x1) pattern, figure 7-13 (c). The LEED pattern taken after 700 K annealing shows the same P(4x1) pattern with sharper spots, figure 7-13 (d). After 750 K annealing, the LEED pattern is complex, figure 7-13 (e), with extra (1/2, 1/2) features appearing while the 1/4 fractional beams are still present. The same pattern is observed after further annealing at 800 K, figure 7-13 (f). Annealing the sample to higher temperature, 850 K, for 10 minutes results in a C(2x2) LEED pattern characterized by the (1/2, 1/2) order beams, figure 7-13 (g). This same pattern is also observed after 900 K annealing, figure

Figure 7-13. LEED patterns observed with an electron beam energy of 200 eV from a low nitrogen coverage W(100) sample, prepared by ammonia adsorption at 300 K. (a) the clean W(100) surface; (b) after ammonia adsorption with a gas flux 5.7×10^{15} molecules cm^{-2} s^{-1} for 10 minutes; (c) after 600 K annealing; (d) after 700 K annealing; (e) after 750 K annealing; (f) after 800 K annealing; (g) after 850 K annealing; and (h) after 900 K annealing. At each temperature the sample was annealed in vacuum for 10 minutes.

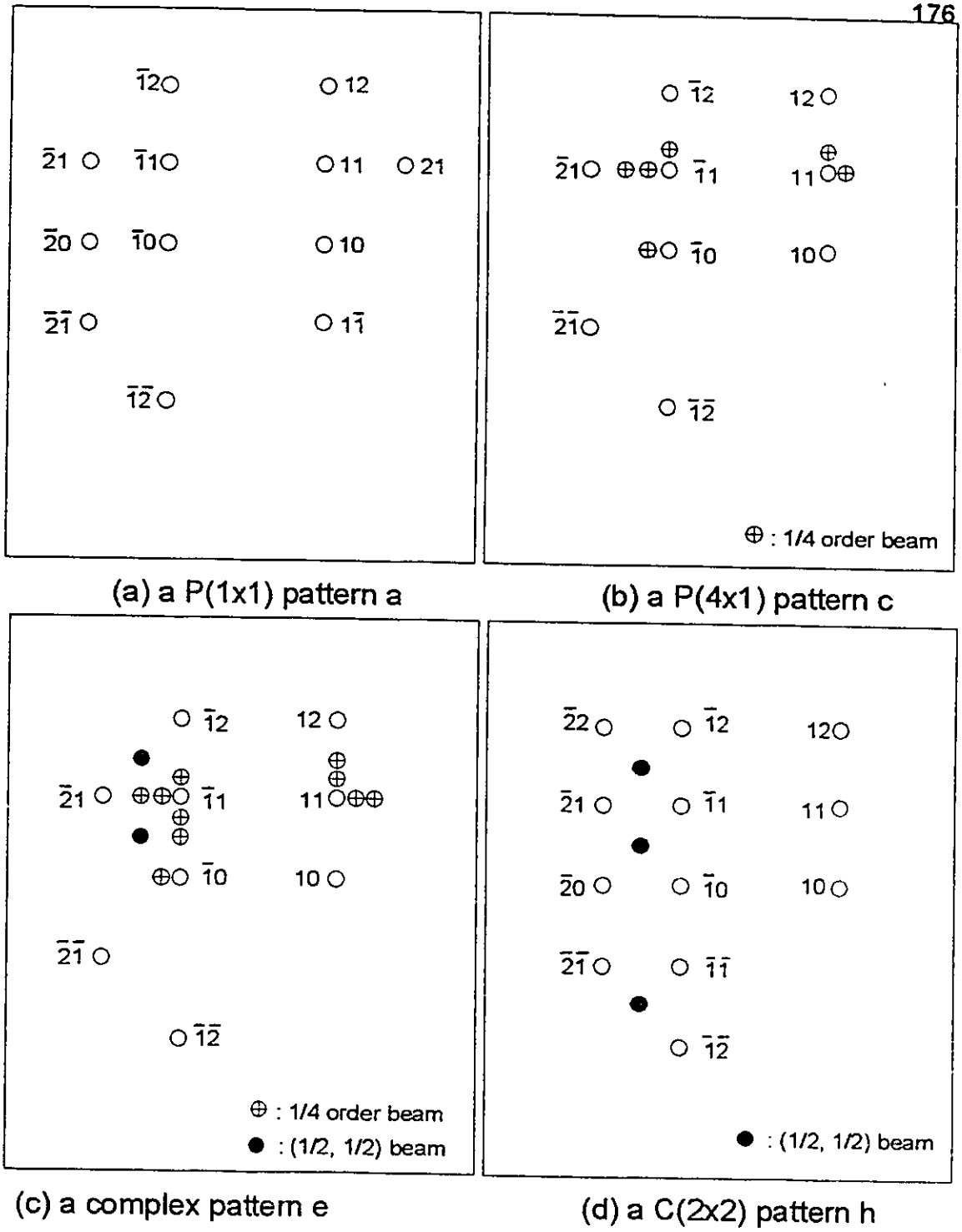

Figure 7-14. LEED beam indexing: (a) for pattern a, (b) for pattern c, (c) for pattern e, and (d) for pattern h shown in figure 7-13.

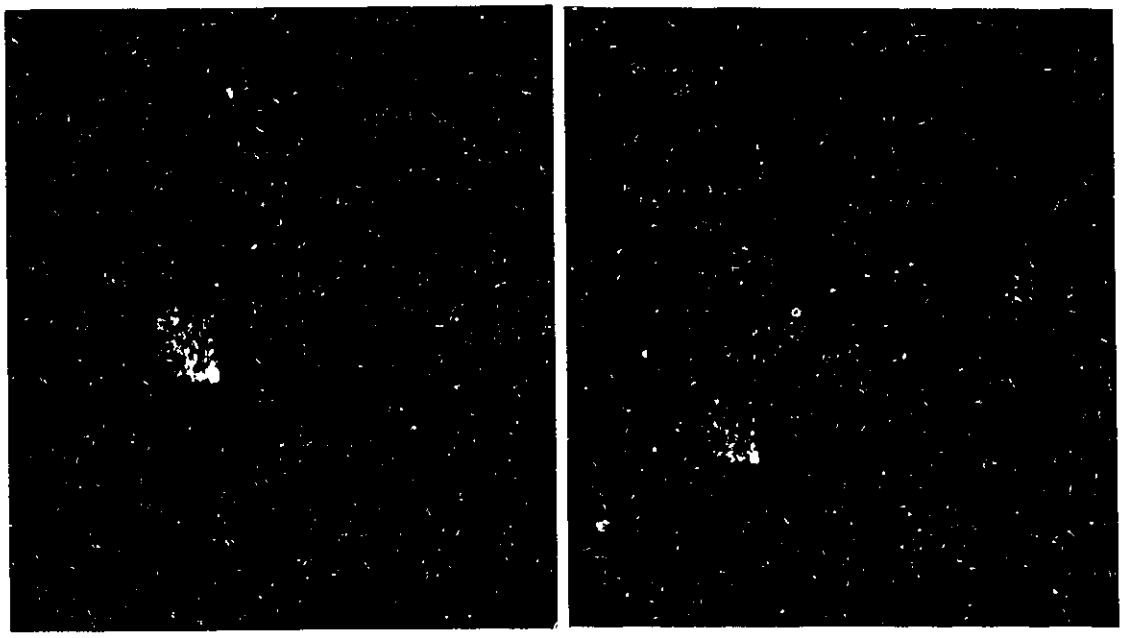

(a) after 700 K annealing (b) after 750 K annealing

Figure 7-15. LEED results with a beam energy of 200 eV from a fully-covered nitrogen on W(100) surface prepared by electron beam stimulated ammonia adsorption at 300 K. (a) after 700 K annealing; (b) after 750K annealing.

7-13 (h).

LEED experiments were also carried out in the same manner for the fully-covered nitrogen on W(100) surface prepared by electron beam stimulated ammonia adsorption. After the electron beam stimulated adsorption, the LEED experiment showed only a bright background and this continued even after high temperature annealing. A few spots from the (1x1) lattice start to be seen after 700 K annealing, figure 7-15 (a), and although the background is still bright, the 1/4 fractional beams indicating a P(4x1) structure, can be recognized after 750 K annealing, figure 7-15 (b).

7.3. DISCUSSION OF THE AES STUDIES OF AMMONIA ADSORPTION ON W(100), W(110) AND W(111) SURFACES

7.3.1. Determination of surface composition in the N-W system

As discussed in Chapter 3, the most accurate method for quantitative surface analysis with AES is through the use of well characterized standards. The cleaning procedure for tungsten samples involves high temperature oxygen treatment to burn out carbon impurities followed by annealing at ~2000 K to decompose surface oxide. Since tungsten nitride decomposes at a relatively low temperature, ~800°C, it is difficult to obtain an impurity-free tungsten nitride standard sample for the purpose of composition calibration. For submonolayer coverage, the ratio of the intensity of N(KLL) Auger peak to the extremely small W(NNN) Auger peak at 350 eV has been used to measure the surface concentration of nitrogen atoms [Housley and King, 1977; Somerton and King, 1979]. Reed and Lambert [1984] have pointed out that this method is unreliable for the following reasons: first of all, the tungsten peak attenuates significantly with increasing nitrogen overlayer density; more importantly, of the three most intense nitrogen Auger transitions, (KL_1L_1) at 357 eV, ($KL_1L_{2,3}$) at 366 eV, and ($KL_{2,3}L_{2,3}$) at 387 eV, the first overlaps significantly with the tungsten 350 eV peak, figure 7-2. Finally, the line shape of the 357 eV nitrogen peak changes during nitriding. These facts make the intensity of 350 eV peak unreliable for use as a straightforward reference peak in determining nitrogen concentration. The problem is similar to that of N-Ti AES spectrum, where the nitrogen peak overlaps with titanium 384 eV peak. The calculation based on an

assumption of constant titanium peak ratios produces anomalous nitrogen peak heights, as discussed in section 5.4.3.

As the W(NNN) Auger peaks in the energy range 150-180 eV are much stronger than the 350 eV peak, and do not overlap with any nitrogen peak, they have been used in this study. Table 7-1 shows that the magnitudes of the W(NNN) peaks from the three tungsten single crystal surface, W(100), W(110) and W(111) are different. The strongest magnitude is obtained from W(110) surface and the weakest from W(111) surface. Drawings of the surface structures for W(100), W(110) and W(111) are shown in figure 7-16. The atomic densities and the distances between two nearest-neighbour atomic planes for these three orientations are also given in figure 7-16. The greater the atomic density of the plane the greater is the planar spacing for that orientation as required for a constant bulk density. Since the Auger signal from the outermost layer has the greatest contribution to the total peak intensity, one can expect a higher Auger peak intensity from the crystal orientation with a higher layer atomic density. The experimentally determined intensities for the three crystal orientations, table 7-1, do increase in the sequence of increasing planar atomic density.

The variation in intensity of the W(NNN) Auger peaks in the 150 to 180 eV energy range and the N(KLL) peak at 387 eV, i.e. the nitrogen ($KL_{2,3}L_{2,3}$) transition, have been used to determine surface composition changes during the interaction of ammonia with tungsten surfaces.

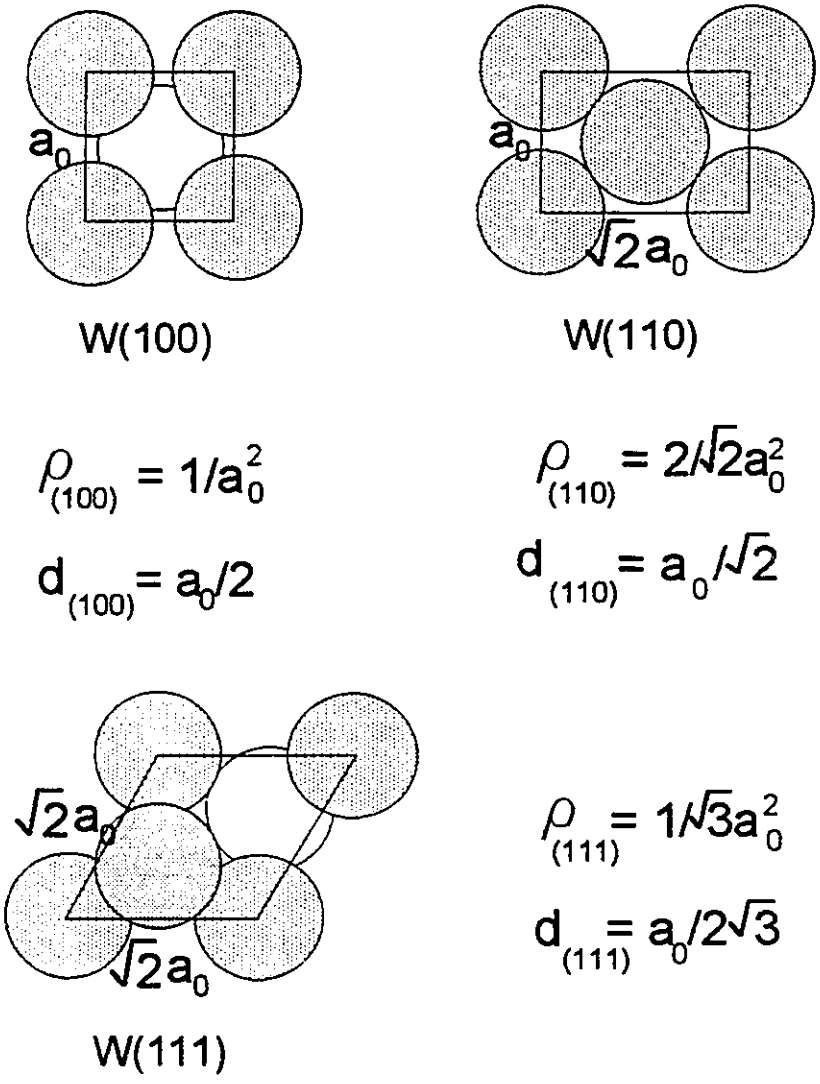

Figure 7-16. A scale drawing of the W(100), W(110) and W(111) planes; the planar atomic density, ρ, and the distance between the nearest planes, d, for these three orientations are given.

7.3.2. Ammonia adsorption on W(100), W(110) and W(111) surfaces at 300K and the effect of electron beam stimulation

The ammonia adsorption behaviour on the W(100), W(110) and W(111) surfaces at 300 K is similar to that observed on the polycrystalline tungsten sample, section 5.3.1. Comparing the nitrogen KLL peak-to-peak heights (not peak ratios) listed in table 7-2 and table 7-3, it is apparent that the saturation nitrogen uptake can be raised by a factor of ~2 with electron beam stimulation during ammonia adsorption on all three low index tungsten single crystal surfaces. Since the bulk diffusion of nitrogen atoms is not likely to happen at 300 K, we assume that ammonia adsorption at 300 K without electron beam bombardment leads to a nitrogen half-covered surface, and a nitrogen fully-covered surface can be generated by electron stimulated ammonia adsorption.

The attenuation, $\{[PPHt_W]-[PPHt_{W(N)}]\}/[PPHt_W]$, of the W(NNN) peaks at 150-180 eV with increasing surface coverage is obvious, table 7-1 to 7-3. For a half monolayer coverage, it attenuates ~19% on W(110), ~18% on W(100), and ~13% on W(111); for a monolayer coverage, it attenuates ~55% on W(110), ~50% on W(100) and ~40% on W(111) surfaces. The attenuation decreases with decreasing surface W atom density of the plane.

The inelastic mean free path of Auger electrons can be estimated from the attenuation of the tungsten signal. The relative Auger signal intensities contributed by the first 10 layers calculated with different electron inelastic mean free path values are listed in table 7-5. The summation of the intensities for the first 10 layers produces a total intensity of $2.05I_0$ if λ_m=1.5 monolayer, and $2.52I_0$ for λ_m=2 monolayer. Consequently,

Table 7-5. Relative contributions from the zth and 0th layers, I_z/I_0 calculated with different inelastic electron mean free path values, λ_m.

I_z/I_0 λ_m / z	1	1.5	2	2.5	3
0	1.00	1.00	1.00	1.00	1.00
1	0.37	0.51	0.61	0.67	0.72
2	0.14	0.26	0.37	0.45	0.51
3	0.05	0.14	0.22	0.30	0.37
4	0.02	0.07	0.14	0.20	0.26
5	0.01	0.04	0.08	0.14	0.19
6	0.00	0.02	0.05	0.09	0.14
7		0.01	0.03	0.06	0.10
8		0.00	0.02	0.04	0.07
9			0.01	0.03	0.05
ΣI_z	1.59	2.05	2.52	2.98	3.41

where z is the depth in monolayers; λ_m is the inelastic electron mean free path in monolayers; I_z/I_0 is the relative intensity of Auger signal contributed by zth layer, calculated from $I_z/I_0 = \exp(-z/\lambda_m \cos\theta)$, simplified by using $\theta=0$.

fully covering the tungsten atoms in the outermost layer will cause 1/1.59, i.e. ~0.63 peak attenuation for λ_m=1 monolayer, 1/2.05, ~50%, for λ_m=1.5 monolayer, and 1/2.52, ~40%, for λ_m=2 monolayer. Therefore, the estimated λ_m value for these three single crystal orientations is 1.5 to 2 monolayers. The experimental data show an attenuation length of 1.5 monolayers for the W(100) plane and 2.0 monolayers for W(111). However, since the monolayer spacing for the (100) plane is $\sqrt{2}$ times that for the (111) plane, these correspond to very similar inelastic mean free paths. The success of this correlation suggests that more accurate data might further our understanding of electron attenuation and further improve the accuracy of surface analysis in the N-W system.

7.3.3. Comparison of Auger spectra from ammonia adsorbed and ion implanted into W(100)

Figure 7-4 shows the Auger spectrum of fully-covered nitrogen on the W(100) surface prepared by electron beam stimulated ammonia adsorption, (a), and the spectrum of an NH_3^+ ion implanted W(100) sample, (b). Spectra (a) and (b) show the same magnitude for the N(KLL) Auger peaks, but a large difference in the magnitude of the W(NNN) Auger peaks. The ion implanted sample has a much larger W peak. The nitrogen atoms from electron stimulated ammonia adsorption will be situated in the outermost layer of the sample, but with 2 keV ion implantation, they will be implanted into the tungsten lattice, and distributed throughout a deeper surface zone. Thus, although the intensities of the N(KLL) Auger peaks in spectrum (a) and (b) are of the same magnitude, they represent different nitrogen depth distributions. For spectrum (a), the

peak intensity is contributed solely by the Auger signal from the outermost layer, while for spectrum (b), it is contributed by several layers,

$$I = \sum n_z I_z = n_0 I_0 + n_1 I_1 + n_2 I_2 + \ldots \ ,$$

where n_z is the nitrogen concentration in zth layer, and I_z is the attenuated intensity of Auger signal contributed by nitrogen atoms in the zth layer. The large intensity of W(NNN) Auger peaks observed in spectrum (b) suggests that the tungsten atoms in the outermost layer of the ion implanted sample are not covered, and n_0 is close to zero. This is a surprising result since one would expect a surface saturated by adsorption for the following reason. During the ammonia ion implantation experiment, ammonia gas filled the chamber to a pressure of 5×10^{-5} torr. After the ion beam was turned off, the sample was still in an ammonia-rich environment for more than ten minutes before AES analysis because of the slow pumping speed of ammonia gas. This was necessary to prevent electron stimulation effects during analysis. This observation suggests that the nitride thin film surface, made by ammonia ion implantation of W(100) is inert to ammonia adsorption. This behaviour is echoed by that of the surface prepared by reaction with ammonia gas at 800 K.

7.4. DISCUSSION OF THE RESULTS FROM TUNGSTEN SINGLE CRYSTAL SURFACES AFTER AMMONIA REACTION AT 800K

7.4.1. Depth profiles after ammonia surface reaction on W(100), W(110) and W(111) at 800 K

It is a surprise to see that the nitrogen Auger peak intensities obtained after one hour ammonia reaction at 800 K, table 7-4, are no greater than for a saturated surface produced by ammonia adsorption at 300 K on these three tungsten single crystal surfaces, table 7-2. Furthermore the nitrogen intensities after 800 K reaction are much less than those for the fully-covered surfaces obtained by electron stimulated adsorption at 300 K, table 7-3. The nitrogen depth distributions revealed by sputter profiling, figure 7-5, show strong crystallographic orientation effects. Two calculated nitrogen sputter depth profiles for different nitrogen distribution models are shown in figure 7-17. Model (a) has nitrogen atoms distributed only in underlayers, whereas model (b) has nitrogen atoms distributed from the outermost layer. In the calculation, the measured profile is

$$I(z) = \int c(z)g(z)dz, \qquad (7\text{-}2)$$

where I(z) is the measured profile, c(z) is the true profile and g(z) is the resolution function. In the resolution function, the escape depth effect of Auger has been considered as

$$I_z = I_{z=0} \sum n(z)\exp[-z/\lambda_m],$$

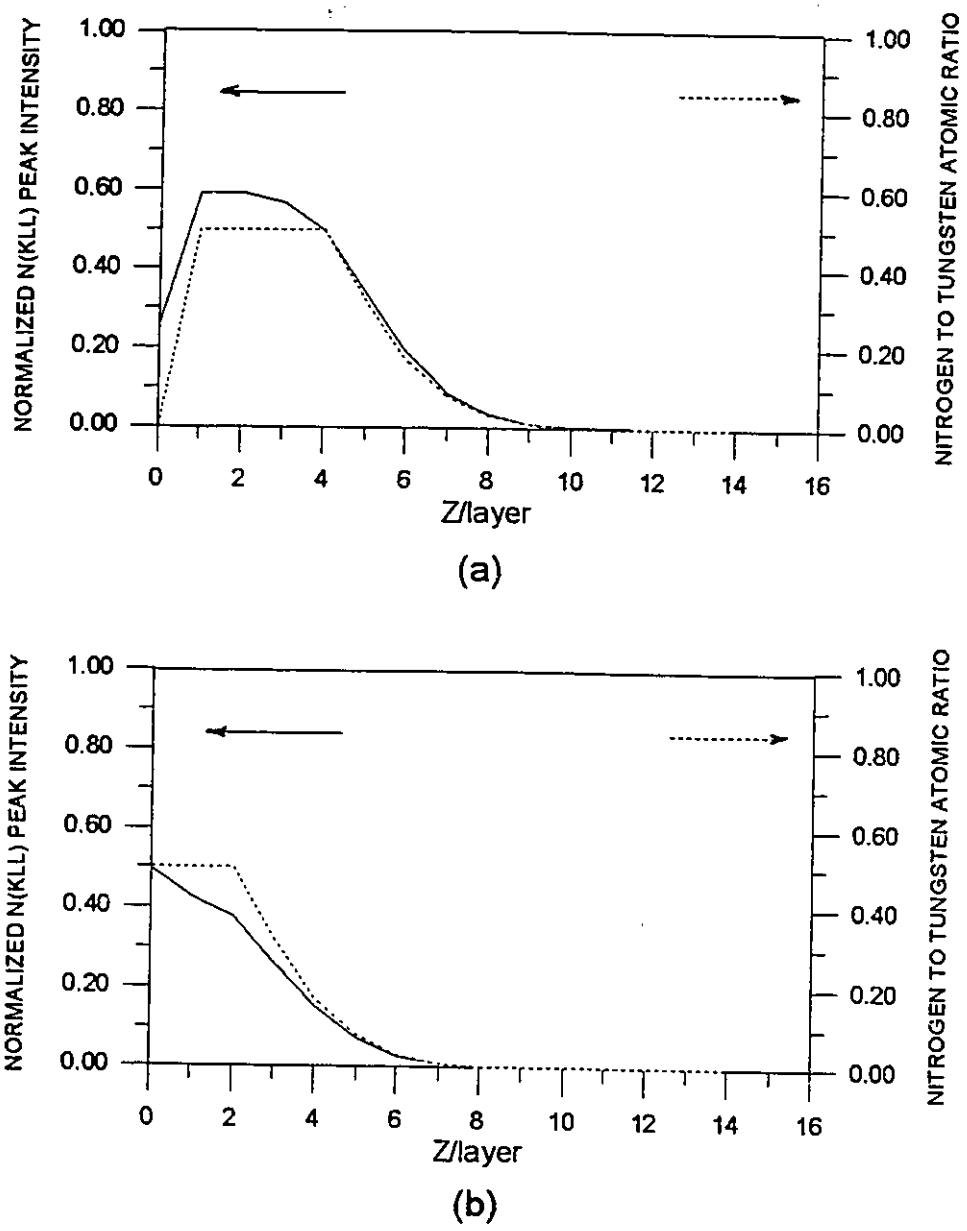

Figure 7-17. Calculated sputter depth profiles for (a) a nitrogen underlayer distribution model, and (b) a nitrogen overlayer model are shown with solid lines. The initial nitrogen distribution models are shown with dashed lines.

and all the other profile distortion effects, such as atomic mixing, enhanced diffusion and sputtering-induced roughness etc., are corrected by an error function [1-erf(z/Δz)], where Δz is the broadening of the measured profile. Comparing the experimental depth profiles, figure 7-5, with the model calculations, it is apparent that on W(111), nitrogen atoms are distributed from the outermost layer, while on W(100), the nitrogen atoms are restricted to the underlayers. The depth profile of W(110) fits neither of these two models, and is possibly a hybrid.

7.4.2. The Auger results with normal and glancing incidence electron beams

Auger analysis with glancing primary beam incidence increases the sensitivity of Auger electron spectroscopy to outer surface atoms [Palmberg, 1969], thus variation of the angle of incidence can be used to obtain an indication of the atom positions in the direction normal to the surface [Sormerton and King, 1979]. An increase of primary beam incidence angle from 0 to β will change the effective interaction length of the beam with the sample surface from d to D, figure 7-18. If the incident

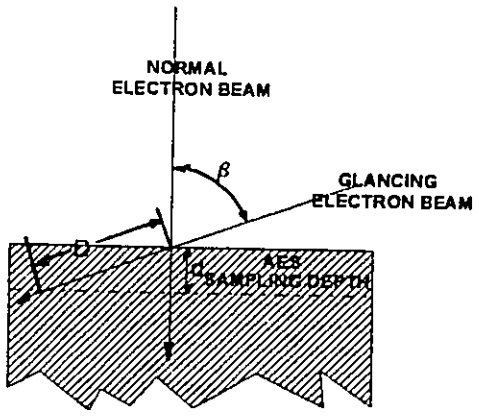

Figure 7-18. The effective interaction length of a primary beam with a sample surface for normal and glancing incidence.

electrons maintained their initial direction during passage through the first 10 Å of the surface, the magnitude of all Auger peaks vary of $\cos^{-1}\beta$ with incident beam angle β [Palmberg, 1969], i.e. D/d. The decay of primary beam with depth, z, is

$$I_z/I_{z=0} = \exp(-z/\lambda_p\cos\beta), \qquad (7\text{-}3)$$

where λ_p is the inelastic electron mean free path of the primary beam. With normal beam incidence, $\beta=0$,

$$[I_z/I_{z=0}]_{\beta=0} = \exp(-z/\lambda_p). \qquad (7\text{-}4)$$

For pure tungsten, the ratio of the peak intensity obtained with the glancing electron gun, I_G, to that with a normal electron gun, I_N, can be written as

$$R_W = I_G/I_N = k'_W\cos^{-1}\beta \int_0^\infty \exp(-z/\lambda_p\cos\beta)dz \,/\, k_W \int_0^\infty \exp(-z/\lambda_p)dz. \qquad (7\text{-}5)$$

It has been reported [Chambers et al., 1986; Armitage et al., 1980; Andersen and Howie, 1975] that the change in AES sensitivity with primary beam incidence angle has other contributions such as back-scattering, diffraction etc. In equation 7-5 all these factors affecting the sensitivity are represented by k'_W and k_W for glancing and normal beam incidence respectively. Integration of the above equation produces a constant, dependent only on the magnitudes of k' and k,

$$R_W = k'_W\lambda_p\cos\beta \,/\, k_W\lambda_p\cos\beta = k'_W / k_W = K. \qquad (7\text{-}6)$$

For a tungsten sample with nitrogen atoms distributed only in underlayers, figure

7-19 (a) , the above analysis is still valid, which gives

$$R_{WN} = k'_{WN} / k_{WN} = K'. \qquad (7\text{-}7)$$

If the matrix properties are dominated by tungsten, a reasonable expectation, then K' will equal K, and

$$R_{WN} / R_W \approx 1. \qquad (7\text{-}8)$$

For a model assuming a nitrogen-covered tungsten surface, figure 7-19 (b), the ratio of peak intensity obtained with the glancing electron gun, I_G, to that of with a normal electron gun, I_N, becomes

$$R_{WN} = I_G/I_N = k'_W \cos^{-1}\beta \int_0^\infty \exp(-z+D/\lambda_p \cos\beta)dz \,/\, k_W \int_0^\infty \exp(-z+D/\lambda_p)dz, \qquad (7\text{-}9)$$

where D is the diameter of a nitrogen atom. The integration of equation (7-9) produces

$$R_{WN} = K \exp[-D/\lambda_p(\cos^{-1}\beta - 1)], \qquad (7\text{-}10)$$

and with incidence angle $\beta > 0$, $\qquad R_{WN} < R_W$. $\qquad (7\text{-}11)$

According to the analysis above, by comparing R_{WN} with R_W, i.e. the ratio of *tungsten* Auger peak magnitudes, one can determine whether the *nitrogen* atoms are situated on the outermost layer or in an underlayer. The results, figure 7-7 (a) and (b), show that $R_{WN} \approx R_W$ for W(100), which means that the outermost layer of tungsten atoms is uncovered, while for W(111), the R_{WN} value is significantly smaller than R_W, suggesting a high coverage on the outermost layer. For W(110), the R_{WN} value is smaller than R_W, but the difference is smaller than that on W(111). The result obtained for a fully-covered

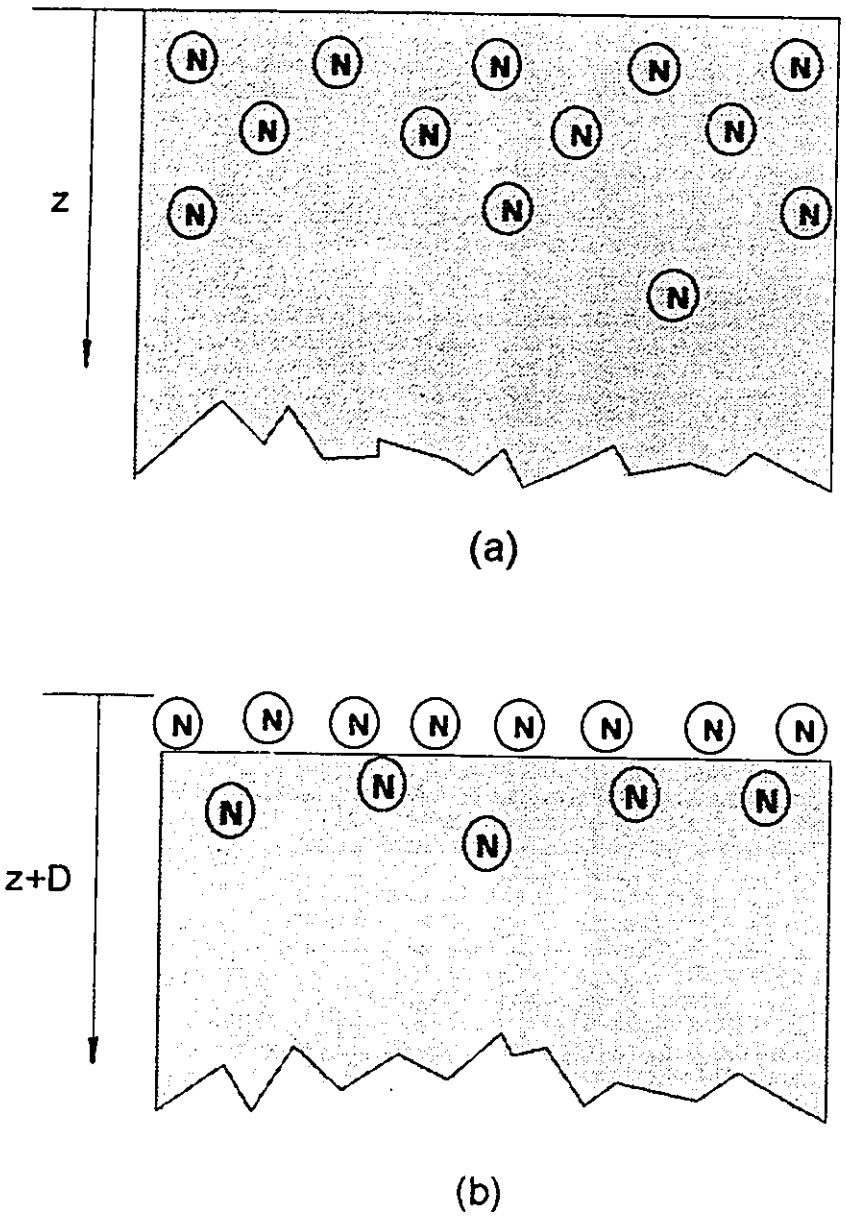

Figure 7-19. A drawing of (a) the nitrogen underlayer distribution model, and (b) the nitrogen overlayer model.

W(100) surface at 300 K, figure 7-7 (c), shows that once the surface is covered, the R_{WN} value indeed becomes smaller than R_W as expected.

The results of Auger analysis with normal and glancing incidence of the primary electron beam are consistent with the sputter depth profiles. The analysis confirms that after ammonia surface reaction at 800 K, nitrogen atoms are located on the outermost layer of W(111), but on W(100) the surface is bare and nitrogen sorption is restricted to the underlayers. Results from depth profiles and the AES analysis with different beam incidence show that the nitrogen distribution on W(110) is in a mode between that for W(100) and W(111) with nitrogen atoms distributed in both the sub-surface and on the outermost surface. An underlayer model for N/W(110), from nitrogen adsorption, has been proposed by Somerton and King [1979] based on the results of angle resolved AES experiments. They found that the chemisorbed nitrogen adatoms on the close-packed W(110) plane did not occupy conventional overlayer sites, but are sandwiched between the top two layers of tungsten atoms.

It is worth pointing out that the different structure of the sorption layers on the W(111) and W(110) surfaces from that on W(100) is possibly kinetic in origin. After a prolonged interaction at 800 K on the (111) and (110) planes the nitrided sub-surfaces may also be inert in these orientations just as was found after one hour for the W(100) surface.

The results discussed so far show that, for the W(100) surface, a fully-covered

nitrogen adlayer at 300 K is an overlayer structure whereas reaction at 800 K produces an underlayer structure. Information about such an "overlayer" to "underlayer" transition might be obtained by a careful analysis of the experiments in which the adsorbed layer produced at 300 K is annealed to progressively higher temperatures, figure 7-10. Since LEED pattern changes were observed in these experiments, some insight may be provided into the geometry of the structural transition.

7.5. DISCUSSION OF THE NATURE OF THE TRANSITION PROCESS OBSERVED ON N/W(100)

7.5.1. Anneal profile of NH_3/W(100)

The inactivity towards ammonia adsorption of the W(100) surface after high temperature ammonia treatment is extremely interesting. It also has very important implications for the mechanism of nitride thin film growth. The annealing profiles for the NH_3/W(100) sample, figure 7-10, show a transition beginning at ~700 K for high ammonia coverage and at ~620 K for low ammonia coverage, in which the nitrogen and tungsten Auger signals decrease and increase, respectively, over a narrow temperature range. There are two processes which could cause these changes of Auger signal intensity, either nitrogen thermal desorption or a reconstruction of the nitrogen adlayer.

7.5.2. Nitrogen thermal desorption studies

7.5.2.1. On nitrogen half-covered tungsten surface

Thermal desorption of nitrogen from tungsten surfaces has an extensive literature [Estrup and Anderson, 1968; May et al., 1969; Yates and Madey, 1969; Peng and Dawson, 1970; 1972; Clavenna and Schmidt, 1970; Sellidj and Erskine, 1989]. Estrup and Anderson [1968] showed that the nitrogen thermal desorption spectrum from the W(100) surface saturated by ammonia adsorption at 300 K only has one nitrogen desorption feature, and the calculated nitrogen coverage from the peak area is approximately

equivalent to a half-monolayer. As they found simultaneous hydrogen desorption, the feature was interpreted as a half-monolayer of NH_2. Peng and Dawson [1971] demonstrated that ammonia adsorption on tungsten surface at 300 K only produce one desorption feature, the β-state nitrogen, which has a desorption peak temperature at ~1400K. However they found no simultaneous hydrogen desorption, in disagreement with the previous work. The β-state nitrogen obeys second-order desorption kinetics, and the rate of desorption can be calculated as

$$-dn/dt = \nu n^2 \exp(-E_a/RT), \qquad (7\text{-}12)$$

where ν is the pre-exponential factor, n is the surface coverage and E_a is the activation energy. It was determined by Clavenna and Schmidt [1970] for N/W(100) that

$$\nu = 0.23 \text{ cm}^2 \text{ molecule}^{-1} \text{ s}^{-1},$$

and

$$E_a = 73.5 \text{ kcal mole}^{-1}$$

for a saturated β-state nitrogen coverage, $n = 2.5\times10^{14}$ molecules cm^{-2}. The desorption rates of β-N at 650, 750, and 800 K calculated by equation 7-12 are 2.79×10^{3}, 5.47×10^{6}, and 1.81×10^{9} molecules $cm^{-2}\,s^{-1}$, respectively, and annealing at these temperatures for 10 minutes will cause 1.68×10^{6}, 3.28×10^{9} and 1.08×10^{12} molecules cm^{-2} nitrogen desorb from the surface. It can be concluded that β-N desorption is negligible at these temperatures.

7.5.2.2. On nitrogen fully-covered tungsten surface

Nitrogen desorption at lower temperatures than β desorption has been observed

in the range 800-1200 K and can result from:

(a) adsorption with activated nitrogen or electron bombardment of the low-temperature γ-state nitrogen can produce a desorption feature at lower temperature, which were attributed to a λ-state [Yates and Madey, 1969];

(b) high exposure of nitrogen at 78 K with intermittent heating to 300 K leads to a nitrogen desorption feature at ~900 K and was assigned to β_1-states of nitrogen with desorption peak temperatures at ~900 K [Clavenna and Schmidt, 1970];

(c) adsorption of ammonia on a tungsten surface at 300 K, heating to 800 K to desorb hydrogen, and repeating this procedure several times can lead to a desorption feature in this range [Matsushita and Hansen, 1969; Dawson and Peng, 1970], which were attributed to a δ-state.

Since little precise information as to the chemical stoichiometries and structure of these states can be determined by thermal desorption spectra alone, usually clearly resolved desorption peaks are assigned a letter in the Greek alphabet, and incompletely resolved features are assigned a substate number. Some confusion is caused by the fact that the desorption peak position can shift with coverage, the higher the coverage the lower the temperature [Clavenna and Schmidt, 1970]. Dawson and Peng [1972] pointed out that the δ-state is identical with the λ-state, since the λ-state which can be prepared from nitrogen gas, has desorption features strongly resembling those of the δ-state and the same stoichiometry.

Figure 7-20 shows the thermal nitrogen desorption spectra obtained by Dawson and Peng [1972], where the thermal desorption spectra from activated nitrogen adsorption are compared with those from non-activated nitrogen adsorption. The spectra from non-activated nitrogen adsorption show the well known β-states with peak temperature ~1400 K, and the spectra from activated nitrogen adsorption show desorption features of λ-state nitrogen at lower temperatures superimposed on the β-desorption peak. It can be seen from figure 7-20 that the β-nitrogen peak is actually depleted somewhat as the coverage increases. Dawson and Peng [1972] used several desorption models to fit their fast desorption spectra and found that all demanded considerable depletion of the β-state to achieve a satisfactory fit. The depletion of the β-state can be interpreted by a model assuming immobile nitrogen atoms during λ-nitrogen desorption. Thus, if the rate of desorption is much faster than the rate of migration, and desorption occurs by combination of adjacent nitrogen atom-pairs, this will leave a number of isolated single atoms on the surface, which desorb at much higher temperature as β-nitrogen. Using the immobile adjacent adatom-pair desorption model, the kinetic study of λ-nitrogen provided the following equation for calculating the activation energy for λ-nitrogen desorption,

$$E_{\lambda}(\theta)=E_0 - \alpha\theta, \qquad (7\text{-}13)$$

where E_0= 81 kcal mole^{-1}, and $\alpha \sim 24$ kcal mole. For a full coverage, θ=1, the activation energy calculated from equation 7-13 will be 238 kJ mole^{-1}. The isotope exchange experiments reported by them showed that the population of β- and λ-states with different isotopes led to complete scrambling on desorption, suggesting that both states are atomic

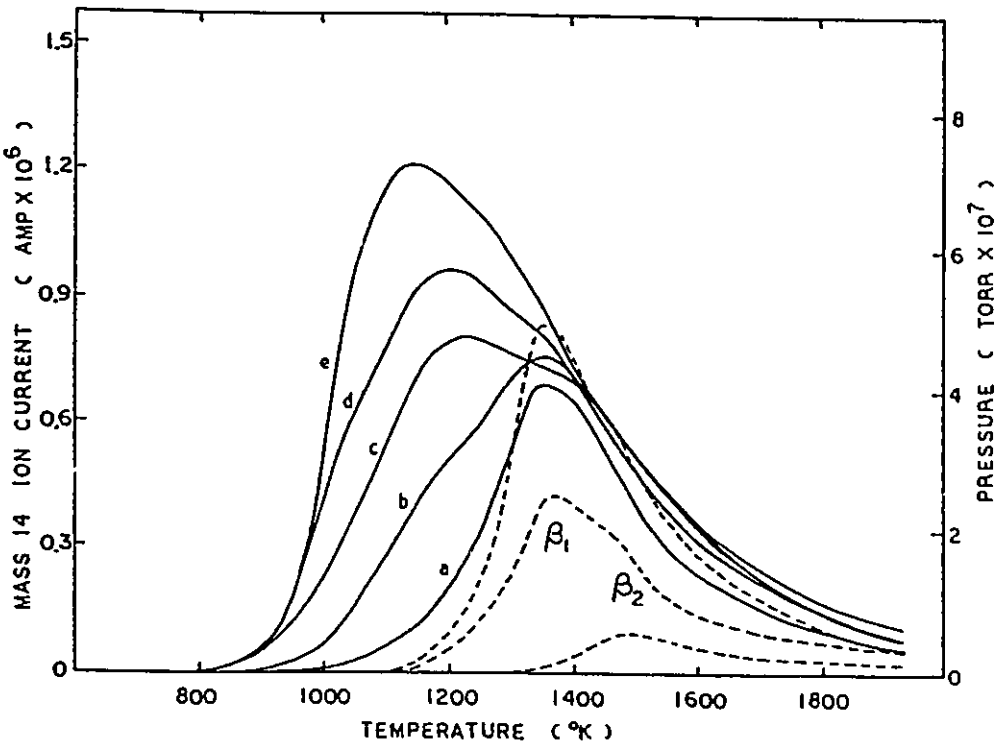

Figure 7-20. Thermal desorption spectra obtained from activated nitrogen adsorption at 300 K for 2, 5, 10, 15, and 30 minutes, curves (a) to (e) respectively. Adsorption of non-activated nitrogen for $6x10^{-7}$, $5x10^{-6}$ and $6x10^{-4}$ torr sec produced the spectra indicated by the dashed curves. The heating rate for the spectra is 18 K s^{-1}. After Dawson and Peng [1972].

and exist on the same crystal planes. Based on this strong experimental evidence, they argued that the β- and λ-states actually represent different desorption mechanisms rather than different desorption states.

As discussed above the high coverage λ-state of nitrogen on tungsten desorbs at lower temperature than the β-state of nitrogen. By using the kinetic parameters determined by Dawson and Peng [1972], the desorption rate of the λ-state of nitrogen at 700 and 750 K can be estimated as 9.2×10^{10} and 1.4×10^{12} molecules $cm^{-2} s^{-1}$, respectively. Desorption would be complete in 10 minutes at 750 K and therefore desorption cannot be ignored for the fully covered surface in the present work. Remarkably, the kinetic study using AES to monitor the depletion of nitrogen on the high coverage tungsten surface, figure 7-12, indicated an apparent activation energy of 256 kJ mol^{-1} for the process, which matches the value of 238 kJ mol^{-1} determined by monitoring the nitrogen partial pressure in gas phase in a thermal desorption experiment [Dawson and Peng, 1972] within a reasonable experimental error. This should not be just a coincidence. It suggests that the desorption of λ-state nitrogen is responsible for the drop in the nitrogen AES signal for the fully-covered surface.

7.5.3. Structures resulting from the interaction of ammonia with the W(100) surface

It is well known that the surface of W(100) easily undergoes reconstruction [Debe and King 1977; Felter et al., 1977; Landskron et al., 1989], which can be induced by temperature changes or interaction with adsorbates [Kankaala et al., 1990; Chabal et al., 1987; Griffiths et al., 1981; Mahan et al., 1980]. The activation energy for the

reconstruction is negligible and the substrate responds readily to changes in temperature or adsorbate coverage [Estrup, 1994].

7.5.3.1. The LEED pattern from the high nitrogen coverage on the W(100) surface

On the high coverage W(100) surface, the LEED beams from the (1x1) lattice start to be seen after 700 K annealing with a very bright background, figure 7-15 (a). It can be seen from the anneal profile, figure 7-10, at this temperature the drop in nitrogen AES signal begins. As discussed in section 7.5.2.2, the desorption rate for λ-state nitrogen at this temperature is high, and so the nitrogen coverage drops to one-half, or less, by desorption. Therefore, it is not surprising that the 1/4 fractional LEED beams, similar to those observed on the half-covered surface, are visible after 750 K annealing. These structural changes will be discussed in the next section.

7.5.3.2. The LEED results from the low-coverage W(100) surface

The LEED pattern from a nitrogen half-covered W(100) surface, figure 7-13 (b) shows that the (1x1) pattern of W(100) is unchanged after ammonia adsorption. It could be interpreted as an ordered (1x1) nitrogen or NH_x lattice on the W(100) surface, but this is in conflict with the coverage determined by Auger. It is known that for high energy electrons the back-scattered intensity falls off rapidly with decreasing atomic number. Germer et al. [1963] and May [1965] assumed that this effect was important also at low energies, so light adsorbates would contribute negligibly to the observed LEED intensity. According to this assumption, the (1x1) LEED pattern with 200 eV primary electron

beam, figure 7-13 (b), still arises from electron scattering contributed by the W atoms.

After annealing to 600 K, a P(4x1) LEED pattern was formed and sharpened in the annealing temperature range 600-800 K, figure 7-13. This implies a structure whose unit cell periodicity is (4x1). This structure could be formed either by the displacement of tungsten atoms or by the ordering of nitrogen adatoms with a (4x1) symmetry. If we consider that the contribution from nitrogen atom to the LEED intensity is negligible compared with that of tungsten atoms, the changes of LEED pattern shown in figure 7-13 really demonstrate the surface structure changes of W(100). In addition to the structural changes revealed by LEED, the annealing profile, figure 7-10, shows that another transition happens within this temperature range, which is characterized by a drop in the nitrogen Auger signal and a corresponding increase in that of tungsten. The annealing temperature at which the 1/4 fractional LEED beams start to appear is lower than that where the drop in nitrogen signal begins, and it still exists even after this drop is complete. This suggests that the surface structure change is responsible for the observed transition in the nitrogen Auger signal intensity. Thermal desorption is negligible, section 7.5.2.1.

A C(2x2) LEED pattern was observed after 850 K annealing, figure 7-13 (g), and the corresponding nitrogen Auger signal intensity is about half of that after 300 K adsorption, figure 7-10. Since the nitrogen desorption caused by 10 minutes annealing at 850 K is 1.08×10^{12} molecules cm^{-2}, which is only 0.4% of the initial nitrogen coverage, it can be concluded that the C(2x2) structure is a structure with nitrogen atoms distributed

in an underlayer.

7.5.3.3. Structural models for the observed P(4x1) LEED pattern

Sellidj and Erskine [1989] observed a P(4x1) LEED pattern in their study of nitrogen adsorption on W(100). They proposed a model for the P(4x1) structure, in which nitrogen atoms occupy a combination of four-fold and bridge sites. However, there were no experimental nitrogen surface concentration data to support this model.

As our experimental results suggest that the observed transition is caused by surface reconstruction of W(100), the structural models discussed here are focused on those structural changes of W(100) which can produce a P(4x1) symmetry. The W(110) surface has a rectangular lattice with the same lattice parameter a_0 as the square lattice of W(100) on one edge, but $\sqrt{2}a_0$ on the other. Thus, the length of three unit cells of W(110) matches that of four unit cells of W(100) with an error of only 6%,

$$(3\sqrt{2}\,a_0 - 4a_0) / 4a_0 = 0.06.$$

This structural model, shown in figure 7-21, consists of a pseudo W(110) plane superimposed on the W(100) lattice. The plane is not flat, in order to maintain atom contacts normal to the surface. The rumpling of the surface effectively compensates the 6% error, and so the structure has a P(4x1) symmetry. However, according to this model, the planar atomic density increases by a factor of $\sqrt{2}$, implying long range tungsten atom migration. As discussed in section 7.5.2., for the half-covered surface, nitrogen desorption is negligible in the temperature range of 600-800 K. The transfer of

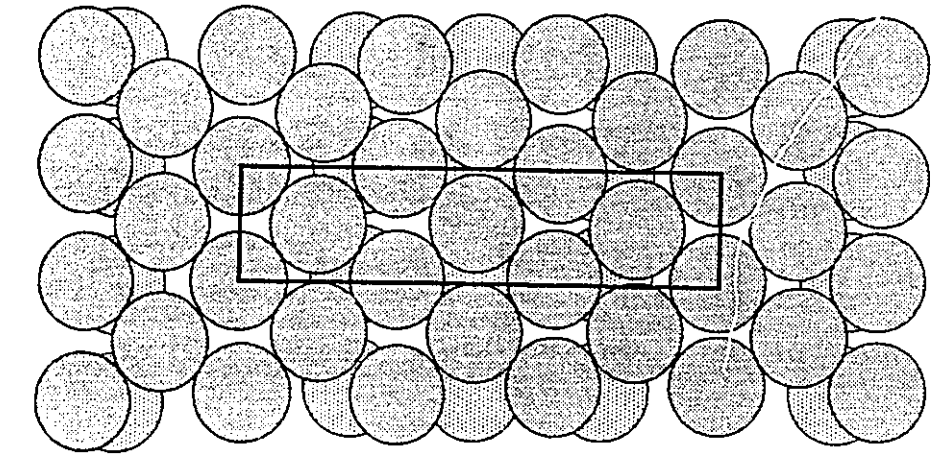

TOP VIEW

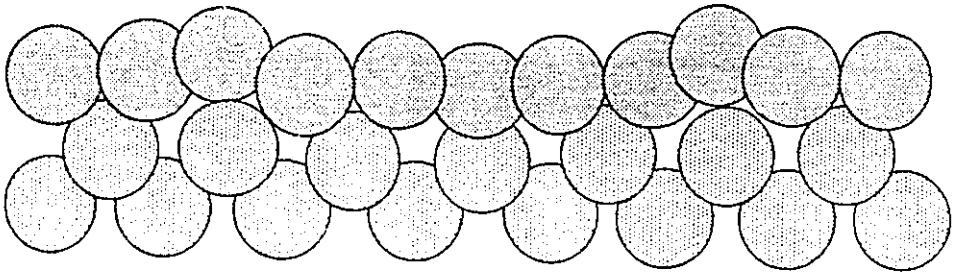

SIDE VIEW

Figure 7-21. A structural model consisting of a rumpled W(110) plane superimposed on the W(100) lattice. The length of three unit cells of the pseudo W(110) lattice matches that of four unit cells of the W(100) lattice, and therefore the structure has P(4x1) symmetry.

nitrogen atoms from the outermost layer to the underlayer must be responsible for the drop in nitrogen Auger signal in this temperature range. It is not clear in this model how the reconstruction could favour the transfer of nitrogen atoms from the outermost layer to the underlayer with such a high density surface. We can propose an alternative model which suffers from neither of these objections.

The alternative structural model involves the displacement of tungsten atoms in the first two layers as shown in figure 7-22. The structure has a P(4x1) symmetry, and has the same planar atomic density as the non-reconstructed W(100) surface. The reconstruction creates distorted octahedral holes between the first two layers. The distorted and normal octahedral holes are compared in figure 7-23. The distorted octahedral hole has a significantly larger aperture than the unreconstructed octahedral hole in the W(100) structure and, therefore, the reconstruction favours the transfer of nitrogen atoms from the outermost layer to the underlayer. With every distorted octahedral hole filled, the structure can accommodate a half-monolayer of nitrogen atoms in the underlayer.

7.5.4. The nature of the transition processes

7.5.4.1. On the low nitrogen coverage W(100) surface

As discussed in section 7.5.2., the nitrogen thermal desorption spectrum from a W(100) surface half-covered by ammonia adsorption at 300 K only has one desorption feature, the β-state, which has negligible desorption rate in the temperature range of 650-

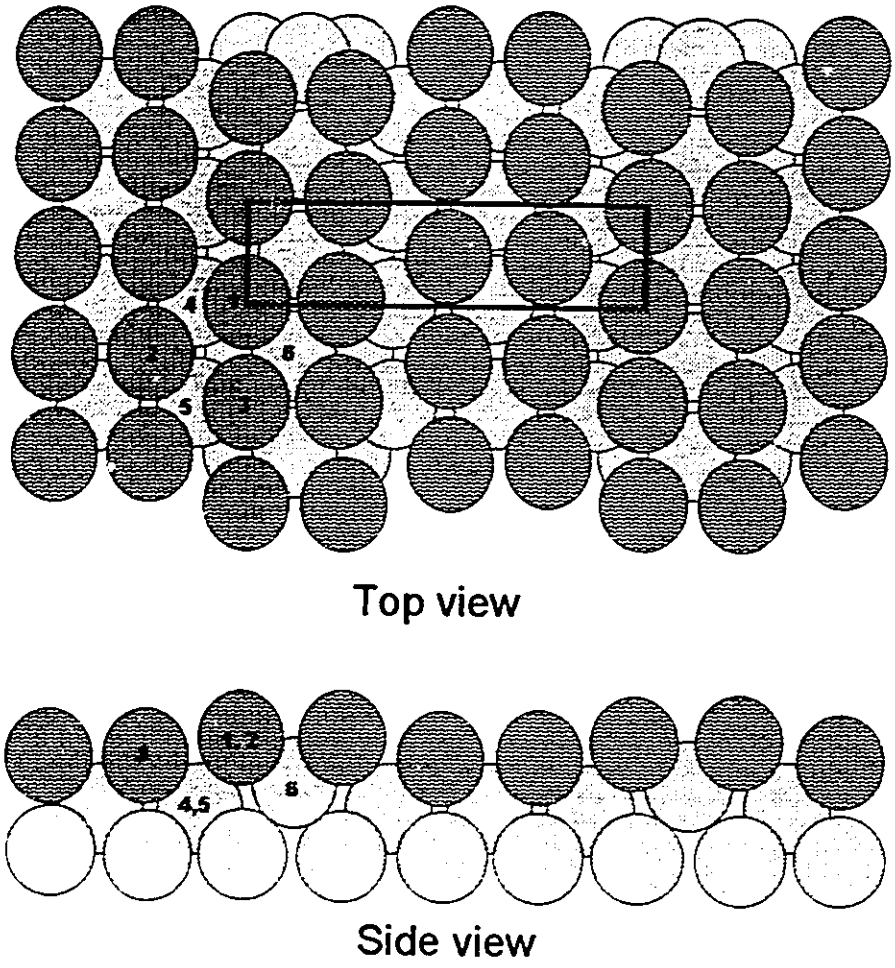

Figure 7-22. A P(4x1) structural model for reconstruction of the W(100) surface involving the displacement of tungsten atoms in the first two layers. The reconstruction creates distorted octahedral holes between the first two layers. With all these distorted octahedral holes filled, the structure can accommodate a half-monolayer of nitrogen atoms in the underlayer. One of the distorted octahedral holes is shown by the six labelled tungsten atoms and also be seen in figure 7-23.

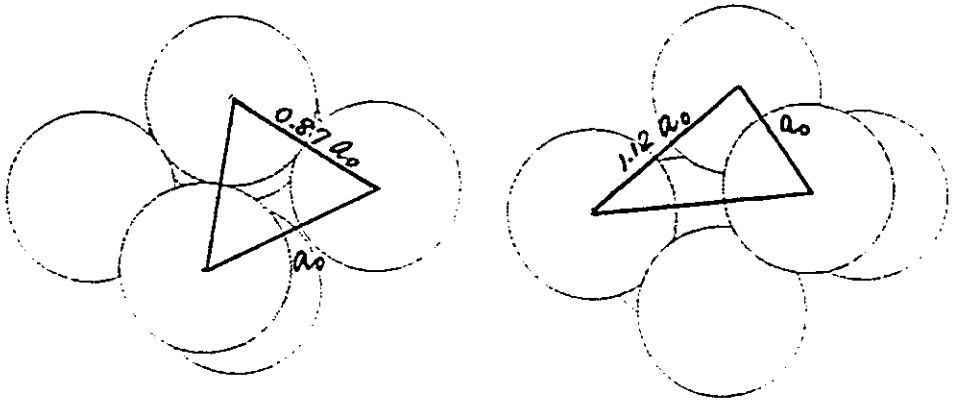

Regular octahedral hole **Distorted octahedral hole**

Figure 7-23. A distorted octahedral hole is compared with the symmetric octahedral hole in the W(100) structure. The aperture of the distorted hole is significantly larger than that of the un-distorted hole.

850 K. Thus it is extremely unlikely that nitrogen desorption is involved in the transition process for the half-coverage sample. The underlayer distribution of nitrogen atoms for W(100) after 800 K ammonia interaction provides evidence for bulk diffusion of nitrogen atoms. It suggests that the transition process could be the transfer of nitrogen atoms from the outermost layer to the second layer. This is supported by the LEED observations which show a P(4x1) reconstruction at the beginning of this transition. The P(4x1) structure, as discussed in section 7.5.3, could be formed by the displacement of tungsten atoms in the first two layers. This creates distorted octahedral holes which assists the transfer of nitrogen atoms to the underlayer. Once the transition is complete, there must be another reconstruction in which the P(4x1) structure changes to a C(2x2) structure. It is believed that these transitions observed for the half-covered W(100) sample are really the initial stage of nitride film growth.

7.5.4.2. On the high nitrogen coverage W(100) surface

For the full nitrogen coverage sample, the λ-state nitrogen desorbs at low temperatures and the LEED observations suggest that the same surface reconstruction as that of the half-covered surface also occurs. In one model, the enhanced desorption rate for λ nitrogen arises simply because of the increased adatom repulsion in the fully covered surface. Once the coverage drops to one-half, or less, by adjacent atom pair desorption [Dawson and Peng, 1972], the transition observed for the half-covered surface would follow. In an alternative picture, the surface reconstruction occurs first permiting the transfer of nitrogen atoms from the overlayer to the underlayer. This produces a

surface on which the binding energy for nitrogen is reduced and this leads to the desorption of the excess nitrogen which cannot be accommodated in the C(2x2) underlayer. In support of this model, we cite the observed inertness of the bare surface with a nitrogen underlayer to ammonia adsorption, section 7.2.6, figure 7-8. Adsorption on this surface is difficult and requires electron stimulation.

7.6. SUMMARY

Electron stimulation of the adsorption of ammonia has been observed on all three low index tungsten single crystal surfaces, W(100), W(110) and W(111). Interaction of ammonia with these surfaces at 800 K can produce nitride thin films. The depth distribution of nitrogen atoms is orientation dependent. It forms an underlayer distribution on the W(100) surface and an overlayer distribution on the W(111) surface.

Upon heating an ammonia covered W(100) sample a surface reconstruction, characterized by a P(4x1) structure and involving transfer of nitrogen atoms from the outermost layer to the second layer, occurs in the temperature range, 600-800 K. This is actually the initial stage of nitride film growth on the W(100) surface. After the surface reconstruction, nitrogen atoms are distributed in underlayers but the surface remains inert to ammonia adsorption at 300 K. Therefore, the adsorption of ammonia becomes the rate determining step for nitride film growth. This surface can be activated again by electron beam stimulation, an observation of considerable potential importance in the commercial growth of the thin nitride films.

CHAPTER EIGHT

SUMMARY AND CONCLUSIONS

The main conclusions from the previous chapters will be summarized and highlighted in this chapter, and suggestions for future work are included.

8.1. AES STUDIES OF TRANSITION METAL NITRIDE SURFACES

Auger electron spectroscopy is a powerful tool for surface science studies, and in the current work, it has been successful in the following applications:

8.1.1. Quantitative methods for surface analysis

Although it is difficult, AES can be used for surface quantification of transition metal nitrides by using external standards, high resolution techniques and spectral deconvolution techniques. In the N-Zr system, the intensity variations of Auger peaks over a wide energy range have been studied in great detail. It has been found that all zirconium Auger peaks involving valence band electrons attenuate with increasing nitrogen concentration and the extent of attenuation can be used to determine the surface nitrogen concentration. Furthermore, as the low energy Auger electrons have short inelastic mean free paths, the low energy Zr Auger peak at 23 eV is very surface

sensitive. This provides a good probe to monitor composition changes on the outermost layer, the most important layer in surface science processes.

Applying observations on the variation in the relative peak height of the MNN and MNV transitions in Zr on nitriding to the N/Ti system satisfactorily removes anomalies in the literature for N/Ti surface analysis.

8.1.2. Structural information

The intensity variations of the "metal" and "nitride" Auger features in the N-Zr system give considerable insight into the relationship between Auger emission and the geometric and electronic structure of the interstitial alloy. The low energy "metal" features attenuate linearly with increase in the nitrogen to zirconium atomic ratio, x, while the low energy "nitride" feature has a maximum intensity around x=0.5. It has been found that the intensity variation of the "metal" feature is consistent with the variation of the number of unoccupied octahedral holes in the nitride structure, and the intensity variation of the "nitride" feature is consistent with the requirement for a pair of adjacent occupied and unoccupied holes for the Auger cross transition to occur.

In the N-W system, the annealing profiles use AES to monitor surface composition changes and show a transition characterized by a decrease of nitrogen and increase of tungsten Auger peak intensity. This intensity variation of Auger peaks led to the discovery of a surface reconstruction process, in which the nitrogen adatoms move from overlayer to underlayer positions. Further information was provided by LEED

observations, but the AES data was vital in identifying the nature of the reconstruction.

It has been shown that when AES is used for surface analysis, the effect of electron beam in inducing changes in the surface concentration of the specimen under study should be carefully investigated. Proper experimental procedures should be followed to prevent, or at least to minimize, these effects.

8.2. ELECTRON BEAM STIMULATED PROCESSES

When a surface is bombarded by an electron beam, several electronic excitation processes can occur.

8.2.1. Electron beam stimulated ammonia adsorption at 300 K

During simultaneous electron irradiation and gas exposure, electron beam stimulated adsorption can occur on some surfaces. The effect of electron stimulation on ammonia adsorption has been studied on polycrystalline titanium, chromium, zirconium and tungsten surfaces and three low index tungsten single crystal surfaces. Although titanium, chromium and tungsten are situated in the three corners of the group of nine transition metals, table 1-1, and have different chemical properties, it has been found that similar electron beam effects on ammonia adsorption occur on these three transition metal surfaces. The adsorption of ammonia at 300 K without electron beam irradiation on these three transition metal surfaces saturates with a half-monolayer nitrogen coverage. Electron beam stimulation increases the saturation coverage to a full monolayer.

This behaviour has also been observed on the three tungsten single crystal samples, W(100), W(110) and W(111). Ammonia adsorption at 300 K without electron beam irradiation saturates with a half-monolayer nitrogen coverage. Electron bombardment leads to a full monolayer nitrogen coverage on these three single crystal sample surfaces.

Zirconium shows a totally different behaviour. Ammonia adsorption without electron beam irradiation can lead to a full monolayer coverage on a zirconium surface at 300 K. Zirconium has the largest metal-metal atomic separation within this group of transition metals and this suggests an important geometric factor in the interaction of ammonia with transition metal surfaces.

8.2.2. Electron beam stimulation of titanium nitride film growth

The initial stage of titanium nitride film growth involves the chemisorption of nitrogen on the surface, and the diffusion of nitrogen atoms into the titanium lattice. In the absence of electron beam bombardment, the rate of nitride film growth is limited by the rate of nitrogen gas adsorption, which is totally different from the behaviour observed with electron beam stimulation. Nitrogen adsorption on titanium at 300 K produces an adlayer which is only half-covered. At elevated temperatures, the nitrogen coverage increases because the sticking probability for activated adsorption increases. However, the activation energy for dissociative chemisorption beyond a half monolayer is so high that bulk diffusion of nitrogen atoms commences at ~760 K, and the population of nitrogen never attains full coverage. As the rate of diffusion is proportional to the concentration

gradient, the growth of the nitride film is limited by the low nitrogen coverage on the surface.

With electron beam stimulation, the adsorption rate increases so that full nitrogen coverage is maintained, even at temperatures between 600 and 1000 K. The behaviour of the nitrogen gas on titanium with electronic excitation, is indistinguishable from that observed with ammonia gas without electron beam stimulation.

8.2.3. Electron beam stimulation of tungsten nitride film growth

Experimental results show that upon heating a half-covered nitrogen on W(100) surface at temperatures from 600 to 800 K, a remarkable surface reconstruction occurs in which nitrogen atoms transfer from the overlayer to the underlayer of W(100). This surface reconstruction is characterized by a P(4x1) LEED pattern, which could be interpreted by a structural model involving the displacement of the tungsten atoms in the first two layers. The displacement of tungsten atoms creates distorted octahedral holes with a larger aperture than the regular octahedral holes in the W(100) lattice, and therefore it would favour the transfer of nitrogen atoms from the overlayer to the underlayer. After the reconstruction, this uncovered W(100) surface is inert to ammonia adsorption at 300 K and this may limit the rate of nitride film growth at high temperature. With electron beam excitation, the surface again adsorbs ammonia, and a full monolayer coverage can be obtained, suggesting an important role for electron stimulation in commercial nitride film-growth processes.

8.3. COMPARISON OF NH_3/Ti AND NH_3/W

Titanium and tungsten have very different affinities for nitrogen. Titanium forms a refractory nitride with a melting point as high as 2949°C, whereas tungsten nitride is unstable and decomposes at ~800°C. The interaction of ammonia with these two metals has been studied in this work, and the main results will be compared in this section.

Although these two metals have very different chemical properties and different crystal structures, ammonia adsorption on these two metal surfaces at room temperature produces similar results. In the absence of electron beam stimulation, both surfaces are saturated at about half monolayer coverage, and this can be increased to a full monolayer by electron beam stimulation. At elevated temperature, in the range 600 to 1000 K, electron stimulation is not required to produce a full monolayer with ammonia gas on a titanium surface, but at higher temperatures bulk diffusion causes the nitrogen surface concentration to drop.

The interaction of ammonia gas with tungsten samples at 800 K produces a low nitrogen surface concentration. The depth distribution of nitrogen atoms after the interaction is crystal orientation dependent. Experimental results from NH_3/W(100) show that nitrogen atoms transfer from the outermost layer to the second layer at temperatures from 600 to 800 K. After the transition, this uncovered surface becomes inert to ammonia adsorption at 300 K, and electron beam excitation is required for the surface to adsorb ammonia.

8.4. SUGGESTIONS FOR FUTURE WORK

8.4.1. Further investigation of beam effects on single crystals

Due to the important industrial applications of the transition metal nitrides, the investigation of the effect of electron beam bombardment during surface analysis and film growth is worthy of further investigation. In this study, zirconium has been found to behave differently from titanium, chromium and tungsten, and it is suggested that the length of M-M bond might be the key factor. The investigation has been extended to tungsten single crystal surfaces with known surface lattice geometries, but the results showed similar behaviours on W(100), W(110) and W(111) surfaces. Since these three planes have different surface lattices and therefore different adsorption sites for ammonia adsorption, no conclusion can be made at this point. A comparison of the adsorption behaviour on single crystals of titanium and zirconium would be extremely relevant, however this would be difficult because the phase transition temperatures for these two metals are low, 1155 K for Ti ($\alpha \rightarrow \beta$) and 1135 K for Zr ($\alpha \rightarrow \beta$) respectively. This makes it impossible to grow macroscopic single crystals. Other candidates for further investigation are tantalum and vanadium. Tantalum and vanadium have the same bcc crystal structure, but their lattice parameters, a_0, differ by 9.2%. Single crystal work of tantalum and vanadium hopefully will answer this question: does the M-M distance determine the extent of ammonia adsorption in the absence of electron beam stimulation?

8.4.2. Further study of the NH_3-W system

8.4.2.1. Structural studies of the N-W(100) surface

Although the N-W(100) system is one of the most extensively studied systems in surface science, a full understanding of this system has not been achieved. The present work demonstrates a new level of complexity. It has been suggested by Alnot et al. [1989] that N_{ads} poisons the ammonia chemisorption step, therefore a critical factor for ammonia decomposition on W(100) surface is the nitrogen surface coverage. An interesting surface reconstruction whereby nitrogen atoms transfer from the outermost layer to the second layer has been revealed in this thesis, and it has been found that the adsorption properties of the surface change with the reconstruction. Detailed structural studies of this surface reconstruction are very important for an understanding of the mechanism of nitride film growth and the mechanism of the ammonia decomposition reaction. The scanning tunnelling microscope (STM) is a suitable tool which could be used for further structural studies with its powerful ability to provide images for both local and long range structure of the surface under investigation. In STM measurements, a sharp metal tip is placed in a distance of a few Ångstrom to the sample surface. By recording the height of the tip as a function of the position, z(x, y), at constant tunnelling current, a topographical image can be obtained. STM has been successfully used to study the CO induced phase transition on a Pt(110) surface [Gritsch et al., 1989; 1991]. Hopefully it could provide a spatial structure pattern showing the development of the reconstruction process across the W(100) surface in the presence of surface nitrogen.

In this thesis, detailed studies were restricted to the W(100) surface and these studies need to be extended to other crystal orientations, especially to the W(111) surface. This was found to differ from W(100) in nitrogen depth distribution after ammonia gas interaction at 800 K, a difference worthy of detailed investigation.

8.4.2.2. Surface hydrogen effects

In the present work the role played by surface hydrogen from dissociated ammonia has nit been studied directly. AES gives no direct information about the surface hydrogen concentration. For the case of tungsten surfaces some information is available from previous thermal desorption studies. However new models have been proposed for this system and the possible effects of surface hydrogen need to be determined, even though the direct surface analysis for hydrogen is very difficult. The solubility of hydrogen in tungsten is very small, whereas that in titanium is very high. It is quite possible that titanium provides a infinite sink for hydrogen. However, experiments should confirm this hypothesis.

8.4.3. Nitride film growth with electron beam stimulation

It has been demonstrated that electron beam bombardment profoundly affects the kinetics of transition metal nitride film growth. In the case of titanium nitriding, electron beam stimulation of diatomic N_2 gas makes it as active as NH_3. In the case of tungsten, electron beam bombardment can activate the inert surface which forms when nitrogen atoms undergo an underlayer reconstruction on the W(100) lattice. This knowledge

suggests that novel techniques for nitride film growth can be developed. The technology would include simultaneous electron beam bombardment of the transition metal surface and exposure to a nitrogen containing gas. The substrate would be kept at a temperature at which nitrogen atoms can efficiently travel into the bulk of the transition metal lattice. The control of nitrogen concentration at the surface of the growing film would be achieved by adjustment of the beam voltage, current and the gas pressure. The ability to rapidly grow nitride films in a very clean high vacuum system would be the main advantage of the technique. This is important since the properties of the nitride film are degraded by the presence of impurities.

8.5. CONCLUDING REMARKS

The work presented in this thesis ranges from the highly stable refractory titanium nitride system to the unstable tungsten nitride system. Since these transition metal nitrides have important industrial applications as coating materials and heterogeneous catalysts, the understanding of the surface nitriding processes has tremendous technological importance.

The comprehensive AES studies on N/Zr system in a wide energy range lead to the identification of new Auger cross transition features and an understanding of the intensity variation and energy shift of Auger features during nitriding. Consequently, a quantitative surface analysis method has been established for this system.

The extensive investigation of the effect of electron beam stimulation on the

adsorption processes essential for nitriding provides a basic knowledge about these processes. On the one hand, this demonstrates how to perform experiments properly when surface science tools using electron probes are used. On the other hand, it provides a potential application for developing new techniques for preparing transition metal nitride films.

The detailed studies of the N-Ti system and the N-W(100) system demonstrate that by using surface science tools, such as AES and LEED to monitor the change of surface nitrogen concentration and the change of surface structure, an understanding of many surface processes including the adsorption of nitrogen containing gas molecules, the diffusion of nitrogen atoms into the bulk and the initial stage of nitride film growth can be achieved.

REFFERENCES

Adamson, S., O'Carroll, C. and McGilp, J. F., Vacuum, 38(4-5), 341 (1988)

Alnot, P., Cassuto, A., and King, D. A., Faraday Discuss. Chem. Soc., 87, 291(1989)

Altman, M. S., Estrup, P. J., and Robinson, I. K., Phys. Rev. B, 38(8), 5211 (1988)

Andersen, S. K., and Howie, A., Surf. Sci., 50, 197 (1975)

Anderson, J., and Estrup, P. J., Surf. Sci., 9, 463, (1968)

Armitage, A. F., Woodruff, D. P., and Johnson, P. D., Surf. Sci., 100, L483, (1980)

Axelsson, K.-O., Keck, K.-E. and Kasemo, B., Surf. Sci., 164, 109 (1985)

Barrer, R. M., Trans. Faraday Soc., 32, 490 (1936)

Bauer, E., J. Vacuum Sci. Technol. 7, 3 (1970)

Benesovsky, F., Kieffer, R., and Ettmayer, P., Nitrides, in Encyclopedia of Chemical Technology, Vol. 15, 3rd ed., John Wiley & Sons, 871 (1981)

Betteridge, J. S., Hocking, W. H., and Hayward, P. J., J. Vac. Sci. Technol., A9(3), 1237 (1991)

Bishop, H. E., and Riviere, J. C., Surf. Sci., 17, 446, (1969)

Briggs, D. and Seah, M. P., Practical Surface Analysis, John Wiley & Sons Ltd., 1983

Brundle, C. R., J. Vac. Sci. Technol., 11, 212 (1974)

Buhl, R., Pulker, H. K., and Moll, E., Thin Solid Films, 80, 265 (1981)

Chabal, Y. J., Christman, S. B., Estrup, P. J., Arrecis, J. J., and Prybyla, J. A., J. Electron Spec. Related Phenomena, 44, 17 (1987)

Chambers, S. A., Chen, H. W., Anderson, S. B. and Weaver, J. H., Phys. Rev. B., 34(5), 3055, (1986)

Campbell, C. T. and Valone, S. M., J. Vac. Sci. Technol. A3(2), 408, (1985)

Chang, C. C., Surf. Sci., 25, 53, (1971)

Clavenna, L. R., and Schmidt, L. D., Surf. Sci., 22, 365, (1970)

Coad, J. P., Bishop, H. E. and Riviere, J. C., Surf. Sci. 21, 253, (1970)

Danielson, L. R., Dresser, M. J., Donaldson, E. E., and Dickinson, J. T., Surf. Sci., 71, 615 (1978)

Davis, L. E., MacDonald, N. C., Palmberg, P. W., Riach, G. E., and Weber, R. E., Handbook of Auger Electron Spectroscopy, 2nd Ed., Physical Electronics Industries Inc., Minnesoda (1976)

Dawson, P. T., Surf. Int. Anal., 17 (6), 335, (1991)

Dawson, P. T. and Tzatzov, K. K., Surf. Sci., 249, 223, (1991)_1

Dawson, P. T. and Tzatzov, K. K. and Chen, Y., J. Phys.: Condens. Matter, 3, s207, (1991) 2

Dawson, P. T., J. Catalysis 33, 47 (1974)

Dawson, P. T. and Hansen, R. S., J. Chem. Phys., 48, 623, (1968)

Dawson, P. T., and Peng, Y. K., J. Chem. Phys., 52, 1014, (1970)

Dawson, P. T., and Peng, Y. K., Surf. Sci., 33, 565, (1972)

Dawson, P. T. and Tzatzov, K. K., Surf. Sci., 171, 139, (1986)

Dawson, P. T. and Tzatzov, K. K., Surf. Sci., 149, 105, (1985)

Dawson, P. T. and Tzatzov, K. K., Surf. Sci., 234, 339, (1990)

Dawson, P. T., and Tzatzov, K. K., Surf. Sci., 171, 239, (1986)

Dawson, P. T., and Tzatzov, K. K., J. Vac. Sci. Technol. A5(4), 1345, (1987)

Dawson, P. T., and Walker, P. C., Experimental Methods in Catalytic Research, Vol. 3 Edited by Anderson, R. B., and Dawson, P. T., Academic Press, New York, 1976, P.211

Debe, M. K., and King, D. A., J. Phys. C. 10, L303, (1977)

Ebel, H., Ebel, M. F., Baldauf, P., and Jablonski, A., Surf. Int. Anal., 12, 172, (1988)

Elsworth, L. and Holland, L., Br. J. Appl. Phys., 14, 593, (1963)

Elsworth, L. and Holland, L. and Laurenson, L., Vacuum, 15, 337, (1965)

Ertl, G. and Kuppers, J., "Low Energy Electrons and Surface Chemistry", Monographs in Modern Chemistry, edited by Ebel, H. F., 1-51, 1974

Estrup, P. J., Surf. Sci., 299/300, 722, (1994)

Estrup, P. J. and Anderson, J., J. Chem. Phys., 49, 532, (1968)

Estrup, P. J., and McRae, E. G., Surf. Sci., 25, 1, (1971)

Feldman, L. C., and Mayer, J. W., Fundamentals of Surface and Thin Film Analysis, New York, North-Holland, (1986)

Felter, T. E., Barker,R. A., and Estrup, P. J., Phys. Rev. Lett. 38, 1138, (1977)

Foord, J. S., Goddard, P. J. and Lambert, R. M., Surf. Sci., 94, 339, (1980)

Germer, L. H., Stern, R. M., and MacRae, A. U., in: Metal Surfaces, American Society of Metals, Metals Park, OH, 1963

Grant, J. T., Surf. Interface Anal., 14, 271, (1989)

Griffiths, K., Kendon, C., King, D. A., and Pendry, J. B., Phys. Rev. Lett. 46 , 1584, (1981)

Grigorov, G. I. and Tzatzov, K., Vacuum, 338, 139 (1983)

Gritsch, T., Coulman, D., Behm, R. J., and Ertl, G., Phys. Rev. Lett., 63(10), 1086 (1989)

Gritsch, T., Coulman, D., Behm, R. J., and Ertl, G., Surf. Sci., 257, 297 (1991)

Grunze, M., Chapter 5, in: The Chemical Physics of Solid Surfaces and Heterogeneous Catalysis, edited by King, D. A. and Woodruff, D. P., Elsevier, 1982, V4, P.143

Haas, T. W., Grant, J. T., Dooley, G. J., Phys. Rev. B. 1(4), 1449, (1970)

Hagg, G., Z. Phys. Chem., Abt. B12, 33, (1931)

Hachenberg, O. and Brauer, W., Advan. Electron. Electron Phys. 11, 413 (1959)

Harra, D. J. and Hayward, W. H., Nuoro Cimento Suppl. 5, 56, (1967)

Harra, D. J., J. Vac. Sci. Technol. 13, 471 (1976)

Harris, L. A., Surf. Sci., 15, 77, (1969)

Harris, L. A., J. Appl. Phys. 39, 1419, (1968)

Harris, L. A., J. Appl. Phys. 39, 1428, (1968)

Hochst, H., Bringans, R. D., Steiner, P. and Th. Wolf, Phys. Rev. B. 25, 7183, (1982)

Hochst, H., Steiner, P., Reiter, G., and Hufner, S., Z. Phys. B.: Condensed Matter 42, 199, (1981)

Housley, M., and King, D. A., Surf. Sci., 62, 93, (1977)

Ichimura,S., Shimizu, R., and Langeron, J. P., Surf. Sci., 124, L49, (1983)

Joyce, B. A. and Neave, J. H., Surf. Sci., 34 , 401, (1973)

Joyce, B. A. and Neave, J. H., J. Phys. D10, 243 (1977)

Jungblut, B., Sicking, G. and Papachristos, T., Surf. Interface Analy., 13, 135, (1988)

Jungers, J. C., and Taylor, H. S., J. Am. Chem. Soc., 57, 679, (1935)

Kankaala, K., Ala-Nissila, T., and Ying, S. C., Physica Scripta T33, 166, (1990)

Khitrova, V. I., and Pinsker, Z. G., Soviet Phys.-Crystallography, 6(6), 712, (1961)

King, B. V., in Surface Analysis Methods in Material Science, edited by O'Connor, D. J., Sexton, B. A., and Smart, R. St. C., Springer-Verlag, Berline Heidelberg, p.97, (1992)

Kirby, R. E. and Lichtman, D., Surf. Sci., 41, 447, (1974)

Komiya, S., Umezu, N., and Hayashi, C., Thin Solid Films, 63, 341, (1979)

Lambert, R. M., Bridge, M. E., Chapter 2, in: The Chemical Physics of Solid Surfaces and Heterogeneous Catalysis, edited by King, D. A. and Woodruff, D. P., Elsevier, Vol. 3B, P.59, (1984)

Landskron, H., Bickel, N., Heinz, K., Schmidtlein, G., and Muller, K., I. Phys.: Condens. Matter 1, 1, (1989)

McAllister, J., and Hansen, R. S., J. Chem. Phys., 59, 414, (1973)

Madey, T. E., Surf. Sci. 33, 355, (1972)

Mahan, A. H., T. W. Riddle, Dunning, F. B., and Walters, G. K., Surf. Sci., 93, 550, (1980)

Matsushita, K. and Hansen, R. S., J. Chem. Phys., 51, 472, (1969)

May, J. W., Ind. Eng. Chem., 57, 18, (1965)

May, J. W., Szostak, R. J. and Germer, L. H., Surf. Sci., 15, 37, (1969)

Mittasch, A., Adv. Catal., 2, 81, (1950)

Nagasaka, M. and Yamashina, T., J. Vac. Sci. Technol., 9, 543, (1972)

Nakasaki, Y., Suguro, K., Shima, S., and Kashiwagi, M., J. Appl. Phys. 64(6), 3263, (1988)

Nanbu, K., Vacuum, 35(12), 573, (1985)

Neave, J. H., Foxon, C. T., and Joyce, B. A., Surf. Sci., 29, 411, (1972)

Palmberg, P. W., The Structure and Chemistry of Solid Surfaces, edited by Somorjai, G. A., John Wiley & Son Inc, New York, P.29, 1969

Pantano, C. G. and Madey, T. E., Application of Surface Science, 7,115, (1981)

Peng, Y. K., and Dawson, P. T., J. Chem. Phys., 54 , 950, (1971)

Peng, Y. K. and Dawson, P. T., Can. J. Chem., 52, 1147, (1974)

Pick, S., Surf. Sci. Reports 12, 99, (1990)

Pokela, P. J., Kwok, C.-K., Kolawa, E., Raud, S., and Nicolet, M.-A., Appl. Surf. Sci., 53, 364, (1991)

Rao, C. N. R., and Rao, G. R., Surf. Sci. Report, 13, 221, (1991)

Reed, A. P. C., and Lambert, R. M., J. Phys. Chem., 88(10),1954, (1984)

Sanz, J. M., Palacio, C., Casas, Y. and Martinez-Duart, J. M., Surf. Interface Analy., 10, 177, (1987)

Schwarzkopf, P., Kieffer, R., Leszynski, W., and Benesovsky, F., Refractory Hard Metals, Macmillan, New York, 1953

Seah, M. P., Surf. Sci. 17, 132, (1969)

Seah, M. P., Surf. Interface Anal., 9, 85, (1986)

Seah, M. P. and Dench, W. A., Surf. Interface Anal., 1, 2, (1979)

Sellidj, A., and Erskine, J. L., Surf. Sci., 220, 253, (1989)

Shimizu, R., Jpn. J. Appl. Phys. 22, 1631, (1983)

Shirley, D. A., Phys. Rev., B5, 4709 (1972)

Sickafus, E. N., Phys. Rev. 16(4), 1436, (1977)

Sormerton, C., and King, D., Surf. Sci., 89, 391, (1979)

Tanabe, T., Tanaka, M. and Imoto, S., Surf. Sci., 187, 499, (1987)

Tanuma, S., Powell, C. J., and Penn, D. R., Surf. Int. Anal., 11, 577, (1988)

Thompson, M., Baker, M. D., Cheistie, A. and Tyson, S. F., Auger Electron Spectroscopy, in Chemical Analysis Vol. 74, John Wiley & Sons, New York, 1984

Toth, L. E., Transition Metal Carbides and Nitrides, Academic Press, New York, 1971

Verhoeven, J. and Los, J., Surf. Sci., 58, 566, (1976)

Werner and Garten, R.P.H., Rep. Prog. Phys. 47, 221, (1984)

Wilf, M. and Folman, F., Surf. Sci., 52(1), 10, (1975)

Wilf, M. and Folman, F., J. Chem. Soc., Faraday Trans. 1, 72(5), 1165, (1976)

Wolff, P. A., Phys. Rev. 95(1), 56, (1954)

Yates, J. T., and Madey, T. E., The Structure and Chemistry of Solid Surfaces, Edited by Somorjai, G. A., Wiley, New York, p.59, 1969

Zhou, M. Y., Milne, R. H., Karolewski, M. A., Frost, D. C. and Mitchell, K. A. R., Surf. Sci., 139, L181, (1984)